Development of Electrochemical Characterization Methods and Advanced Capacitor Materials

Marveh Forghani, MPhil

Thesis submitted to fulfil the requirements of the degree

Doctor of Philosophy

Submitted October 2019

Discipline of Chemistry

University of Newcastle

Callaghan, NSW, 2308, Australia

STATEMENT OF ORIGINALITY

I hereby certify that the work embodied in the thesis is my own work, conducted under normal supervision. The thesis contains no material which has been accepted, or is being examined, for the award of any other degree or diploma in any university or other tertiary institution and, to the best of my knowledge and belief, contains no material previously published or written by another person, except where due reference has been made. I give consent to the final version of my thesis being made available worldwide when deposited in the University's Digital Repository, subject to the provisions of the Copyright Act 1968 and any approved embargo.

Marveh Forghani ……. Date: 10 October, 2019

THESIS BY PUBLICATION

I hereby certify that this thesis is in the form of a series of papers. I have included as part of the thesis a written declaration from each co-author, endorsed in writing by the Faculty Assistant Dean (Research Training), attesting to my contribution to any jointly authored papers.

Marveh Forghani ……. Date: 10 October, 2019

By signing below I confirm that the Research Higher Degree candidate, Marveh Forghani contributed towards data generation/analysis and manuscript preparation for all the publications included in this thesis for which I am a co-author (Reference details in page iv of this thesis).

Supervisor and co-author

Professor Scott Donne ……. Date: 9 October, 2019

Assistant Dean Research Training

Professor Frances Martin …… Date: October 15, 2019

ACKNOWLEDGEMENTS

First of all, I would like to acknowledge my principal supervisor, Professor Scott Donne, who has supervised me and provided me with valuable guidance, knowledge and support throughout my PhD studies.

I would also like to acknowledge the University of Newcastle, Australia for the provision of a PhD scholarship

My thanks also extend to all academic and staff in the chemistry discipline at the University of Newcastle who have helped and supported me during my PhD studies.

Last but not least, I would like to thank the members of my family; my mother Maryam, my father Issa and my brother Reza and also my friends for their continued support throughout my studies.

LIST OF PUBLICATIONS

Publications Included in Thesis

1. **Forghani, M.**, & Donne, S. W., (2018). *"Duty Cycle Effects on the Step Potential Electrochemical Spectroscopy (SPECS) Analysis of the Aqueous Manganese Dioxide Electrode."* Journal of The Electrochemical Society, 165(3), A593-A602.

2. **Forghani, M.**, & Donne, S. W., (2018). *"Method comparison for deconvoluting capacitive and pseudo-capacitive contributions to electrochemical capacitor electrode behavior."* Journal of The Electrochemical Society, 165(3), A664-A673.

3. **Forghani, M.**, & Donne, S. W. (2019). *"Complications When Differentiating Charge Transfer Processes in Electrochemical Capacitor Materials: Assessment of Cyclic Voltammetry Data."* Journal of The Electrochemical Society, 166(8), A1370-A1379.

4. **Forghani, M.**, & Donne, S. W. (2019). *"Modification of the Step Potential Electrochemical Spectroscopy Analysis Protocol to Improve Outcomes."* Journal of The Electrochemical Society, 166(13), A2727-A2735.

Additional Publications

1. Dupont, M. F., **Forghani, M.**, Cameron, A. P., & Donne, S. W. (2018). *"Effect of electrolyte cation on the charge storage mechanism of manganese dioxide for electrochemical capacitors."* Electrochimica Acta, 271, 337-350.

2. Fellows, H. M., **Forghani, M.**, Crosnier, O., & Donne, S. W. (2019). *"Modelling voltametric data from electrochemical capacitors."* Journal of Power Sources, 417, 193-206.

3. Abbas, S. A., **Forghani, M.**, Anh, S., Donne, S. W., & Jung, K. D. (2019). *"Carbon Hollow Spheres as Electrochemical Capacitors: Mechanistic Insights."* Energy Storage Materials, Available online on the 28th June 2019.

4. **Forghani. M.**, McCarthy. J., Mavroudis. H. & Donne. S. W. *"Electroanalytical Characterization of Electrochemical Capacitor Systems."* Electrochimica Acta, Available online on the 7th October 2019.

5. **Forghani. M.**, McCarthy. J. & Donne. S. W. *"Oscillatory Current Behaviour in Energy Storage Electrode Materials."* Submitted on Journal of The Electrochemical Society on the 28th of August 2019.

Conference Presentations

1. **Forghani, M.**, & Donne, S. W., *"Effects of Different Duty Cycle on the Step Potential Electrochemical Spectroscopy (SPECS) Analysis."* PRiME 2016 meeting 2-7 of October 2016, Honolulu, USA.

2. **Forghani, M.**, & Donne, S. W., *"Effect of Temperature the Step Potential Electrochemical Spectroscopy (SPECS) Analysis of Manganese Oxides for Electrochemical Capacitors."* ISEE CAP 2017, 10-14 July 2017, Jena, Germany.

3. **Forghani, M.**, & Donne, S. W., *"Study of Ageing Mechanisms of Electrochemical Capacitor Materials Using Step Potential Electrochemical Spectroscopy (SPECS) Analysis."* ISEE CAP 2017, 10-14 July 2017, Jena, Germany.

4. **Forghani, M.**, & Donne, S. W., *"Deconvoluting Capacitive and Pseudo-Capacitive Contributions to Electrochemical Capacitor Electrode Behaviour."* 232nd ECS MEETING, 1-5 October 2017, National Harbor, MD (greater Washington, DC area), USA.

5. **Forghani, M.**, & Donne, S. W., *"Modelling of Voltammetric Data from Electrochemical Capacitor Electrodes."* AiMES Conference, September 30-October 4, 2018 Cancun Mexico.

6. **Forghani, M.**, & Donne, S. W., *"Temperature Effects on the Performance of Activated Carbon Electrochemical Cell in Aqueous and Non-Aqueous Electrolytes."* AiMES Conference, September 30-October 4, 2018 Cancun Mexico.

7. **Forghani, M.**, & Donne, S. W., *"Effect of Electrolyte Cation on the Electrochemical Performance of AC Electrochemical Capacitor."* AiMES Conference, September 30-October 4, 2018 Cancun Mexico.

8. **Forghani, M.**, & Donne, S. W., *"Electrolyte Concentration Effects for Activated Carbon Electrodes Using Electroanalytical Methods."* ISEECap 2019, 6-10 May, Nantes, France.

9. **Forghani, M.**, & Donne, S. W., *"Electrolyte Ion Effects for Activated Carbon Electrodes Using Electroanalytical Methods."* ISEECap 2019, 6-10 May, Nantes, France.

ABSTRACT

This thesis focuses on developing the most common electrochemical methods; cyclic voltammetry (CV) and step potential electrochemical spectroscopy (SPECS). Although CV and SPECS techniques have previously been used for characterising the performance of various energy storage devices, this study shows that there is always a room for improving the present electrochemical techniques and just repeating the conventional electrochemical methods is not the best approach to study the modern electrochemical storage devices with novel and more complex electrode materials.

This thesis includes nine chapters. Chapter 1 is the introduction to the thesis. Chapters 2 to 4 focus on the literature reviews on the energy storage devices, electrochemical capacitor materials and electrochemical methods. Chapters 5 to 8 present four experimental studies on the electrochemical capacitors and Chapter 9 is the conclusion to this thesis.

Herewith, the various experimental parameters involved in these two techniques have been further explored, and the performance of these methods for characterising the behaviour of electrochemical cells was compared experimentally. This thesis presents the application of CV and SPECS methods on testing electrochemical capacitors with various electrode materials such as activated carbon and manganese dioxide with aqueous and organic electrolytes.

The SPECS method is based on applying a series of equal magnitude potential steps on a working electrode, with sufficient rest time to allow for quasi-equilibrium to be established for each step throughout an applied potential window. This slow sweep rate enables an electrode to approach its maximum charge storage capability. More importantly, it allows separation of charge storage mechanisms, such as electrical double layer charge storage and diffusion-limited processes. The effect of the two main experimental variables in SPECS; namely, the

potential step size and the electrode rest time, on the behaviour of the electrochemical capacitor is described in Chapter 5.

The contribution of the capacitive and diffusion-limited processes can be obtained via the voltammetric current-sweep rate dependence, voltammetric charge-sweep rate dependence and SPECS methods. These three methods were compared experimentally and also their limitations, and their advantages for interpreting the current data and their abilities to distinguish between the different charge storage mechanisms is presented in Chapter 6.

Some of the complications associated with using a common approach; namely voltammetric current-sweep rate dependence, to deconvoluting double layer and diffusion-limited contributions to the performance of an electrochemical capacitor electrode, have been explored and presented in Chapter 7.

Finally, Chapter 8 presents an improved methodology for the interpretation of SPECS data. The revised methodology provides an analysis method that produces performance data much closer to CV data, thus enabling both relative and absolute characterisation of electrochemical capacitor electrodes, as well as increasing the versatility of the SPECS analysis method.

TABLE OF CONTENTS

Chapter 1: Thesis Overview

This work focused on developing and studying the electrochemical methods for characterising the charge storage mechanisms in electrochemical capacitors. Specifically, the step potential electrochemical spectroscopy (SPECS) and cyclic voltammetry (CV), which have been used for deconvoluting capacitive and pseudo-capacitive contributions, have been further developed.

Cyclic voltammetry is one of the most common methods for examining electrochemical energy storage devices. This method provides valuable information about the performance of the electrochemical cell as well as mechanistic information about the electrochemical materials. The cyclic voltammetry can also be modelled to differentiate charge storage mechanisms such as the electrical double layer and diffusion-limited processes. The most common approaches are the current dependence on sweep rate and the charge dependence on sweep rate from cyclic voltammetry data. However, under certain conditions, these approaches could not reliably reproduce the initial electrochemical data, indicating that there may be complications associated with the use of voltammetric data to differentiate charge storage mechanisms in electrochemical capacitors. Hence, in this thesis, some of the complications associated with using a common approach namely known as the voltammetric current dependence on sweep rate have been explored and a model has been developed to deconvolute the various contributions to the overall voltammetric response. These contributions are based on a series RC circuit representing electrical double layer formation, a Nernst equation derived expression representing redox processes in a localized energy domain, the Butler-Volmer equation to describe redox processes at the extremes of potential typically associated with electrode instability, and the ohmic resistance of the electrode.

The SPECS method is based on applying a series of equal magnitude potential steps on a working electrode, with sufficient rest time to allow for equilibrium to be established for each step throughout an applied potential window. This slow scan rate enables an electrode to approach its maximum charge storage capabilities. More importantly, it allows the separation of the charge storage mechanisms, such as electrical double layer and diffusion-limited processes.

This method also can provide fundamental information about electrochemical materials and system behaviour such as kinetics, ESR, diffusional processes, double layer capacitance, fast and slow processes, and also infer electrode instabilities from the residual current. Although the SPECS method has been broadly used to characterise the performance of electrochemical cells, the influence of the two main SPECS experimental parameters, the potential step amplitude and equilibration time, had not been studied thoroughly. This thesis has explored and determined the influence of SPECS experimental parameters, such as different equilibration times and potential steps, on the contribution of charge storage mechanisms and series resistance.

Moreover, the synthetic voltammogram, produced from SPECS data, has been further developed in this thesis. While the previous approach had been shown to provide a good relative comparison between different processes (electrical double layer and diffusion-limited processes) and different electrochemical materials, the absolute performance is different when compared to actual cyclic voltammetry data, except at very slow sweep rates. Therefore, the revised methodology presented in this thesis provides an analysis method that produces performance data much closer to CV data, thus enabling both relative and absolute characterization of electrochemical capacitor electrodes, as well as increasing the versatility of the SPECS analysis method.

The electrochemical cells in this study, have been made from different electrode materials, e.g., electrolytic manganese dioxide, activated carbon and nickel oxide/hydroxide, and they have been tested in aqueous and organic electrolytes.

Three chapters of this thesis are a review of the current literature on electrochemical energy storage technologies, with a focus on electrochemical capacitors. Chapter 2 provides an introduction to energy storage methods and the importance of energy storage systems.

Chapter 3 focuses on the various type of electrochemical capacitors, such as electrical double layer capacitors and pseudo-capacitors or supercapacitors. This chapter provides important information about the two main charge storage mechanisms, electrical double layer process and diffusion-limited processes. This is followed by a review of electrochemical materials and their properties, e.g., carbon-based materials, metal oxides, and conducting polymers.

Chapter 4 provides a discussion on most common electrochemical characterisation techniques such as cyclic voltammetry (CV), step potential electrochemical spectroscopy (SPECS) and electrochemical impedance spectroscopy (EIS).

In chapter 5, the effect of the two main experimental variables in SPECS; namely, the potential step size and the electrode rest time, on the behaviour of the aqueous manganese dioxide electrode, has been studied. The effect of potential step size on the resultant SPECS data arises because of its ability to influence electrode polarisation, and hence the driving force for charge storage in the electrode. Conversely, the rest time between potential steps influences the extent to which the electrode equilibrates before the next step is taken. When combined, these variables essentially influence the rate of electrode cycling, with its corresponding effects on performance.

In chapter 6, the SPECS method has been compared with the CV method (at different sweep rates), which conventionally has been used to differentiate charge storage mechanisms.

Comparison of these methods indicates that at higher sweep rates, the SPECS method was better able to characterise the behaviour of the electrical double layer processes at the surface of the electrode.

In chapter 7, some of the complications associated with using a conventional method to deconvoluting double layer and diffusion-limited contributions in a voltammetry experiment (at different scan rates) have been explored. The models we have used in this study are based on theoretical electrical and electrochemical responses to stimuli for an electrochemical capacitor material, including contributions from double layer capacitance (series RC circuit), charge transfer processes in a localized domain, diffusion-limited processes, and electrode instabilities (Butler-Volmer equation).

In chapter 8, the analysis of SPECS data has been improved to generate a rigorous synthetic voltammogram which is comparable to the actual voltammetric data. The revised methodology for analysing SPECS data is based on this fact that the formation of a double layer on the electrode-electrolyte interface for each subsequent i-t transients in a SPECS experiment are independent of each other. The comparison between the experimental CV data was in a very good agreement with that generated from the revised SPECS analysis.

Chapter 9 provides a summary and conclusion on developed electrochemical methods in this thesis and a discussion on the importance of improving electrochemical characterisation techniques for evaluating the performance of electrochemical materials and devices. Also, the potential areas of future research following on this work have been recommended here.

Chapter 2: Introduction to Energy Storage

2.1. Importance of Energy

Increases in worldwide demand for energy not only leads to growth in the generation of energy from fuels such as oil, natural gas and coal but also from different types of renewable energy such as wind, solar, geothermal, biomass, hydropower and nuclear. The produced energy has been delivered to the three main energy consumption sectors, transportation, industrial and residential and commercial. Currently, fossil fuels contribute the most towards generating electricity, with almost 65% in 2016. Coal contributes the most towards generating electricity with 38% in 2016. After coal, natural gas with 23%, hydro with 16.3% nuclear energy with 10%, non-hydro renewable energy with 8% and oil with 4% were used for electricity generation in 2016 [1-3].

However, fossil fuel is not a reliable source for producing energy due to the rising price of fuels, uncertainties in energy markets, securing supplies of primary energy suppliers and environmental regulations [4-6]. The amount of CO_2 emissions by fossil fuel was 32,316 Mt in 2016 [1]. Hence, there is considerable interest in improving methods of producing clean energy. It is predicted that there is a continuing growth in renewable energy generation worldwide. For instance, the Annual Energy Outlook 2019 in the U.S. has predicted the renewable energy contribution in producing electricity to increase from 18% in 2018 to 31% in 2050 [7].

To achieve this goal, the improvement of efficient energy storage systems is necessary. One of the important applications of energy storage is transportation and grid storage because a large amount of energy has to be transferred or accepted in a short time [8]. The main types of energy storage systems are mechanical energy storage, thermal energy storage and electrochemical energy storage such as batteries and supercapacitors. Chapter 2 presents a review of the current

energy storage systems and especially focuses on the comparison of electrochemical energy storage technologies.

2.2. Energy Storage Systems

The integration of renewable energy into the grid system is a big challenge due to the fluctuating and intermittent nature of renewable sources such as wind power and solar energy [9-11]. Hence, improving the efficiency of energy storage systems for the grid is required due to the continuing growth in renewable generation, managing the peak demands for electricity and increasing the reliability of grid systems. There are several types of energy storage technologies that have been used at a large scale [12, 13];

- Mechanical energy storages such as pumped hydroelectric, compressed air energy storage and flywheels;
- Thermal energy storages such as solar thermal storage integration and thermal storage for heating, ventilation, and air conditioning (HVAC);
- Chemical energy storages such as using hydrogen or other chemicals as energy storage systems;
- Electrical and electrochemical energy storage systems such as supercapacitors, batteries and fuel cells.

Currently pumped hydroelectric is the main energy storage system of worldwide storage capacity, and after that, compressed air storage is in a second place [14]. **Figure 1** shows the general comparison of discharge time and power rating for various energy storage systems. It can be seen that the electrochemical energy storage such as batteries and supercapacitors has a short response time compared with mechanical energy storage such as pumped hydro and compressed air energy storage. Moreover, electrochemical energy

storage is more desirable due to their low environmental impact, high power and energy flexibility, high sweep efficiency and cyclability, and low maintenance [14, 15].

Hence, electrochemical energy storage can potentially be an alternative system for bulk energy storage and for distributing energy loads at any time. However, electrochemical energy storage systems available today are relatively expensive. Thus, the development of electrochemical energy storage products that are cost-effective, safe and have a reliable operation is necessary [14].

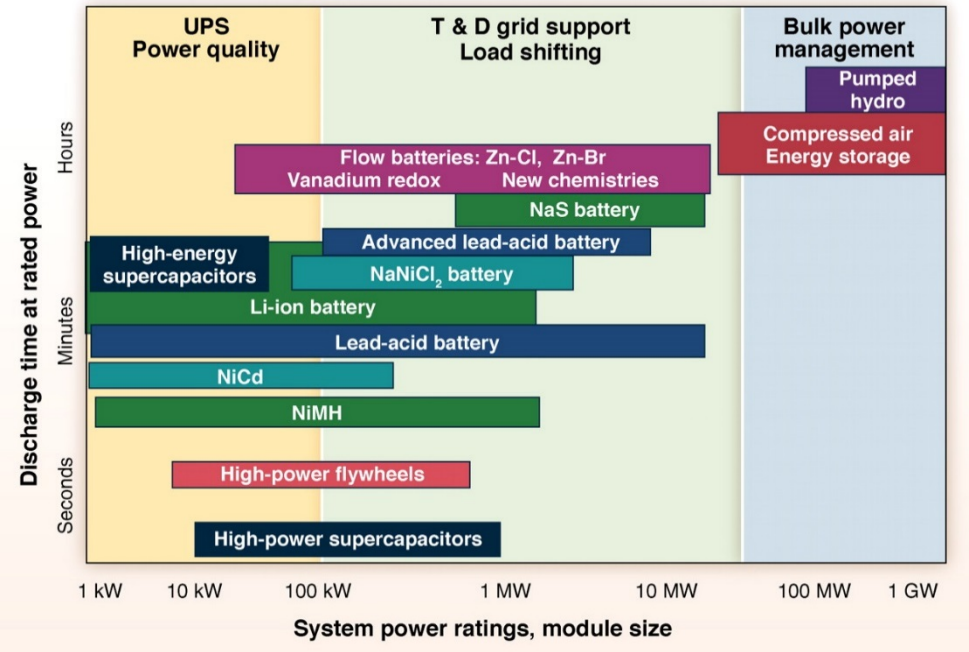

Figure 1 General comparison of discharge time and power rating for various energy storage systems. (T&D = Transmission and Distribution; UPS = Uninterrupted Power Supply) [16]

2.3. Electrochemical Energy Storage

The relationship between the different types of electrochemical energy storage such as batteries, fuel cells, and electrochemical capacitors is described by a Ragone diagram, which is shown in **Figure 2** [17].

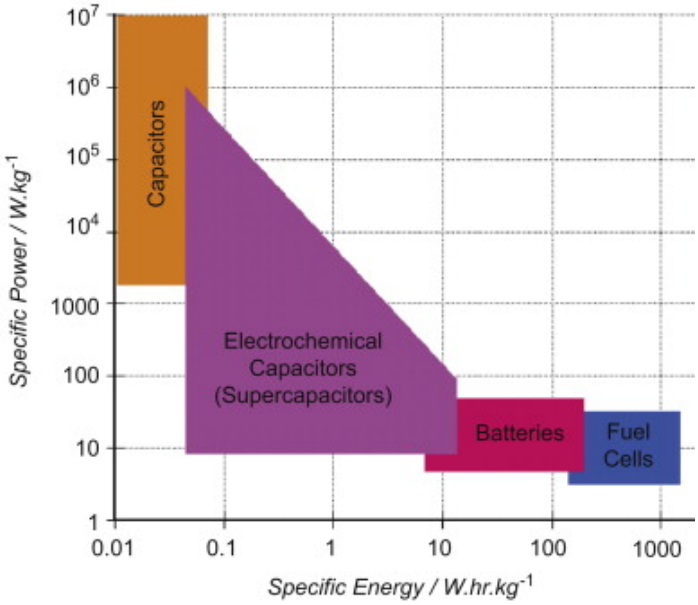

Figure 2 Ragone diagram illustrating the relative specific energy (Wh kg-1) and specific power (W kg-1) of electrochemical devices [15]

The specific energy and power of the electrochemical energy storage systems can be calculated using the specific capacitance of the electrochemical energy storage material. The specific energy E (Wh/kg) of the system is given by [18];

$$E = \frac{1}{2} C \mathrm{V}^2 \tag{1}$$

where C is the specific capacitance (Ah/V/kg) and V is an applied potential window (V). The calculated specific energy can be used to calculate the output power (P; W/kg) of the electrochemical energy storage using [18];

$$P = \frac{E}{t} \tag{2}$$

where t is the time (h) over which the energy is passed.

In general, electrochemical capacitors provide the highest power density (W/kg) at the expense of energy density (Wh/kg). Batteries and fuel cells provide higher energy density compared to electrochemical capacitors [19]. While batteries such as lithium-ion have a higher energy

density and good performance, they are costly and suffer from relatively low power density and limited cyclability. Alternately, electrochemical capacitors with much higher power density can be utilized in some applications, such as for uninterruptible power supplies and load-levelling [20]. Hence, extensive research has been done to increase the specific capacitance and area of electrochemical capacitors and, ultimately, their performance.

2.4. Electrochemical Capacitors

Electrochemical capacitors are energy storage and conversion technologies that provide high power and very good cyclability at the expense of low energy. The energy which is stored in an electrochemical capacitor is proportional to its capacitance and cycling potential. Thus, increasing the specific capacitance and the potential window leads to higher specific energy in an electrochemical capacitor. Current research trends are to develop new materials with higher specific capacitance, larger working potential window, and new capacitor systems with wide electrochemical windows to deliver higher energy [20].

Generally, the capacitive behaviour of the electrochemical capacitors is associated with an electrical double layer at the surface of the electrode, and in some materials pseudo-capacitance, which results from reversible redox processes. Electrochemical double-layer capacitors (EDLCs), store charge directly in the double layer of the electrode-electrolyte interface where charge separation takes place between the electrode and electrolyte [21-23].

Carbon-based materials have been used widely in EDLC, because of their high specific surface area (SSA), high chemical stability, environmentally friendliness and moderate cost. The different types of carbon that have been used in EDLCs are activated carbon, graphite, carbon nanotubes (CNTs), carbon nanofibers (CNFs), fullerenes and nano-onions which, are the most common EDLC material [20, 24-28]. Activated carbon-based systems demonstrate excellent

power densities up to 10^4 W/kg and cyclability more than 10^5 cycles without any significant fade [29-32].

The charge storage mechanism of pseudo-capacitors involves fast reversible redox reactions at the surface of the electrode material coupled with double layer capacitance. The most common EC materials that exhibit the pseudo-capacitive behaviour are conducting metal oxides such as ruthenium dioxide (RuO_2) and manganese dioxide (MnO_2), nitrides, sulfides, and conductive polymers [33-36]. Typically, the specific capacitance of pseudo-capacitors is much higher than EDLCs [20, 24, 37]. For instance, the capacitance of activated carbon-based capacitors is generally around 150 F/g in aqueous electrolytes [38], while electrodeposited thin films of manganese dioxide have exhibited capacitances over 2000 F/g [19]. However, because of the redox reaction, pseudo-capacitors can be unstable during cycling, in contrast with EDLCs, which are highly reversible [24]. The capacitance of ECs is influenced significantly by the surface area and morphology of the material. Thus, many studies have been undertaken to determine the effects of material properties, on the contribution of the different charge storage mechanisms in ECs.

Chapter 3: Electrochemical Capacitors

3.1. Fundamentals of Electrochemical Charging Processes

Generally, the capacitive behaviour of electrochemical capacitors is associated with the electrical double layer at the electrode-electrolyte interface, and in some materials pseudo-capacitance, which is a result of reversible redox processes [21]. This section reviews the fundamentals of electrochemical charging processes, which are mainly the electrical double layer processes (non-faradaic reactions) and the redox processes (faradaic reactions).

3.1.1. Electrical Double Layer

This section reviews the development in the understanding of the electrical double layer, noting the earliest formal treatment by Helmholtz (1853) [39], modifications to the theory by Gouy (1910) [40] and Chapman (1913) [41], then the key advancement by Stern (1924) [42] and the work of Graham (1947) [43] which incorporated a nature of cations and anions to describe the double layer effect.

The electrical double layer is one of the most important models that has been developed for describing the interfacial capacitance of an electrode surface and electrolyte. The term “double layer” was first mentioned by Helmholtz. According to his model, the counter charge in an electrolyte solution resides on the surface of an electrode. Hence, there would be two layers of opposite charge at either side of the interface, which is shown in **Figure 3(a)** [44].

Later Gouy mentioned that the ions on the electrolyte side of the double layer cannot be static due to the effects of thermal fluctuation based on the Boltzmann principle. He modified the Helmholtz model by introducing the diffuse layer shown at **Figure 3 (b)**, where the cations and anions are distributed in the electrolyte side of double layer and having a net charge density equal and opposite to the electron excess on the surface of the electrode. The Gouy model was mathematically treated by Chapman using the Poisson-Boltzmann equation. However, the

double layer capacitance determined by the Gouy-Chapman model is too large because it is defined as an exchange rate of net ionic charge on the electrolyte side and electrode-electrolyte potential difference across the interface.

After that, Stern modified and developed the double layer theory and solved the double layer capacitance problem. According to the Stern model the first layer of ion distribution could be explained by a Langmuir adsorption model, and beyond the first layer is a diffuse region of ionic charges that can be explained by Gouy-Chapman model. Hence, the double layer capacitance can be obtained from a series relation between the capacitance of the first layer or Stern layer and diffuse region of ionic charges.

Later, Grahame modified the Stern model by dividing the inner layer of the Stern model into the inner Helmholtz plane and outer Helmholtz plane. He proved that the distance of the inner layer depends on the population of anions or cations in the electrolyte and the charge of the electrode surface. According to the Grahame model, the distance of the inner layer from the positively charged surface electrode is almost double that of the negatively charged electrode surface, due to the smaller size of cations compared to anions [21]. **Figure 3** shows the comparison of the **(a)** Helmholtz model and **(b)** Stern-Graham model of the electrical double layer.

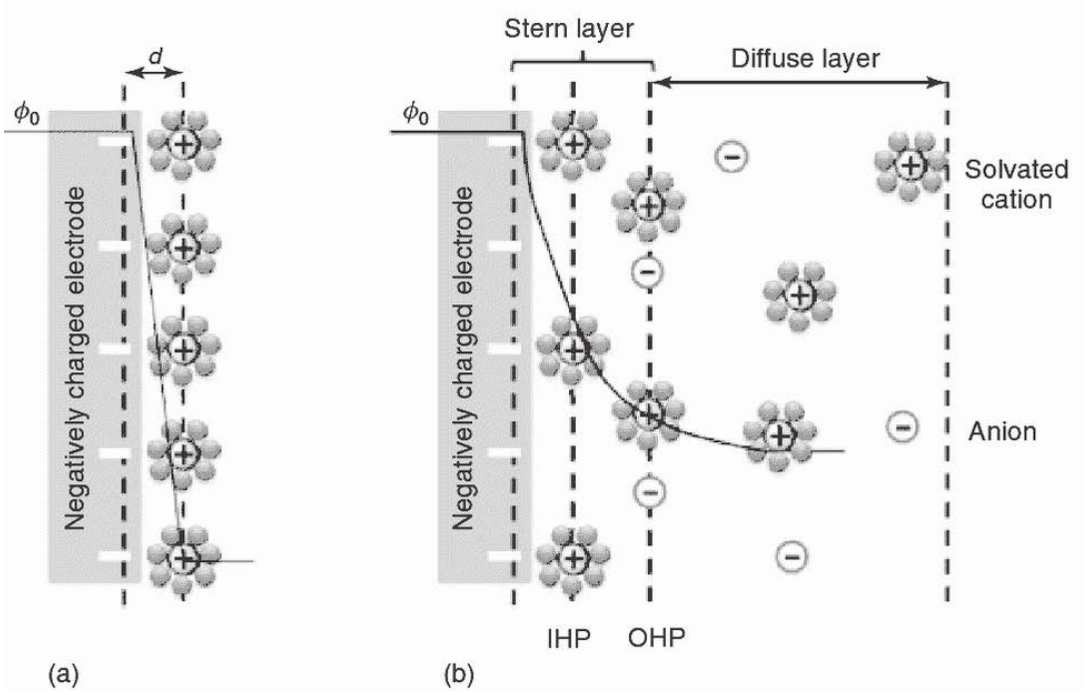

Figure 3: (a) Helmholtz model. (b) Stern-Graham model. Ø◦ refers to the potential of the electrode surface, d is the distance of double layer described by Helmholtz, IHP (Inner Helmholtz Plane) is the distance of the centres of specifically adsorbed ions, and OHP (Outer Helmholtz Plane) is the distance of the centres of non-specifically adsorbed ions [45]

The thickness of the double layer is governed by the ionic concentration of the solution which is less than 100 Å for concentrations greater than 0.01 M. It should be mentioned that the inner layer ions are partially solvated which are different from the outer layer solvated ions. The structure of the electrical double layer is one of the important factors that can affect the rate of electrochemical processes [44].

3.1.2. Pseudo-Capacitance

The pseudo-capacitance mechanism is a kind of charge storage mechanism, which can store charge via fast, reversible redox reactions that occur at the surface or into the bulk of electrode [21, 46, 47]. In contrast with the electrical double layer process, which is an electrostatic mechanism, the pseudo-capacitance mechanism stores charges through a thermodynamically

and kinetically redox reaction. This redox reaction must be reversible or semi reversible for increasing efficiency of pseudo-capacitors. Otherwise, a non-ideal reversible redox reaction can irreversibly damage the capacitance. Generally, the reversibility of a redox reaction is dependent on several factors, such as the chemical structure of the material, kinetics and the rate of the reaction, the potential range of an electrolyte and the chemical reversibility of the reaction [48]. Pseudo-capacitive materials similar to capacitive materials exhibit a dependency on a width of the potential window, but their charge storages originate from different mechanisms [47, 48]. In the electrical double layer process, charging and discharging occur physically at a surface of the electrode, while in the redox reaction, each reactant species in the bulk of the material contributes one or more charges for storing energy. Therefore, the specific capacitance of pseudo-capacitive materials is much higher than that of capacitive materials [48-50].

3.2. Electrode Materials

Generally, the charge is stored in the electrochemical capacitors by means of the electrochemical double layer process which is associated by the surface of the electrode and by the reversible redox processes at the surface or bulk of the electrode. This section reviews the electrode materials which are associated with different charge storage mechanisms. The most common types of electrode materials are carbon-based electrodes, transition metal oxide or nitrides and conductive polymers [20].

3.2.1. Carbon

Carbon is the most common material that has been used in electrochemical double layer capacitors (EDLCs). Carbon-based EDLCs provide high power density due to fast and facile electrochemical double layer process, which equilibrate in a short time. Therefore, they have been used in applications which require high power pulses, e.g., emergency doors on an Airbus A380, car acceleration, tramways and emergency systems [20, 46].

Carbon is a conductive material which has a porous structure, broad pore size distribution and high wettability [51]. Moreover, carbon has a range of different allotropes such as graphite, diamond, fullerenes or nanotubes. Also, it can exist in a variety of forms such as powders, fibres, aerogels, xerogels, foams, fabrics and composites. Furthermore, carbon is chemically stable at range of temperatures and solution pH. Carbon also is a non-toxic material which is widely available at a reasonable low cost. Hence, carbon is the most desirable material for using in the electrochemical capacitors [51, 52].

3.2.1.1. Activated Carbon

Activated carbon is the most attractive material for electrochemical capacitors, due to its high conductivity, low cost, controllable pore size distribution and high surface area. The specific surface area of the activated carbon can be developed up to 3000 m^2/g [31].

Carbonaceous materials such as coal and wood can be activated by means of physical or chemical activation. The physical activation of carbon occurs in the temperature range from 700 - 1200 ^oC, under a gas flow of steam, air or carbon dioxide. However, carbon can be activated chemically at much lower temperatures (400 - 700 ^oC) using activating agents such as phosphoric acid, potassium hydroxide, sodium hydroxide and zinc chloride [31].

Figure 4 shows the aromatic sheets of the activated carbon with slit-formed pores. The specific capacitance of activated carbon is more associated with conductivity rather than the specific surface area. The surface area of the activated carbon increases by increasing the number of pores in the material. While, the conductivity of activated carbon is determined by the size of pores, which pores larger than 0.5 nm being electrochemically accessible in an aqueous medium. Hence, the activated carbon with a larger size of pores can be more conductive than the activated carbon with a higher specific surface area but smaller pores size [31].

Also, the specific capacitance of activated carbon can be affected by the size of electrolyte ions. Generally, the specific capacitance of AC in an organic electrolyte with larger ions is less than 150 F/g, while the specific capacitance of activated carbon in aqueous solutions can range up to 300 F/g [52].

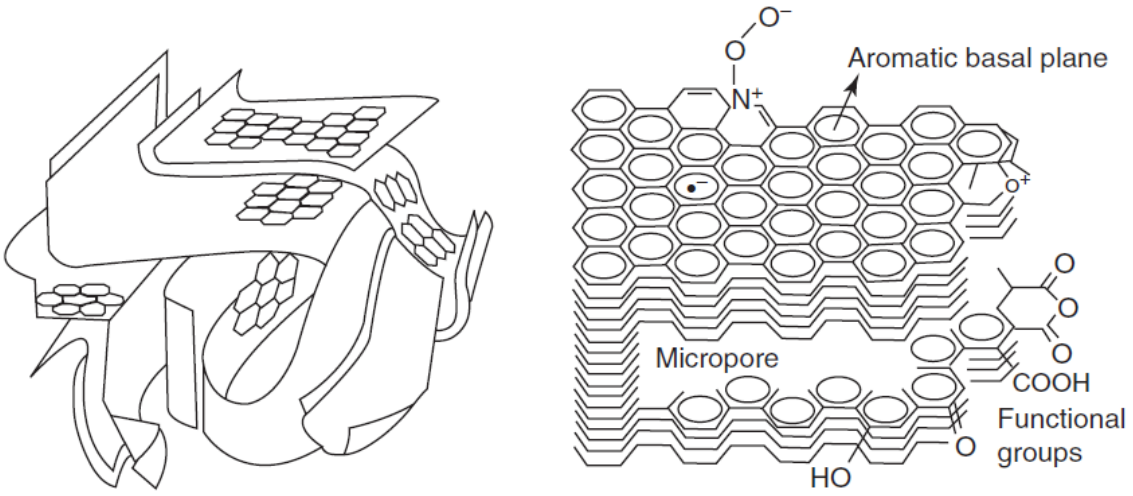

Figure 4 Activated carbon structure [51].

3.2.1.2. Graphene

Graphene is a flat monolayer of carbon atoms that, exhibits high crystal and electronic quality. Graphene can be produced in different dimensions such as zero-dimensional fullerenes, one-dimensional rolled nanotubes or three-dimensional stacked graphite, as shown in **Figure 5**. All of these graphene dimensions can be extracted from the two-dimensional (2D) honeycomb lattice of the tightly packed carbon atoms. It should be mentioned that the electronic structure of graphene diminishes quickly as the number of the graphene layers increases, approaching that of graphite at almost ten layers [53].

Graphene has an extremely high specific surface area and excellent electronic properties. Graphene film for the electrode of electrochemical capacitors has been used, due to its high flexibility and superior electrical, mechanical and optical properties [54]. The structure of graphene has no bulk, so most of its surface area can be accessible to the electrolyte [31, 53].

The performance of electrochemical capacitors is determined by the quality of the graphene, the number of layers and the specific surface area [55]. Generally, graphene has a high surface area (2630 m^2/g [56]) and the highest reported specific capacitance (21 $\mu F/cm^2$ [57]). Thus, graphene is comparable to activated carbon for use in commercial electrochemical capacitors [55].

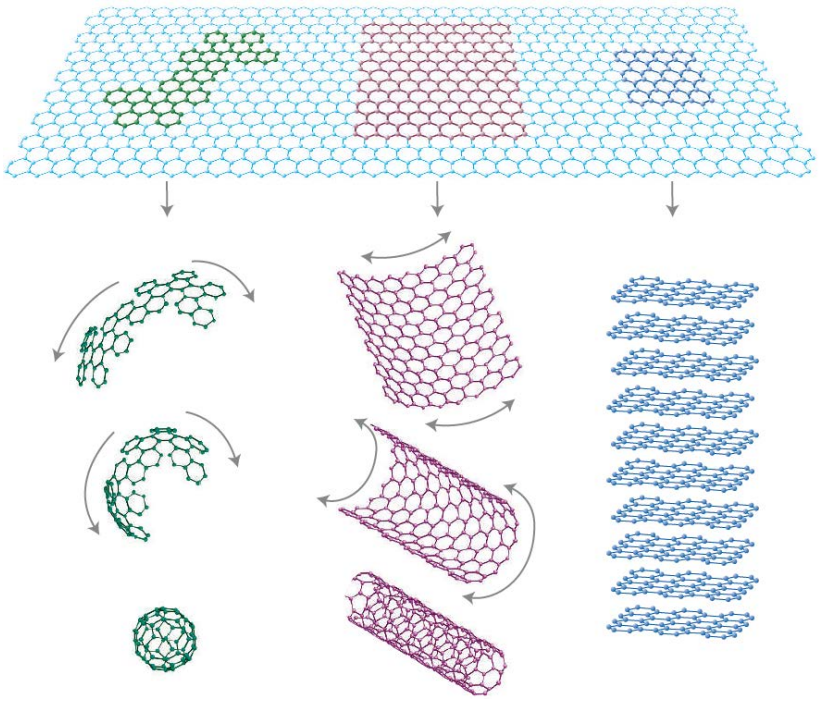

Figure 5 Graphene structure: 0D fullerenes, 1D rolled nanotubes or 3D stacked graphite [53].

3.2.1.3. Carbon Nanotubes (CNTs)

Carbon nanotubes (CNTs) have been widely used in a variety of different applications such as nanowires, molecular electronic devices, micromechanics, catalyst supports and hydrogen storage [51, 52, 58].

CNTs also have been utilized in electrochemical capacitors due to their excellent electrical properties, high thermal and chemical stability, special porous structure and high conductivity. **Figure 6** shows the atomic structure of CNTs. Generally, CNTs are classified as either single-walled (SWCNTs) or multi-walled (MCNTs) carbon nanotubes.

Recent studies have shown that aligned CNTs have better performance in terms of power density than entangled CNTs due to fast charge transportation [59].

However, the energy density of CNTs is lower than activated carbon due to the small specific area of CNTs, which is less than 500 m^2/g [31].

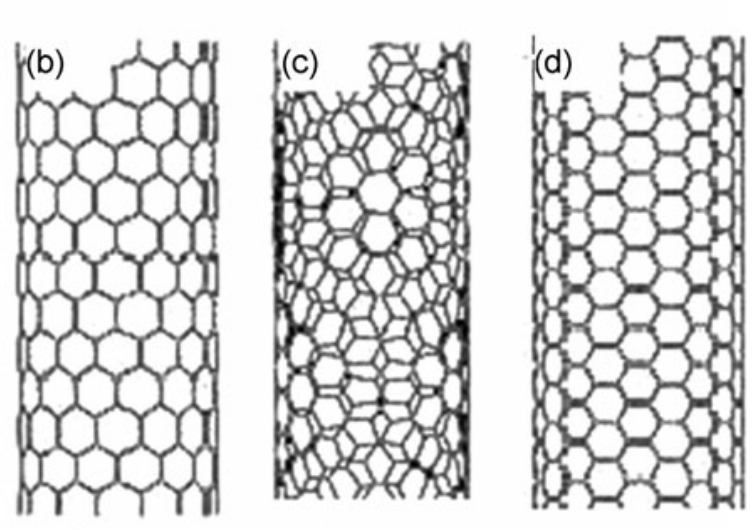

Figure 6 CNTs atomic structure, (a) Zig-zag, (b) Chiral, (c) Armchair [31].

3.2.1.4. Carbon Fibres

Carbon fibres can be made by pyrolysis of the organic materials such as pitch polymers, e.g., polyacrylonitrile (PAN), cellulose (or rayon) or phenolic resins at high temperature. The quality of the carbon fibre depends on its structure and alignment of aromatic constituents. There are several forms of carbon fibres, such as tow (bundles), chopped fibre, mat, felt, cloth, and thread [60]. **Figure 7** shows the structure of the activated carbon fibres at high magnification.

Although the specific surface area of carbon fibres can reach up to 2500-3000 m^2/g at high temperature, it has a low density of 0.2 g/m^3 which lowers the energy density to be comparable with activated carbon [51]. The diameter of carbon fibres can be up to 10 µm with a narrow pore size distribution, with typical pore sizes of less than 2 nm [60].

Carbon fibre is a highly conductive material because most of its pores are located at the surface of the fibre due to the high aspect ratio. Furthermore, the pore length and pore size of carbon fibres can be controlled. Carbon fibres are a desirable material for electrochemical capacitors which mainly can be used for power applications, due to the high porosity, excellent electrical conductivity, lightweight, superior mechanical properties and chemical and environmental resistance [61].

Although carbon fibre has a high specific surface area and great conductivity, it is more expensive than the powdered forms of carbon [60].

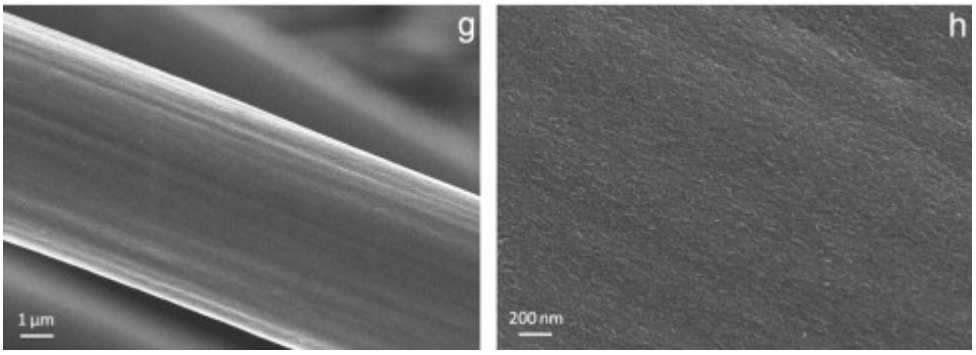

Figure 7 Activated carbon fibres structure at high magnification [61].

3.2.1.5. Carbon Aerogels

Carbon aerogels can be produced by the pyrolysis of an organic aerogel, such as resorcinol-formaldehyde, phenol-furfural gels, phenolic–furfural melamine–formaldehyde, polyurethanes, and polyureas in an inert atmosphere. The carbon aerogel can be produced in three forms; i.e., powders, microspheres, or thin film composites [62].

The monolithic form of carbon aerogel, which is a three-dimensional mesoporous networks of carbon nanoparticles, is suitable for use in electrochemical capacitors due to its high specific surface area (500–900 m^2/g), low density (0.4–2.6 cm^3/g), low thermal conductivity, excellent electrical conductivity, controllable pore size, and low electrical resistance. A specific

capacitance of 70–150 F/g can be obtained from aerogels with pore sizes ranging from 3 to 13 nm [51, 62, 63].

The characteristics of an electrode made with an aerogel are determined by synthesis conditions, pyrolysis temperature, the process of activation, and the presence of doping agent such as ruthenium dopant [62].

3.2.2. Transition Metal Oxides

The transition metal oxides which have been used in batteries and electrochemical capacitors exhibit the pseudo-capacitive behaviour. Generally, the charge storage mechanism in pseudo-capacitors involves fast, reversible redox reactions at the electrode-electrolyte interface. Depending on the material and the experimental conditions, the extent of this redox reaction can progress into the bulk of the material. Hence the energy density of pseudo-capacitors is generally higher than the EDLCs due to the high specific capacitance of the pseudo-capacitive materials. However, pseudo-capacitors may suffer from a lack of stability due to the redox reactions that can change the structure of electrode materials [20, 24, 64, 65].

The transition metal oxides commonly, exhibit a high specific capacitance and low resistance resulting in a high specific power [24, 66]. They can be used as single or mixed metal oxides, composite electrodes with carbon, deposited on carbon or metal-based electrodes. The most common metal oxides that have been used for the electrochemical capacitors are ruthenium oxide (RuO_2), iridium oxide (IrO_2), manganese oxide (MnO_2), nickel hydroxide or oxide ($Ni(OH)_2$), cobalt oxide (CoOOH) and magnetite (Fe_3O_4) [67-75]. Among them, ruthenium dioxide (RuO_2) and manganese dioxide (MnO_2) have been extensively studied due to their excellent electrochemical properties, high specific capacitance and various type of morphologies. Hence, this section reviews the structure of ruthenium and manganese dioxide and their application in electrochemical capacitors.

3.2.2.1. Ruthenium Dioxide

Ruthenium dioxide has been used as a highly conductive electrode material since the late 1970s. This metal oxide has an excellent cyclability and electrochemical reversibility, high specific capacitance and a high rate capability. The redox reactions of ruthenium oxide occur reversibly via a simultaneous proton exchange mechanism; i.e., [20, 21, 65, 177-179]

$$RuO_2 + \delta H^+ + \delta e^- \Leftrightarrow RuO_{2-\delta}(OH)_\delta \qquad 0 \leq \delta \leq 4 \qquad (9)$$

This can be simplified to:

$$RuO_2 + H^+ + e^- \Leftrightarrow RuO(OH) \qquad (10)$$

The value of δ changes continuously during the intercalation of protons over a potential window of about 1.2 V [20]. Specific capacitance values of up to 1300 F/g has been reported for the $RuO_2.xH_2O$ NTs plated by anodic deposition [180].

Although ruthenium oxide is a good choice for electrochemical capacitors, it is costly, toxic and mostly limited to small capacitors due to a relatively small potential window [20].

3.2.2.2. Manganese Dioxide

Manganese dioxide is an ideal candidate for pseudo-capacitors due to its good electrochemical performance, high specific capacitance, fair price, a wide range of structures and morphologies, availability and environmentally friendliness [19].

Manganese dioxide exhibits the pseudo-capacitive behaviour, which results in high specific capacitance. The pseudo-capacitance of MnO_2 arises from the redox cycling between Mn^{+4} and Mn^{+3}, which is given by;

$$MnO_2 + M^+ + e^- \Leftrightarrow MnOOM \qquad (11)$$

This process involves the reduction of Mn^{+4} to Mn^{+3} due to the insertion of an electron from the electrical circuit. Hence, a metal ion from the bulk of electrolyte is inserted through the

electrode surface to maintain charge neutrality [76, 77]. Generally, manganese dioxide has a wide-ranging potential window in neutral electrolytes. However, just like other metal oxides, it is not stable in a strong acidic electrolyte [78]. The electrochemical performance of the manganese oxide can be affected by several factors such as particle size, morphology, and degree of crystallinity [79].

One of the advantages of the manganese dioxide is the variety of the phases and structures which can be used in the electrochemical capacitors. There are more than 30 different structural varieties of manganese dioxide that have been characterized. Manganese has three natural oxidation states of II, III and IV, which form under a different range of chemical and temperature conditions. However, crystal structure and powder diffraction patterns of most of the manganese oxides are similar, so identifying the manganese oxide minerals is challenging [80]. The different polymorphs of manganese dioxide are formed from [MnO_6] octahedra (shown in **Figure 8**) linked in different ways [79]. This section reviews the atomic structures of some of the most important manganese dioxide phases.

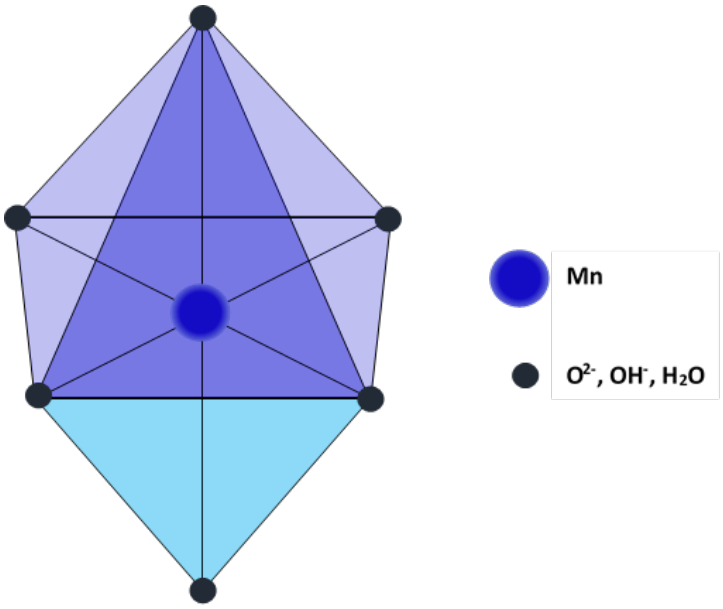

Figure 8 Octahedral MnO_2 unit.

3.2.2.2.1. Pyrolusite (β-MnO_2)

The most stable and abundant polymorph of the manganese dioxide is Pyrolusite, which consists of single chains of edge-sharing [MnO_6] octahedra attached to neighbouring chains by corner-sharing of oxygen between octahedra. Pyrolusite has a tetragonal, rutile-type structure. **Figure 9** shows the (1X1) tunnel structure of Pyrolusite. Other chemical species cannot be located into these tunnels due to very small size. Pyrolusite is naturally occurring in low-temperature hydrothermal deposits [80]. Also, other manganese oxides such as Ramsdellite and manganite can be converted into the more stable Pyrolusite form [80-84].

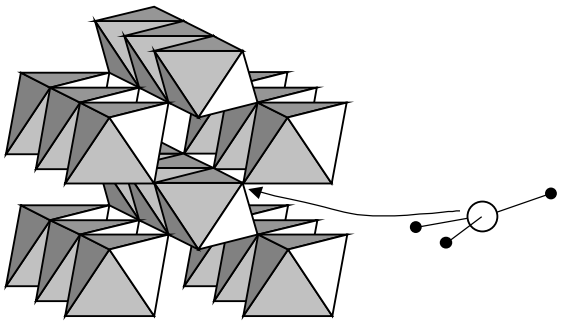

Figure 9 Pyrolusite (β-MnO2); Crystal structures

3.2.2.2.2. Ramsdellite

Ramsdellite is a relatively rare naturally occurring polymorph of manganese dioxide which contains double chains of edge-sharing [MnO_6] octahedra attached to neighbouring single chains by corner-sharing of oxygen between octahedral. **Figure 10** shows the (2X1) octahedral tunnels, which are notionally rectangular, with a length of two octahedral units. Ramsdellite generally, can be found in low-temperature hydrothermal deposits [80, 82, 83].

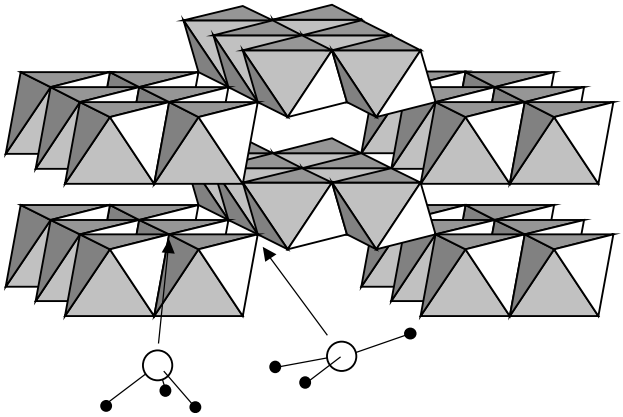

Figure 10 Ramsdellite; Crystal structures

3.2.2.2.3. Nsutite (γ-MnO_2)

Nsutite (γ-MnO_2) is an intergrowth between ramsdellite and pyrolusite polymorphs which has been used as positive electrode material in dry-cell batteries [80, 85]. **Figure 11** shows the accepted crystal structure of nsutite which is an alternating intergrowth of ramsdellite and pyrolusite. The chemical analysis such as TEM revealed that it has a disordered structure consisting of (1x1), (1x2), (1x3) and also (3x3) tunnels also some defects and grain boundaries [86]. It has been reported that, the larger tunnels can be occupied by some minor amounts of minerals such as Na, Ca, Mg, K, Zn, Ni, Fe, Al, and Si as well as water molecules [87]. This disordered structure can affect its chemical and electrical properties. Nsutite can be naturally found in ore deposits and also it can be formed from oxidation of manganese carbonate [80].

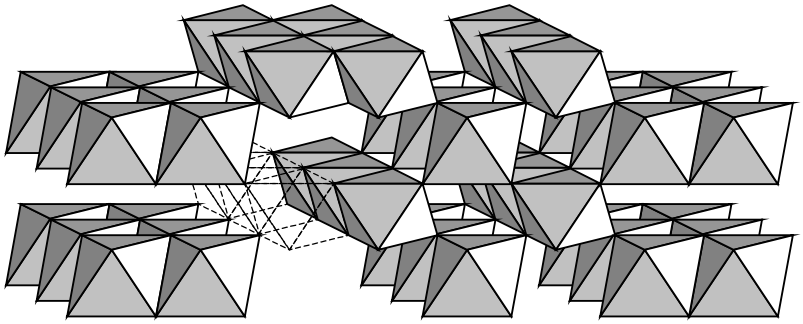

Figure 11 Nsutite γ-MnO2; Crystal structure showing an intergrowth of pyrolusite and Ramsdellite

3.2.2.2.4. λ MnO_2

λ MnO_2 is a spinel structure form of manganese dioxide mineral which is generally synthesised from the acid treatment of $LiMn_2O_4$ which naturally has a spinal structure. In this method, almost all of the lithium removed from the tetrahedral positions, while the manganese is remaining on the octahedral positions, as is shown in **Figure 12** [88]. The $LiMn_2O_4$ can also be electrochemically transformed to the λ MnO_2 phase by extracting lithium at the highest potential of 4.5 V vs Li/Li^+ reference electrode. It worth to mention that the $LiMn_2O_4$ has been used in rechargeable lithium-ion batteries as a cathode material by extraction/insertion of lithium in the range of 3.8 to 4.2 V vs. Li/Li^+ [89-91].

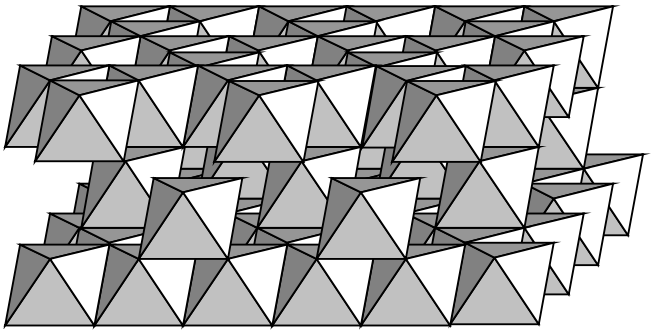

Figure 12 λ-MnO2; Crystal structures

3.2.2.2.5. ε-MnO_2

ε-MnO_2 is an intergrowth structure of manganese dioxide mineral which has a disordered structure consisting of a Ramsdellite and Pyrolusite phases. Generally, ε-MnO_2 has the (1x1) and (1x2) tunnels structure. Its shape is a hexagonal close packed array of O^{2-} ions which has the available octahedral sites randomly filled with Mn^{+4} ions [80, 92].

3.2.2.2.6. Hollandite Group (α-MnO_2)

α-MnO_2 is one of the most important polymorphs of manganese dioxide for ECs because it has excellent electrochemical properties due to its unique structure. It has been used for potential applications as solid ionic conductors and also for the waste storage system to immobilize

radioactive cations. The α-MnO_2 structure involves the double chains of edge-sharing [MnO_6] octahedra which is in turn linked to neighbouring [MnO_6] octahedra to form tunnels with square cross sections of two octahedra units on each side. The (2x2) tunnel structure of the Hollandite group is shown in **Figure 13**. These (2x2) tunnels are usually filled by large cations which define the Hollandite group; i.e., hollandite (Ba^{2+}), cryptomelane (K^{+}), coronadite (Pb^{2+}), and manjiroite (Na^{+}). Many other metals will fill into these tunnels [80, 82].

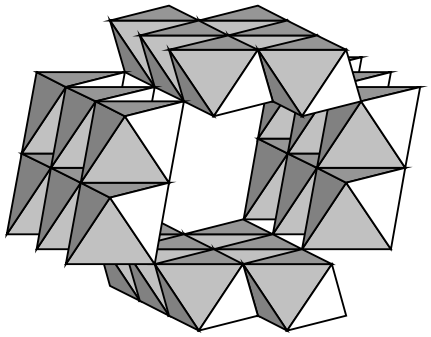

Figure 13 α-MnO2; Crystal structures

3.2.2.2.7. Romanechite

The Romanechite structure consists of double and triple chains of edge-sharing [MnO_6] octahedra linked to each other to form (3x2) tunnels. Usually, cations, such as barium (Ba^{2+}) potassium (K^{+}), sodium (Na^{+}) or Strontium (Sr^{2+}) with water molecules are located in these large tunnels. Romanechite can be converted to Hollandite at a temperature above 550 ^{o}C. This phase has been used in electrochemical applications such as sodium-ion batteries [80, 93].

3.2.2.2.8. Todorokite

Todorokite is one of the most important minerals of manganese oxide, as it can be the host of important metals such as platinum (Pt) and cobalt (Co). The Todorokite structure is constructed of triple chains of edge-sharing [MnO_6] octahedra that link to form large tunnels. Generally, these large tunnels are filled by many cations, including alkali, alkaline-earth and transition-

metal ions as well as water molecules. This phase has been used in applications such as Li-ion and Na-ion cells, and zinc-ion batteries [80, 94, 95].

3.2.2.2.9. Birnessite Group

Birnessite is the main phase in many soils which naturally can be found in the form of fine-grained poorly crystalline particles. The crystal structure of Birnessite as shown in **Figure 14**, consists of several layers of a sheet of [MnO_6] octahedra with cations such as potassium (K^+) and sodium (Na^+) and magnesium (Mg^{2+}), and water molecules, occupying the interlayer space. The space between two layers of [MnO_6] octahedra was reported to be ~7 Å. Birnessite has been used in many applications such as electrochemical capacitors, magnesium batteries and as a water oxidation catalyst due to its low cost, high availability and environmentally friendliness [80, 96-99].

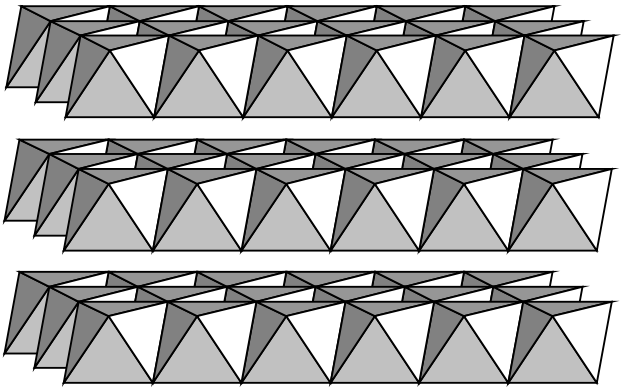

Figure 14 Brinessite; Crystal structures

3.2.3. Conducting Polymers

Conducting polymers can be produced by the chemical or electrochemical oxidation of the polymer chains. These materials can be used in electrochemical applications such as batteries and supercapacitors due to their good conductivity and relatively low price. However, carbon material and transition metal oxides exhibit relatively better electrochemical performance than

conducting polymers in terms of, the specific capacitance, potential window, long-term stability and cyclability [100].

The main polymers which exhibit a good conductivity due to their large degree of π-orbital conjugation are polyacetylene, polyaniline (PANI), polypyrrole (PPy), polythiophene, and similar aromatic polymers. **Figure 15** shows the chemical structure of the main conducting polymers. [100, 101].

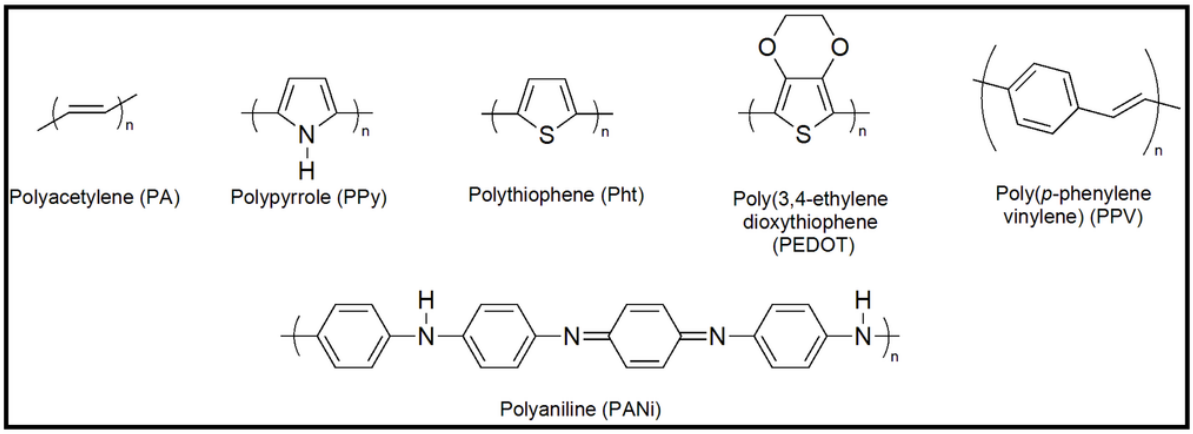

Figure 15 Chemical structure of main conducting polymers [101].

The charge storage mechanisms of conducting polymers are based on redox reactions through the bulk of the material. The oxidation and reduction processes occur via π-orbital conjugation of polymers by withdrawal or injection of electrons, respectively. Although the charge density of the conducting polymers is relatively good, they have a low power density due to the slow process of diffusion of ions within the polymers [100, 102].

Increasing the specific capacitance of the conducting polymers has been a major challenge explored in recent studies. Theoretically, the specific capacitance of the conducting polymers can reach up to 1000 F/g; however, in practice, this has not been reached because the specific capacitance of conducting polymers depends on several factors such as the thickness of the

polymer films and the degrees of oxidation of polymer chains. Some of the specific capacitance of these polymers that have been reported are given in Table 1 [100]:

Table 1: Specific capacitance of some of the conductive polymers.

Conductive Polymer	**Specific Capacitance (F/g)**
PPy on activated carbon, polyisothionaphthene	50
polyethylenedioxythiophene, poly(3-methylthiophene)	100
Poly (1,5-diaminoanthraquinone), PANI on carbon nanotubes, poly [3-(3,4-difluorophenyl) thiophene]	200
Poly (fluorophenylthiophene), PANI on pure and on activated carbons	250

3.3. Electrodeposition

The specific capacitance of electrochemical capacitors is determined mostly by the electrode materials, more specifically, their morphology and structure. Generally, electrode materials used in electrochemical capacitors are in the form of a composite powder or thin film. The powder form of the electrode materials is made by combining an active material such as activated carbon or manganese dioxide, a conductive material, such as carbon black, and a binder, such as PTFE, which can then be attached to a metallic substrate. Generally, a larger amount of active materials can be used in a composite powder form electrode, resulting in higher specific capacitance. However, they may have low conductivity and high series resistance due to their attachment to the substrate.

Thin film electrodes have the active material directly attached to the substrate, which is advantages because it dramatically reduces the electrode resistance. Also, access of electrolyte to the thin film increases due to the low thickness of materials ranging from a nanometer to several microns [103].

There are several methods that have been employed to produce thin films such as spray pyrolysis, spin coating, dip dry, sol-gel, chemical deposition, chemical vapour deposition (CVD) and pulsed laser deposition [103-106].

Thin films also, can be made by electrodeposition from an electrolyte solution to form a thin film over a conductive substrate. The nature of the electrodeposited product depends on the electrolyte composition, temperature and current density. In this method, the thickness, porosity and morphology of the film can be controlled [19]. Adding these advantages to the extremely low resistance, thin films are excellent candidates for supercapacitors electrode [19, 107].

3.3.1. Manganese Dioxide Deposition

Manganese dioxide phased electrodes have been extensively studied due to their low cost and environmental friendliness [108]. Several methods can be applied to produce the manganese dioxide with different crystallographic forms such as spray pyrolysis, thermal, reflux, hydrothermal and sol-gel [109]. Manganese dioxide can be used as the active material in a powder composite mixture to make an electrode. Although the quantity of electroactive material is high, the electrode has lower conductivity in this method of construction. Electrochemical capacitor electrodes are also constructed from the electrodeposition of thin film of manganese dioxide [110, 111]. Hence, the hydrous and amorphous manganese dioxide electrode can be obtained using the electrodeposition technique, which has been shown to lead to higher power and energy densities [108]. Electro-deposited thin films of manganese dioxide have been shown to exhibit capacitance values of up to 2000 F/g [19]. Thus, for improving the performance electro-deposited of thin films of manganese dioxide, the mechanism of electrodeposition and the morphology of electro-deposited manganese oxide needs to be investigated. There are several factors that can affect the process of electrodeposition, such as deposition potential and electrolyte composition [112].

The general reaction for electrodeposition of manganese dioxide in the acidic solution such as $MnSO_4$. + H_2SO_4 is:

Anode: $$Mn^{+2}{}_{(aq)} + 2H_2O \rightarrow MnO_{2_{(s)}} + 4H^+ + 2e^- \quad (12)$$

Cathode: $$2H^+ + 2e^- \rightarrow H_2 \quad (13)$$

However, the mechanistic pathway of the electrodeposition of manganese dioxide is more complicated. The first step in the electrodeposition of the manganese dioxide is the oxidation of Mn^{2+} to Mn^{3+};i.e.;

$$Mn^{2+} \rightarrow Mn^{3+} + e^- \quad (14)$$

In weakly acidic solution, the Mn^{3+} can undergo hydrolysis to form solid phase of MnOOH. MnO_2 then is formed by topotactic solid-state oxidation of MnOOH.

$$MnOOH \rightarrow MnO_{2_{(s)}} + H^+ + e^- \quad (15)$$

It may also, possible that two oxidation reactions happen continuously, in which case Mn^{+2} is oxidised to $Mn^{+3,}$ and then Mn^{+3} is oxidised to Mn^{+4}. Hence, Mn^{+4} can immediately undergo hydrolysis to form MnO_2. However, there is no evidence supporting the existence of two sequential redox processes [19].

Another pathway that can occur in highly acidic electrolytes is the reaction between two Mn^{+3} ions which can immediately undergo disproportionating to form Mn^{+2} and Mn^{+4}, from which the Mn^{+4} can hydrolyse to deposit MnO_2 on the electrode.

It should be mentioned that in reality, a combination of all of these reactions can happen to produce MnO_2 [19, 113].

Moreover, in the study of the anodic deposition of hydrous manganese oxides, Hu et al. showed that the number of Mn species in the oxidation reactions is a function of deposition potential.

It was mentioned that the amounts of Mn^{3+} and Mn^{4+} were dominant in the oxidations of Mn^{2+} to Mn^{3+} and the Mn^{3+} to Mn^{4+} which occurred at 0.6 and 1 V respectively [181].

3.3.2. Carbon Deposition

Carbon has been used extensively as electrode material in electrochemical double layer capacitors (EDLCs) due to its high heat resistance, corrosion resistance, ready availability and low cost. The metal-coated carbon has high conductivity, and it is generally produced by chemical vapour deposition method (CVD), which is expensive due to its high temperature (~ 1500 ^{o}C). Hence the electrodeposition of carbon over a metal substrate such as nickel or copper can be an alternative method due to its lower cost and temperature. The electrodeposition of carbon can be carried out in several electrolytes, such as pure molten carbonate or the solution of carbonate in molten chlorides or fluorides [106].

The reduction of carbon can be described by [114-116]:

$$CO_3^{2-} + 4e^- \rightarrow C + 3O^{2-} \quad (16)$$

Also, it can happen in a two-step mechanism which is consists of creating CO_2^{2-} as an intermediate product [115]:

$$CO_3^{2-} + 2e^- \rightarrow CO_2^{2-} + O^{2-} \quad (17)$$

$$CO_2^{2-} + 2e^- \rightarrow C + 2O^{2-} \quad (18)$$

Carbon nanotubes (CNTs) have been used in many different electrochemical applications such as batteries and electrochemical capacitors due to their high specific surface area, high electrical conductivity and excellent chemical stability. CNTs also can be deposited over different substrates such as carbon fibres using electrophoretic deposition (EPD). The EPD is an excellent method to deposit CNTs due to its simple process, low cost and ability to thickness. However, the CNTs needs to be charged before the EPD, with several methods such as

chemical functionalization, which can change the structure of the CNTs. The use of surfactants such as CTAB and SDS is a less destructive method that can also be used for charging and dispersing the CNTs [117-120].

Chapter 4: Electrochemical Characterization Methods

Several methods have been developed for characterising the electrochemical performance of active materials and systems. This chapter reviews the fundamentals of electrochemical techniques (CV, SPECS and EIS) which have been applied to examine the performance of electrochemical capacitors. The most common methods are cyclic voltammetry (CV) and constant current charge-discharge cycling (CC), both throughout a number of cycles [121]. Generally, these conventional methods can provide information about the performance of materials and devices such as the specific capacitance (F/g) as a function of cycling rate, and also material characteristics such as an equivalent series resistance (ESR). However, these methods are relatively poor at differentiating processes occurring in the electrode [18]. While the charge storage mechanisms of EC materials such as activated carbon and manganese dioxide is different, they exhibit similar performance when they are being cycled. Hence, the CV and CC methods are not a rigorous technique to obtain the contribution of different charge storage mechanisms such as the electrical double layer and diffusion-limited processes alone [122].

Electrochemical impedance spectroscopy (EIS) has also been used to provide different information about EC materials and systems such as characterisation and corrosion of materials, double layer capacitance, diffusional characteristics, equivalent series resistance (ESR), charge transfer resistance, mass transport and time constant using a small AC excitation signal [121, 123, 124]. Although EIS can provide the fundamental information about the charge mechanisms and material characteristics, it is most often applied at one potential within the potential window, and as such it does not cover the whole potential window [125, 126].

Step potential electrochemical spectroscopy (SPECS) is a promising method that has been used successfully for characterising the performance of electrochemical energy storage systems and devices. This method has been applied previously to study the diffusional characteristics of

battery materials [127-130]. In the SPECS method, a small potential step is applied with a sufficient rest time to allow for equilibrium to be established for each step throughout an applied potential window. This small scan rate enables an electrode to approach its maximum charge storage capabilities. More importantly, it allows separation of charge storage mechanisms, such as via electrical double layer charge storage and diffusion-limited processes [18, 64, 77, 122, 131, 132]. The SPECS data can be modelled, using combined resistance, double layer, diffusional and residual currents, to separate different charge storage mechanisms. Thus, the SPECS method can provide fundamental information about EC behaviour such as kinetics, equivalent series resistance (ESR), diffusional processes, double layer capacitance, fast and slow processes and also, infer electrode instabilities from the residual current.

4.1. Evaluating the Performance of Electrochemical Systems

Electrochemical cells are usually classified into two types; galvanic and electrolytic cells. Normally, just one half of an electrochemical cell is considered when observing the performance of the cell because the nature of the reactions that occur in an electrode is independent of the type of electrochemical cell. The potential of the electrode of interest is recorded with respect to a reference electrode. The electrical circuit of such that cell is shown in **Figure 16**, where C_d and C_{SCE} representing the capacitance of the electrode of interest and the reference electrode, respectively, and R_s, represents the solution resistance. However, C_d and C_{SCE} are series capacitance, and the capacitance of a reference electrode usually is much higher than the electrochemical cell electrode, so the total capacitance is essentially equal to C_d. Hence the C_{SCE} capacitance can be neglected, and the cell can be approximated by the electrical circuit of C_d and R_s.

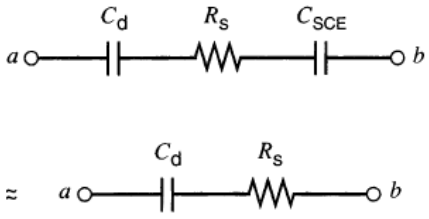

Figure 16 RC electrical circuit of the cell [44].

The characteristics of an electrochemical system are usually obtained by applying an electrical perturbation to the system such as a voltage step, current step or voltage ramp. A certain response is measured while other variables such as the electrode material, electrolyte concentration, temperature and pressure are held constant [44].

In potential step methods, a certain potential is applied to the system which can be approximated by contributions of resistors and capacitors. Hence, the total potential drop across the resistor, E_R, and the capacitor, E_C, equal to the applied voltage. So,

$$E = E_R + E_c = iR_s + \frac{q}{C_d} \tag{19}$$

where R_s is the series resistance in an equivalent circuit (Ω), C_d is the double layer capacitance (F), i is the current (A) and q is the charge stored on the capacitor (C)[44].

In this method the change of current with time can be obtained by **Equation 20**; *i.e.*,

$$i = \frac{E}{R_s} e^{-t/R_s C_d} \tag{20}$$

Thus, the current decays exponentially with a time (τ) constant of $R_s C_d$ for the applied potential step [44]. **Figure 17** shows the behaviour of the current for an applied potential step *E*.

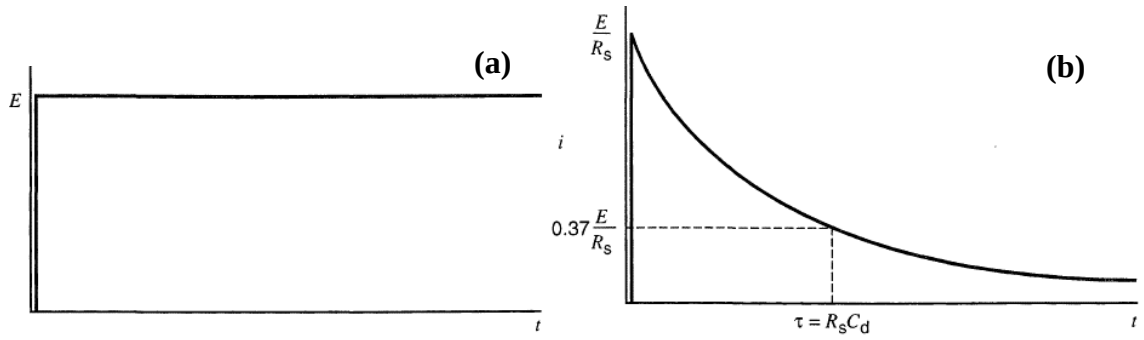

Figure 17 (a) Applied E, **(b)** Resultant i obtained by applied potential step E [44].

In the controlled current method, a constant current i is applied to the system. Hence, the potential of the circuit is obtained by **Equation 21**; *i.e.*,

$$E = E_R + E_c = i(R_s + \frac{t}{C_d}) \tag{21}$$

Figure 18 shows the increasing the potential with time for a constant current i [44].

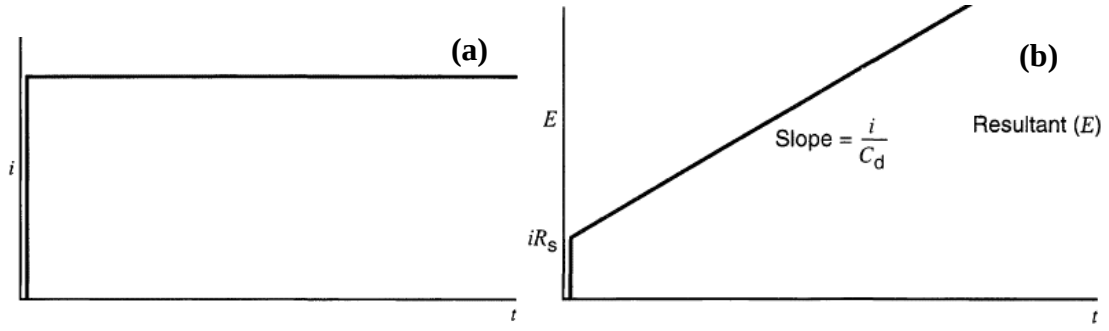

Figure 18 (a) Applied i, **(b)** Resultant E obtained by applied current step i [44].

Using potential sweep techniques, the applied potential changes with a sweep rate of υ (V/s). In this method, the current increases gradually until it reaches a steady state point with the value of υC_d. The current for a potential sweep is given by **Equation 22**; *i.e.*,

$$i = \upsilon C_d[1 - e^{-t/R_s C_d}] \tag{22}$$

Figure 19 shows the result for a system using cyclic linear potential sweep with constant C_d [44].

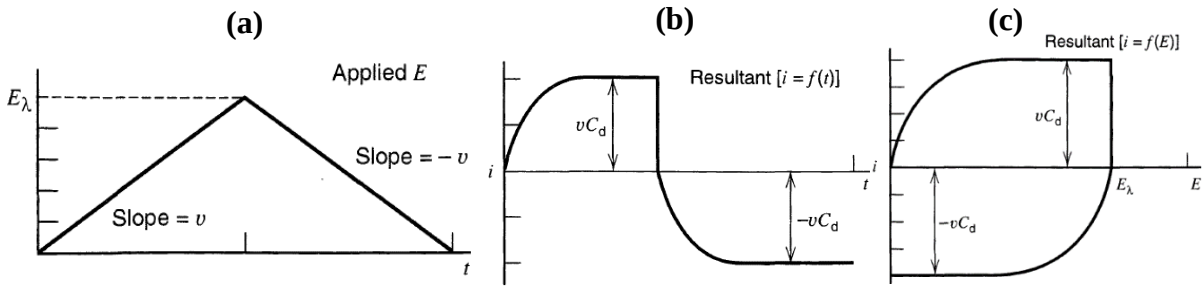

Figure 19 (a) Applied $\boldsymbol{E = \upsilon t}$, **(b)** Current-time plot and **(c)** Current-Potential plot obtained by applied potential sweep [44].

4.2. Cyclic Voltammetry (CV)

Cyclic voltammetry is one of the most common methods for characterizing the behaviour of electrochemical capacitors. The specific capacitance of the electrochemical capacitor can be found using cyclic voltammetry. The charge passed during the cathodic and anodic scans can be obtained by integrating the current per mass of the active material in the electrode with respect to time. The specific capacitance can then be obtained from the calculated charge and the employed potential window [133, 134] using:

$$C = \frac{Q}{V \times m} \tag{23}$$

where C is the specific capacitance (F/g), Q is the total charge passed (C), V is the potential window (V), and m is the mass of the active material (g).

The electrochemical behaviour of an electrode can be found from its cyclic voltammogram. For instance, a box-like voltammogram indicates the behaviour of an electrical double layer capacitor [133]. **Figure 20** shows a series of cyclic voltammograms for activated carbon for 1000 cycles at 25 mV/s. The voltammogram of the activated carbon has a rectangular shape with no explicit redox peaks which the behaviour expected for capacitive material.

Also, cycling efficiency can be obtained by the ratio of anodic to cathodic average specific capacitance [77].

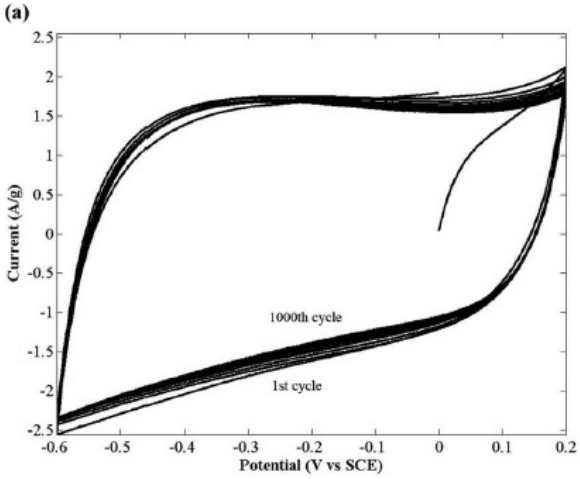

Figure 20 Cyclic voltammetry of the activated carbon electrode in 0.5 M H_2SO_4 [122]

Cyclic voltammetry (CV) method, has also been developed to determine the contribution of different charge storage mechanisms such as via the electrical double layer and diffusion-limited processes. CV data at different scan rates have been used to obtain the relationship between a voltammetric current and scan rate and also, the relationship between a voltammetric charge and scan rate.

The relationship between current and potential scan rate has been widely inspected by several researchers since the middle of the nineteenth century [135-137]. Initially, the relationship between peak current and scan rate was at the centre of attention as it was revealed that the peak current (i_p) for a totally irreversible reaction or diffusion-limited process is proportional to the square root of scan rate ($v^{1/2}$) [44]

The correlation between the peak current and the scan rate then has been given in a related analysis by plotting a log-log plot of $i_p\ vs. v$ [138]:

$$i_p = av^b \tag{24}$$

where a and b are adjustable parameters. Naturally, the b value in a log-log plot of $i_p\ vs.\ v$ should be between 0.5 and 1. It has been suggested that when the current is capacitive the ,b

value is 1 and also, when the b value is 0.5, the current is controlled by diffusion-limited processes [139].

Thus, the peak current (i_p) has been assumed to be the sum of the peak currents for cathe pacitive or electrical double layer (outer surface) and diffusion-limited (inner surface) processes [140]:

$$i_p = k_1 v + k_2 v^{1/2} \tag{25}$$

where k_1 & k_2 are proportionality constants related to the capacitive and diffusion-limited processes, respectively. Although k_1 and k_2 can be determined from the slope and y-intercept of the plot of $i_p/v^{1/2}$ *vs.* $v^{1/2}$, respectively [141, 142], this relationship is not always linear in a desired range of scan rate perhaps for reasons such as non-porosity of the surface electrode and a different kinetic behaviour at various ranges of scan rate [140, 143, 144].

Studies on the relationship between peak current and scan rate eventually have led to the investigation of the relationship between voltammetric current at a particular potential and the scan rate. Cyclic voltammetric data at different scan rates have been used to obtain the relationship between voltammetric current and scan rate (v). In this method, it can be assumed that the total current response for a particular potential, $i(V)$, is a summation of the current associated with a capacitive process and a current associated with a diffusion-limited process. Thus while the capacitive current is proportional to v, the diffusion limited current is proportional to $v^{1/2}$ [145]:

$$i(V) = k_1 v + k_2 v^{1/2} \tag{26}$$

Again, the contributions of the capacitive and diffusion-limited charge storage mechanisms can be obtained from the slope (k_1) and y-intercept (k_2) of the plot of $i(V)/v^{1/2}$ *vs.* $v^{1/2}$ at a specific potential of V, respectively. Although this method has been widely used to find the contributions of the different charge storage mechanisms, a plot of $i(V)/v^{1/2}$ *vs.* $v^{1/2}$ usually

gives a straight line in a very small range of scan rate [146-150] and sometimes it is non-linear in a selected range of scan rate or for a particular potential [145, 151, 152]. Later, it was argued that the scan rate dependence of the current obtained from the CV data at a particular potential probably cannot be used for distinguishing between the different charge storage mechanisms in large potential ranges [153, 154].

The relationship between the voltammetric charge and scan rate has been studied to identify the behaviour of electrode materials during charging and discharging at different scan rates [155, 156]. This relationship was explained mathematically in the method proposed by Trasatti et al. [157]. They developed their method based on the hypothesis that the changes in voltammetric charge at different scan rates are related to a diffusion-limited process at the inner surface of electrode materials, as by increasing the scan rate the inner surface such as the pores and cracks becomes less accessible for the diffusion of protons. They also suggested that the voltammetric charge related to the outer surface of the electrode remains constant over the range of different scan rates. The contribution of voltammetric charge at the outer surface of the electrode q_o^* and the inner bulk of elthe ectrode q_i^* gives the total voltammetric charge [157]:

$$q_T^* = q_o^* + q_i^* \tag{27}$$

As the scan rate is increased, the voltammetric charge of the inner surface, which is assumed to be governed by semi-infinite linear diffusion, decreases with a rate of $\upsilon^{-1/2}$. However, the voltammetric charge of the outer surface is independent of the scan rate so at an infinite scan rate q_o^* can be obtained from the intercept of the plot of $q^*(\nu)$ *vs.* $\upsilon^{-1/2}$ as given in the equation below [157]:

At $\nu \to \infty$

$$q^*(\nu) = q_o^* + C_1\nu^{-1/2} \tag{28}$$

where $q^*(\nu)$ is a measured voltammetric charge and C_1 is a numerical constant.

On the other hand, they assumed that as the scan rate is decreased, the voltammetric charge should increase with a rate of $\nu^{1/2}$. Hence, at very low scan rate ,the total voltammetric charge which is composed of the voltammetric charge, at the outer surface and at the inner surface of the electrode can be obtained by [157]:

At $\nu \to 0$

$$1/q^*(\nu) = 1/q_T^* + C_2\nu^{1/2} \quad (29)$$

where C_2 is a numerical constant. Therefore, the voltammetric charge contributed to the inner surface area q_i^* can be obtained by subtraction of q_T^* and q_o^*.

This method has been widely used for distinguishing between different charge storage mechanisms and also for finding the porosity of electrode materials [158-165]. However, plots of $q^*(\nu)$ *vs.* $\upsilon^{-1/2}$ and $1/q^*(\nu)$ *vs.* $\upsilon^{1/2}$ are not always linear in the desired range of scan rate [139, 149, 166-172]. Furthermore, this method has been criticised because it generates two different equations from the same experimental data and also for correlating the experimental data over only a limited range of values [173]. Moreover, it has been argued that the state of infinite scan rate capacitance is physically unrealistic and scientifically invalid [174].

4.3. Step Potential Electrochemical Spectroscopy (SPECS)

Step potential electrochemical spectroscopy is classified as chronoamperometry or controlled-potential voltammetry, which is the measurement of the current as a function of time after a potential step [175]. The SPECS method is based on applying a series of equal magnitude potential steps on a working electrode, with sufficient rest time to allow for equilibrium to be established for each step throughout an applied potential window. This slow scan rate enables an electrode to approach its maximum charge storage capabilities. More importantly, it allows separation of the charge storage mechanisms, such as electrical double layer charge storage and diffusional processes [18, 64, 77, 122, 131, 132].

Figure 21 (a) shows the current response for a single potential step during a SPECS experiment for electrolytic manganese dioxide (EMD). It can be seen that immediately after the potential step, the current reaches its maximum value, but then it decays sharply to eventually reach a constant value at the end of the equilibration time.

The full current response for the SPECS experiment with 25 mV potential steps and 300 s equilibration time after each step is shown in **Figure 21 (b)** with the staircase potential step profile overlaid. This figure shows that the current spikes vary over the potential window, which shows that the charging process is dependent on potential and also composition[64]. It is also evident that the rate of the decreasing in current is not the same for each potential step, which indicates the different performance of the fast electrical double layer and slow diffusion-limited charging processes, at each potential. The peak in current occurs as a result of the fast and facile electrical double layer charging process which is the result of the immediate gathering of the ionic charges at the electrode-electrolyte interface, as soon as the potential step is applied. However, this current decays quickly as a result of equilibration of the electrical double layer processes.

Figure 21 (b) also, indicates that for most of the potential steps, the current does not reach zero. This implies that there are some other processes in addition to the electrical double layer and diffusional processes that do not equilibrate by the end of the equilibration time. This process has been called a residual process, which is the result of the unfinished redox reactions perhaps related to electrode instability [64].

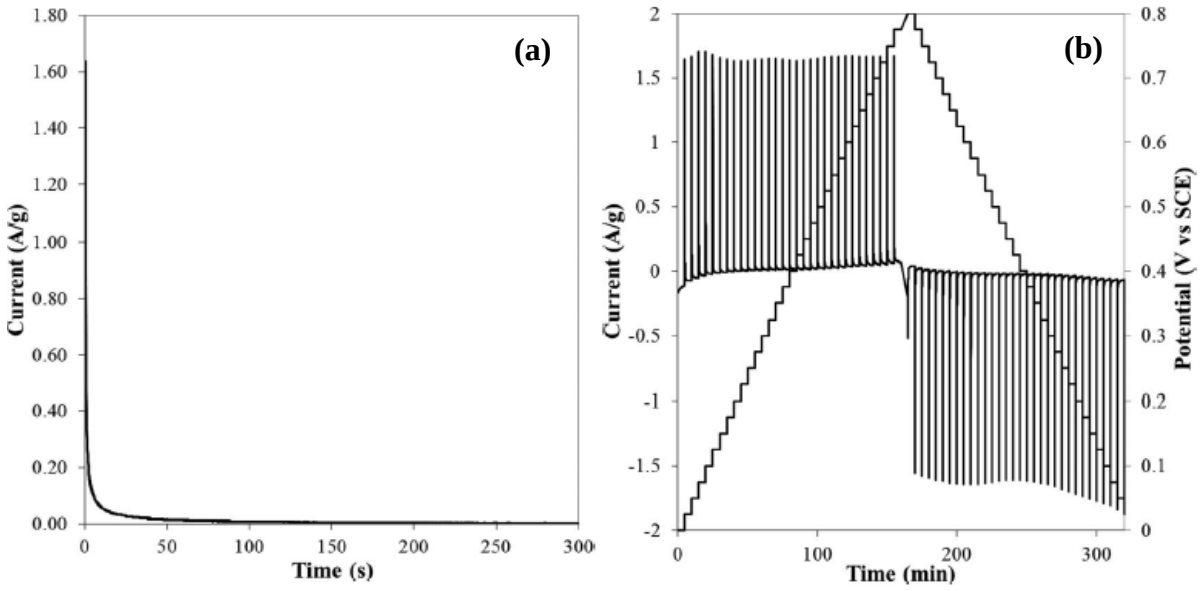

Figure 21 (a) Current response for a single potential step, **(b)** Current response for a SPECS experiment of EMD with a potential step of 25 mV and equilibration time of 300 s [132].

The SPECS data can be modelled to separate the current response for each different charge storage mechanism; i.e., double layer, diffusion-limited and residual processes.

The fast and facile electrical double layer charging process can occur at the geometric surface of the electrode as well as the surface of pores in the bulk of the electrode. The electrical double layer current (i_{DL}; A/g), in a simple RC circuit when applying a potential step of E (V), is given by [44]:

$$i_{DL} = \frac{E}{R_s}\exp(-\frac{t}{R_s C_{DL}}) \tag{30}$$

where R_s (Ω/g) is the series resistance, t (s) is the time and C_{DL} (F/g) is the capacitance of the electrical double layer.

This equation can be used for the electrical double layer capacitance of the geometric surface area. Also, the electrical double layer capacitance is dependent on the pore size of the electrode and the ion diameter of the electrolyte [176]. Therefore, two capacitances are considered for

the electrical double layer process; C_{DL1} (F/g) which is associated with the geometric surface area and C_{DL2} (F/g) which is related to the porous surface area of the electrode material [64].

The diffusion-limited process is much slower than the electrical double layer processes due to continuous redox reactions [122]. Therefore, the diffusional current decreases slowly over the extended equilibration time. This current can be modelled using the Cottrell equation for semi-infinite planar diffusion, i.e. [44]:

$$i_D = \frac{nFAD^{1/2}C}{\pi^{1/2}t^{1/2}} \quad or \quad i_D \propto \frac{B}{t^{1/2}} \tag{31}$$

where n is the number of electrons involved in an electrode reaction, F is Faraday's constant (96496.7 C/mol), A (m^2) is the electrode area, D (m^2/s) is the diffusion coefficient of the species, C is the concentration of the species at the surface of the electrode (mol/m^3), and B is proportional to the capacitance of the diffusion-limited process C_D (F/g).

It is expected that the SPECS current reaches zero at the end of the equilibration time, but in reality, this cannot happen due to the existence of some residual processes, alongside with electrical double layer and diffusion-limited processes that do not equilibrate by the end of the equilibration time. The residual process is probably the result of unfinished redox reactions in a given equilibration time. Hence, the residual current (i_R; A/g) is another term that needs to be added to the SPECS model to equilibrate the total current.

Thus, the SPECS model consists of the electrical double layer current at the geometric and porous surface areas and the current related to the diffusion-limited process and residual process. The total current of SPECS data can be given by:

$$i_{Total} = i_{DL1} + i_{DL2} + i_D + i_R = \frac{E}{R_{s1}}\exp\left(-\frac{t}{R_{s1}C_{DL1}}\right) + \frac{E}{R_{s2}}\exp\left(-\frac{t}{R_{s2}C_{DL2}}\right) + \frac{B}{t^{1/2}} + i_R \tag{32}$$

where R_{s1}, R_{s2}, C_{DL1}, C_{DL2}, B and i_R are fitted parameters, obtained by linear least-squares regression.

Eventually, the capacitance of the electrical double layer, diffusion-limited and residual processes, can be calculated by integrating the corresponding current with respect to time.

The SPECS method has been applied in several studies to determine the characteristic of various electrode materials and charging storage mechanisms. The SPECS method was applied to an activated carbon electrode, revealed the significant contribution of diffusion-limited processes, more than 50 % of total capacitance at some potentials, in contrast with the general assumption that the electrical double layer is dominant charge storage in the activated carbon [122].

This method was also applied to a range of manganese dioxide phases, indicating that, the pseudo-capacitance contribution is different for different crystal structures, with electrolytic manganese dioxide (EMD) having the highest contribution from pseudo-capacitance. It also showed the inverse relationship between the diffusion-limited capacitance and the series resistance, indicating that the series resistance increases due to the diffusion of protons cations through the electrode materials [132]. Moreover, the SPECS results show that the double layer capacitance can be affected not only by the surface area and pore size distribution but also by the crystal structure of MnO_2 [77].

Moreover, the contributions made by each charge storage mechanism were determined as a function of different scan rates in a series of EMDs using the SPECS method. It was observed that the contribution of electrical double layer capacitance is much larger at higher scan rates, and also that, the charge is stored primarily via diffusion-limited processes at low scan rates. The total capacitance was increased with decreasing the scan rate, because of the longer equilibration time available at low scan rates which leads to a greater extent of proton (cation) diffusion through the structure [64].

4.4. Electrochemical Impedance Spectroscopy (EIS)

Electrochemical impedance spectroscopy (EIS) has been applied to characterize the electrochemical properties of electrode material by applying an AC potential to an electrochemical cell and measuring the phase shift and amplitude of the resulting current at that frequency. It can be used to determine the dynamics of bound or moving charges in any solid or liquid form material such as ionic, semiconducting, mixed electronic-ionic and insulators [121, 123, 124].

In this method a sinusoidal (monochromatic) voltage signal of $V(t) = V_0 \sin(\omega t)$ with a single frequency of ω is applied to the electrode. The resultant steady state current ($I(t)$; A) is measured; i.e.,

$$I(t) = I_0 \sin(\omega t + \theta) \tag{33}$$

where θ is the phase difference of the voltage and current, which can be zero for purely resistive material and I_0 is the amplitude of the current.

The relationship between alternating current and a monochromatic voltage signal of $V(t) = V_0 \sin(\omega t)$ for a pure electrochemical double layer capacitance can be obtained at a frequency of ω. The immediate charge on an ideal ECDL is given by; i.e.,

$$q = CV(t) = CV_0 \sin(\omega t) \tag{34}$$

where q is a charge (C), and C is a capacitance (F). The corresponding current of charge q at time t is [21]; i.e.,

$$I(t) = \frac{dq}{dt} = \frac{CdV(t)}{dt} = \omega CV_0 \cos \omega t \tag{35}$$

The current reaches its maximum value when $\omega t = 1$ so the maximum current is given by;

$$I_{(\max)} = \omega CV_0 = V_0/(\frac{1}{\omega C}) \tag{36}$$

The term $(1/\omega C)$ is called the reactive capacitance Z_c which equivalents to an impedance of a capacitor; e.i., I=E/R. However, it is an imaginary quantity so it is written as equation below;

$$Z_c'' = (\frac{-j}{\omega C}) \tag{37}$$

where $= \sqrt{1}$. Also, the resistance of the resistor R which is a real quantity is equal to

$$Z_R' = R \tag{38}$$

Hence, the total impedance for a series RC circuit is given by;

$$Z_R' + Z_c'' = R - (\frac{j}{\omega C}) \tag{39}$$

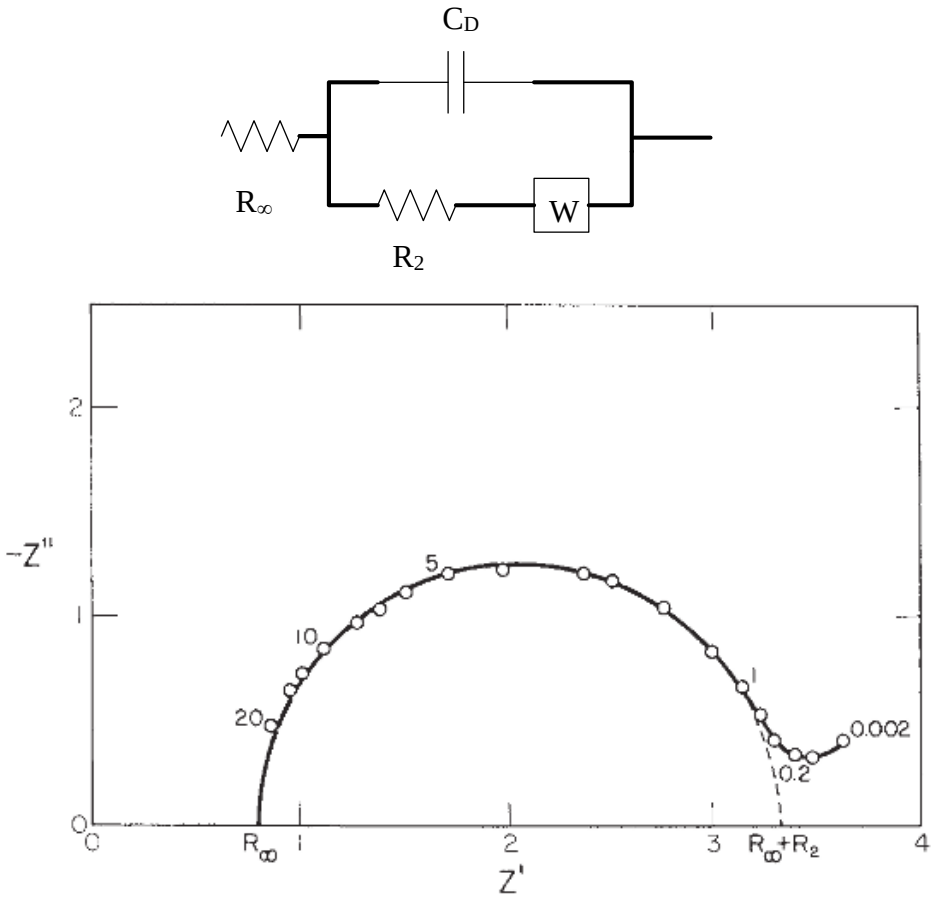

Figure 22 Equivalent circuit and its corresponding impedance plot of a Zn(Hg)/Zn^{2+} couple [124].

Figure 22 shows an impedance plot of a $Zn(Hg)/Zn^{2+}$ couple and its equivalent circuit. Warburg impedance component (W) represents the diffusion behaviour. The Y and X axis represent the imaginary and real quantity, respectively. The numbers over the graph are different frequencies in kilohertz.

Although EIS can provide the fundamental information about the charge mechanisms and material characteristics, it is only limited to one potential within the potential window, and it does not cover the whole potential window [125, 126]. However, in general, several EIS tests are applied to an electrochemical cell, consecutively at different desired potentials [182].

4.5. Method Comparison: CV, EIS and SPECS

CV, EIS and SPECS are the common electrochemical methods which can provide information about the performance of materials and devices such as the specific capacitance, capacitive and diffusional characteristics and the equivalent series resistance (ESR).

Although these methods could provide the same characteristics of the electrochemical system such as the specific capacitance and ESR, they should be carefully chosen based on their applications, experimental design and priorities of a research study. For instance, the EIS method is a non-destructive test which can be applied for checking the quality of final products without damaging electrodes of the electrochemical cell. Also, EIS is the fastest method to find the ESR and provide information about the capacitive and diffusional behaviour of the electrode material from the shape of the graph of the EIS test.

On the other hand, CV is the best method to study the cyclability of the electrochemical cell and ageing process of the electrode materials. The time of the CV test varies based on the sweep rate and cycle numbers. CV also is a reliable method to find and determine the potential window of the new electrochemical systems with new electrode materials and electrolytes. The shape of the graph of the CV test can provide valuable information about the electrode materials

and the electrochemical cell such as the oxidation and reduction peaks, the ESR and the cyclability of the electrode materials.

Among these three techniques, the SPECS is the most rigorous method to obtain the contribution of different charge storage mechanisms, such as electrical double layer and diffusion-limited processes due to its slow sweep rate which allows an electrode to approach its maximum charge storage capabilities. SPECS method also can infer electrode and device instabilities from the residual current, which is an important factor for designing the engineering of the electrochemical cell. The duration of one cycle (charging/discharging) of the SPECS experiment depends on the potential step and the equilibration time after each potential step, but generally, it is a long experiment due to its slow sweep rate.

Overall, the advantage of the CV, EIS and SPECS techniques over each other are based on their applications, electrode materials and electrochemical cell under study and the experimental design. Hence, before applying these methods, preparing the precise experimental plan based on the electrochemical system under study is necessary to take the full advantage of these three reliable electrochemical techniques.

References

1. *Key World Energy Statistics 2018.*
2. Shafiee, S. and E. Topal, *When will fossil fuel reserves be diminished?* Energy policy, 2009. 37(1): p. 181-189.
3. Kaygusuz, K., *Energy for sustainable development: A case of developing countries.* Renewable and Sustainable Energy Reviews, 2012. 16(2): p. 1116-1126.
4. *Annual Energy Outlook 2015*.
5. Chester, L., *Conceptualising energy security and making explicit its polysemic nature.* Energy policy, 2010. 38(2): p. 887-895.
6. Singh, R.K., A. Sarkar, and J.P. Chakraborty, *Influence of Alternate Fuels on the Performance and Emission from Internal Combustion Engines and Soot Particle Collection Using Thermophoretic Sampler: A Comprehensive Review*. Waste and Biomass Valorization, 2018: p. 1-23.
7. *Annual Energy Outlook 2019.*
8. Augustyn, V., P. Simon, and B. Dunn, *Pseudocapacitive oxide materials for high-rate electrochemical energy storage.* Energy & Environmental Science, 2014. 7(5): p. 1597-1614.
9. Gahleitner, G., *Hydrogen from renewable electricity: An international review of power-to-gas pilot plants for stationary applications.* International Journal of Hydrogen Energy, 2013. 38(5): p. 2039-2061.
10. Østergaard, P.A., *Transmission-grid requirements with scattered and fluctuating renewable electricity-sources.* Applied Energy, 2003. 76(1): p. 247-255.
11. Andersen, A.N. and H. Lund, *New CHP partnerships offering balancing of fluctuating renewable electricity productions.* Journal of Cleaner Production, 2007. 15(3): p. 288-293.

12. *Andris Abele, Ethan Elkind, Jessica Intrator, Byron Washom, et al (University of California, Berkeley School of Law; University of California, Los Angeles; and University of California, San Diego) 2011, 2020 Strategic Analysis of Energy Storage in California, California Energy Commission. Publication Number: CEC-500-2011-XXX.*

13. Soloveichik, G.L., *Battery technologies for large-scale stationary energy storage.* Annual review of chemical and biomolecular engineering, 2011. 2: p. 503-527.

14. Dunn, B., H. Kamath, and J.-M. Tarascon, *Electrical energy storage for the grid: a battery of choices.* Science, 2011. 334(6058): p. 928-935.

15. Hall, P.J. and E.J. Bain, *Energy-storage technologies and electricity generation.* Energy policy, 2008. 36(12): p. 4352-4355.

16. *Electric Power Research Institute. 2010a. Electrical Energy Storage Technology Options: A White Paper Primer on Applications, Costs and Benefits. EPRI. Palo Alto, CA 1020676.*

17. *D. Ragone, in: Proceedings of the Society Automotive Engineers. Conference, Detroit, MI, USA, May 1968.*

18. Dupont, M.F. and S.W. Donne, *A Step Potential Electrochemical Spectroscopy Analysis of Electrochemical Capacitor Electrode Performance.* Electrochimica Acta, 2015. 167: p. 268-277.

19. Cross, A., et al., *Enhanced manganese dioxide supercapacitor electrodes produced by electrodeposition.* Journal of Power Sources, 2011. 196(18): p. 7847-7853.

20. Simon, P. and Y. Gogotsi, *Materials for electrochemical capacitors.* Nature materials, 2008. 7(11): p. 845-854.

21. B.E. Conway, *Electrochemical Supercapacitors. Scientific Fundamentals and Technological Applications*. 1999, New York: Kluwer Academic/Plenum Publishers.

22. Mastragostino, M. and F. Soavi, *Capacitors—electrochemical capacitors: ionic liquid electrolytes.* Encyclopedia of Electrochemical Power Sources, 2009: p. 649-657.

23. Dyer, C.K., et al., *Encyclopedia of Electrochemical Power Sources*. 2013: Elsevier Science.

24. Zhang, Y., et al., *Progress of electrochemical capacitor electrode materials: A review.* International journal of hydrogen energy, 2009. 34(11): p. 4889-4899.

25. Okajima, K., et al., *High rate performance of highly dispersed C60 on activated carbon capacitor*. Electrochimica Acta, 2005. 51(5): p. 972-977.

26. Pech, D., et al., *Ultrahigh-power micrometre-sized supercapacitors based on onion-like carbon.* Nature nanotechnology, 2010. 5(9): p. 651.

27. Zhang, H., G. Cao, and Y. Yang, *Carbon nanotube arrays and their composites for electrochemical capacitors and lithium-ion batteries.* Energy & Environmental Science, 2009. 2(9): p. 932-943.

28. Barranco, V., et al., *Amorphous carbon nanofibers and their activated carbon nanofibers as supercapacitor electrodes.* The Journal of Physical Chemistry C, 2010. 114(22): p. 10302-10307.

29. Mombeshora, E.T. and V.O. Nyamori, *A review on the use of carbon nanostructured materials in electrochemical capacitors.* International Journal of Energy Research, 2015. 39(15): p. 1955-1980.

30. Khomenko, V., E. Raymundo-Piñero, and F. Béguin, *High-energy density graphite/AC capacitor in organic electrolyte.* Journal of Power Sources, 2008. 177(2): p. 643-651.

31. Zhang, L.L. and X. Zhao, *Carbon-based materials as supercapacitor electrodes.* Chemical Society Reviews, 2009. 38(9): p. 2520-2531.

32. Frackowiak, E. and F. Béguin, *Carbon materials for the electrochemical storage of energy in capacitors.* Carbon, 2001. 39(6): p. 937-950.

33. Vangari, M., T. Pryor, and L. Jiang, *Supercapacitors: review of materials and fabrication methods.* Journal of Energy Engineering, 2012. 139(2): p. 72-79.

34. Obreja, V.V., *On the performance of supercapacitors with electrodes based on carbon nanotubes and carbon activated material—a review*. Physica E: Low-dimensional Systems and Nanostructures, 2008. 40(7): p. 2596-2605.

35. Lu, X., G. Li, and Y. Tong, *A review of negative electrode materials for electrochemical supercapacitors.* Science China Technological Sciences, 2015. 58(11): p. 1799-1808.

36. Han, Y. and L. Dai, *Conducting Polymers for Flexible Supercapacitors.* Macromolecular Chemistry and Physics, 2019. 220(3): p. 1800355.

37. Pell, W.G. and B.E. Conway, *Analysis of power limitations at porous supercapacitor electrodes under cyclic voltammetry modulation and dc charge.* Journal of Power Sources, 2001. 96(1): p. 57-67.

38. Ruiz, V., et al., *Long-term cycling of carbon-based supercapacitors in aqueous media.* Electrochimica acta, 2009. 54(19): p. 4481-4486.

39. H. von Helmholtz, Ann. Phys. (leipzig), 1853. 89,(211).

40. Gouy, G., *Ann. Phys., Paris,7, 129, (1917).* J. de Phys., 1910. 9,(457).

41. Chapman, D.L., Phil. Mag. , 1913. 25,(475).

42. Stern, O., Zeit. Elektrochem., 1924. 30,(508).

43. Grahame, D.C., Chem. Rev., 1947. 41,(441).

44. Allen J. Bard and L.R. Faulkner, *Electrochemical Methodes : Fundamentals and Applications* SECOND EDITION ed. 2001: John Wiley & Sons.

45. Max Lu, Francois Beguin, and Elzbieta Frackowiak, *New Materials for Sustainable Energy and Development : Supercapacitors*. 2013: John Wiley & Sons.

46. Lu, M., F. Beguin, and E. Frackowiak, *Supercapacitors: materials, systems and applications*. 2013: John Wiley & Sons.

47. Brousse, T., D. Bélanger, and J.W. Long, *To be or not to be pseudocapacitive?* Journal of The Electrochemical Society, 2015. 162(5): p. A5185-A5189.

48. Yu, A., V. Chabot, and J. Zhang, *Electrochemical Supercapacitors for Energy Storage and Delivery: Fundamentals and Applications*. 2013: Taylor & Francis.

49. Burke, A., *Ultracapacitors: why, how, and where is the technology.* Journal of Power Sources, 2000. 91(1): p. 37-50.

50. Miller, J.R. and A.F. Burke, *Electrochemical capacitors: challenges and opportunities for real-world applications.* The Electrochemical Society Interface, 2008. 17(1): p. 53.

51. Kurzweil, P., *Capacitors: electrochemical double-layer capacitors.* Encyclopedia of Electrochemical Power Sources, 2009. 1.

52. Frackowiak, E. and F. Beguin, *Carbon materials for the electrochemical storage of energy in capacitors.* Carbon, 2001. 39(6): p. 937-950.

53. Geim, A.K. and K.S. Novoselov, *The rise of graphene.* Nature materials, 2007. 6(3): p. 183-191.

54. El-Kady, M.F., et al., *Laser scribing of high-performance and flexible graphene-based electrochemical capacitors.* Science, 2012. 335(6074): p. 1326-1330.

55. Vivekchand, S., et al., *Graphene-based electrochemical supercapacitors.* Journal of Chemical Sciences, 2008. 120(1): p. 9-13.

56. Liu, C., et al., *Graphene-based supercapacitor with an ultrahigh energy density.* Nano letters, 2010. 10(12): p. 4863-4868.

57. Xia, J., et al., *Measurement of the quantum capacitance of graphene.* Nature nanotechnology, 2009. 4(8): p. 505-509.

58. Futaba, D.N., et al., *Shape-engineerable and highly densely packed single-walled carbon nanotubes and their application as super-capacitor electrodes.* Nature materials, 2006. 5(12): p. 987-994.

59. Zhang, H., et al., *Comparison between electrochemical properties of aligned carbon nanotube array and entangled carbon nanotube electrodes.* Journal of the Electrochemical Society, 2008. 155(2): p. K19-K22.

60. Pandolfo, A. and A. Hollenkamp, *Carbon properties and their role in supercapacitors.* Journal of power sources, 2006. 157(1): p. 11-27.

61. Qian, H., et al., *Activation of structural carbon fibres for potential applications in multifunctional structural supercapacitors.* Journal of colloid and interface science, 2013. 395: p. 241-248.

62. Pekala, R., et al., *Carbon aerogels for electrochemical applications.* Journal of non-crystalline solids, 1998. 225: p. 74-80.

63. Zuo, L., et al., *Polymer/carbon-based hybrid aerogels: preparation, properties and applications.* Materials, 2015. 8(10): p. 6806-6848.

64. Dupont, M.F. and S.W. Donne, *Faradaic and Non-Faradaic Contributions to the Power and Energy Characteristics of Electrolytic Manganese Dioxide for Electrochemical Capacitors.* Journal of The Electrochemical Society, 2016. 163(6): p. A888-A897.

65. Kurzweil, P., *Capacitors electrochemical metal oxides capacitors, in encyclopedia of electrochemical power sources*. 2009, Amsterdam: Elsevier.

66. Zhou, X., et al., *Study on the electrochemical behavior of vanadium nitride as a promising supercapacitor material.* Journal of Physics and Chemistry of solids, 2009. 70(2): p. 495-500.

67. Zhang, C., et al. *Advanced RuO_2/PEDOT Architecture for Flexible and Transparent Supercapacitors*. in *Meeting Abstracts*. 2016. The Electrochemical Society.

68. Yu, J., et al., *MnO_2 nanosheets grown on internal surface of macroporous carbon with enhanced electrochemical performance for supercapacitors.* ACS Sustainable Chemistry & Engineering, 2016.

69. Huang, Z., et al., *Electrochemical Deposition of Nanostructured Manganese Oxide on Carbon Cloth for Flexible High-Performance Supercapacitor Electrodes.* Journal of Nanoscience and Nanotechnology, 2016. 16(6): p. 5668-5675.

70. Harvey, A., et al., *Production of Ni $(OH)_2$ nanosheets by liquid phase exfoliation: from optical properties to electrochemical applications.* Journal of Materials Chemistry A, 2016. 4(28): p. 11046-11059.

71. Pang, M., et al., *Ethanol-assisted solvothermal synthesis of porous nanostructured cobalt oxides (CoO/Co 3 O 4) for high-performance supercapacitors.* Chemical Engineering Journal, 2015. 280: p. 377-384.

72. Nithya, V. and N.S. Arul, *Progress and development of Fe_3O_4 electrodes for supercapacitors.* Journal of Materials Chemistry A, 2016.

73. Wang, L., et al., *Preparation and electrochemical characteristic of porous NiO supported by sulfonated graphene for supercapacitors.* Electrochimica Acta, 2015. 151: p. 407-414.

74. Ullah, N., M.A. McArthur, and S. Omanovic, *Iridium-ruthenium-oxide coatings for supercapacitors.* The Canadian Journal of Chemical Engineering, 2015. 93(11): p. 1941-1948.

75. Long, J.W., et al., *Voltammetric characterization of ruthenium oxide-based aerogels and other RuO_2 solids: the nature of capacitance in nanostructured materials.* Langmuir, 1999. 15(3): p. 780-785.

76. Toupin, M., T. Brousse, and D. Bélanger, *Charge storage mechanism of MnO_2 electrode used in aqueous electrochemical capacitor.* Chemistry of Materials, 2004. 16(16): p. 3184-3190.

77. Dupont, M.F. and S.W. Donne, *Electrolytic Manganese Dioxide Structural and Morphological Effects on Capacitive Performance.* Electrochimica Acta, 2016. 191: p. 479-490.

78. Wen, S., et al., *The role of cations of the electrolyte for the pseudocapacitive behavior of metal oxide electrodes, MnO_2 and RuO_2.* Electrochimica acta, 2004. 50(2): p. 849-855.

79. Chen, K., C. Sun, and D. Xue, *Morphology engineering of high performance binary oxide electrodes.* Physical Chemistry Chemical Physics, 2015. 17(2): p. 732-750.

80. Post, J.E., *Manganese oxide minerals: Crystal structures and economic and environmental significance.* Proceedings of the National Academy of Sciences, 1999. 96(7): p. 3447-3454.

81. Ostwald, J., *Mineralogy of the Groote Eylandt manganese oxides: A review.* Ore Geology Reviews, 1988. 4(1-2): p. 3-45.

82. Dong, Y., et al., *Simple hydrothermal preparation of [small alpha]-, [small beta]-, and [gamma]-MnO2 and phase sensitivity in catalytic ozonation.* RSC Advances, 2014. 4(74): p. 39167-39173.

83. Van Tendeloo, G., et al., *Advanced electron microscopy and its possibilities to solve complex structures: application to transition metal oxides.* Journal of Materials Chemistry, 2009. 19(18): p. 2660-2670.

84. Poinsignon, C., et al., *Electrochemical and surface properties of nanocrystalline β-MnO_2 in aqueous electrolyte.* Electrochimica acta, 2006. 51(15): p. 3076-3085.

85. Julien, C., et al., *Study of structural defects in γ-MnO_2 by Raman spectroscopy.* Journal of Raman Spectroscopy, 2002. 33(4): p. 223-228.

86. Turner, S. and P.R. Buseck, *Defects in nsutite (γ-MnO_2) and dry-cell battery efficiency.* 1983.

87. Zwicker, W., H. JAFFE, and W. MEIJER, *Nsutite-A widespread manganese oxide mineral.* American Mineralogist, 1962. 47(3-4): p. 246-&.

88. Hunter, J.C., *Preparation of a new crystal form of manganese dioxide: λ-MnO_2.* Journal of Solid State Chemistry, 1981. 39(2): p. 142-147.

89. Berg, H., H. Rundlöv, and J.O. Thomas, *The $LiMn_2O_4$ to λ-MnO_2 phase transition studied by in situ neutron diffraction.* Solid State Ionics, 2001. 144(1-2): p. 65-69.

90. Raveendranath, K., et al., *Thermal diffusivity measurement on $LiMn_2O_4$ and its de-lithiated form (λ-MnO2) using photoacoustic technique.* Materials Science and Engineering: B, 2006. 131(1-3): p. 210-215.

91. Manev, V., et al., *Rechargeable lithium battery with spinel-related λ-MnO_2 III. Scaling-up problems associated with $LiMn_2O_4$ synthesis.* Journal of power sources, 1995. 54(2): p. 323-328.

92. Kim, C.-H., et al., *The structure and ordering of ε-MnO_2.* Journal of Solid State Chemistry, 2006. 179(3): p. 753-774.

93. Li, J.-Y., et al., *Romanechite-structured Na 0.31 MnO 1.9 nanofibers as high-performance cathode material for a sodium-ion battery.* Chemical Communications, 2015. 51(80): p. 14848-14851.

94. Byles, B., et al., *Todorokite-type manganese oxide nanowires as an intercalation cathode for Li-ion and Na-ion batteries.* RSC Advances, 2015. 5(128): p. 106265-106271.

95. Lee, J., et al., *Todorokite-type MnO_2 as a zinc-ion intercalating material.* Electrochimica Acta, 2013. 112: p. 138-143.

96. Nam, K.W., et al., *The high performance of crystal water containing manganese birnessite cathodes for magnesium batteries.* Nano letters, 2015. 15(6): p. 4071-4079.

97. Shareef, M., et al. *Synthesis of Novel Birnessite Type MnO_2 Nanochains by Electrospinning and their Application as Supercapacitor Electrodes*. in *APS March Meeting Abstracts*. 2016.

98. Deibert, B.J., et al., *Surface and Structural Investigation of a MnO_x Birnessite-Type Water Oxidation Catalyst Formed under Photocatalytic Conditions.* Chemistry–A European Journal, 2015. 21(40): p. 14218-14228.

99. Post, J.E. and D.R. Veblen, *Crystal structure determinations of synthetic sodium, magnesium, and potassium birnessite using TEM and the Rietveld method.* American Mineralogist, 1990. 75(5-6): p. 477-489.

100. Kurzweil, P., *Capacitors| Electrochemical Polymer Capacitors.* Encyclopedia of Electrochemical Power Sources, Editor-in-Chief: G. Jürgen, Editor, 2009: p. 679-684.

101. Llorens, E., et al., *Nanomembranes and nanofibers from biodegradable conducting polymers.* Polymers, 2013. 5(3): p. 1115-1157.

102. Snook, G.A., P. Kao, and A.S. Best, *Conducting-polymer-based supercapacitor devices and electrodes.* Journal of Power Sources, 2011. 196(1): p. 1-12.

103. Fang, Q., et al., *Ruthenium oxide film electrodes prepared at low temperatures for electrochemical capacitors.* Journal of The Electrochemical Society, 2001. 148(8): p. A833-A837.

104. Lucio-Porto, R., et al., *VN thin films as electrode materials for electrochemical capacitors.* Electrochimica Acta, 2014. 141: p. 203-211.

105. Lokhande, C., D. Dubal, and O.-S. Joo, *Metal oxide thin film based supercapacitors.* Current Applied Physics, 2011. 11(3): p. 255-270.

106. Massot, L., et al., *Electrodeposition of carbon films from molten alkaline fluoride media.* Electrochimica Acta, 2002. 47(12): p. 1949-1957.

107. Cross, A.D., et al., *Active mass analysis on thin films of electrodeposited manganese dioxide for electrochemical capacitors.* Electrochimica Acta, 2013. 87: p. 133-139.

108. Chun, S.-E., S.-I. Pyun, and G.-J. Lee, *A study on mechanism of charging/discharging at amorphous manganese oxide electrode in 0.1 M Na_2 SO_4 solution.* Electrochimica acta, 2006. 51(28): p. 6479-6486.

109. Wang, X. and Y. Li, *Synthesis and formation mechanism of manganese dioxide nanowires/nanorods.* Chemistry–A European Journal, 2003. 9(1): p. 300-306.

110. Dupont, M.F. and S.W. Donne, *Nucleation and Growth of Electrodeposited Manganese Dioxide for Electrochemical Capacitors.* Electrochimica Acta, 2014. 120: p. 219-225.

111. Poinsignon, C., et al., *Electrochemical response of nanocrystalline tetragonal manganese dioxides prepared by spray vapor pyrolysis and ball milling.* The Journal of Physical Chemistry C, 2007. 111(27): p. 9644-9651.

112. Dupont, M.F., W.M. Dose, and S.W. Donne, *In-Situ Investigation of the Electrodeposition of Manganese Dioxide Using Small Angle X-Ray Scattering.* Journal of The Electrochemical Society, 2015. 162(9): p. A1809-A1815.

113. Clarke, C.J., G.J. Browning, and S.W. Donne, *An RDE and RRDE study into the electrodeposition of manganese dioxide.* Electrochimica acta, 2006. 51(26): p. 5773-5784.

114. Kawamura, H. and Y. Ito, *Electrodeposition of cohesive carbon films on aluminum in a LiCl–KCl–K2CO3 melt.* Journal of applied electrochemistry, 2000. 30(5): p. 571-574.

115. Stern, K., *Electrodeposition of refractory carbide coatings from fluoride melts.* Journal of applied electrochemistry, 1992. 22(8): p. 717-721.

116. Massot, L., et al., *Studies of carbon nucleation phenomena in molten alkaline fluoride media.* Electrochimica Acta, 2003. 48(5): p. 465-471.

117. Chen, H., et al., *Electrodeposition of carbon nanotube/carbon fabric composite using cetyltrimethylammonium bromide for high performance capacitor.* Electrochimica Acta, 2012. 60: p. 449-455.

118. Bekyarova, E., et al., *Multiscale carbon nanotube-carbon fiber reinforcement for advanced epoxy composites.* Langmuir, 2007. 23(7): p. 3970-3974.

119. Du, C. and N. Pan, *Supercapacitors using carbon nanotubes films by electrophoretic deposition.* Journal of Power Sources, 2006. 160(2): p. 1487-1494.

120. Rodriguez, A.J., et al., *Mechanical properties of carbon nanofiber/fiber-reinforced hierarchical polymer composites manufactured with multiscale-reinforcement fabrics.* Carbon, 2011. 49(3): p. 937-948.

121. Dupont, M.F., A.F. Hollenkamp, and S.W. Donne, *Large Amplitude Electrochemical Impedance Spectroscopy for Characterizing the Performance of Electrochemical Capacitors.* Journal of The Electrochemical Society, 2014. 161(4): p. A648-A656.

122. Dupont, M.F. and S.W. Donne, *Separating Faradaic and Non-Faradaic Charge Storage Contributions in Activated Carbon Electrochemical Capacitors Using Electrochemical Methods: I. Step Potential Electrochemical Spectroscopy.* Journal of the Electrochemical Society, 2015. 162(7): p. A1246-A1254.

123. Orazem, M.E. and B. Tribollet, *Electrochemical Impedance Spectroscopy*. 2011: Wiley.

124. Barsoukov, E. and J.R. Macdonald, *Impedance Spectroscopy: Theory, Experiment, and Applications*. 2005: Wiley.

125. Niu, C., et al., *High power electrochemical capacitors based on carbon nanotube electrodes.* Applied Physics Letters, 1997. 70(11): p. 1480-1482.

126. Emmenegger, C., et al., *Investigation of electrochemical double-layer (ECDL) capacitors electrodes based on carbon nanotubes and activated carbon materials.* Journal of Power Sources, 2003. 124(1): p. 321-329.

127. Bailey, M.R. and S.W. Donne, *Electrochemical impedance spectroscopy study into the effect of titanium dioxide added to the alkaline manganese dioxide cathode.* Journal of The Electrochemical Society, 2011. 158(7): p. A802-A808.

128. Bowden, W., et al., *Battery comprising manganese dioxide having a high power coefficient*. 2003, Google Patents.

129. Browning, G. and S. Donne, *Proton diffusion in γ-manganese dioxide.* Journal of applied electrochemistry, 2005. 35(9): p. 871-878.

130. Bowden, W., et al., *Lithiation of ramsdellite–pyrolusite MnO 2; NMR, XRD, TEM and electrochemical investigation of the discharge mechanism.* Journal of power sources, 2006. 153(2): p. 265-273.

131. Gibson, A.J., et al., *Mesoscale Morphological Control of Electrodeposited Manganese Dioxide Films.* Electrochimica Acta, 2015. 170: p. 343-352.

132. Dupont, M.F. and S.W. Donne, *Separating the Faradaic and Non-Faradaic Contributions to the Total Capacitance for Different Manganese Dioxide Phases.* Journal of The Electrochemical Society, 2015. 162(5): p. A5096-A5105.

133. Madeleine F. Dupont and Scott W. Donne, *A Step Potential Electrochemical Spectroscopy Analysis of Electrochemical Capacitor Electrode Performance.* Electrochimica Acta, 2015. 167: p. 268-277.

134. Madeleine F. Dupont and Scott W. Donne, *Separating the Faradaic and Non-Faradaic Contributions to the Total Capacitance for Different Manganese Dioxide Phases.* Journal of The Electrochemical Society, 2015. 162(5): p. A5096-A5105.

135. Delahay, P. and G. Perkins, *Oscillographic Polarography. Phenomena Occurring during the Quiescent Period of the Voltage Wave.* The Journal of Physical Chemistry, 1951. 55(4): p. 586-591.

136. Nicholson, R.S. and I. Shain, *Theory of stationary electrode polarography. Single scan and cyclic methods applied to reversible, irreversible, and kinetic systems.* Analytical Chemistry, 1964. 36(4): p. 706-723.

137. Srinivasan, S. and E. Gileadi, *The potential-sweep method: A theoretical analysis.* Electrochimica Acta, 1966. 11(3): p. 321-335.

138. Lindström, H., et al., *Li^+ ion insertion in TiO_2 (anatase). 2. Voltammetry on nanoporous films.* The Journal of Physical Chemistry B, 1997. 101(39): p. 7717-7722.

139. Augustyn, V., et al., *Lithium-ion storage properties of titanium oxide nanosheets.* Materials Horizons, 2014. 1(2): p. 219-223.

140. Conway, B. and D. Kannangara, *Zinc Oxidation and Redeposition Processes in Aqueous Alkali and Carbonate Solutions II. Distinction Between Dissolution and Oxide Film Formation Processes.* Journal of the Electrochemical Society, 1987. 134(4): p. 906-918.

141. Saidman, S., E. Bellocq, and J. Bessone, *Stationary and non-stationary electrochemical response of polycrystalline indium in alkaline media.* Electrochimica acta, 1990. 35(2): p. 329-338.

142. Bolza, A., *Phenomenological aspects related to the electrochemical behaviour of smooth palladium electrodes in alkaline solutions.* Journal of Electroanalytical Chemistry, 1995. 380(1-2): p. 127-138.

143. Jaegfeldt, H., *Adsorption and electrochemical oxidation behaviour of NADH at a clean platinum electrode.* Journal of Electroanalytical Chemistry and Interfacial Electrochemistry, 1980. 110(1-3): p. 295-302.

144. Come, J., et al., *Electrochemical kinetic study of $LiFePO_4$ using cavity microelectrode.* Journal of The Electrochemical Society, 2011. 158(10): p. A1090-A1093.

145. Liu, T.C., et al., *Behavior of molybdenum nitrides as materials for electrochemical capacitors comparison with ruthenium oxide.* Journal of the Electrochemical Society, 1998. 145(6): p. 1882-1888.

146. Haetge, J., C. Suchomski, and T. Brezesinski, *Ordered mesoporous MFe_2O_4 (M= Co, Cu, Mg, Ni, Zn) thin films with nanocrystalline walls, uniform 16 nm diameter pores and high thermal stability: template-directed synthesis and characterization of redox active trevorite.* Inorganic chemistry, 2010. 49(24): p. 11619-11626.

147. León-Reyes, Á., et al., *Analysis of the Different Mechanisms of Electrochemical Energy Storage in Magnetite Nanoparticles.* Int. J. Electrochem. Sci, 2014. 9: p. 3837-3845.

148. López, M.a.C., et al., *Improved energy storage solution based on hybrid oxide materials.* ACS Sustainable Chemistry & Engineering, 2012. 1(1): p. 46-56.

149. Shao, J., et al., *Mechanism analysis of the capacitance contributions and ultralong cycling-stability of the isomorphous MnO_2@ MnO_2 core/shell nanostructures for supercapacitors.* Journal of Materials Chemistry A, 2015. 3(11): p. 6168-6176.

150. Wang, J., et al., *Pseudocapacitive contributions to electrochemical energy storage in TiO_2 (anatase) nanoparticles.* The Journal of Physical Chemistry C, 2007. 111(40): p. 14925-14931.

151. Kim, J.-H., et al., *Tailoring oriented TiO_2 nanotube morphology for improved Li storage kinetics.* Electrochimica Acta, 2013. 88: p. 123-128.

152. Ranjusha, R., et al., *Fabrication and performance evaluation of button cell supercapacitors based on MnO_2 nanowire/carbon nanobead electrodes.* RSC Advances, 2013. 3(38): p. 17492-17499.

153. Yue, J., et al., *Mesoporous niobium-doped titanium dioxide films from the assembly of crystalline nanoparticles: study on the relationship between the band structure, conductivity and charge storage mechanism.* Journal of Materials Chemistry A, 2017.

154. Opitz, M., et al., *Mechanisms of Charge Storage in Nanoparticulate TiO_2 and $Li_4Ti_5O_{12}$ Anodes: New Insights from Scan rate-dependent Cyclic Voltammetry.* Electrochimica Acta, 2015. 168: p. 125-132.

155. Galizzioli, D., F. Tantardini, and S. Trasatti, *Ruthenium dioxide: a new electrode material. I. Behaviour in acid solutions of inert electrolytes.* Journal of Applied Electrochemistry, 1974. 4(1): p. 57-67.

156. Lodi, G., et al., *On some debated aspects of the behaviour of RuO_2 film electrodes.* Materials Chemistry, 1978. 3(3): p. 179-188.

157. Ardizzone, S., G. Fregonara, and S. Trasatti, *"Inner" and "outer" active surface of RuO_2 electrodes.* Electrochimica Acta, 1990. 35(1): p. 263-267.

158. Dan, Y., et al., *Ti/PbO_{2+} nano-$Co3O_4$ composite electrode material for electrocatalysis of O_2 evolution in alkaline solution.* International journal of hydrogen energy, 2011. 36(3): p. 1949-1954.

159. Baronetto, D., N. Krstajić, and S. Trasatti, *Reply to "note on a method to interrelate inner and outer electrode areas" by H. Vogt.* Electrochimica acta, 1994. 39(16): p. 2359-2362.

160. Hu, C.C. and Y.H. Huang, *Cyclic voltammetric deposition of hydrous ruthenium oxide for electrochemical capacitors.* Journal of The Electrochemical Society, 1999. 146(7): p. 2465-2471.

161. Xing, J., et al., *Preparation and characterization of a novel porous Ti/SnO_2–Sb_2O_3–CNT/PbO_2 electrode for the anodic oxidation of phenol wastewater*. RSC Advances, 2015. 5(66): p. 53504-53513.

162. Zhang, W., et al., *Fabrication, characterization and electrocatalytic application of a lead dioxide electrode with porous titanium substrate.* Journal of Alloys and Compounds, 2015. 650: p. 705-711.

163. Zhao, W., et al., *Study on the performance of an improved Ti/SnO_2–Sb_2O_3/PbO_2 based on porous titanium substrate compared with planar titanium substrate.* Rsc Advances, 2015. 5(34): p. 26530-26539.

164. Doubova, L.M., S. Daolio, and A. De Battisti, *Examination of RuO_2 single-crystal surfaces: charge storage mechanism in H_2SO_4 aqueous solution.* Journal of Electroanalytical Chemistry, 2002. 532(1): p. 25-33.

165. Muller, G.A., et al., *High performance pseudocapacitor based on 2D layered metal chalcogenide nanocrystals.* Nano letters, 2015. 15(3): p. 1911-1917.

166. Kodintsev, I., et al., *X-ray photoelectron spectroscopy and electrochemical surface characterization of iridium (IV) oxide+ ruthenium (IV) oxide electrodes.* Langmuir, 1992. 8(1): p. 283-290.

167. Toupin, M., T. Brousse, and D. Bélanger, *Influence of microstucture on the charge storage properties of chemically synthesized manganese dioxide.* Chemistry of Materials, 2002. 14(9): p. 3946-3952.

168. Yoon, S.-B., et al., *Study on the Electrochemical Kinetics of Manganese Dioxide/Multiwall Carbon Nanotube Composite by Voltammetric Charge Analysis.* Journal of The Electrochemical Society, 2014. 161(1): p. A137-A141.

169. Augustyn, V., et al., *High-rate electrochemical energy storage through Li^+ intercalation pseudocapacitance.* Nature materials, 2013. 12(6): p. 518-522.

170. Duay, J., et al., *Self-limiting electrodeposition of hierarchical MnO_2 and $M(OH)_2/MnO_2$ nanofibril/nanowires: mechanism and supercapacitor properties.* Acs Nano, 2013. 7(2): p. 1200-1214.

171. Hu, C.-C., Y.-S. Lee, and T.-C. Wen, *The physicochemical/electrochemical properties of binary Ni–Co oxides.* Materials Chemistry and physics, 1997. 48(3): p. 246-254.

172. Montilla, F., et al., *Preparation and characterization of antimony-doped tin dioxide electrodes. Part 1. Electrochemical characterization.* The Journal of Physical Chemistry B, 2004. 108(16): p. 5036-5043.

173. Vogt, H., *Note on a method to interrelate inner and outer electrode areas.* Electrochimica acta, 1994. 39(13): p. 1981-1983.

174. Bandaru, P., et al., *Charge transfer and storage in nanostructures.* Materials Science and Engineering: R: Reports, 2015. 96: p. 1-69.

175. Oldham, K. and J. Myland, *Fundamentals of Electrochemical Science*. 2012: Elsevier Science.

176. Endo, M., et al., *Capacitance and pore-size distribution in aqueous and nonaqueous electrolytes using various activated carbon electrodes.* Journal of the Electrochemical Society, 2001. 148(8): p. A910-A914.

177. Hadz, S., et al., *Reversibility and growth behavior of surface oxide films at ruthenium electrodes.* Journal of The Electrochemical Society 1978. 125(9): p.1471.

178. Hu CC., Huang YH., *Cyclic voltammetric deposition of hydrous ruthenium oxide for electrochemical capacitors.* Journal of The Electrochemical Society, 1999. 146(7): p.2465.

179. Hu CC., et al., *How to Achieve Maximum Utilization of Hydrous Ruthenium Oxide for Supercapacitors.* Journal of The Electrochemical Society, 2004. 151(2): p. A281-A290.

180. Hu, C. C., Chang, K. H., Lin, M. C., & Wu, Y. T., *Design and tailoring of the nanotubular arrayed architecture of hydrous RuO_2 for next generation supercapacitors.* Nano letters, 2006. 6(12): p.2690-2695.

181. Hu CC., et al., *Tafel and Electron Paramagnetic Resonance Studies of the Anodic Deposition of Hydrous Manganese Oxides with the Presence of Acetate Ions.* Journal of The Electrochemical Society, 2004. 152(11): p.C723-C729.

182. Hu CC., et al., *The Synergistic Influences of OH^- Concentration and Electrolyte Conductivity on the Redox Behavior of $Ni(OH)_2/NiOOH$* Journal of The Electrochemical Society, 2008. 155(8): p. F196-F200.

Note: Figures in this thesis, reprinted by permission from Publishers.

Chapter 5: Duty Cycle Effects on the Step Potential Electrochemical Spectroscopy (SPECS) Analysis of the Aqueous Manganese Dioxide Electrode

Overview

This chapter focusses on the duty cycle effects on the step potential electrochemical spe

ctroscopy (SPECS) technique. This method has been used for characterising the charge storage mechanisms of electrochemical capacitors. The SPECS technique is based on applying a series of equal magnitude potential steps on a working electrode, with sufficient rest time to allow for quasi-equilibrium to be established for each step throughout an applied potential window. This slow sweep rate enables an electrode to approach its maximum charge storage capability. More importantly, it allows separation of charge storage mechanisms, such as electrical double layer charge storage and diffusion-limited processes. The effect of changing the potential step size and rest time on the performance of the electrolytic manganese dioxide electrode has been presented here.

The following publication is reproduced from the Journal of the Electrochemical Society, Volume 165, Issue 3, p. A593 - A602 (2018), with permission of the Electrochemical Society.

Journal of The Electrochemical Society, **165** (3) A593-A602 (2018)
0013-4651/2018/165(3)/A593/10/$37.00 © The Electrochemical Society

Duty Cycle Effects on the Step Potential Electrochemical Spectroscopy (SPECS) Analysis of the Aqueous Manganese Dioxide Electrode

Marveh Forghani* **and Scott W. Donne** **,z

Discipline of Chemistry, University of Newcastle, Callaghan NSW 2308, Australia

Step potential electrochemical spectroscopy (SPECS) has previously been demonstrated as an effective method for deconvoluting charge storage processes in electrochemical capacitor materials. Herewith is described the effect of the two main experimental variables in SPECS; namely the potential step size and the electrode rest time, on the behavior of the aqueous manganese dioxide electrode. The potential step size dictates polarization at the electrode-electrolyte interface, and hence the driving force for charge storage, while the electrode rest time effects the extent to which the electrode has equilibrated before the subsequent potential step. The extent to which these experimental variables influence geometric and porous double layer formation, as well as diffusional and residual electrode processes, in the manganese dioxide electrode have been described and explained based on the current physical understanding of this electrode system. Furthermore, functional relationships were also established between the diffusional capacitance and the inverse square root of the scan rate ($v^{-1/2}$), as well as the residual capacitance and the inverse of the scan rate (v^{-1}).
 [DOI: 10.1149/2.0841803jes]

Manuscript submitted January 17, 2018; revised manuscript received February 19, 2018. Published March 1, 2018.

Energy and energy storage.—The demand for energy continues to increase, primarily as a result of a growing global population and increased industrialization. This demand for energy is met by many sources, although primarily from fossil fuel combustion, as well as other more renewable sources such as wind, solar and geothermal.[1,2] However, fossil fuel consumption is becoming a less reliable source of energy due to the rising price of fuels, uncertainties in energy markets, securing supplies of primary energy, and environmental regulations. Hence, there is considerable interest in producing energy from renewable energy sources which are more sustainable and environmentally friendly. To achieve this goal, development of efficient energy storage systems is necessary due to the fluctuating and intermittent nature of some renewable sources, such as wind power and solar energy.[3–5] The main type of energy storage technologies that have been used on the large scale are mechanical, thermal, chemical and electrochemical energy storage.[6] Of these, electrochemical energy storage is attractive for many reasons including technological flexibility and high efficiency.[7]

Electrochemical energy storage and conversion technologies encompass the various capacitor, battery and fuel cell systems available. A common method of comparing these technologies is a Ragone diagram[8] (comparing energy and power output), although there are many other important considerations including cyclability, cost per unit output, and environmental friendliness. In general, the various capacitor technologies are typified by very high power densities (W/kg) and excellent cyclability, at the expense of energy density (Wh/kg), meaning that their cost per unit energy is quite high. At the other end of the spectrum, fuel cells are characterized by high energy densities and efficiencies, albeit with low output power density. In general, battery systems are typically intermediate between capacitor and fuel cell systems, and hence they are much more widespread because of their balanced power and energy outputs.[9–10] The shortfall in energy output of electrochemical capacitors compared to other technologies has made this a topic of considerable research, and as such this is the focus of this work.

Electrochemical capacitors.—As mentioned above, electrochemical capacitors are energy storage and conversion technologies that provide high output power and excellent cyclability at the expense of low output energy. The energy (E) which is stored in an electrochemical capacitor is given by:

$$E = \frac{CV^2}{2} \quad [1]$$

Thus, increasing the specific capacitance (C; F/kg) and/or the potential window (V) leads to a higher specific energy in an electrochemical capacitor. Current research trends are to develop new materials with higher specific capacitance, and new capacitor systems with wide electrochemical windows to deliver higher energy.[10]

Generally, energy storage within electrochemical capacitors is associated with charge separation in the electrical double layer at the electrode-electrolyte interface. Additionally, some materials exhibit pseudo-capacitance, which results from fast reversible redox reactions also at the electrode-electrolyte interface. All electrode systems will develop an electrical double layer. To make it a viable means of energy storage what is required primarily is that the electrode-electrolyte interface is very large and that the conductivity of both phases is sufficiently high over as broad a potential window as possible.[11–13] The development of pseudo-capacitive materials was to specifically increase the amount of charge stored by accessing the near surface (3D) regions of the electrode material via redox processes rather than only the 2D electrode-electrolyte interface. This enables access to a larger number of charge storage sites; however, for it to be a viable approach the kinetics of the redox processes (charge transfer and mass transport) have to be fast and highly reversible. In this regard, materials that are conventionally considered to be battery materials are finding application as materials for electrochemical capacitors because of their redox capabilities.

Carbon-based materials have been used widely in electrical double layer capacitors (EDLCs) because of their high specific surface area and variable pore size distribution, high chemical stability, environmentally friendliness and moderate cost. The different types of carbon that have been used in EDLCs include, but are not limited to, carbon nano-tubes (CNTs), carbon nanofibers (CNFs) and activated carbon, the latter of which is the most common EDLC material.[10,14]

The most common materials that exhibit the pseudo-capacitive behavior are conducting metal oxides such as ruthenium dioxide (RuO_2) and manganese dioxide (MnO_2), nitrides, and conductive polymers, although redox activity in surface-functionalized carbons, particularly in aqueous media, can also contribute to pseudo-capacitance. Typically, the specific capacitance of materials that exhibit pseudo-capacitance is much higher than electrical double layer capacitor materials.[10,14,15] For instance the capacitance of activated carbon-based materials is generally around 150 F/g in aqueous electrolytes,[16] and around 110 F/g in non-aqueous media, while electrodeposited thin films of manganese dioxide have exhibited capacitances in excess of 2000 F/g.[9] However, because of the redox processes, pseudo-capacitive materials can be unstable during cycling, in contrast with EDLCs which are highly reversible.[14] The capacitance of various materials is influenced significantly by the surface area and morphology

*Electrochemical Society Student Member.
**Electrochemical Society Member.
zE-mail: scott.donne@newcastle.edu.au

of the material. Thus, many studies have been undertaken to determine the effects of material properties on the contribution of the different charge storage mechanisms in electrochemical capacitors.

Electrochemical characterization methods.—Several methods have been developed for characterizing the electrochemical performance of electrochemical capacitor materials and systems. The most common methods are cyclic voltammetry (CV) and constant current charge-discharge cycling (CC), both conducted over the course of many cycles.[17] Generally, these conventional methods can provide information about the performance of materials and devices under specific circumstances such as the specific capacitance (F/g), and also material characteristics such as the equivalent series resistance (ESR). However, these methods are relatively poor at differentiating the various charge storage processes occurring in the electrode during cycling.[18] This is important because while the charge storage mechanisms of electrochemical capacitor materials such as activated carbon and manganese dioxide is totally different, they exhibit similar performance when they are cycled. Hence the contributions made by the different charge storage mechanisms, such as the electrical double layer and diffusion limited processes, cannot be determined by CV and CC methods alone.[19]

Electrochemical impedance spectroscopy (EIS) has also been used to provide different information about electrochemical capacitor materials and systems such as stability of materials, double layer capacitance, diffusional characteristics, equivalent series resistance (ESR), charge transfer resistance, mass transport and time constant using a small AC excitation signal.[17,20,21] Although, EIS can provide the fundamental information about the charge mechanisms and material characteristics, it is most often applied at one potential within the potential window and as such it is of little value in representing the processes over the entire potential window.[22,23]

Step potential electrochemical spectroscopy (SPECS), otherwise known as the potentiostatic intermittent titration technique (PITT), is a promising method that has been used successfully for characterizing the performance of electrochemical energy storage and conversion materials and systems. This method has been applied previously to study the diffusional characteristics of battery materials,[24–27] but in our own recent work it has been applied to electrochemical capacitors. In the SPECS method a small potential step is applied with a sufficient rest time to allow for quasi-equilibrium to be established for each step throughout an applied potential window. This small scan rate enables an electrode to approach its maximum charge storage capabilities. More importantly, it allows separation of charge storage mechanisms, such as via electrical double layer charge storage and diffusional processes.[18,19,28–31] The SPECS data can be modelled, using combined resistance, double layer, diffusional and residual currents, to separate different charge storage mechanisms. Thus, the SPECS method can provide fundamental information about material and system behavior such as kinetics, ESR, diffusional processes, double layer capacitance, fast and slow processes, and also infer electrode instabilities from the residual current. However, further work is required to determine the influence of SPECS experimental parameters, such as different equilibration times and potential steps, on the contribution of charge storage mechanisms and series resistance.

This work.—Step potential electrochemical spectroscopy (SPECS) has been developed and applied in our group to study the performance of materials used in electrochemical capacitors. In previous works in this area one set of conditions (potential step amplitude and equilibration time) for SPECS experiments have been used, but now we intend to examine a matrix of duty cycle conditions to examine the effectiveness of the SPECS analysis method with different step sizes and step times. Additionally, previous work has examined a range of EMDs with different crystal structures, unit cell dimensions, cation vacancy fractions and BET surface area.[28,29] In this work here, a single EMD as an active material will be examined, so the sole focus is on the effects of different conditions used for a SPECS experiment on the charge storage mechanisms. In this technique the resolution of the SPECS experiments is changed by applying three different potential step sizes combined with three different equilibration times. For instance, a larger potential step sizes will lead to less resolution in the final data. Also, the effect of extended equilibration times on the behavior of the charge storage mechanisms while the material is fully discharged can be found. The analysis of these experiments has identified how the electrical double layer capacitance and diffusion-limited processes change as a function of potential step size and equilibration step time. It is expected that a larger potential step size leads to higher overall capacitance. A larger equilibration time can also lead to more charge through the electrode-electrolyte interface and electrode structure, which eventually increases the capacitance. Furthermore, electrode performance under a range of different scan rates (extracted from SPECS) was examined. For instance, the larger potential step sizes at the short equilibration step times represent the fast scan rates and vice versa.

Experimental

Electrode preparation.—In this study the working electrode comprised a mixture of carbon black as a conductive agent (Cabot Vulcan XC72R), electrolytic manganese dioxide (EMD; γ-MnO_2 from Delta EMD Australia Pty Ltd) as the electro-active material, and polyvinylidenedifluoride (PVdF; Fluka) as a binder all with a mass ratio of 80:15:5. The dry ingredients were lightly ground using a ceramic mortar and pestle for ∼5 minutes. A working electrode ink was then made by adding N-methyl-2-pyrrolidinone (NMP; >99%; Sigma-Aldrich) to the dry powder mixture in a weight ratio of 20:1, after which it was stirred for 30 minutes using a magnetic stirrer to obtain a homogenized ink. The home-made activated carbon which was produced in previous works[18,19] was used as an active material for the counter electrode ink, which was made in a similar way. Then 50 μL of the electroactive material ink and 100 μL of the counter electrode ink were dropped onto the ends of a previously cleaned 13 mm diameter stainless steel rod (5 cm long), to make the working electrode and counter electrode, respectively. All substrates had been previously polished with 1200 grit emery paper and then washed thoroughly using Milli-Q water (resistivity >18.2 MΩ.cm), before being used. Finally, coated electrodes were dried in an oven under air and atmospheric pressure at 60° for ∼8 hours.

Electrochemical cell construction.—The electrochemical cell was based on a 13 mm diameter perfluoroalkoxy alkane (PFA) T-junction Swagelok cell. Firstly, the dried counter electrode was inserted into one end of the straight through part of the Swagelok cell. Two layers of porous paper which were used as a separator were soaked in electrolyte solution (0.5 M K_2SO_4) to ensure a fast equilibration, before they were placed over the counter electrode. The working electrode was then inserted into the Swagelok cell directly opposite the already inserted counter electrode. The electrodes were then pressed at 1.7 MPa using a hydraulic press to increase conductivity within the cell and then secured in place while under load. After that, the electrochemical cell was filled with electrolyte solution. The reference electrode (saturated calomel electrode (SCE); Radiometer Analytical) was then inserted into the perpendicular port of Swagelok cell and sealed in place using Parafilm. Finally, the electrochemical cell was left for 1 hour to equilibrate at open circuit potential before starting the experiment. Unless otherwise stated, all potentials stated are with respect to the SCE.

Electrochemical protocols.—An Iviumstat Multichannel Potentiostat controlled by Iviumstat software was used to run experiments in this study. In each experiment the working electrode was tested using cyclic voltammetry to establish reversible cycling, followed by a SPECS experiment. All of the electrochemical cells were cycled in the range 0.0–0.8 V for 250 cycles at 25 mV/s.

A matrix of nine duty cycles was used to examine the effectiveness of the SPECS experiment at different potential step amplitudes and equilibration times. Hence, nine different SPECS experiments were run using potential step sizes of 10, 25 or 50 mV, with equilibration

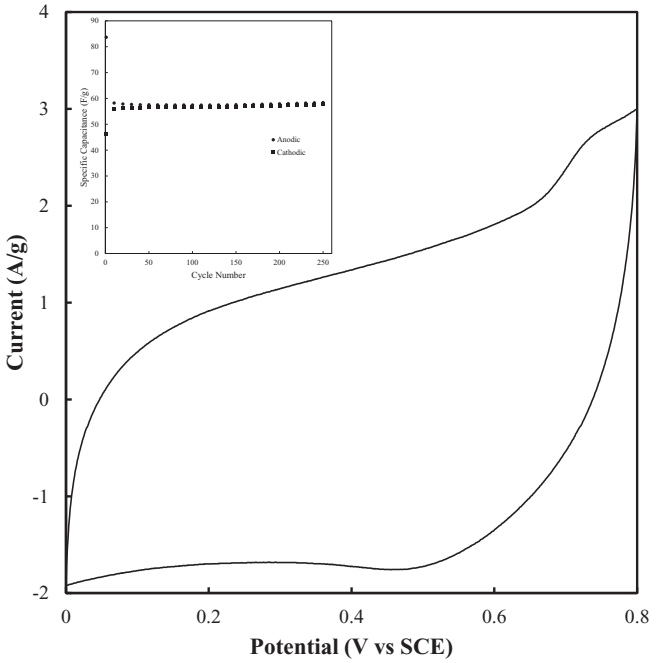

Figure 1. Representative cyclic voltammogram for an EMD electrode cycled at 25 mV/s in 0.5 M K_2SO_4. Inset: Specific capacitance as a function of cycle number.

times of 120, 300 or 600 s. For instance, the potential step size of 10 mV was applied to the working electrode with equilibration times of 120, 300 or 600 s. The following protocol was used to conduct the SPECS experiment for each potential step size (SS) and step time (ST). At the end of the cyclic voltammetry experiment conducted on each electrode the potential was stopped at 0.0 V. From here a series of equally sized potential steps (10, 25, or 50 mV) were applied to the working electrode. After each potential step, the working electrode was allowed to equilibrate (current decay) for a certain step time (120, 300 or 600 s) before applying the next potential step. This was repeated until a full potential window (0.0–0.8 V) was covered. This process was then reversed from the maximum potential of 0.8 V to the minimum potential of 0.0 V. The current response to each potential step was recorded as a function of time until, one entire charge/discharge cycle had been completed.

Results and Discussion

Cyclic voltammetry.—The open circuit potential of the manganese dioxide electrodes used in this work was ~0.4 V versus SCE. The potential of all electrodes was swept initially from this point up to 0.8 V, before then being cycled in the potential window 0.0–0.8 V (vs SCE) in an electrolyte of 0.5 M K_2SO_4 at a scan rate of 25 mV/s for 250 cycles prior to the corresponding SPECS experiment. Figure 1 shows a typical example of a voltammogram from the EMD electrodes studied. It exhibits a roughly rectangular voltammogram with a small peak evident at anodic potentials during the anodic scan for which there appears to be no matching cathodic peak. The current also does tend to increase at higher potentials, likely due to additional anodic redox reactions and potentially an increasing electrode resistance.[31] Pseudo-capacitive charge storage in manganese dioxide based electrochemical capacitor materials is due to cycling of the $Mn^{4+/3+}$ redox couple together with the intercalation or deintercalation of cationic species (M^+; e.g., H^+ and K^+) through the electrode-electrolyte interface; i.e.,

$$MnO_2 + xM^+ + xe^- \leftrightarrow M_xMnO_2 \qquad [2]$$

where x is the depth of discharge. The intercalation of cationic species into the manganese dioxide structure enables utilization of 3D charge storage, with the depth of penetration of the cations into the structure enabling a greater utilization of the active material.

The specific capacitance (C; F/g) was then determined from each voltammogram by firstly determining the anodic and cathodic charge passed (Q; C/g) by integrating the normalized current flow (i; A/g) as a function of cycle time (t; s). This either anodic or cathodic charge is then divided by the operating potential window (V; V) for the process; i.e.,

$$C = \frac{1}{V}\int_0^t idt \qquad [3]$$

The inset in Figure 1 shows the determined anodic and cathodic capacitance as a function of cycle number. During initial cycles there was a substantial difference between the anodic and cathodic specific capacitances. However, when stable cycling had been established after ~50 cycles the charge efficiency was ~101% indicating a slight excess of anodic charge input into the electrode. The cause of this is likely the anodic redox processes evident at high potentials being not completely reversible.[28] Between different electrodes used in this study there was some variability in terms of the specific capacitance, although all values fell within ±4% of the average of the nine electrodes studied. Nevertheless, this variability in performance was accounted for in the subsequent SPECS experiments by normalizing the current flow in each step according to the deviation from average performance in the cyclic voltammetry experiments.

Analysis and deconvolution of SPECS data.—Step potential electrochemical spectroscopy is variant of chronoamperometry or controlled-potential voltammetry, in which the current is measured as a function of time.[32] The SPECS method is based on applying a series of equal magnitude potential steps on the working electrode, with sufficient rest time to allow for quasi-equilibrium to be established for each step throughout an applied potential window. This slow effective scan rate enables an electrode to approach its maximum charge storage capabilities, all the while enabling the kinetics of charge storage to be evaluated. More importantly, it allows for the separation of charge storage mechanisms, such as via electrical double layer charge storage and pseudo-capacitive (specifically diffusional) processes.[18,19,28–31]

Immediately after a potential step the current reaches its maximum value, but it then decays away relatively quickly to approach a quasi-equilibrium value. Ideally this should be zero current; however, the relatively slow kinetics of charge transfer and mass transport, together with inherent electrode instabilities dictate that most often it is a non-zero current. As an example, Figure 2 shows the data for a SPECS experiment using a 50 mV potential step combined with a 120 s relaxation time, together with the staircase potential profile overlaid. It can be seen that the current spikes vary over the potential window which shows clearly that the charging and discharging processes are dependent on potential.[29] It is also evident that the rate of current decay is not the same for each step, which also indicates variability in the charge storage processes at these potentials.

The current flow after each potential step is the result of a number of different charge storage and dissipation mechanisms occurring at the electrode-electrolyte interface. For an electrical double layer at this interface the current response can be simulated by an equivalent circuit consisting of a resistor (R_s; Ωg) and a capacitor (C_{dl}; F/g) in series. A step in potential (ΔE; V) applied to this equivalent circuit gives the following current response (i_{dl}; A/g):[33]

$$i_{dl} = \frac{\Delta E}{R_s}\exp\left(-\frac{t}{R_s C_{dl}}\right) \qquad [4]$$

where t is the time after the potential step (s). Given that many materials used for electrochemical capacitors are porous, it is appropriate to discuss the various sites at the electrode-electrolyte interface and the effect that they may have on charge storage. Most electrodes used for electrochemical capacitors are composite electrodes, consisting of a particulate electroactive material together with a conductive agent and

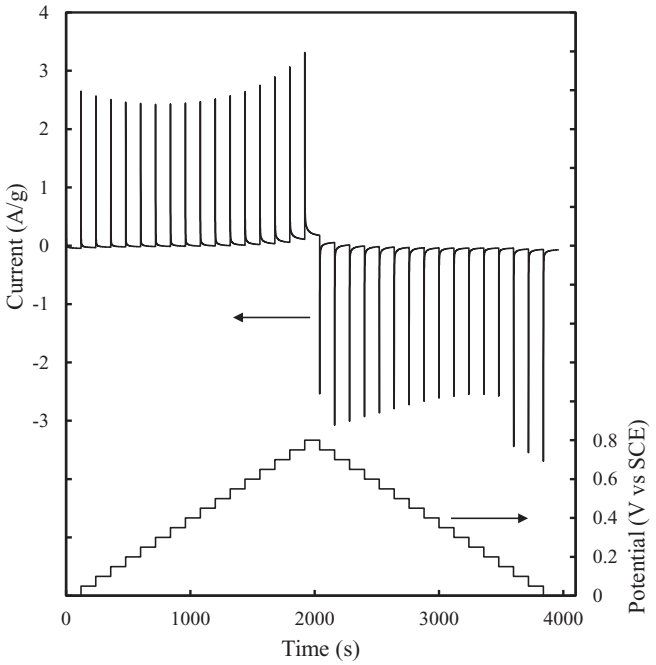

Figure 2. Example of the step potential electrochemical spectroscopy data – EMD in 0.5 M K_2SO_4 using a 50 mV potential step and 120 s rest time.

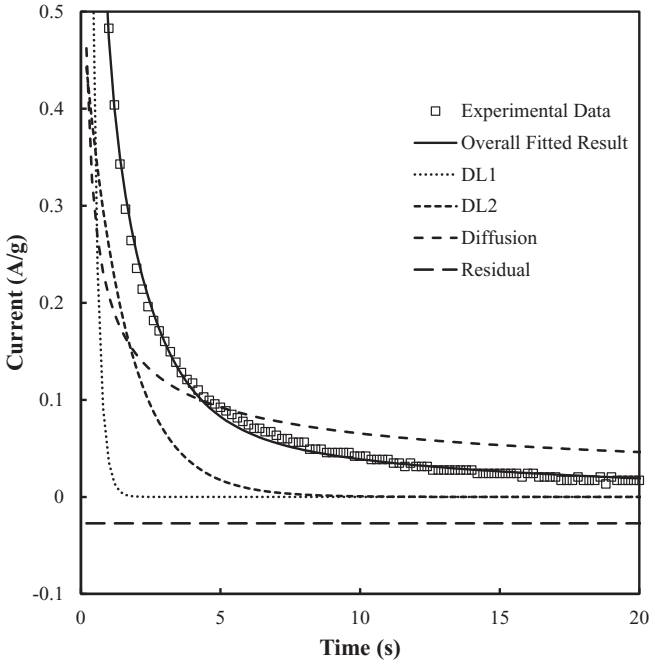

Figure 3. Example of the deconvolution of transient i-t data into various components – DL1: geometric, DL2: porous, diffusional and residual processes.

a binder. Initial charge storage in the electrode is expected to occur on the outer geometric surface area of the electroactive material. This process will be quite facile, with low apparent resistance (R_s) and hence a small time constant ($\tau = R_sC_{dl}$; s). Any resistance will be due to the intrinsic resistivity of the electrode and electrolyte being used. The behavior of the electrode-electrolyte interface within the pores of the electroactive material is, however, expected to be different. While the nature of the charge storage is expected to be the same, the resistance associated with the process is expected to be different compared to charge storage on the geometric surface. Specifically, the need for ionic charge in the electrolyte to move through pores is much more resistive compared to the bulk electrolyte adjacent to the geometric surface. This is due to the need for solvated electrolyte ions to move through pores that are often not much larger than the ion itself.[34] Therefore, a higher resistance, coupled with the interfacial capacitance of the porous surface, leads to a charge storage process with a slightly larger time constant. As such, two expressions based on Eq. 4 have been used to model the experimental data, one representing charge storage on the geometric surface, and another representing charge storage on the porous surface.[29]

For pseudo-capacitive electrodes, redox processes will occur at the electrode-electrolyte interface. The nature of these redox processes depends very much on the electroactive material being used. For example, the manganese oxides used in this work undergo intercalation or deintercalation of electrolyte ions through the interface, much like they would when used as battery materials. With charge injection into the structure a concentration gradient is produced meaning that the intercalated species will diffuse into the bulk of the manganese dioxide particles. This diffusion process enables ongoing intercalation through the interface, and hence a sustained, although decreasing, current. In general, solid state diffusion processes such as this are kinetically much slower than interfacial charge storage, and as a result the time basis for these processes is considerably longer.[19] To interpret this mass transport process by diffusion we have made use of the Cottrell equation, which was derived for semi-infinite planar diffusion,[33] in which case:

$$i_d \propto \frac{1}{t^{1/2}} \text{ or } i_d = \frac{B}{t^{1/2}} \quad [5]$$

where i_d (A/g) is the diffusion limited current, and B is a proportionality constant used for the fitting process. This scenario can be justified given that diffusion in the solid state is so slow that over the duration of each potential step the core of each particle is not reached by the diffusing species.

Figure 2 also shows that for most of the positive and negative 0.05 V steps the current does not reach zero at the end of equilibration time. This demonstrates that there are some residual (kinetically slow) processes occurring in the electrode alongside electrical double layer formation and diffusional processes that do not equilibrate by the end of the rest time. Hence, a residual current (i_{res}; A/g) is included into the overall model; i.e.,

$$\begin{aligned} i_{tot} &= i_{dl1} + i_{dl2} + i_d + i_{res} \\ &= \frac{\Delta E}{R_{s1}} \exp\left(-\frac{t}{R_{s1}C_{dl1}}\right) + \frac{\Delta E}{R_{s2}} \exp\left(-\frac{t}{R_{s2}C_{dl2}}\right) + \frac{B}{t^{1/2}} + i_{res} \end{aligned} \quad [6]$$

where R_{s1}, C_{dl1}, R_{s2}, C_{dl2}, B and i_{res} are fitting parameters, determined using linear least squares regression.

Figure 3 shows an example of a comparison between experimental and predicted data using the model in Eq. 6 for a 0.05 V potential step. In this figure only the first 20 s of the data are shown for clarity. In general the double layer processes, either at the geometric or porous surface area, have a current response that decays away to zero very quickly (<10 s). However, the double layer associated with the geometric surface area has a much faster response compared to that of the porous surface area, essentially due to the differences in environment between the bulk electrolyte and pore confined electrolyte. The diffusional current has a much slower response, it being the dominant characteristic at times >10 s. These capacitive and diffusional processes are all superimposed onto the background residual current, which may or may not be of opposite polarity compared to the potential step.

Synthetic voltammograms.—One of the more recent developments with the analysis of SPECS data is the generation of synthetic voltammograms using the i-t transients at each step potential.[18,19] The foundation for this approach lies in the way in which a

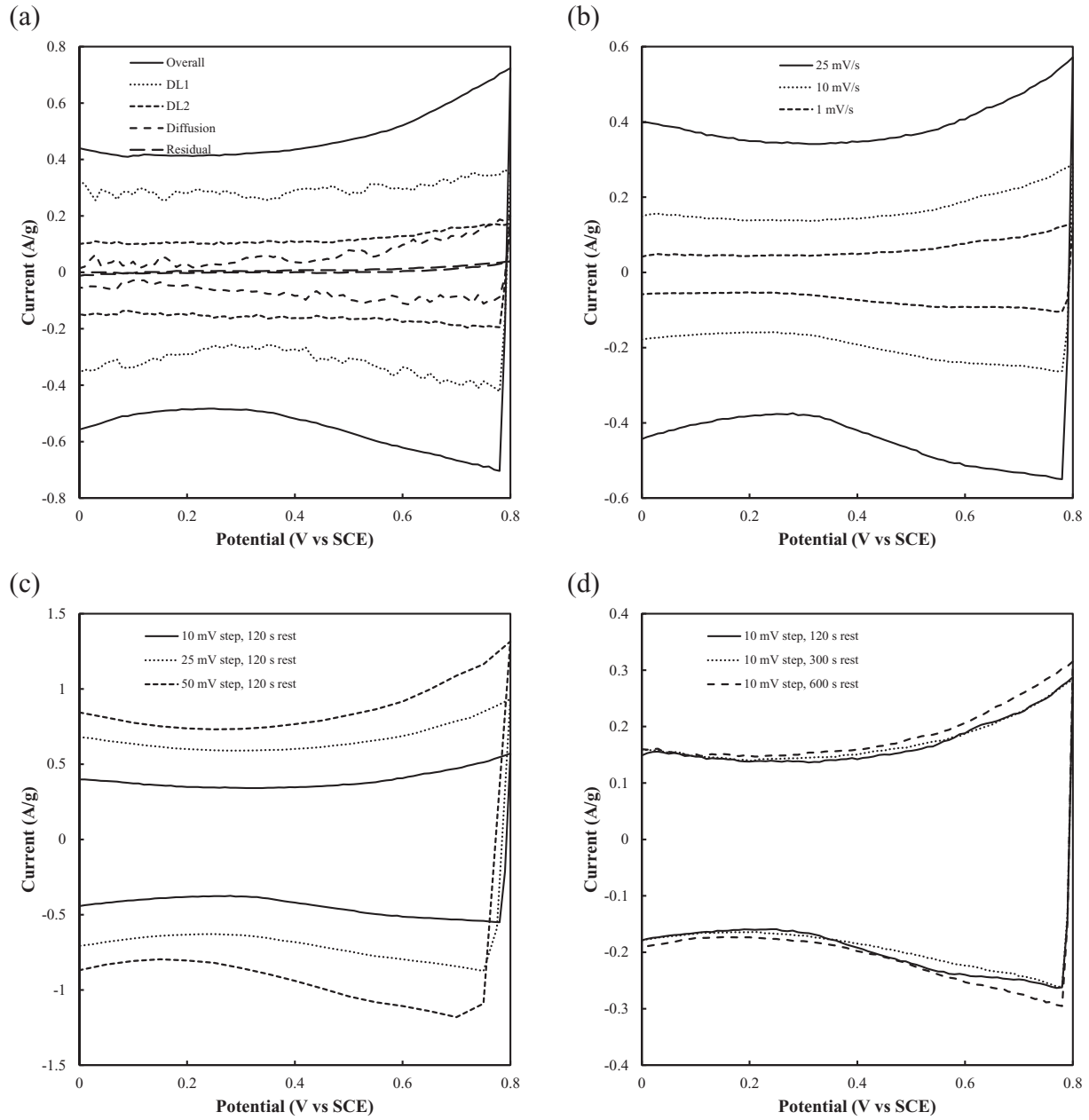

Figure 4. Examples of synthetic voltammogram generated from various duty cycle conditions showing (a) breakdown of overall voltametric behavior into individual components (10 mV step, 600 s rest time, corresponding to a 25 mV/s scan rate); (b) the effect of different effective scan rates on overall behavior (10 mV step, 120 s rest time); (c) the effect of different step sizes on overall behavior (120 rest period, 25 mV/s); and (d) the effect of rest time on overall behavior (10 mV step size, 5 mV/s scan rate).

digital potentiostat carries out a linear potential scan. Instead of using a truly linear potential scan, as is the case with an analog potentiostat using the discharge of a capacitor, a digital potentiostat breaks the potential scan down into a series of small steps and short rest times that overall correspond to the required scan rate. The current response during an individual potential step is then averaged and reported as the current flow at that particular potential. Commercial potentiostats often have the capability of averaging the current over a selected portion of the rest time, basically to achieve what we are aiming to do; namely, separate the fast response capacitive behavior from the slower faradaic processes. Therefore, for each potential step the average current was determined for all preceding current values up to and including the required time. As such an average current can be determined for each data point after the potential step. Furthermore, each average current then corresponds to an effective scan rate; e.g., for a potential step of 50 mV over the first 50 s the effective scan rate is 1 mV/s. If such a process is carried out for each potential step then synthetic voltammograms can be generated. Of course with the deconvolution of the SPECS data mentioned above, it also means that synthetic voltammograms can be generated for each component, or charge storage mechanism, of the overall behavior. Examples of the synthetic voltammograms are shown in Figure 4, in this case for (a) the breakdown of voltametric behavior, (b) the effect of scan rates, (c) the effect of step size, and (d) the effect of rest time.

Figure 4a shows an example of the way in which the various charge storage mechanisms contribute to the overall voltammogram. This example is for a relatively high cycling rate (25 mV/s), for which it can be seen that the capacitive charge storage mechanisms, whether on the geometric surface or on the porous surface, contribute

the most to the current. Conversely, at lower scan rates the slower processes such as diffusion, and also the residual current, contribute the most to the overall current. Figure 4b shows a very typical result for different scan rates. The examples in this figure were calculated from the 10 mV step, 120 s rest time SPECS experiment. Here the current increases as the scan rate was increased because the time base of the average current calculation is shorter, and so the average current should be larger because of the current spike during the initial stages of each potential step. Of course this is consistent with direct CV measurements. Figure 4c shows that the average current for duty cycles with a larger potential step is higher. Duty cycles with a larger potential step have a greater driving force for the movement (diffusion or otherwise) of ions through the electrode-electrolyte interface, and hence a greater flux, which is reflected as a larger current. Finally, Figure 4d shows that there is little variation in the voltammogram with rest time as the only variable changing. What this indicates is that the method used for calculating the average current is acceptable because the passage of subsequent current does not affect the overall current measurements.

Duty cycle effects on the electrode capacitance.—With the processing of SPECS data to produce voltametric data, we are now in the position of being able to calculate the electrode capacitance in the same way that is done conventionally; i.e., Eq. 3. The added benefit here is that because we have also deconvoluted the SPECS data into individual processes, from which we have calculated the contributions made by each process to the overall voltammogram, we can also calculate the capacitance of the individual processes. Therefore, the overall capacitance is given by:

$$C_{tot} = C_{dl1} + C_{dl2} + C_d + C_{res} \quad [7]$$

where C_{dl1} and C_{dl2} (F/g) are the capacitance determined from the electrical double layers formed at the geometric and porous electrode-electrolyte interfaces, respectively, C_d (F/g) is the capacitance from diffusion limited processes, and C_{res} is the capacitance arising from residual processes in the electrode. An example of the rate performance of each of these processes is shown in Figure 5, in this case for the experiment with a 10 mV potentials step and a 120 s rest time. Also in this figure is the percent contribution that each component makes to the overall capacitance at the particular scan rate. At high rates the geometric interfacial capacitance (DL1) dominates performance, followed by the diffusional contributions, geometric capacitance (DL2) and then the residual capacitance. As the scan rate decreases both DL1 and DL2 plateau in capacitance, effectively reaching a saturation point depending on the electrode material and conditions. The rate at which plateau capacitance is reached as a function of decreasing scan rate can be summarized by a time constant ($\tau = RC$; s), which in this case is the average time constant for the process across the full potential window, in either the anodic or cathodic direction. For future comparisons of different duty cycles, the plateau capacitance and time constant will be used to compare capacitive processes.

As the scan rate decreases both the diffusion based capacitance (C_d) and the residual capacitance (C_{res}) increase dramatically, indicating that they are much slower processes. Through the processing of SPECS data for the diffusional processes it has been determined that the resultant capacitance for a particular duty cycle is proportional to the inverse square root of the scan rate; i.e., $v^{-1/2}$, as shown in the examples in Figure 6a. Now the slope of the data set in this figure is an indicator of the rate of change of the diffusional capacitance with scan rate – specifically, a steep slope indicates that the diffusional capacitance decreases relatively faster with an increasing scan rate. Likewise, processing of SPECS data for the residual processes has shown that the residual capacitance for a particular duty cycle is dependent on the inverse of the scan rate; i.e., v^{-1}, as shown in Figure 6b. As before, the slope in this plot is an indicator of how fast the residual capacitance changes with scan rate. The slope in both of these analyses will be used to make comparisons between different duty cycles.

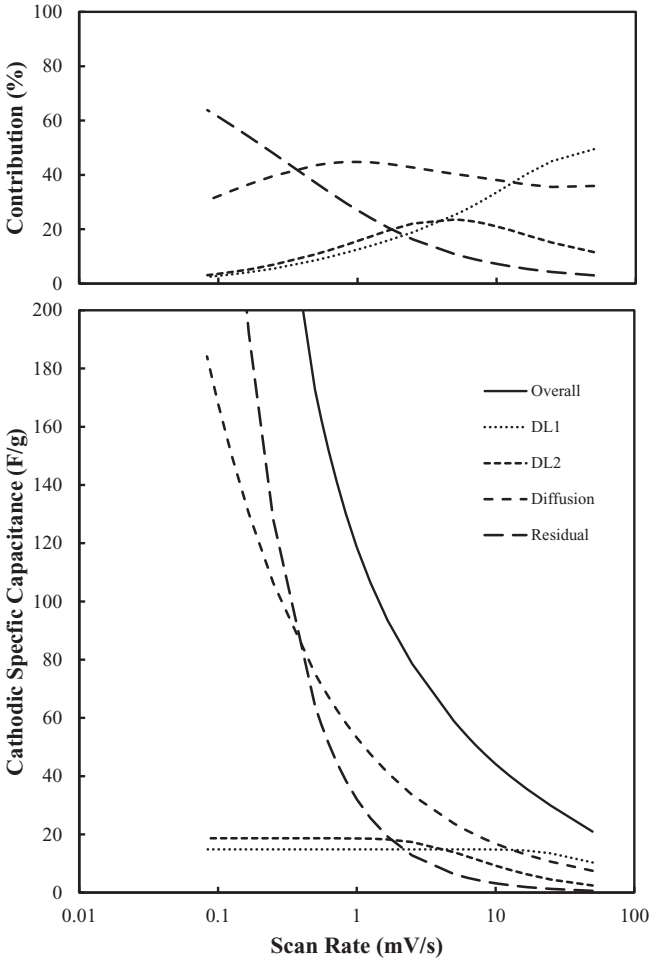

Figure 5. Breakdown of the overall specific capacitance into its capacitive, diffusional and residual components for the aqueous EMD electrode (EMD; 0.5 M K2SO4; ±10 mV potential step; 120 s rest time). Also shown is the percentage contribution made by each process.

Table I presents a comparison of the metrics for each component of the SPECS analysis using different duty cycles. To aid in the interpretation of how these parameters change with duty cycle we have used an empirical modelling approach; i.e.,

$$X = a_0 + a_1(t) + a_2(\Delta E) + a_3(t\Delta E) \quad [8]$$

where X is the metric under consideration, and a_i are fitted model coefficients. a_0 represents the background, a_1 considers the effect of rest time, a_2 the effect of step potential, and a_3 takes into account the interaction between the rest time and step potential. Fitting was carried out using a linear least squares approach. Furthermore, before fitting was carried out, the matrix of experimental values and variables were normalized from 0–1 to place equal weighting on each of the variables. Each of the fitting parameters for each component are shown in Table II. While recognized as not providing mechanistic information, this approach will provide insight into the effect of the duty cycle parameters on component performance.

Geometric capacitance (C_{dl1}).—The geometric capacitance arises as a result of double layer formation at the interface between the outer surface of the electro-active manganese dioxide and the electrolyte. Here it is expected that charge storage processes are expected to be quite facile since it is expected that there is little to inhibit the passage of charge to the surface. This is reflected quite nicely in the average time constant for this process, which is ~0.2 s (see Table I). Analysis of the time constant data for the geometric capacitance data in

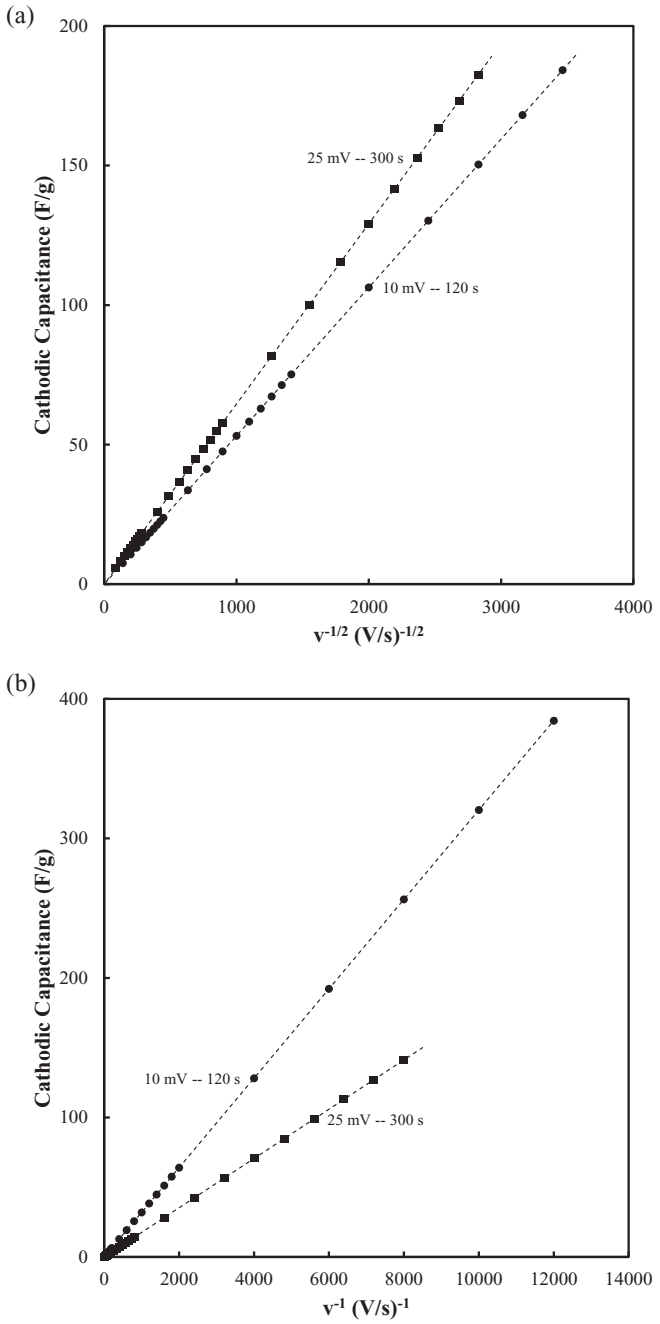

Figure 6. Examples of data showing the relationship between (a) diffusional capacitance and $v^{-1/2}$, and (b) residual capacitance and v^{-1}, where v is the applied scan rate.

Table I using the model in Eq. 8 indicates that individual increases in both the step potential and rest time tend to increase the time constant, with the rest time being the most significant variable. However, simultaneously increasing both the step potential and rest time decreases the time constant. In terms of the plateau capacitance, increasing the rest time was found to have a substantial positive influence; however, an increase in the magnitude of the potential step diminished the plateau capacitance. When combined, increases in both the rest time and the potential step detracted from the plateau capacitance.

Porous capacitance (C_{dl2}).—Most materials used in electrochemical capacitors are highly porous so as to maximize the interface between electroactive material and the electrolyte, and hence maximize the amount of charge stored in the double layer. While a high surface area does most often lead to an increased double layer capacitance, the pore size distribution is also important because electrolyte transport in micropores can be restricted. As such, the pore size distribution is also important, enabling optimization of the balance between outright surface area and electrolyte accessibility to that surface. This potentially restricted access of electrolyte to the porous surface area is reflected in the relatively larger average time constant for this process; i.e., ∼1.88 s, compared to the geometric double layer capacitance. In terms of the time constant for the porous capacitance increasing the rest time led to a slight decrease in the time constant for this process, while an increase in the step size led to a dramatic increase in the time constant. Combining these two experimental variables also led to an increase in time constant, suggesting that the potential step size is dominant with regards to the time constant. In terms of plateau capacitance each of the experimental variables made a positive contribution; however, of these the rest time was the most significant.

Diffusion.—Mass transport in the solid state is the process whereby energy can be stored in the bulk, greatly enhancing the capacitance of the material. This effectively enables the transition from (pseudo) 2D to 3D charge storage. Therefore, instead of charge storage via electrostatic charge interaction in the double layer, charge storage via redox processes can occur; i.e., pseudo-capacitance. The ability of a material to transfer charge through the solid state enables the introduction of what were traditionally battery materials into the electrochemical capacitor domain. Manganese dioxide has long been a good performing material in battery systems, where charge is stored via electron and cation intercalation into the host structure, as shown in Eq. 2. This process occurs with charge injection into the bulk through the electrode-electrolyte interface. Initially this introduces an activity gradient between the surface and core of particles, leading to a driving force for diffusion of intercalated species into the bulk.

The analysis conducted on the diffusional contribution to the SPECS data was based on Eq. 4 where the diffusional contribution to the current was proportional to $t^{-1/2}$. From this the average diffusional current ($i_{ave,d}$; A/g) for a particular time (t; s) after the potential step was determined using:

$$i_{ave,d} = \frac{Q_{s,d}}{t} = \frac{B\int_0^t t^{-1/2}dt}{t} = \frac{2Bt^{1/2}}{t} = 2Bt^{-1/2} \quad [9]$$

where $Q_{s,d}$ is the corresponding charge (C/g) passed in an individual potential step and B is the fitting parameter for each step (Eq. 4). The charge passed across the entire potential scan ($Q_d^* = Q_{a,d}$ or $Q_{c,d}$), either for an anodic ($Q_{a,d}$) or cathodic sweep ($Q_{c,d}$), corresponds then to the integration of $i_{ave,d}$ with respect to time, where in this case the time corresponds to the time taken for a scan conducted at a specified rate (t^*; s); i.e.,

$$Q_d^* = \int_0^{t^*} i_{ave,d}dt = 2B\int_0^{t^*} t^{-1/2}dt = 4B(t^*)^{1/2} \quad [10]$$

The electrode capacitance is then:

$$C_d = \frac{Q_d^*}{V} = \frac{4B(t^*)^{1/2}}{V} \propto v^{-1/2} \quad [11]$$

where V is the voltage window (V), and v is the scan rate (V/s). Therefore, a linear response should be expected between the measured electrode capacitance and the inverse square root of the voltage scan rate, as was shown in Figure 6a.

The fitting parameters for the relationship between the experimental variables and the extracted diffusional parameter are shown in Table II. These values show a strong negative correlation between the diffusional parameter and rest time, as well as a strong positive correlation with potential step size. The parameter representing the combined effects is slightly negative, suggesting that the rest time is the dominant effect.

Table I. Output metrics used for the comparing the behavior of different SPECS duty cycles on the cathodic performance of EMD in 0.5 M K_2SO_4. DL1 (geometric capacitance; C_{dl1}) and DL2 (porous capacitance; C_{dl2}) are characterized by the time constant (τ) and plateau capacitance (C). Diffusion is characterized by the slope of a plot of diffusion capacitance (C_d) versus $v^{-1/2}$, while the residual processes are characterized by the slope of a plot of residual capacitance (C_{res}) versus v^{-1}. In both of the latter cases v is the voltametric scan rate (V/s).

Potential Step	Rest Time	DL1		DL2		Diffusion	Residual
(V)	(s)	τ (s)	C (F/g)	τ (s)	C (F/g)	Slope ($Fs^{1/2}/g/V^{1/2}$)	Slope (Fs/g/V)
0.010	120	0.17±0.01	14.9	1.42±0.15	18.7	0.053	0.032
	300	0.17±0.02	24.5	1.30±0.24	22.3	0.028	0.012
	600	0.17±0.03	24.2	1.40±0.34	24.4	0.024	0.002
0.025	120	0.18±0.01	17.3	1.92±0.11	17.5	0.084	0.036
	300	0.22±0.02	19.2	2.31±0.41	30.2	0.065	0.018
	600	0.23±0.03	21.6	1.99±0.52	40.6	0.054	0.009
0.050	120	0.22±0.02	16.2	1.64±0.26	18.8	0.099	0.032
	300	0.20±0.02	15.5	2.75±0.53	28.3	0.097	0.024
	600	0.18±0.02	22.1	2.17±0.51	29.8	0.063	0.001
Average		0.192	19.5	1.877	25.6	0.063	0.018

Residual processes.—As can be seen in the example in Figure 2, the current flowing at the end of the rest period is not always zero. The implication here is that there are ongoing processes occurring within the electrode that are kinetically very slow, even slower than that dictated by the scan rate of each SPECS experiment. The origin of the residual current certainly depends on the material under study. For instance, some materials may be destabilized at high or low potentials, in which case the residual current flowing may be the result of the oxidation or reduction of the electro-active material or the electrolyte. Alternatively, pseudo-capacitive materials that undergo intercalation processes may be subject to very slow mass transport through the solid state, slower than that allowed by the diffusional contributions. Under these circumstances the residual current may be viewed as an indicator of the long term stability of the electrode material, accessed in one very slow cycle which is perhaps more convenient than in a large number of fast cycles.

In the analysis of SPECS data conducted here the residual current (i_{res}) was a constant value for each potential step. The charge passed due to these residual processes ($Q_{res}{}^*$), whether anodic ($Q_{a,res}$) or cathodic ($Q_{c,res}$), then corresponds to the integration of the residual current with respect to time, where the time in this case refers to the time base chosen for the specified rate; i.e.,

$$Q_{res}{}^* = \int_0^{t^*} i_{res} dt = i_{res}(t^*) \quad [12]$$

The specific capacitance (C_{res}) is then:

$$C_{res} = \frac{Q_{res}{}^*}{V} = \frac{i_{res}(t^*)}{V} \propto v^{-1} \quad [13]$$

Therefore, a linear relationship should be expected between the residual capacitance and the inverse of the scan rate, as is shown in Figure 6b. The proportionality (slope) expected here is then an indicator of how significant a contribution the residual capacitance makes to the overall electrode capacitance. Table II shows the proportionality between the residual capacitance and the inverse scan rate. The data here shows that there is a strong negative correlation in capacitance with rest time, a slightly positive correlation with the amplitude of the potential step, and a slightly negative correlation with the combined effects, perhaps suggesting that the rest time was the dominant variable.

Insights into electrode behavior.—Based on the observed effects the experimental variables of potential step size and rest time have on the output from a SPECS experiment we are now in the position of understanding more deeply the role that these variables have on electrode behavior.

Potential step size.—The size of the potential step used during the SPECS experiment determines the extent of polarization at the electrode-electrolyte interface, essentially setting the driving force for charge storage, either via non-faradaic accumulation or dissipation of charge in the double layer on the geometric or porous surface, or via intercalation into the electroactive material structure. As Table II shows, an increase in potential step size increases the time constant for both geometric and porous capacitances, increases the contributions made by diffusive and residual processes, but has a negative or negligible impact on the plateau capacitance for both capacitive charge storage locations.

The time constant for the capacitive processes is essentially an indicator of how fast charge can be accumulated in or dissipated from the double layer at the electrode-electrolyte interface. Initial considerations may suggest that with a greater driving force the rate at which charge is stored should be faster. That would likely be the case if there were a fixed amount of charge to be passed; however, a larger potential step size enables access to more charge for storage. Therefore, the implication here is that with a larger potential step size, the rate at which charge is stored is slowed down (larger time constant) due to the possibility of more charge being available for storage. This is analogous to using a higher voltametric scan rate to generate more current; however, the efficiency of charge storage is

Table II. Fitting parameters linking the output data (i.e., time constant, plateau capacitance, diffusional slope of capacitance versus $v^{-1/2}$, and residual slope of capacitance versus v^{-1}) to the input experimental parameters.

	DL1		DL2			
Parameters	Time Constant	Capacitance	Time Constant	Capacitance	Diffusion	Residual
a_0 (Background)	0.012	0.300	0.181	0.061	0.377	0.817
a_1 (Rest Time)	0.425	0.723	−0.040	0.507	−0.343	−0.776
a_2 (Potential Step)	0.801	−0.266	0.384	0.082	0.721	0.140
a_3 (Combined)	−0.854	−0.140	0.285	0.091	−0.156	−0.106
R^2	0.342	0.692	0.492	0.582	0.899	0.898

compromised because the intrinsic rate of charge storage is limited compared to the voltametric rate.

The plateau capacitance for the capacitive processes is an indicator of the net amount of charge that can be accommodated in the double layer under the prevailing conditions. For the geometric capacitance an increase in potential step size led to a decrease in the plateau capacitance, which is consistent with the hypothesis presented previously regarding the time constant. Essentially, with a larger step size the efficiency of charge accumulation is compromised and so less can be effectively stored at the interface. The effect of potential step size on the plateau capacitance for the porous interfacial processes was negligible, indicating that the restricted ion movement in the pores of the electroactive material was limiting rather than the driving force for charge storage. This conclusion certainly has implications on the design of materials for electrochemical capacitors, in particular higher energy materials. Specifically, if the porous surface area is to be utilized then sufficient ion transport needs to be facilitated through larger pores.

Diffusion in the case of the manganese dioxide electrode involves firstly the intercalation of cationic species through the electrode-electrolyte interface (cf. Eq. 2), followed by the movement of these species into the bulk of the material as a result of the concentration gradient (diffusion). As mentioned previously, the application of a larger potential step size leads to greater polarization between the electrode-electrolyte interface and the bulk of the particle, thus creating a larger driving force for ion intercalation or deintercalation. The net result is that more charge can be stored within the bulk of the electro-active material, thus improving electrode capacitance and energy.

The residual current used to model the SPECS data was in most cases non-zero indicating that there were processes ongoing within the electrode that were slower than that dictated by the combination of potential step size and rest time. For the broad cross-section of electrochemical capacitor electrode materials available for study this could represent many different system features. For instance, it may represent electrode material instability at certain potentials, slow mass transport of electrolyte through micro-pores or intercalated ions through electrode material structures. Whatever, the cause of the residual current it is an indicator of a slow background process that would only become apparent or manifest itself after extended cycling at higher cycling rates, as traditionally done with electrochemical capacitor testing. If this slow process is a chemical instability of the electro-active material, then the residual current is an indicator of an electrode failure mechanism that the SPECS process identifies in one slow cycle that would otherwise only become apparent after extended cycling. In the case of the manganese dioxide electrodes considered here, the origin of the residual current is likely to be the slow mass transport of intercalated ions into and out of the structure. Table II indicates that there is a slight positive correlation between the potential step size and the residual capacitance. The likely cause of this is to do with the slow mass transport of intercalated ions (H^+ or K^+) through manganese dioxide structure. As discussed above, a larger potential step size increases electrode polarization and hence the driving force for ion transport through the structure. However, these intercalated ions only move at a finite rate that would seem to be quite slow compared to the potential scan rate. Therefore, while the application of a sequence of potential steps causes an increase in electrode polarization, and hence an increasing flux of intercalated species into the electrode structure, the rate of transport of these ions is insufficient to fully equilibrate the electro-active species. Hence, the residual current represents the leftover mass transport that is too slow to be accommodated immediately after the potential step.

Electrode rest time.—The rest time between potential steps in a SPECS experiment is essentially the period of equilibration allowed for the electrode, with of course longer rest times allowing the electrode to approach quasi-equilibrium. This has been shown to have some quite dramatic effects on the manganese dioxide electrode behavior (Table II), with a longer rest time being linked positively to an increasing time constant for geometric double layer formation, as well as both the geometric and porous plateau capacitance. However, the rest time had a negligible effect on the time constant for porous double layer formation. The rest time also contributed negatively to the diffusion and residual electrode processes.

For geometric double layer charge storage an increasing time constant is consistent with an increasing plateau capacitance. With a longer rest time more charge is able to be stored on the geometric surface, and with more charge being stored, as we have discussed previously, the time necessary to store that charge also becomes greater. In a somewhat similar manner, a longer equilibration time has also been shown to lead to greater charge storage on the porous surface. However, in this case the time constant for this process does not change appreciably. This is likely due to the confined nature of the electrolyte within the manganese dioxide pores. We have already established that mass transport of the electrolyte within the manganese dioxide pores is quite restricted, essentially meaning that the electrolyte volume within the pores is fixed during the course of the experiment. The manganese dioxide phase used here is very microporous in nature,[35] implying that they have a very high aspect ratio; i.e., ~0.7 nm in diameter, and potentially 20 μm in length (approximately half the mean particle size), as well as being very tortuous (as deduced from TEM imaging).[36] Under these circumstances it appears therefore that an increasing rest time utilizes the pore-bound electrolyte more thoroughly by allowing charge storage on a larger fraction of the porous surface area, thus leading to a higher plateau capacitance. However, because of the confined nature of the electrolyte, its time constant does not change.

Both the diffusion and residual terms had significant negative correlation with the electrode rest time. This is perhaps counterintuitive because with a longer rest time more of the slower processes, like diffusion and residual processes, should have more time to contribute further to the overall electrode behavior. However, a longer rest time implies that the electrode is closer to equilibrium before the next potential step occurs, and as a result, the net driving force for diffusional and residual processes is not as great. To further explain this consider a single direction (anodic or cathodic) duty cycle that involves a sequence of closely spaced potential steps (short rest time) on an electrode material that has relatively slow mass transport, like manganese dioxide. The first step polarizes the electrode material, but before it can completely equilibrate the next potential step is applied, and so on. At the end of this sequence of potential steps the potential difference between the surface of the electro-active material and the bulk material could be as large as the full potential window used. This high polarization leads to a substantial diffusional current and hence capacitance, even though the efficiency of material utilization will be relatively poor. However, consider the alternative where we use a series of potential steps with a much longer rest time in between. During the rest period the extent to which the electrode equilibrates will be much greater meaning that over the course of the potential step sequence, the extent of polarization between the surface and bulk will be considerably less. As such, the driving force for diffusion will be lower, the resultant diffusional current will be lower, and hence the diffusional capacitance will be less, despite the apparent efficiency of material utilization increasing.

Conclusions

The effects of potentials step size and electrode rest time have been explored in the context of using step potential electrochemical spectroscopy (SPECS) to understand the behavior of electrochemical capacitor electrodes, in this particular case, for the aqueous manganese dioxide electrode. The purpose behind these experiments was to expand the applicability of SPECS as an electrochemical capacitor characterization method, as well as understand further the behavior of the manganese dioxide electrode. A summary of the key activities and findings from this study are as follows:

(i) A matrix of SPECS experimental parameters were examined, including potential step size (10, 25 and 50 mV) and electrode

rest time (120, 300 and 600 s). Combined, these parameters describe the SPECS duty cycle. The effects of these parameter changes were examined for the aqueous (0.5 M K_2SO_4) manganese dioxide (γ-MnO_2) electrode.

(ii) Individual i-t transients within the overall SPECS experiment were modelled using a combination of capacitive, diffusional and residual processes. The capacitive processes were further differentiated in terms of geometric (small time constant) and porous (larger time constant) processes. This deconvoluted data was then converted into synthetic voltametric data, from which the specific capacitance for each process was determined as a function of effective scan rate.

(iii) For the purposes of comparison, the geometric and porous capacitive processes were characterized by the time constant and plateau capacitance. Diffusional processes were characterized by the slope of a plot of capacitance versus $v^{-1/2}$ (v is the scan rate), which was found to be a linear relationship. Similarly, residual processes were characterized by the slope of a plot of capacitance versus v^{-1}, which was also found to be a linear relationship. The relationship between diffusional and residual capacitance and $v^{-1/2}$ and v^{-1}, respectively, was also justified. The effects of potential step size and electrode rest time on the resultant capacitance were modelled empirically.

(iv) The effect of potential step size on the resultant SPECS data arises because of its ability to influence electrode polarization, and hence the driving force for charge storage in the electrode. Conversely, the rest time between potential steps influences the extent to which the electrode equilibrates before the next step is taken. When combined, these variables essentially influence the rate of electrode cycling, with its corresponding effects on performance.

Acknowledgments

The authors acknowledge the financial support provided by the University of Newcastle for the provision of a PhD scholarship (MF).

ORCID

Scott W. Donne https://orcid.org/0000-0001-9389-7870

References

1. Annual Energy Outlook (2015).
2. S. Shafiee and E. Topal, "When will fossil fuel reserves be diminished?," *Energy policy*, **37**(1), 181 (2009).
3. G. Gahleitner, "Hydrogen from renewable electricity: An international review of power-to-gas pilot plants for stationary applications," *International Journal of Hydrogen Energy*, **38**(5), 2039 (2013).
4. A. N. Andersen and H. Lund, "New CHP partnerships offering balancing of fluctuating renewable electricity productions," *Journal of Cleaner Production*, **15**(3), 288 (2007).
5. J. A. Turner, "A realizable renewable energy future," *Science*, **285**(5428), 687 (1999).
6. G. L. Soloveichik, "Battery technologies for large-scale stationary energy storage," *Annual review of chemical and biomolecular engineering*, 2011. **2**: 503.
7. B. Dunn, H. Kamath, and J.-M. Tarascon, "Electrical energy storage for the grid: a battery of choices," *Science*, **334**(6058), 928 (2011).
8. D. Ragone, in: *Proceedings of the Society Automotive Engineers. Conference*, Detroit, MI, USA, May 1968.
9. A. Cross et al., "Enhanced manganese dioxide supercapacitor electrodes produced by electrodeposition," *Journal of Power Sources*, **196**(18), 7847 (2011).
10. P. Simon and Y. Gogotsi, "Materials for electrochemical capacitors," *Nature materials*, **7**(11), 845 (2008).
11. B. E. Conway, Electrochemical Supercapacitors. *Scientific Fundamentals and Technological Applications*, 1999, New York: Kluwer Academic/Plenum Publishers.
12. M. Mastragostino and F. Soavi, "Capacitors—electrochemical capacitors: ionic liquid electrolytes," *Encyclopedia of Electrochemical Power Sources*, **2009**: 649.
13. C. K. Dyer et al., *Encyclopedia of Electrochemical Power Sources*, 2013: Elsevier Science.
14. Y. Zhang et al., "Progress of electrochemical capacitor electrode materials: A review," *International Journal of Hydrogen Energy*, **34**(11), 4889 (2009).
15. W. G. Pell and B. E. Conway, "Analysis of power limitations at porous supercapacitor electrodes under cyclic voltammetry modulation and dc charge," *Journal of Power Sources*, **96**(1), 57 (2001).
16. V. Ruiz et al., "Long-term cycling of carbon-based supercapacitors in aqueous media," *Electrochimica acta*, **54**(19), 4481 (2009).
17. M. F. DuPont, A. F. Hollenkamp, and S. W. Donne, "Large Amplitude Electrochemical Impedance Spectroscopy for Characterizing the Performance of Electrochemical Capacitors," *Journal of the Electrochemical Society*, **161**(4), A648 (2014).
18. M. F. DuPont and S. W. Donne, "A Step Potential Electrochemical Spectroscopy Analysis of Electrochemical Capacitor Electrode Performance," *Electrochimica acta*, **167**, 268 (2015).
19. M. F. DuPont and S. W. Donne, "Separating faradaic and Non-faradaic Charge Storage Contributions in Activated Carbon Electrochemical Capacitors Using Electrochemical Methods: I. Step Potential Electrochemical Spectroscopy," *Journal of the Electrochemical Society*, **162**(7), A1246 (2015).
20. M. E. Orazem and B. Tribollet, *Electrochemical Impedance Spectroscopy*, 2011: Wiley.
21. E. Barsoukov and J. R. Macdonald, *Impedance Spectroscopy: Theory, Experiment, and Applications*, 2005: Wiley.
22. C. Niu et al., "High power electrochemical capacitors based on carbon nanotube electrodes," *Applied Physics Letters*, **70**(11), 1480 (1997).
23. C. Emmenegger et al., "Investigation of electrochemical double-layer (ECDL) capacitors electrodes based on carbon nanotubes and activated carbon materials," *Journal of Power Sources*, **124**(1), 321 (2003).
24. M. R. Bailey and S. W. Donne, "Electrochemical impedance spectroscopy study into the effect of titanium dioxide added to the alkaline manganese dioxide cathode," *Journal of the Electrochemical Society*, **158**(7), A802 (2011).
25. W. Bowden et al., *Battery comprising manganese dioxide having a high power coefficient*, 2003, Google Patents.
26. G. Browning and S. Donne, "Proton diffusion in γ-manganese dioxide," *Journal of applied electrochemistry*, **35**(9), 871 (2005).
27. W. Bowden et al., "Lithiation of ramsdellite–pyrolusite MnO_2; NMR, XRD, TEM and electrochemical investigation of the discharge mechanism," *Journal of Power Sources*, **153**(2), 265 (2006).
28. M. F. DuPont and S. W. Donne, "Electrolytic Manganese Dioxide Structural and Morphological Effects on Capacitive Performance," *Electrochimica acta*, **191**, 479 (2016).
29. M. F. DuPont and S. W. Donne, "faradaic and Non-faradaic Contributions to the Power and Energy Characteristics of Electrolytic Manganese Dioxide for Electrochemical Capacitors," *Journal of the Electrochemical Society*, **163**(6), A888 (2016).
30. A. J. Gibson et al., "Mesoscale Morphological Control of Electrodeposited Manganese Dioxide Films," *Electrochimica acta*, **170**, 343 (2015).
31. M. F. DuPont and S. W. Donne, "Separating the faradaic and Non-faradaic Contributions to the Total Capacitance for Different Manganese Dioxide Phases," *Journal of the Electrochemical Society*, **162**(5), A5096 (2015).
32. K. Oldham and J. Myland, *Fundamentals of Electrochemical Science*, 2012: Elsevier Science.
33. Allen J. Bard and L. R. Faulkner, *Electrochemical Methodes: Fundamentals and Applications*, SECOND EDITION ed. 2001: John Wiley & Sons.
34. M. Endo et al., "Capacitance and pore-size distribution in aqueous and nonaqueous electrolytes using various activated carbon electrodes," *Journal of the Electrochemical Society*, **148**(8), A910 (2001).
35. A. P. Malloy and S. W. Donne, *J. Electrochem. Soc.*, **155**, A817 (2008).
36. C. H. Kim, Z. Akase, L. Zhang, A. H. Heuer, A. E. Newman, and P. J. Hughes, *J. Solid State Chem.*, **179**, 753 (2006).

Chapter 6: Method Comparison for Deconvoluting Capacitive and Pseudo-Capacitive Contributions to Electrochemical Capacitor Electrode Behavior

Overview

This chapter presents the comparison between three common electrochemical methods which have been used for characterising the contribution of different charge storage mechanisms such as electrical double layer and diffusion-limited processes in electrochemical cells. The voltammetric current dependence on sweep rate, voltammetric charge dependence on sweep rate and step potential electrochemical spectroscopy (SPECS) methods were compared experimentally and their limitations and their advantages for interpreting the current data and their abilities to distinguish between the different charge storage mechanisms have been discussed here.

The following publication is reproduced from the Journal of the Electrochemical Society, Volume 165, Issue 3, p. A664-A673 (2018), with permission of the Electrochemical Society.

Journal of The Electrochemical Society, **165** (3) A664-A673 (2018)
0013-4651/2018/165(3)/A664/10/$37.00 © The Electrochemical Society

Method Comparison for Deconvoluting Capacitive and Pseudo-Capacitive Contributions to Electrochemical Capacitor Electrode Behavior

Marveh Forghani* and **Scott W. Donne** **,z

Discipline of Chemistry, University of Newcastle, Callaghan NSW 2308, Australia

Several electrochemical methods have been developed to determine the contribution of different charge storage mechanisms, such as via the electrical double layer and diffusion-limited processes, to electrochemical capacitor behavior. This includes using cyclic voltammetry (CV) data at different sweep rates to obtain the relationship between voltammetric current and sweep rate, and also the relationship between voltammetric charge and sweep rate. Step potential electrochemical spectroscopy (SPECS) also has been used to effectively differentiate between different charge storage mechanisms. Herein we compare these three methods experimentally and also discuss their advantages and limitations toward differentiating between different charge storage mechanisms. These methods have been applied to electrolytic manganese dioxide (EMD) in 0.5 M K_2SO_4 between 0.0–0.8 V (vs SCE). It was found that in all cases, the specific capacitance was decreased by increasing the sweep rate. The capacitance-sweep rate dependence was only found to be accurate in a short range of low sweep rates. Overall there was good agreement between the SPECS and current-sweep rate dependence models over the full range of sweep rates. However, the SPECS method provided more precise information about the kinetic behavior of the electrochemical cell through a full range of sweep rates.
 [DOI: 10.1149/2.0931803jes]

Manuscript submitted January 23, 2018; revised manuscript received February 20, 2018. Published March 8, 2018.

The integration of renewable energy into the grid system is a big challenge due to the fluctuating and intermittent nature of renewable sources such as wind power and solar energy.[1,2] Electrochemical energy storage can potentially be a reliable system for bulk energy storage and for distributing energy loads due to their low environmental impact, high power and energy flexibility, high efficiency and recyclability, and low maintenance.[3] The relationship between the different types of electrochemical energy storage such as batteries, fuel cells, and electrochemical capacitors is described by a Ragone diagram. In general, electrochemical capacitors provide the highest power density (W/kg) at the expense of energy density (Wh/kg). Electrochemical capacitors with much higher power density can be utilized in some applications, such as for uninterruptible power supplies and load-levelling.[4,5]

Generally, the capacitive behavior of electrochemical capacitors is associated with the formation of an electrical double layer at the surface of the electrode, and in some materials pseudo-capacitance, which results from faradaic processes. Electrical double-layer capacitors (EDLCs) store charge directly in the double layer of the electrode-electrolyte interface where charge separation takes place between the electrode and electrolyte.[6] Carbon-based materials have been used widely in EDLCs because of their high specific surface area (SSA), high stability and moderate cost.

The charge storage mechanism of pseudo-capacitors involves fast reversible redox reactions at the surface of the electrode material coupled with double layer capacitance. These pseudo-capacitive charge storage mechanisms are also different to standard faradaic mechanisms, as discussed by Brousse et al.[7] The most common electrochemical capacitor (EC) materials that exhibit pseudo-capacitive behavior are conducting metal oxides such as ruthenium dioxide (RuO_2) and manganese dioxide (MnO_2), nitrides, and conductive polymers.[5,8,9]

While the charge storage mechanisms of EC materials such as activated carbon and manganese dioxide are totally different, they exhibit similar performance when they are being cycled. Hence, several electrochemical methods have been developed for determining the contribution of different charge storage mechanisms such as the electrical double layer and diffusion-limited processes. These includes using cyclic voltammetry at different sweep rates to obtain the relationship between voltammetric current and sweep rate,[10] and the relationship between a voltammetric charge and sweep rate for both capacitive and diffusion-limited processes.[11] Step potential electrochemical spectroscopy (SPECS) also has been used to effectively differentiate between different charge storage mechanisms.

Cyclic Voltammetry and Step Potential Electrochemical Spectroscopy

Cyclic voltammetry (CV) has been widely used for the characterization of the performance of electrochemical systems. CV is classified as a linear potential sweep or ramp technique where the potential (E; V) is changed from an initial value E_i (V) at sweep rate v (V/s);[12] i.e.,

$$E = E_i + vt \quad [1]$$

where t is the time in seconds after starting the potential sweep. CV can provide several useful pieces of information including the cyclability of the process, the total capacitance of the electrode under study by integration of the voltammetric current with respect to time, the optimum potential window, the electrochemical kinetics of electrodes and an ability to distinguish the capacitive and diffusion-limited charge storage mechanisms by altering the sweep rate.[10,13]

Step potential electrochemical spectroscopy (SPECS) is, however, classified as chronoamperometry, which is the measurement of the current as a function of time after an applied potential step.[14] The SPECS method is based on applying a series of equal magnitude potential steps on a working electrode, with sufficient rest time to allow for quasi-equilibrium to be established for each step throughout an applied potential window. This slow sweep rate enables an electrode to approach its maximum charge storage capability. More importantly, it allows separation of charge storage mechanisms, such as electrical double layer charge storage and diffusion-limited processes.

In the SPECS method the potential changes as per Eq. 1; however, the sweep rate (v; V/s) is broken down into the ratio of a potential step (ΔE; V) and equilibration time (Δt; s); i.e.,

$$E = E_i + vt = \frac{\Delta E}{\Delta t} t \quad [2]$$

This method was used originally to study the diffusional characteristics of battery materials.[15,16] SPECS also has been used successfully for characterising the performance of electrochemical capacitor materials with different materials such as activated carbon and manganese dioxide.[17–22]

Figure 1 shows a comparison between the current-time plots for a CV experiment at a sweep rate of 25 mV/s and a SPECS experiment with 25 mV potential steps and a 300 s equilibration time, with each applied potential profile superimposed. In both methods, the potential was gradually increased from the initial potential up to the maximum

*Electrochemical Society Student Member.
**Electrochemical Society Member.
zE-mail: scott.donne@newcastle.edu.au

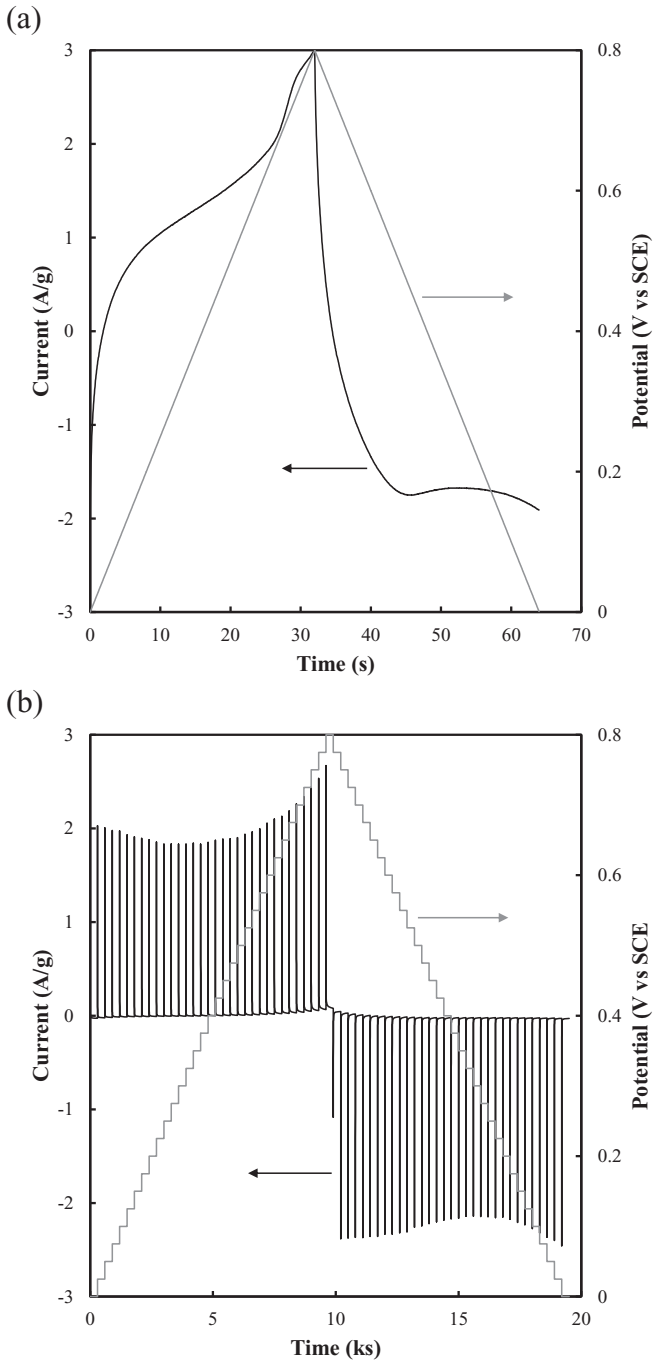

Figure 1. Current response for (a) a CV experiment (EMD in 0.5 M K_2SO_4) cycled in the range 0.0–0.8 V vs SCE at a scan rate of 25 mV/s, and (b) for a SPECS experiment (EMD in 0.5 M K_2SO_4) with ±25 mV potential steps and a 300 s equilibration time.

vertex potential of the electrochemical window. The process was then reversed until the minimum potential was reached. It can be seen that these methods have significantly different sweep rates, as the CV current was obtained in a very short amount of time (64 s), while the SPECS current was extended over a much greater time (>5.5 hours) for the same potential window (0.0 to 0.8 V). Although it has been suggested that a steady-state diffusion front can be realized from CV,[23] the long relaxation time in the SPECS method leads to the extrapolation of kinetic behavior of electrode materials at different times.

Current Dependence on Sweep Rate from Cyclic Voltammetry

The relationship between current and potential sweep rate has been examined extensively.[24–26] Initially, the relationship between peak current and sweep rate was at the center of attention as it was determined that the peak current (i_p) for a totally reversible, diffusion-limited process is proportional to the square root of sweep rate ($v^{1/2}$).[12] In more general terms the relationship between peak current is given by:[27]

$$i_p = av^b$$

or

$$\log(i_p) = \log(a) + b\log(v) \quad [3]$$

where a and b are adjustable parameters. It has been suggested that when the current is due to capacitive processes the b value is 1, while when the b value is 0.5, the current is controlled by diffusion-limited processes.[28] For more complex systems with multiple charge storage processes being apparent, the peak current has been assumed to be the sum of the currents for capacitive processes (electrical double layer or outer surface) and diffusion-limited (inner surface) processes;[29] i.e.,

$$i_p = k_1v + k_2v^{1/2} \quad [4]$$

where k_1 and k_2 are proportionality constants related to the capacitive and diffusion-limited processes, respectively. Although k_1 and k_2 can be determined from the slope and Y-intercept of the plot of $i_p/v^{1/2}$ versus $v^{1/2}$,[30,31] this relationship is not always linear in the desired sweep rate range for reasons such as non-porosity of the surface electrode and different kinetic behavior at different sweep rates.[29,32,33]

Studies on the relationship between peak current and sweep rate eventually led to the investigation of the relationship between voltammetric current at a particular potential and the sweep rate. As with the peak current, CV data at different sweep rates has also been used to obtain the relationship between voltammetric current and sweep rate. In this method, it can be assumed that the total current response at a particular potential (i(V)) is the sum of the current associated with capacitive process and diffusion-limited process. Thus, while the capacitive current is proportional to v, the diffusion limited current is proportional to $v^{1/2}$;[10] i.e., cf. Eq. 4,

$$i(V) = k_1v + k_2v^{1/2}$$

or

$$\frac{i(V)}{v^{1/2}} = k_1v^{1/2} + k_2 \quad [5]$$

Again, the contributions from capacitive and diffusion-limited charge storage mechanisms can be obtained from the slope (k_1) and Y-intercept (k_2) of the plot of $i(V)/v^{1/2}$ versus $v^{1/2}$ at a specific potential. Although this method has been widely used to find the contributions of the different charge storage mechanisms, a plot such as this usually only gives a straight line in a very small sweep rate range,[34–38] and sometimes it is non-linear in a selected range of sweep rates or for a particular potential.[10,39,40] Later, it was argued that the sweep rate dependence of the current obtained from the CV data at a particular potential probably cannot be used for distinguishing between the different charge storage mechanisms in large potential ranges.[41,42]

Voltammetric Charge Dependence on Sweep Rate

The relationship between the voltammetric charge and sweep rate has been studied to identify the behavior of electrode materials during charging and discharging at different sweep rates.[43,44] This relationship was explained mathematically in the method proposed by Trasatti et al.[11] They developed their method based on the hypothesis that the changes in voltammetric charge at different sweep rates are related to a diffusion-limited process at the inner surface of electrode materials, as by increasing the sweep rate the inner surface such as the pores and cracks becomes less accessible for the diffusion of protons. They also suggested that the voltammetric charge related to the outer surface of the electrode remains constant over the range of different sweep

rates. The contribution of voltammetric charge at the outer surface of the electrode (q_o) and the inner bulk of electrode (q_i) gives the total voltammetric charge (q_T);[11] i.e.,

$$q_T = q_o + q_i \quad [6]$$

As the sweep rate is increased, the voltammetric charge of the inner surface, which is assumed to be governed by semi-infinite linear diffusion, decreases with a rate of $v^{-1/2}$. However, the voltammetric charge of the outer surface is independent of the sweep rate, so at an infinite sweep rate q_o can be obtained from the intercept of the plot of q(v) versus $v^{-1/2}$;[11] i.e., when $v \to \infty$,

$$q(v) = q_o + C_1 v^{-1/2} \quad [7]$$

where q(v) is the measured voltammetric charge and C_1 is a numerical constant.

Furthermore, it was also assumed that as the sweep rate was decreased, the voltammetric charge should increase with $v^{1/2}$. Hence, at very low sweep rates the total voltammetric charge, which is composed of the voltammetric charge at the outer surface and at the inner surface of electrode, can be obtained by;[11] i.e., as $v \to 0$,

$$\frac{1}{q(v)} = \frac{1}{q_T} + C_2 v^{1/2} \quad [8]$$

where C_2 is a numerical constant. Therefore, the voltammetric charge contributed to the inner surface area q_i can be found from the difference between q_T and q_o.

This method has been widely used for distinguishing between different charge storage mechanisms and also for finding the porosity of electrode materials.[23,45–51] However, plots of q(v) versus $v^{-1/2}$ and 1/q(v) versus $v^{1/2}$ are not always linear in the desired sweep rate range.[13,28,37,52–57] Furthermore, this method has been criticized because it generates two different equations from the same experimental data, and also for correlating the experimental data over only a limited range of sweep rates.[58] Moreover, it has been argued that the state of infinite sweep rate capacitance is physically unrealistic and scientifically invalid.[59]

Step Potential Electrochemical Spectroscopy (SPECS)

In the SPECS method, current is measured as a function of time after a series of potential steps over the full potential window. The SPECS current is a result of the diffusion-limited processes and electrical double layer formation at the surface and bulk of the electrode. The fast and facile electrical double layer charging process can occur at the geometric surface of the electrode, as well as the surface of the pores in the bulk of the electrode. The capacitive current (i_{DL}; A/g) resulting from a series RC circuit when applying a potential step of magnitude ΔE (V), is given by:[12]

$$i_{DL} = \frac{\Delta E}{R_S} \exp\left(-\frac{t}{R_S C_{DL}}\right) \quad [9]$$

where R_S (Ω/g) is the series resistance, t (s) is the time and C_{DL} (F/g) is the capacitance of the electrical double layer. This expression can be used to represent the electrical double layer capacitance of the geometric surface area. Also, the electrical double layer capacitance is dependent on the pore size of the electrode and the ion diameter of the electrolyte.[60] Therefore, two capacitances are considered for the electrical double layer process; i.e., C_{DL1} (F/g) which is associated with the geometric surface area, and C_{DL2} (F/g) which is related to the porous surface area of the electrode material.[21]

Diffusion limited processes are much slower than the electrical double layer processes due to the slower kinetics associated with redox reactions.[19] Therefore, the diffusional current (i_D; A/g) decreases slowly over the extended equilibration time. This current can be modelled using the Cottrell equation for semi-infinite planar diffusion; i.e.,[12]

$$i_D = nFA\Delta C\left(\frac{D}{\pi t}\right)^{1/2} = \frac{B}{t^{1/2}} \quad [10]$$

where n is the number of electrons involved in an electrode reaction, F is Faraday's constant (96486.7 C/mol), A is the electrode area (m^2), D is the diffusion coefficient of the species (m^2/s), ΔC is the concentration change of the species intercalated into the host structure (mol/m^3), and B is proportionality constant.

It is expected that the SPECS current reaches zero at the end of the equilibration time but in reality this does not happen due to the existence of slow rate residual processes, alongside electrical double layer and diffusion-limited processes that do not equilibrate by the end of the equilibration time. Residual processes are likely the result of incomplete redox reactions in a given equilibration time, and can contribute to the self-discharge of the electrode material. Hence, the residual current (i_R; A/g) is another term that needs to be added to the SPECS model to represent the total current.

Thus the SPECS model consists of a current representing formation of an electrical double layer at the geometric and porous surface, as well as a current related to the diffusion-limited process and residual process. The total current (i_T; A/g) of SPECS data can be given by:

$$\begin{aligned} i_T &= i_{DL1} + i_{DL2} + i_D + i_R \\ &= \frac{\Delta E}{R_{S1}} \exp\left(-\frac{t}{R_{S1}C_{DL1}}\right) + \frac{\Delta E}{R_{S2}} \exp\left(-\frac{t}{R_{S2}C_{DL2}}\right) + \frac{B}{t^{1/2}} + i_R \end{aligned} \quad [11]$$

where R_{S1}, R_{S2}, C_{DL1}, C_{DL2}, B and i_R are fitted parameters, obtained by linear least-squares regression.

Current Work

The common electrochemical methods that can be applied for the characterization of different charge storage mechanisms of electrode materials have been briefly reviewed above. The contributions of the capacitive and diffusion-limited processes can be obtained via the sweep rate dependences of the voltammetric current and charge, and the SPECS method. The aim of this study is to compare these three methods experimentally and also to discuss their limitations and their advantages for interpreting the data and their ability to distinguish between the different charge storage mechanisms. In this work, the combined CV and SPECS methods have been applied to electrolytic manganese dioxide (EMD) in 0.5 M K_2SO_4.

Experimental

Electrode preparation.—The working electrode ink which was used in this study was made from a mixture of carbon black as a conductive agent (Cabot Vulcan XC72R), electrolytic manganese dioxide (EMD; γ-MnO_2 from Delta EMD Australia) as an active material,and poly(vinylidene difluoride) (PVdF; Fluka) as a binder with a ratio of 80:15:5. Firstly, the powdered mixture was lightly ground using a ceramic mortar and pestle for ~5 minutes. Then the solvent 1-methyl-2-pyrrolidinone (NMP; 99+%; Sigma-Aldrich) was added to the dry powdered mixture in a weight ratio of 20:1 after which it was stirred for 30 min using a magnetic stirrer to obtain a homogenized ink. The counter electrode ink was also produced in the same manner using home-made activated carbon[19,22] as the active material. The stainless steel electrode substrates were polished with 1200 grit emery paper and subsequently washed with Milli-Q water before being used. Amounts of 50 and 100 μL of the produced ink were dropped onto the ends of a 13 mm diameter stainless steel rod substrate, to make the working electrode and counter electrode, respectively. All coated electrodes were then dried in an oven at 60°C in air and at atmospheric pressure for ~8 hours. This equates to ~0.3 mg/cm^2 of manganese dioxide on the working electrode and ~0.6 mg/cm^2 of activated carbon on the counter electrode.

Electrochemical cell.—The electrochemical cell was based on a 13 mm diameter perfluoroalkoxyalkane (PFA) T-junction Swagelok

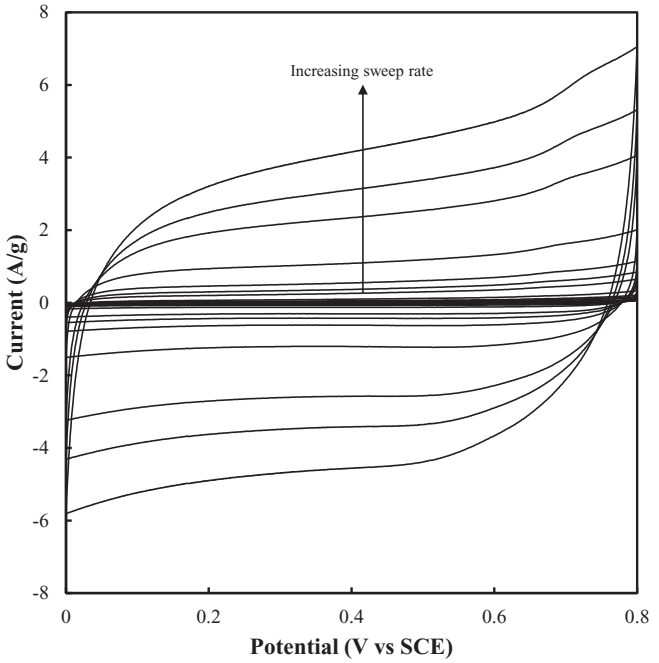

Figure 2. CV experiments at different sweep rates ranging from 0.1 to 100 mV/s.

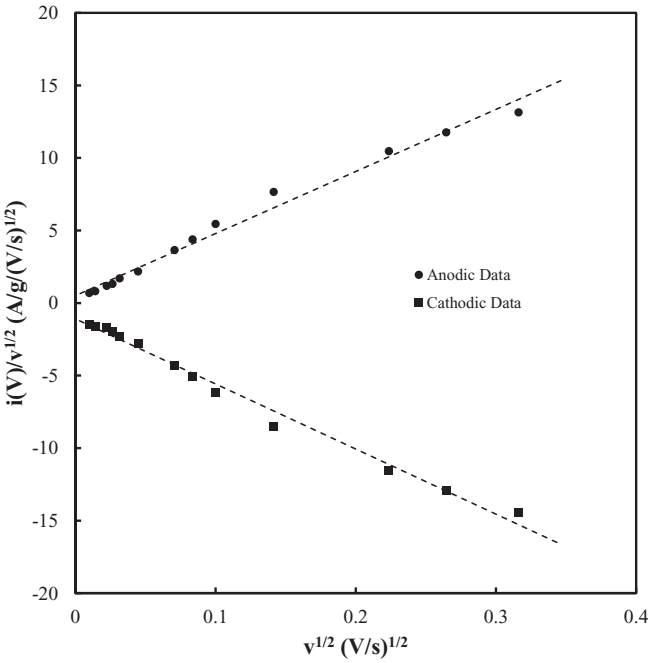

Figure 3. Plots of $i(V)/v^{1/2}$ versus $v^{1/2}$ used to calculate the constants k_1 and k_2 at E = 0.4 V for the anodic and cathodic sweeps, with sweep rates varied from 0.1 to 100 mV/s.

cell. Firstly, the dried counter electrode was inserted into the Swagelok cell. Two layers of porous paper, which were to be used as a separator, were wetted with electrolyte solution to ensure a fast equilibration before they were placed over the counter electrode. Then the working electrode was inserted into the opposite ends of the electrochemical cell. The electrodes were pressed at 1.7 MPa using a hydraulic press to increase the conductivity and secured in place while under load. After that the electrochemical cell was filled with 0.5 M K_2SO_4 electrolyte solution. The reference electrode (saturated calomel electrode; SCE; Radiometer Analytical) was then inserted into the perpendicular port of the Swagelok cell and sealed using Parafilm. Finally, the electrochemical cell was left to equilibrate for an hour before use. Unless otherwise stated, all potentials are with respect to the SCE.

Experimental protocol.—In this study, an Iviumstat Multichannel Potentiostat controlled by Iviumstat software, was used to run the electrochemical experiments. The electrochemical cell was cycled in the range 0.0–0.8 V for 5 cycles at sweep rate ranging from 0.1 to 100 mV/s. This was followed by the SPECS experiment with a 25 mV potential step and 300 s equilibration time. In the SPECS experiment from the open circuit potential (0.0 V), a series of equally sized ±25 mV potential steps were applied to the working electrode. After each potential step, the working electrode was allowed to equilibrate for 300 s before applying the next potential step, until the full potential window (0.0–0.8 V) was covered. This process was then reversed from the maximum potential of 0.8 V to the minimum potential of 0.0 V. The current response from each potential step was recorded as a function of time until one entire charge/discharge cycle was completed. The time base for data collection was 0.02 s.

Results and Discussion

i-v Analysis from cyclic voltammetry data.—The cyclic voltammetry (CV) data for the EMD electrode at different sweep rates (Figure 2) was used to determine the contributions of the electrical double layer and diffusion-limited processes to the overall current. In this analysis, the current at a particular potential was analyzed using Eq. 5, where k_1 and k_2 are related to the electrical double layer and diffusion-limited processes, respectively, and they were determined from the slope and y-intercept of the plot of $i(V)/v^{1/2}$ versus $v^{1/2}$ for each particular potential. Figure 3 shows a plot based on Eq. 5 at a potential of 0.4 V. The plots of both the anodic and cathodic sweeps are almost linear with an R-squared value of 98%. The values of k_1 and k_2 were obtained at each particular potential so as to calculate the capacitive and diffusive currents. Figure 4 shows the contribution made by diffusion-limited (i_D) and electrical double layer (i_{DL}) currents at sweep rates of 0.1 and 100 mV/s. It can be seen that a ratio of the diffusion-limited current over the total current decreased with increasing sweep rate, while this value increased for the capacitive current. The specific capacitance for each component was then calculated from its voltametric data at the different sweep rates used, as shown in Figure 5. It can be seen that the diffusion-limited capacitance (C_D) decreases with increasing sweep rate. In contrast, the electrical double layer capacitance (C_{DL}) remains almost constant over the full range of sweep rates. This could be the result of the typical behavior of pseudo-capacitive materials such as EMD. At a low sweep rate, there is more time for ions to diffuse through the bulk of the electrode material. As the sweep rate increases the rate of diffusion of the ions becomes limiting which leads to a lower diffusive capacitance. Figure 5 also indicates that at lower sweep rates (<0.5 mV/s), the contribution made by the diffusion-limited capacitance is greater than the electrical double layer capacitance. This indicates that the contribution of the diffusion-limited process is more significant at lower sweep rates. The constant value of the electrical double layer capacitance throughout the full range of sweep rates indicates that this charge storage process is saturated, and thus independent of sweep rate.

q-v Analysis from cyclic voltammetry data.—The specific capacitance of each voltammogram was calculated by integrating the current with respect to time to obtain the charge passed (q(v); C/g) for the anodic and cathodic sweeps. The relationship between the voltametric charge and the sweep rate was then analyzed using the method of Trasatti et al.[10] (Eqs. 6–8). When this method has been used in the literature authors use either the charge, as was done by Trasatti, or the electrode capacitance, which is equivalent because the capacitance is

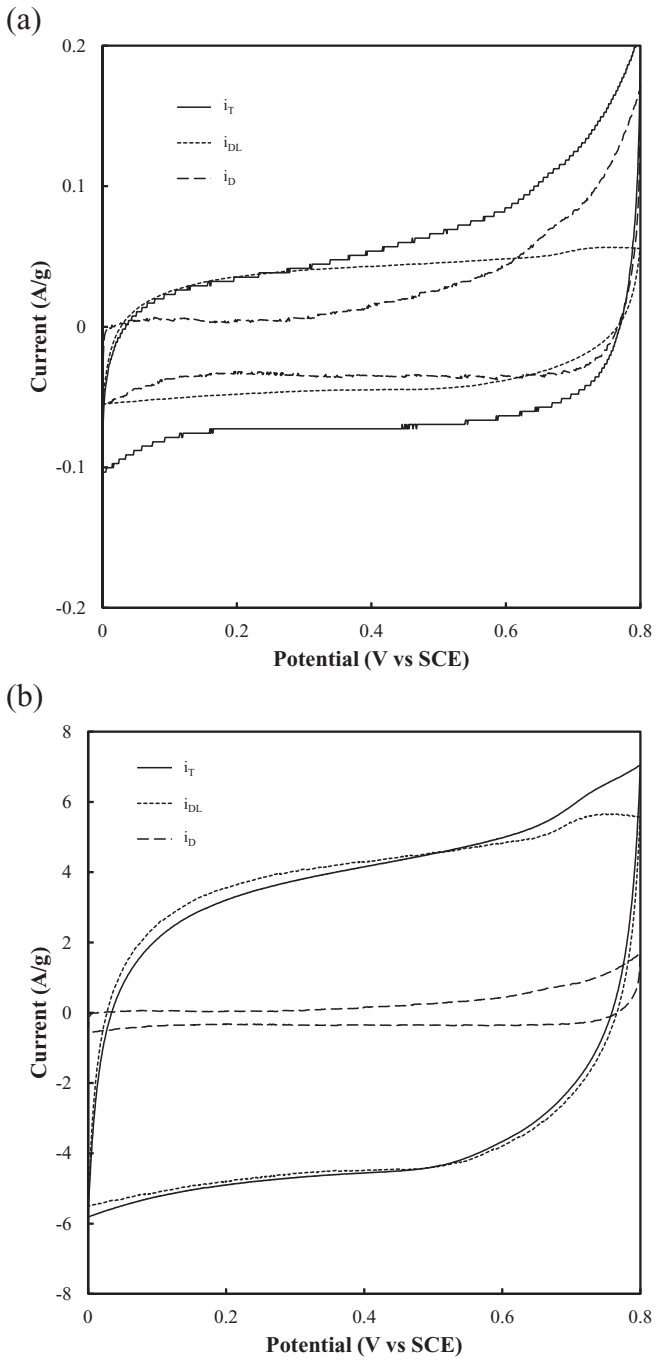

Figure 4. Contribution of the diffusion-limited (i_D) and the electrical double layer (i_{DL}) processes for the EMD electrode at the sweep rates of (a) 0.1 mV/s and (b) 100 mV/s.

directly proportional to the charge; i.e.,

$$C = \frac{q}{V} \qquad [12]$$

where V is the potential window used.

According to this method, when $v \rightarrow \infty$, as per Eq. 7, charge will only be stored at the surface of electrode. Hence the maximum double layer capacitance (C_{DL}) can be obtained from the intercept of the plot of C(v) versus $v^{-1/2}$, which is shown in Figure 6a. In contrast, when $v \rightarrow 0$, there will be sufficient time for the electrode to store the maximum amount of charge, and hence reach its maximum capacitance. Hence, the total capacitance (C_T) can be found from the

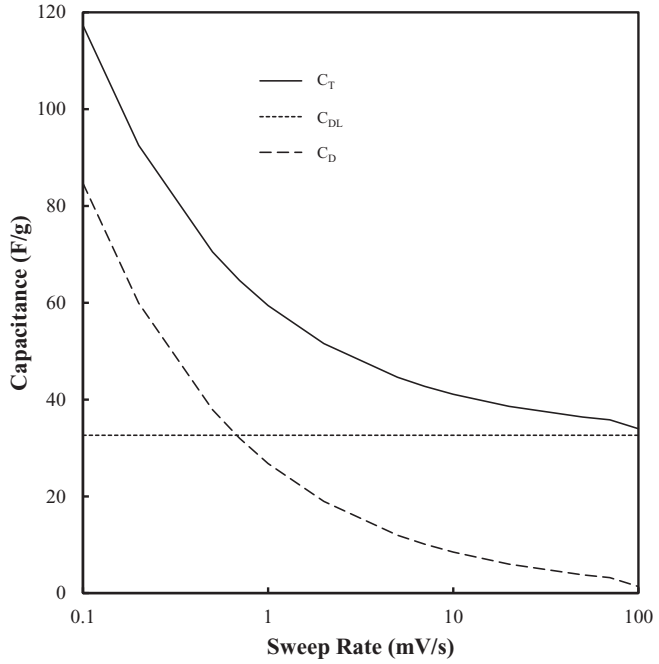

Figure 5. Contribution of diffusion-limited (C_D) and electrical double layer (C_{DL}) processes for the EMD electrode cycled in 0.5 K_2SO_4, using the current-sweep rate dependence method.

intercept of the plot of 1/C(v) versus $v^{1/2}$, as per Eq. 8, and as shown in Figure 6b. In this case, a linear fit was only found at low sweep rates in the range 0.1–2.0 mV/s. It is evident that at a high sweep rate the data also deviated from linearity. It has been suggested that the irreversibility of redox transitions, as well as uncompensated ohmic drops, are two main factors which result in this deviation at high sweep rates.[13,37,61] There is also the possibility that residual or self-discharge processes become apparent at low discharge rates, the outcome of which would affect the linearity of these plots. The diffusion-limited capacitance (C_D) then can be calculated by subtracting the value of the electrical double layer capacitance (C_{DL}) from the value of total capacitance (C_T), both of which are given in Table I.

SPECS Analysis.—The EMD was charged and discharged in a series of the small potential steps of 25 mV in both the anodic and cathodic directions. This small sweep rate allows the charge storage processes to approach their maximum capacitances during the equilibration time. Figure 1b shows the SPECS current response for the EMD electrode which was cycled in 0.5 M K_2SO_4. It can be seen that the current changes in each potential step, which indicates the potential dependence of the charging processes.[21] Figure 7 shows a current response at the potential of 0.4 V during the anodic sweep. When the potential is applied the current spikes immediately, which is the result of the formation of the electrical double layer on the electrode surface. Charge continues to distribute among the different storage mechanisms in the electrode until equilibrium values are reached. The electrical double layer process equilibrates very quickly (exponentially; Eq. 9) which results in the initial sharp decay in the current, while the diffusion-limited process equilibrates slowly (Eq. 10), which results in the slower current decay during the equilibration time. It is expected that the current response would eventually decay to zero at the end of the equilibration time. However, some of the current responses are non-zero due to slow redox processes which do not equilibrate in the allowed time.[62]

The SPECS current response was modeled using Eq. 11. Inset in Figure 7 is an example of the breakdown of the fitted current at a potential of 0.4 V during the anodic sweep in terms of the double layer currents on the geometric (i_{DL1}) and porous (i_{DL2}) surfaces, the

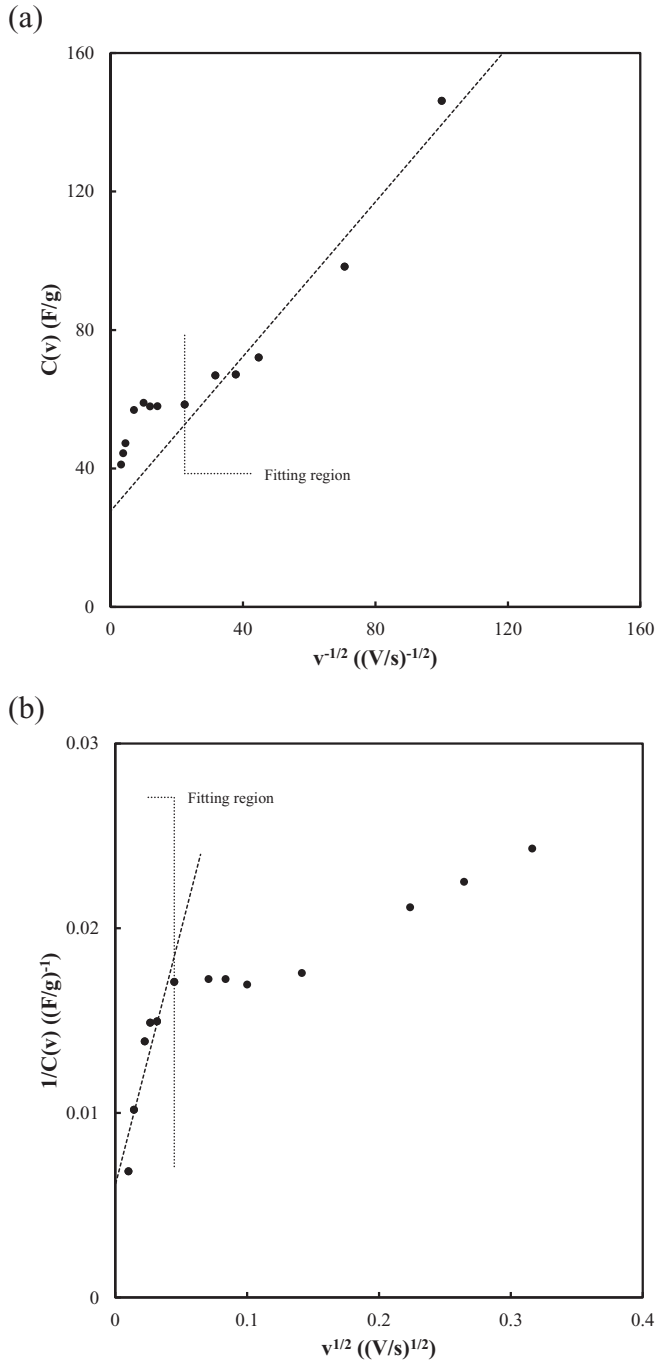

Figure 6. (a) Plot of C(v) versus $v^{-1/2}$ and (b) a plot of 1/C(v) versus $v^{1/2}$ for the EMD electrode cycled in 0.5 M K_2SO_4 at sweep rates in the range 0.1–100 mV/s. The fitted region indicated on each graph corresponds to sweep rates of 0.1–2.0 mV/s, where a linear fit was applied.

diffusion-limited current (i_D), and the residual current (i_R). It can be seen that both of the electrical double layer currents decay to zero very quickly (<10 s), while the diffusion-limited current decays much slower over the equilibration time.

The SPECS data can also be used to generate voltammetric data. To accomplish this the current response for an individual potential step is averaged out to a specific time after the potential step. This is repeated for each potential step such that the average current can be determined at each potential throughout the potential window for the electrode. By changing the time over which the current is averaged different effective voltametric sweep rates can be achieved; e.g., the

Table I. Specific capacitance obtained by the capacitance-sweep rate (C-v) dependence method.

Total Capacitance C_T (F/g)	Double Layer Capacitance C_{DL} (F/g)	Diffusion-limited Capacitance C_D (F/g)
164.4	27.7	136.7

sweep rate corresponding to each specified time can be calculated by dividing the potential step size (in this case ±25 mV) over that specified time. An added advantage of the SPECS approach is that since the current response for each potential step has previously been deconvoluted into its individual components (Eq. 11), voltammograms for each component can be generated in a similar manner. Figures 8a compares the voltametric data at a range of sweep rates (125, 25 and 1.25 mV/s). As expected, the average current increases with an increasing sweep rate.

Voltammetric data can also be calculated for the electrical double layer and diffusion-limited currents extracted from the SPECS data. Figures 8b and 8c show the synthetic voltammograms for the electrical double layer currents at the geometric and porous surface areas, diffusion-limited and total currents at 125 and 1.25 mV/s, respectively. At the higher sweep rate, the electrical double layer current at the geometric surface area provides the main contribution, while at the lower sweep rate of 1.25 mV/s, the diffusion-limited current exceeds the double layer current in the anodic sweep between 0.6 V to 0.8 V. This is associated with the kinetically slower redox reactions now having more time to develop at lower sweep rates.

The synthetic voltammograms can also be used to determine the specific capacitance as a function of sweep rate. The same approach to calculating the specific capacitance from CV data as used previously was applied to the synthetic voltammograms determined from the SPECS data. The charge passed for the anodic and cathodic sweeps was obtained by integrating the average current with respect to time corresponding to the range of sweep rates. The specific capacitance was calculated by dividing the value of the charge passed by the magnitude of the applied potential window. Figures 9 shows the total specific capacitance (C_T), the electrical double layer specific

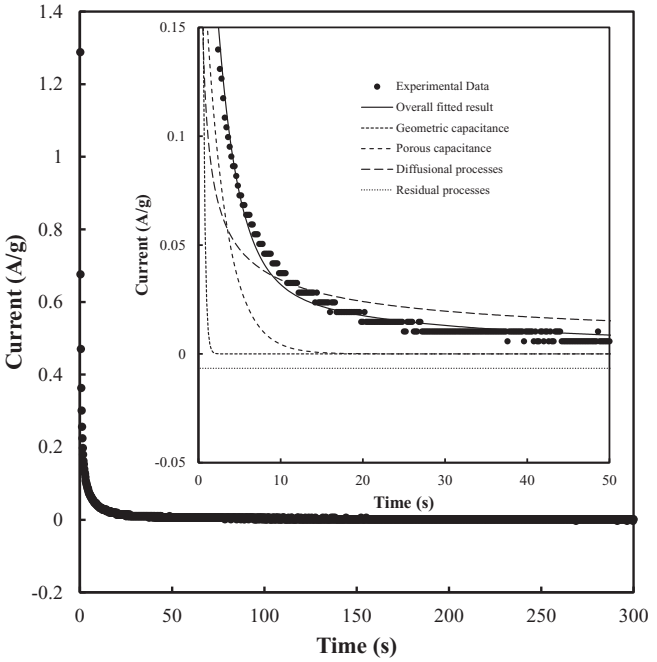

Figure 7. Example of the SPECS current response for the EMD electrode in 0.5 M K_2SO_4, in this case at E = 0.4 V during the anodic sweep. The inset shows the breakdown of the fitted data.

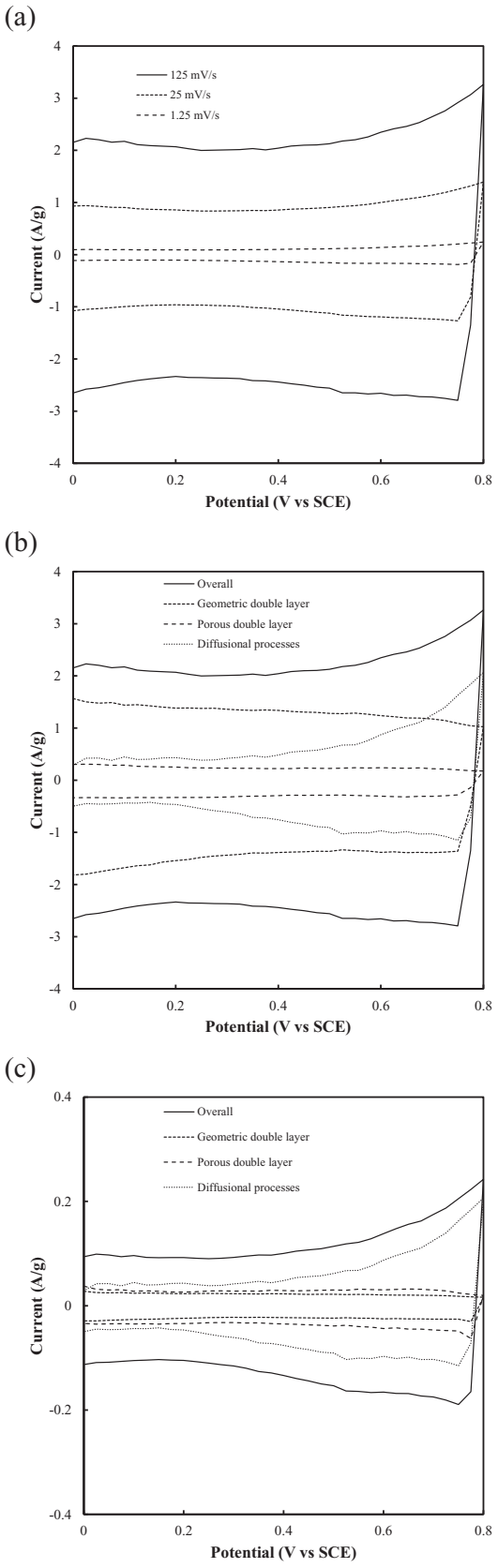

Figure 8. (a) Synthetic voltammogram obtained from the SPECS data comparing behavior at different rates. The breakdown of contributions to the total current data for (b) 125 mV/s and (c) 1.25 mV/s.

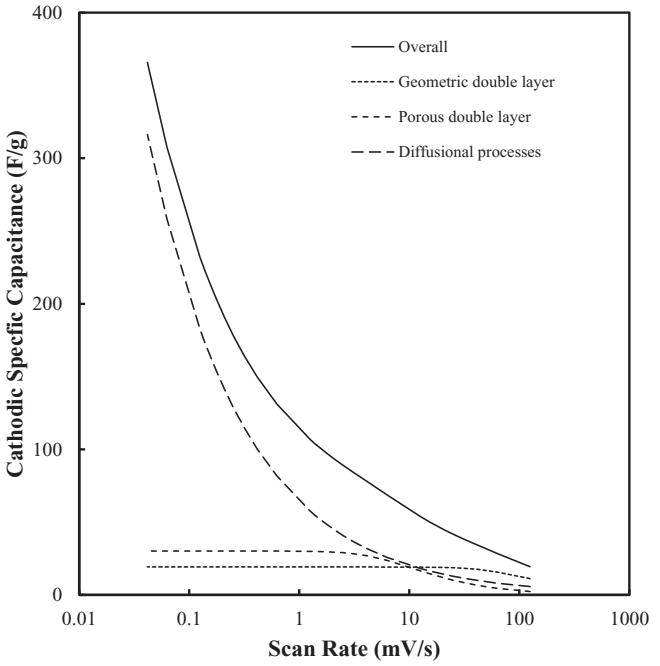

Figure 9. The total specific capacitance, the electrical double layer capacitances associated with the geometric and porous surface areas and the diffusional capacitance obtained from the SPECS data for the EMD electrode with a potential step size of 25 mV and an equilibration time of 300 s.

capacitances on the geometric (C_{DL1}) and porous (C_{DL2}) surfaces, and the diffusion-limited capacitance (C_D), obtained from the SPECS data as a function of the sweep rate. Residual capacitance was ignored here so the focus can be solely on capacitive and diffusional processes. Figure 9 shows firstly that the total specific capacitance decreases with increasing sweep rate. The diffusion-limited capacitance provides the main contribution at lower sweep rates, and it decays quickly with increasing sweep rate. The reasons for this include the kinetically slow redox reactions and the relatively slow mass transport of ions through the bulk of the electrode. Hence, at lower sweep rates there is more time for ions to diffuse through the bulk of the electrode, leading to a higher diffusional capacitance at lower sweep rates. However, as the sweep rate increases the time of diffusion decreases too, which results in a lower specific capacitance. The electrical double layer capacitance associated with the geometric area has a greater contribution at higher sweep rates, while the electrical double layer capacitance related to the porous surface area is close to the diffusional capacitance at higher sweep rates. This could be the result of the limited time for the diffusion of ions through the micropores of the bulk of the electrode at higher sweep rates. It can be observed that both the electrical double layer capacitances at the geometric and porous surface areas plateau at lower sweep rates. The reason is that the geometric and porous surface areas of the electrode are saturated with ions achieving their maximum capacitances at lower sweep rates.

Comparison between different analysis methods.—In this section the outcomes from the three different methods of analysis are compared. The breakdown of the specific capacitance for the EMD electrode considered here using the SPECS, current-sweep rate and capacitance-sweep rate dependence methods are given in Figures 10–12. It was expected that the capacitance-sweep rate dependence method would give the maximum diffusional, capacitive and total capacitances because the method itself is based on extrapolation to either infinite or zero sweep rates. Although this method gives the highest diffusional and overall capacitances, Figure 11 indicates that the electrical double layer capacitance obtained by this method is actually lower than the values given by the SPECS and current-sweep

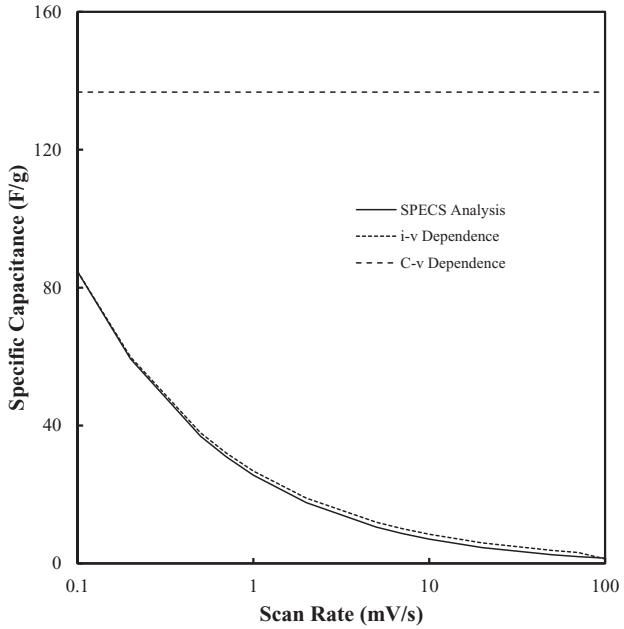

Figure 10. Comparison of the diffusion-limited capacitances obtained from the SPECS, current-sweep rate (i-v) dependence, and capacitance-sweep rate (C-v) dependence methods.

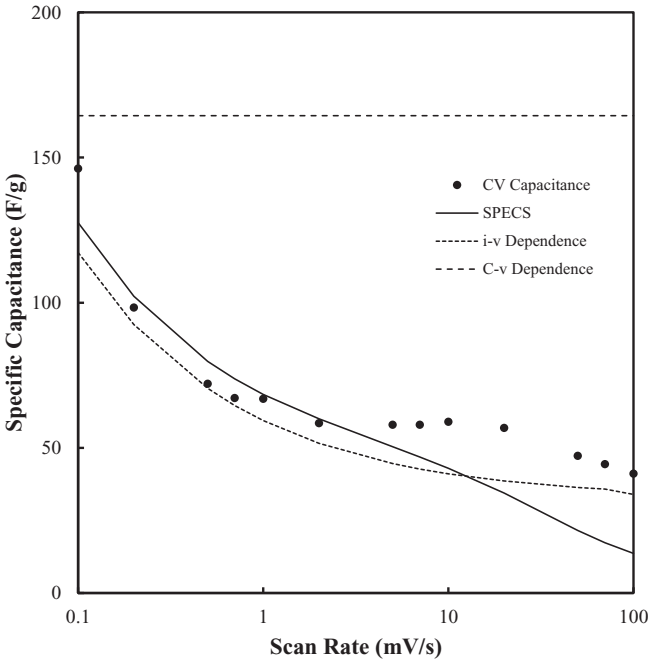

Figure 12. Comparison of the overall specific capacitances obtained from the CV data, with the SPECS, current-sweep rate (i-v) dependence and capacitance-sweep rate (C-v) dependence models.

rate dependence methods. However, the value of the electrical double layer capacitance obtained by the capacitance-sweep rate method is similar to the value of the electrical double layer capacitance associated with a geometric surface area obtained by the SPECS method at lower sweep rates. Figure 10 indicates that there is very good agreement between the values of the diffusion-limited capacitance obtained by the SPECS and current-sweep rate methods over a wide range of sweep rates. Both models show that the diffusion-limited capacitance is increased by decreasing the sweep rate. As has already been discussed, this is likely the result of a longer equilibration time at low sweep rates which leads to the diffusion of a greater proportion of ions through the bulk of the electrode material. The electrical double layer capacitance of the three models are compared in Figure 11. The SPECS model gives the greater electrical double layer capacitance at sweep rates < 10 mV/s. The value of the electrical double layer capacitance obtained by the current-sweep rate dependence model remains almost constant over the full range of sweep rates. However, according to the SPECS model the electrical double layer capacitance decreases the sweep rate is increased. In this case, the SPECS method shows a more realistic performance, as at higher sweep rates a shorter equilibration time and a higher rate of diffusion of ions influences the formation of an optimum electrical double layer at the surface of the electrode. It can be seen that at higher sweep rates, the electrical double layer capacitance at the porous surface area decreases more dramatically than the electrical double layer capacitance at the geometric surface area. The reason is that at higher sweep rates there is less time for ions to diffuse through the porous structure and to form the electrical double layer at the surfaces of the pores. The comparison of the overall capacitances of these three models, as well as the data obtained directly from the CV experiments, is given in Figure 12. The capacitance-sweep rate dependence model shows the highest overall specific capacitance, as expected. The overall capacitance obtained from the CV data, SPECS and current-sweep rate dependence methods increases with decreasing sweep rate so that they show similar behavior at a full range of sweep rates. The SPECS model when compared with the current-sweep rate dependence method has a greater overall capacitance at sweep rates < 10 mV/s. However, the SPECS method gives the lowest overall capacitance at higher sweep rates in the range 20–100 mV/s. This is associated with the lower values of the electrical double layer capacitance of the SPECS model at higher sweep rates.

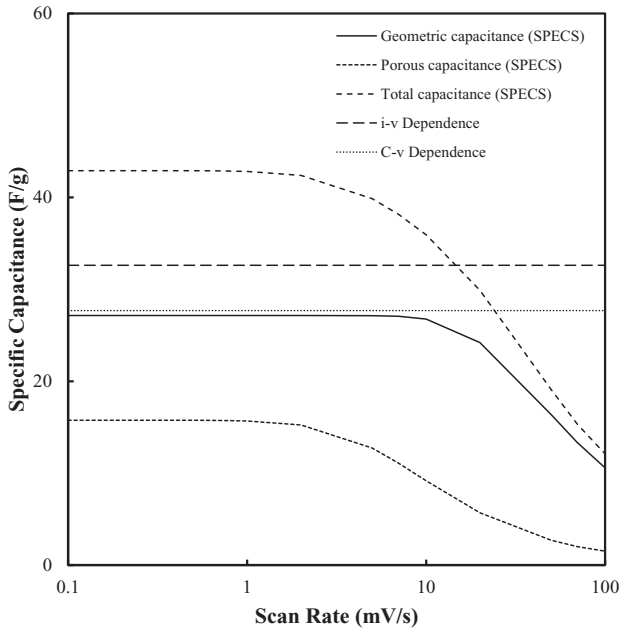

Figure 11. Comparison of the electrical double layer capacitances (both geometric and porous) obtained from the SPECS method with the current-sweep rate (i-v) dependence and the capacitance-sweep rate (C-v) dependence models.

Conclusions

This study reports on a comparison between the three common electrochemical methods that can be applied to characterize the different charge storage mechanisms of materials used in electrochemical

capacitors. The contribution of the capacitive and diffusion-limited processes can be obtained via the current-sweep rate dependence, capacitance-sweep rate dependence and SPECS methods. These three methods were compared experimentally and also their limitations and their advantages for interpreting the current data and their abilities to distinguish between the different charge storage mechanisms were discussed.

In all cases, the specific capacitance decreased with increasing the sweep rate. It was found that the capacitance-sweep rate dependence method was only accurate at low sweep rates. Overall, there was a good agreement between the SPECS and current-sweep rate dependence models over the full range of sweep rates. Comparison of the specific capacitances indicates that both models behave similarly, especially at lower sweep rates. However, at higher sweep rates the SPECS method was better able to characterize the behavior of the electrical double layer processes at the surface of the electrode. Moreover, the SPECS method could differentiate between different charge storage mechanisms such as via electrical double layer processes at the geometric and porous surface areas, diffusional process and residual process.

Overall, comparison of these three methods has shown that the SPECS method presents a rigorous approach toward characterising electrochemical capacitor materials. This technique has the ability to characterize the kinetic behavior of the material or electrode under study over a full range of sweep rates and also to provide additional information about the existence of the residual current and stability of electrode materials.

Acknowledgments

The authors acknowledge the University of Newcastle for the provision of a PhD scholarship (MF).

ORCID

Scott W. Donne https://orcid.org/0000-0001-9389-7870

References

1. G. Gahleitner, "Hydrogen from renewable electricity: An international review of power-to-gas pilot plants for stationary applications." *International Journal of Hydrogen Energy*, **38**(5), 2039 (2013).
2. A. N. Andersen and H. Lund, "New CHP partnerships offering balancing of fluctuating renewable electricity productions." *Journal of Cleaner Production*, **15**(3), 288 (2007).
3. B. Dunn, H. Kamath, and J.-M. Tarascon, "Electrical energy storage for the grid: a battery of choices." *Science*, **334**(6058), 928 (2011).
4. D. Ragone, in: *Proceedings of the Society Automotive Engineers. Conference*, Detroit, MI, USA, May 1968.
5. P. Simon and Y. Gogotsi, "Materials for electrochemical capacitors." *Nature Materials*, **7**(11), 845 (2008).
6. B. E. Conway, *Electrochemical Supercapacitors. Scientific Fundamentals and Technological Applications.*, 1999, New York: Kluwer Academic/Plenum Publishers.
7. T. Brousse et al.; *J. Electrochem. Soc.*, **162**, A5185 (2015).
8. Y. Zhang et al., "Progress of electrochemical capacitor electrode materials: A review." *International Journal of Hydrogen Energy*, **34**(11), 4889 (2009).
9. W. G. Pell and B. E. Conway, "Analysis of power limitations at porous supercapacitor electrodes under cyclic voltammetry modulation and dc charge." *Journal of Power Sources*, **96**(1), 57 (2001).
10. T. C. Liu et al., "Behavior of molybdenum nitrides as materials for electrochemical capacitors comparison with ruthenium oxide." *Journal of the Electrochemical Society*, **145**(6), 1882 (1998).
11. S. Ardizzone, G. Fregonara, and S. Trasatti, ""Inner" and "outer" active surface of RuO_2 electrodes." *Electrochimica Acta*, **35**(1), 263 (1990).
12. Allen J. Bard and L. R. Faulkner, *Electrochemical Methods: Fundamentals and Applications*, 2nd Edition, 2001: John Wiley & Sons.
13. S.-B. Yoon et al., "Study on the Electrochemical Kinetics of Manganese Dioxide/Multiwall Carbon Nanotube Composite by Voltammetric Charge Analysis." *Journal of The Electrochemical Society*, **161**(1), A137 (2014).
14. K. Oldham and J. Myland, *Fundamentals of Electrochemical Science*, 2012: Elsevier Science.
15. M. R. Bailey and S. W. Donne, "Electrochemical impedance spectroscopy study into the effect of titanium dioxide added to the alkaline manganese dioxide cathode." *Journal of The Electrochemical Society*, **158**(7), A802 (2011).
16. W. Bowden et al., "Lithiation of ramsdellite–pyrolusite MnO_2; NMR, XRD, TEM and electrochemical investigation of the discharge mechanism." *Journal of Power Sources*, **153**(2), 265 (2006).
17. A. J. Gibson et al., "Mesoscale Morphological Control of Electrodeposited Manganese Dioxide Films." *Electrochimica Acta*, **170**, 343 (2015).
18. M. F. DuPont and S. W. Donne, "Separating the faradaic and Non-faradaic Contributions to the Total Capacitance for Different Manganese Dioxide Phases." *Journal of The Electrochemical Society*, **162**(5), A5096 (2015).
19. M. F. DuPont and S. W. Donne, "Separating faradaic and Non-faradaic Charge Storage Contributions in Activated Carbon Electrochemical Capacitors Using Electrochemical Methods: I. Step Potential Electrochemical Spectroscopy." *Journal of the Electrochemical Society*, **162**(7), A1246 (2015).
20. M. F. DuPont and S. W. Donne, "Electrolytic Manganese Dioxide Structural and Morphological Effects on Capacitive Performance." *Electrochimica Acta*, **191**, 479 (2016).
21. M. F. DuPont and S. W. Donne, "faradaic and Non-faradaic Contributions to the Power and Energy Characteristics of Electrolytic Manganese Dioxide for Electrochemical Capacitors." *Journal of The Electrochemical Society*, **163**(6), A888 (2016).
22. M. F. DuPont and S. W. Donne, "A Step Potential Electrochemical Spectroscopy Analysis of Electrochemical Capacitor Electrode Performance." *Electrochimica Acta*, **167**, 268 (2015).
23. D. Baronetto, N. Krstajić, and S. Trasatti, "Reply to "note on a method to interrelate inner and outer electrode areas" by H. Vogt. *Electrochimica acta*, **39**(16), 2359 (1994).
24. P. Delahay and G. Perkins, "Oscillographic Polarography. Phenomena Occurring during the Quiescent Period of the Voltage Wave." *The Journal of Physical Chemistry*, **55**(4), 586 (1951).
25. R. S. Nicholson and I. Shain, "Theory of stationary electrode polarography. Single sweep and cyclic methods applied to reversible, irreversible, and kinetic systems." *Analytical Chemistry*, **36**(4), 706 (1964).
26. S. Srinivasan and E. Gileadi, "The potential-sweep method: A theoretical analysis." *Electrochimica Acta*, **11**(3), 321 (1966).
27. H. Lindström et al., "Li^+ ion insertion in TiO_2 (anatase). 2. Voltammetry on nanoporous films." *The Journal of Physical Chemistry B*, **101**(39), 7717 (1997).
28. V. Augustyn et al., "Lithium-ion storage properties of titanium oxide nanosheets." *Materials Horizons*, **1**(2), 219 (2014).
29. B. Conway and D. Kannangara, "Zinc Oxidation and Redeposition Processes in Aqueous Alkali and Carbonate Solutions II. Distinction Between Dissolution and Oxide Film Formation Processes." *Journal of the Electrochemical Society*, **134**(4), 906 (1987).
30. S. Saidman, E. Bellocq, and J. Bessone, "Stationary and non-stationary electrochemical response of polycrystalline indium in alkaline media." *Electrochimica Acta*, **35**(2), 329 (1990).
31. A. Bolza, "Phenomenological aspects related to the electrochemical behavior of smooth palladium electrodes in alkaline solutions." *Journal of Electroanalytical Chemistry*, **380**(1-2), 127 (1995).
32. H. Jaegfeldt, "Adsorption and electrochemical oxidation behavior of NADH at a clean platinum electrode." *Journal of Electroanalytical Chemistry and Interfacial Electrochemistry*, **110**(1-3), 295 (1980).
33. J. Come et al., "Electrochemical kinetic study of $LiFePO_4$ using cavity microelectrode." *Journal of The Electrochemical Society*, **158**(10), A1090 (2011).
34. J. Haetge, C. Suchomski, and T. Brezesinski, "Ordered mesoporous MFe_2O_4 (M = Co, Cu, Mg, Ni, Zn) thin films with nanocrystalline walls, uniform 16 nm diameter pores and high thermal stability: template-directed synthesis and characterization of redox active trevorite." *Inorganic Chemistry*, **49**(24), 11619 (2010).
35. Á. León-Reyes et al., "Analysis of the Different Mechanisms of Electrochemical Energy Storage in Magnetite Nanoparticles." *Int. J. Electrochem. Sci*, **9**, 3837 (2014).
36. M. A. C. LoF́pez et al., "Improved energy storage solution based on hybrid oxide materials." *ACS Sustainable Chemistry & Engineering*, **1**(1), 46 (2012).
37. J. Shao et al., "Mechanism analysis of the capacitance contributions and ultralong cycling-stability of the isomorphous MnO_2 core/shell nanostructures for supercapacitors." *Journal of Materials Chemistry A*, **3**(11), 6168 (2015).
38. J. Wang et al., "Pseudocapacitive contributions to electrochemical energy storage in TiO_2 (anatase) nanoparticles." *The Journal of Physical Chemistry C*, **111**(40), 14925 (2007).
39. J.-H. Kim et al., "Tailoring oriented TiO_2 nanotube morphology for improved Li storage kinetics." *Electrochimica Acta*, **88**, 123 (2013).
40. R. Ranjusha et al., "Fabrication and performance evaluation of button cell supercapacitors based on MnO_2 nanowire/carbon nanobead electrodes." *RSC Advances*, **3**(38), 17492 (2013).
41. J. Yue et al., "Mesoporous niobium-doped titanium dioxide films from the assembly of crystalline nanoparticles: study on the relationship between the band structure, conductivity and charge storage mechanism." *Journal of Materials Chemistry A*, (2017).
42. M. Opitz et al., "Mechanisms of Charge Storage in Nanoparticulate TiO_2 and $Li_4Ti_5O_{12}$ Anodes: New Insights from Sweep rate-dependent Cyclic Voltammetry." *Electrochimica Acta*, **168**, 125 (2015).
43. D. Galizzioli, F. Tantardini, and S. Trasatti, "Ruthenium dioxide: a new electrode material. I. Behaviour in acid solutions of inert electrolytes." *Journal of Applied Electrochemistry*, **4**(1), 57 (1974).
44. G. Lodi et al., "On some debated aspects of the behavior of RuO_2 film electrodes." *Materials Chemistry*, **3**(3), 179 (1978).
45. Y. Dan et al., "Ti/PbO_2 nano-Co_3O_4 composite electrode material for electrocatalysis of O_2 evolution in alkaline solution." *International journal of hydrogen energy*, **36**(3), 1949 (2011).

46. C. C. Hu and Y. H. Huang, "Cyclic voltammetric deposition of hydrous ruthenium oxide for electrochemical capacitors." *Journal of The Electrochemical Society*, **146**(7), 2465 (1999).
47. J. Xing et al., "Preparation and characterization of a novel porous Ti/SnO 2–Sb 2 O 3–CNT/PbO 2 electrode for the anodic oxidation of phenol wastewater." *RSC Advances*, **5**(66), 53504 (2015).
48. W. Zhang et al., "Fabrication, characterization and electrocatalytic application of a lead dioxide electrode with porous titanium substrate." *Journal of Alloys and Compounds*, **650**, 705 (2015).
49. W. Zhao et al., "Study on the performance of an improved Ti/SnO $-Sb_2O_3/PbO_2$ based on porous titanium substrate compared with planar titanium substrate." *Rsc Advances*, **5**(34), 26530 (2015).
50. L. M. Doubova, S. Daolio, and A. De Battisti, "Examination of RuO_2 single-crystal surfaces: charge storage mechanism in H_2SO_4 aqueous solution." *Journal of Electroanalytical Chemistry*, **532**(1), 25 (2002).
51. G. A. Muller et al., "High performance pseudocapacitor based on 2D layered metal chalcogenide nanocrystals." *Nano Letters*, **15**(3), 1911 (2015).
52. I. Kodintsev et al., "X-ray photoelectron spectroscopy and electrochemical surface characterization of iridium (IV) oxide and ruthenium (IV) oxide electrodes." *Langmuir*, **8**(1), 283 (1992).
53. M. Toupin, T. Brousse, and D. Bélanger, "Influence of microstucture on the charge storage properties of chemically synthesized manganese dioxide." *Chemistry of Materials*, **14**(9), 3946 (2002).
54. V. Augustyn et al., "High-rate electrochemical energy storage through Li^+ intercalation pseudocapacitance." *Nature Materials*, **12**(6), 518 (2013).
55. J. Duay et al., "Self-limiting electrodeposition of hierarchical MnO_2 and $M(OH)_2/MnO_2$ nanofibril/nanowires: mechanism and supercapacitor properties." *ACS Nano*, **7**(2), 1200 (2013).
56. C.-C. Hu, Y.-S. Lee, and T.-C. Wen, "The physicochemical/electrochemical properties of binary Ni–Co oxides." *Materials Chemistry and Physics*, **48**(3), 246 (1997).
57. F. Montilla et al., "Preparation and characterization of antimony-doped tin dioxide electrodes. Part 1. Electrochemical characterization." *The Journal of Physical Chemistry B*, **108**(16), 5036 (2004).
58. H. Vogt, "Note on a method to interrelate inner and outer electrode areas." *Electrochimica Acta*, **39**(13), 1981 (1994).
59. P. Bandaru et al., "Charge transfer and storage in nanostructures." *Materials Science and Engineering: Reports*, **96**, 1 (2015).
60. M. Endo et al., "Capacitance and pore-size distribution in aqueous and nonaqueous electrolytes using various activated carbon electrodes." *Journal of the Electrochemical Society*, **148**(8), A910 (2001).
61. C. De Pauli and S. Trasatti, "Electrochemical surface characterization of IrO_2 and SnO_2 mixed oxide electrocatalysts." *Journal of Electroanalytical Chemistry*, **396**(1-2), 161 (1995).
62. M. F. DuPont and S. W. Donne, "Charge storage mechanisms in electrochemical capacitors: Effects of electrode properties on performance." *Journal of Power Sources*, **326**, 613 (2016).

Chapter 7: Complications when Differentiating Charge Transfer Processes in Electrochemical Capacitor Materials: Assessment of Cyclic Voltammetry Data

Overview

This chapter focuses on some of the complications associated with using a conventional method of voltammetric current dependence on sweep rate to deconvoluting double layer and diffusion-limited contributions in a voltammetry experiment. The models which have been presented in this study are based on theoretical electrical and electrochemical responses to stimuli for an electrochemical capacitor material, including contributions from the electrical double layer capacitance using the series RC circuit, charge transfer processes in a localized domain, diffusion-limited processes, and electrode instabilities at the extremes of potential redox reactions using the Butler-Volmer equation.

The following publication is reproduced from the Journal of the Electrochemical Society, Volume 166, Issue 8, p. A1370-A1379 (2019), with permission of the Electrochemical Society.

Journal of The Electrochemical Society, **166** (8) A1370-A1379 (2019)
0013-4651/2019/166(8)/A1370/10/$38.00 © The Electrochemical Society

Complications When Differentiating Charge Transfer Processes in Electrochemical Capacitor Materials: Assessment of Cyclic Voltammetry Data

Marveh Forghani* and Scott W. Donne **,z

Discipline of Chemistry, University of Newcastle, Callaghan NSW 2308, Australia

Voltammetric data representing the response of an electrochemical capacitor electrode has been generated containing known contributions from double layer formation, localized and diffusion limited redox processes, electrode instabilities and ohmic resistance. This data has then been modelled using a common approach to differentiating faradaic and non-faradaic processes; namely relating the voltametric current (i(V)) to sweep rate (v); i.e., $i(V) = k_1 v + k_2 v^{1/2}$, where k_1 and k_2 are constants. Outcomes from the analysis indicate that this approach is complicated by the resistance associated with double layer formation, electrode instabilities in the electrolyte under study, and also increased electrode resistance.
 [DOI: 10.1149/2.1021906jes]

Manuscript submitted December 19, 2018; revised manuscript received March 18, 2019. Published April 24, 2019.

The reliable and sustainable supply of energy is one of the most critical challenges faced by humanity.[1] Presently, this supply of energy is dominated by the combustion of fossil fuels. This is problematic because of the environmental impact of the resultant emissions, as well as the finite non-sustainable nature of the fuel supply.[2,3] As such, the future of energy supply is much more likely to be based upon renewable technologies, such as solar, wind, hydroelectric and geothermal.[4,5] The output from these technologies is affected by intermittency, geographical and social considerations.[6]

As a complement to these technologies, particularly solar energy, some form of energy storage is necessary to improve the quality of the energy output.[7] In this role electrochemical energy storage and conversion devices are ideal. This includes various battery, fuel cell and capacitor-based systems. They already provide energy for the myriad of small portable electronic devices used in society, but now their scope of application is broadening to much larger technologies such as electric or hybrid electric vehicles and grid energy storage.[8,9] This expanding range of applications is due to the wide range of technologies available, as well as their always improving performance characteristics, including power and energy density, cyclability and cost.[10,11] The various battery systems available occupy the bulk of applications because of their all-around good performance. The use of electrochemical capacitors is expanding rapidly because of the growing number of high power applications, as well as the need for extended cyclability.[12]

Electrochemical capacitors are typified by a high specific power density ($\sim 10^4$ W/kg), as well as excellent cyclability ($>10^5$ cycles).[13,14] They are limited by relatively poor specific energy density (<10 Wh/kg), and hence cost per unit energy.[15] Nevertheless, considerable research is ongoing globally to address these performance limitations. Many different materials have been used in electrochemical capacitors including various forms of carbon (e.g., activated carbon, carbon nanotubes, fullerenes, graphene, etc.), metal oxides (e.g., RuO_2, MnO_2, etc.) and conducting polymers (e.g., polypyrrole, polypyridine, polythiophene, etc.).[16–21] Present-day commercial electrochemical capacitors are based typically on activated carbon electrodes in a non-aqueous electrolyte like tetraethylammonium tetrafluoroborate in acetonitrile or propylene carbonate.[22,23] Charge storage in these devices is primarily via physical charge separation at the electrode-electrolyte interface through the formation of an electrical double layer.[24] Electrodes within these devices have a specific capacitance of ~120 F/g.[23] The specific energy (E; J/g) of these devices is given by:

$$E = \frac{CV^2}{2} \qquad [1]$$

where C is the specific capacitance (F/g) and V is the voltage window (V). This expression forms the basis for most research activities in the sense that the specific energy can be increased by increasing both the intrinsic capacitance of the device; i.e., through the design of advanced materials, or by increasing the operating voltage.

To increase the intrinsic capacitance many researchers have adopted the strategy of using materials that exhibit pseudo-capacitance, a process that is associated with fast, reversible redox processes at the electrode-electrolyte interface.[25] These redox processes will of course depend on the nature of the material being used, but may involve oxygen functionalities on carbon surfaces, metal oxides and conducting polymers.[26–29] The use of metal oxides is of particular interest because this has enabled the repurpose of materials initially used in battery systems.[30,31]

Of course with the use of materials that exhibit pseudo-capacitance the issue arises about how much of the total charge passed is associated with electrical double layer formation compared to that associated with charge transfer processes.[32] A number of analysis methods have been devised including examining (i) the current flowing as a function of sweep rate from a series of cyclic voltammetry experiments;[33] (ii) the charge passed during a series of cyclic voltammetry experiments at different sweep rates;[34–36] and (iii) step potential electrochemical spectroscopy (SPECS), which is based on analysis of the i-t transients arising from a series of small potential steps across the full potential window.[37–44] In a recent publication from our laboratory we made a comparison between these three methods to examine their ability to differentiate the various charge storage mechanisms.[32] The outcomes from this work demonstrated that the use of the electrode charge method[34] did not adequately describe electrode behavior and thus it has not been considered any further. In the present manuscript we are carrying out a further assessment on method (i) to differentiate charge storage mechanisms using synthetic cyclic voltammetry data,[45] where the contributions by various processes to the total current are known.

Data Generation

The generation of data to be used here arises from our previous work focused on the development of appropriate models to simulate experimental electrochemical capacitor data.[45] The initial indication that there may be complications associated with the use of voltametric data to differentiate charge storage mechanisms in electrochemical capacitors arose as a result our efforts to compare currently available approaches to charge storage differentiation.[32] In this case it was demonstrated that under certain conditions these approaches could not reliably reproduce the initial electrochemical data, suggesting a flawed approach.

The models we have used here[45] are based on theoretical electrical and electrochemical responses to stimuli for an electrochemical capacitor material, including contributions from double layer capacitance (series RC circuit), charge transfer processes in a localized domain,

*Electrochemical Society Student Member.
**Electrochemical Society Member.
zE-mail: scott.donne@newcastle.edu.au

diffusion limited processes, and electrode instabilities (Butler-Volmer equation). They should provide awareness to others in the field as to the nature and variety of processes that can occur within an electrochemical capacitor electrode material, as well as provide an approach to simulate these processes. Of course there are a myriad of materials used in electrochemical capacitor electrodes, each with their own range of charge storage mechanisms. As such, the intent here is to use more generic models to simulate data. The details of specific material behavior is beyond the scope of the present manuscript; however, the models developed by us previously[45] and used here are best regarded as the starting point for specific material characterization.

Electrical double layer capacitor.—The voltametric behavior of an electrical double layer capacitor (EDLC) can be simulated using the series arrangement of a resistor (R; Ω.g) and capacitor (C; F/g);[46] i.e.,

$$i = vC\left(1 - \exp\left(-\frac{t}{RC}\right)\right) \quad [2]$$

where i is the response current (A/g), v is the potential sweep rate, and t is the time (s) after starting the potential sweep. In this regard, the potential axis is somewhat arbitrary, and is dependent on the potential window of the electrode. As an example, Figure 1a shows the effect of changing sweep rate during the anodic half cycle on a series RC circuit, in this case with R = 0.005 Ω.g and C = 100 F/g. The effects on the voltametric behavior have been described in detail previously.[45] In short, the maximum current is obtained when t is large compared to RC, otherwise known as the time constant (τ = RC; s). With reference to Figure 1a, this occurs toward the end of the anodic sweep, at high potentials. Increasing the resistance also has the effect of increasing

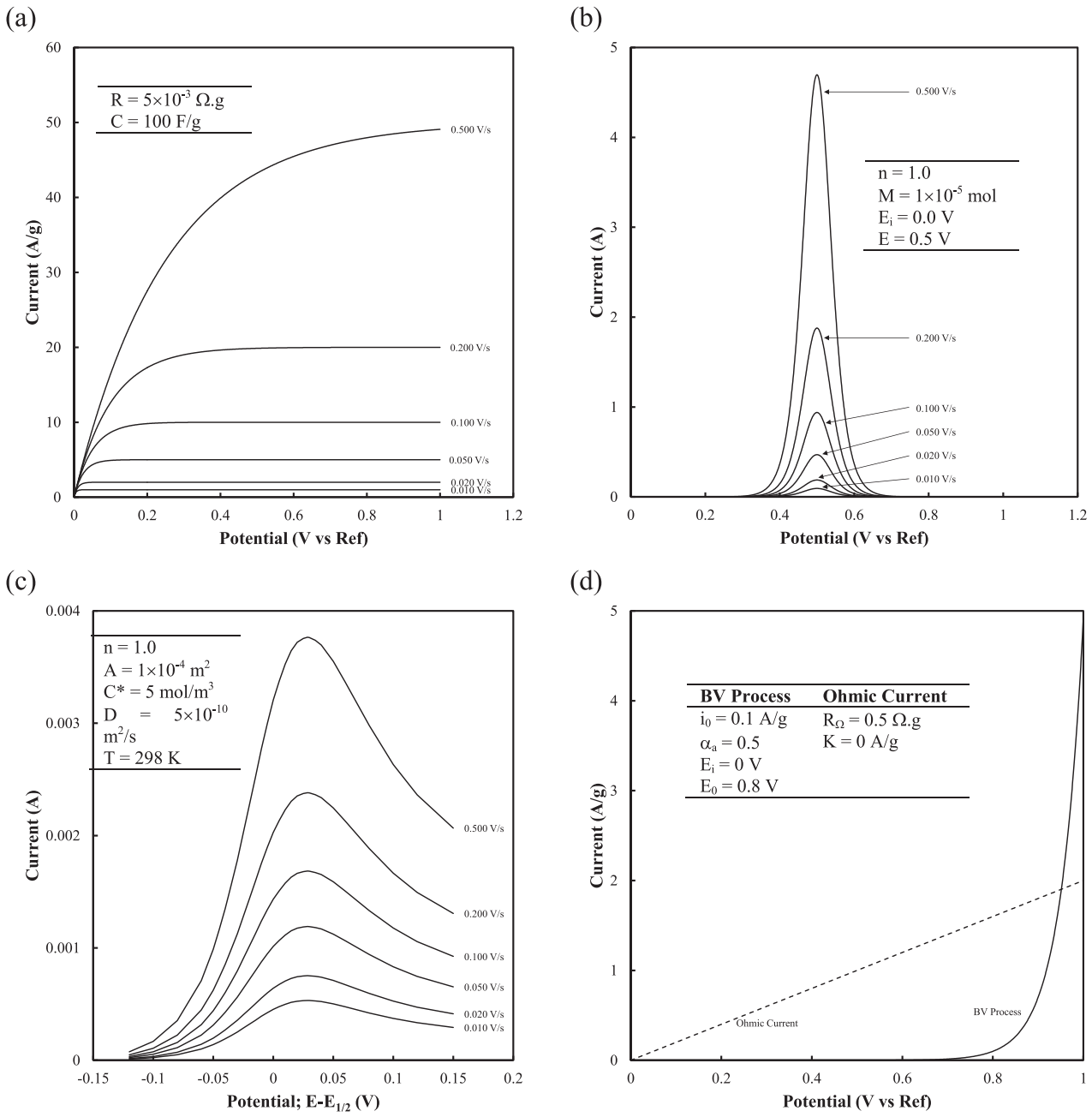

Figure 1. Voltametric response at a range of different sweep rates (anodic half cycle) of (a) of a series RC circuit to an applied potential sweep (cf. Eq. 2); (b) a redox process within a specific or localized domain (c.f. Eq. 3); (c) a reversible diffusion limited redox process (cf. Eq. 4); and (d) an anodic Butler-Volmer kinetically limited process together with an ohmic electrode resistance contribution. Specific parameters are included on each individual figure.

the time constant, which has the effect of delaying the point at which the maximum current is achieved.

The notion of a capacitor in this instance is as an electrical circuit element that simulates the electrode-electrolyte interface as parallel layers of opposing charge. This is of course a very ideal situation compared to real electrochemical capacitor electrodes which tend to be very porous, with pore sizes approaching size of the solvated ions expected to adsorb on the surface. As a result, given that material pore sizes tend to be a distribution it is likely that there will be a corresponding distribution of R and C values that are best used to simulate the porous electrode-electrolyte interface in a material. Differentiating interfaces has already been used in the step potential electrochemical spectroscopy (SPECS) analysis of electrochemical capacitor electrodes in the sense that porous and geometric surfaces have been identified with different time constants.[39–44]

Redox processes in a localized domain.—In a recent publication from our research group the response of a redox process in a specific or localized domain was derived.[45] This response was derived from the Nernst equation, and shown to have the following form:

$$i = \frac{\frac{n^2MF^2v}{RT}\exp\left(\frac{nF}{RT}(E_i + vt - E)\right)}{\left[1 + \exp\left(\frac{nF}{RT}(E_i + vt - E)\right)\right]^2} \quad [3]$$

where n, which is traditionally associated with the number of electrons transferred in the redox process, is in this instance an indicator of the kinetics of the redox process, M is the total number of moles of the electroactive species (mole), v is the potential sweep rate (V/s), E_i is the initial potential (V), t is the time after the starting the potential sweep (s), E is the reversible potential for the redox couple (V), and F, R and T have their usual electrochemical significance. Figure 1b shows the effect of varying the sweep rate on the voltametric response of such a process. The data here were generated with $n = 1$, $M = 1 \times 10^{-5}$ mol, $E_i = 0$ V and $E = 0.5$ V. As expected from Eq. 3, changing the sweep rate leads to a proportional change in the resultant current. A key feature about Eq. 3 is that it dictates the current response for a finite and unchanging amount of redox active species, as what may be expected from a surface bound redox process, or a solid electrode material which has redox active species available for charge transfer.

The origin of this type of process depends very much on the material under study. Examples of where such a response has been observed include the grafting of electroactive moieties, such as anthroquinone,[47,48] onto an activated carbon surface, hydrogen adatom formation as a precursor to gaseous hydrogen evolution as in the Volmer-Heyrovsky-Tafel mechanisms,[49] and also the reduction of specific Mn(IV) states in γ-MnO_2 in alkaline electrolytes.[50] Whatever the example used, the overriding condition here is that the redox process occurs in a localized domain in which there is no distribution of charge beyond that domain.

Reversible diffusion-limited redox processes.—The base case to explore diffusion-limited processes subjected to a linear sweep voltammetry profile is focused on semi-infinite linear diffusion of a reversible redox couple to a planar electrode surface.[46] Being reversible, the starting point for the analysis is the Nernst equation, which is then subjected to appropriate initial and boundary conditions to arrive at the following expression for the interfacial current (i; A):

$$i = nFAC^*\left(\frac{\pi nFD}{RT}v\right)^{1/2}\chi(\sigma t) \quad [4]$$

where C^* and D are the bulk concentration (mol/m^3) and diffusion coefficient (m^2/s) of the species about to undergo oxidation or reduction, n, F, A, R and T have their usual electrochemical significance, and $\chi(\sigma t)$ is a unitless function describing the shape of the reversible voltametric behavior. The complexity of this expression arises as a result of the need to solve the problem numerically.[46] Values for $\chi(\sigma t)$ as a function of an arbitrary potential axis ($E - E_{1/2}$; V) are shown in literature tables. Nevertheless, the key function of this expression is that the current is proportional to C^* and $v^{1/2}$. An example of the effects of sweep rate on Eq. 4 is shown in Figure 1c, in this case for $n = 1$, $A = 1 \times 10^{-4}$ m^2, $C^* = 5$ mol/m^3, and $D = 5 \times 10^{-10}$ m^2/s. Unlike the redox processes occurring in a localized domain, where there was a finite and unchanging amount of charge available for transfer, the nature of semi-infinite processes is that more or less charge is available depending on the sweep rate, or more correctly the time base of the experiment. At low sweep rates, or longer experiments, more charge is passed compared to experiments conducted with high sweep rates. The impact of this will become apparent later when an attempt is made to differentiate the charge storage mechanisms.

As mentioned above, this diffusion expression (Eq. 4) is described for semi-infinite planar diffusion, which is an idealized situation best suited for molecular electrochemistry. More complex diffusion models have been developed for porous solid electrodes, particularly battery cathode materials, including planar, spherical and double planar models,[51] but also bounded porous diffusion in activated carbon.[52] The solid state diffusion models proposed above are relevant to battery electrode systems that undergo solid solution, or single phase, redox processes, such as for the alkaline manganese dioxide electrode. Other models involving moving boundary methods are required for systems that undergo two-phase redox processes, such as the alkaline $NiOOH/Ni(OH)_2$ and non-aqueous $LiFePO_4/FePO_4$ systems. The point being emphasized here is that the choice of diffusion model is dependent on the nature of the redox processes occurring.

Surface based redox processes can have a diffusion component associated with a reactant necessary from the electrolyte. For example, anthraquinone moieties on an activated carbon surface require protons from the electrolyte, which depending on the electrochemical conditions, may be diffusion limited. Whether this is associated with diffusion of the necessary species to the geometric or porous surface area will be dependent on the electrode material under study. Diffusion of a reacting species to the geometric surface area can be characterized by the bulk diffusion coefficient; however, diffusion in a porous material will be considerably hindered.

Diffusion in the solid state is also a possibility for pseudo-capacitive materials like manganese dioxide. In this case diffusion is related to movement of the intercalated species away from the surface into the bulk of the electro-active material.[51] Again, this can be characterized by a diffusion coefficient provided the intercalated species can be identified.

The issue of diffusion in highly porous materials with surface based processes is a very relevant but complex issue. Firstly, it is dependent on the electrode material and electrolyte combination under study, as well as the electrochemical cycling conditions used. For non-porous materials, or at least those with large macro-pores, electrolyte accessibility to the electrode surface is essentially unhindered, meaning that planar, semi-infinite diffusion conditions can be satisfied. At the other extreme, for a highly micro-porous material diffusion to the electrode surface becomes affected by the other side of the pore wall meaning that lateral diffusion along the length of the pore is required to sustain electrochemical activity. Diffusion under these circumstances would be considerably hindered, likely to the point that apart from the consumption of the electroactive species in the pore, beyond this the porous surface would contribute little more to charge storage. Of course most materials fall within the bounds of these extreme conditions and so a gradient would exist in terms of the porous contribution to charge storage. In addition to the electroactive material, the nature of the electrolyte is also very important. Factors such as ion charge density and solvation number will strongly interact with the porosity of the electrode material.

Electrode-Electrolyte instability and electrode resistance.—At the extremes of potential redox reactions have been observed to occur in many systems involving the instability of the electrode-electrolyte interface.[53,54] The reversibility of these processes is very much dependent on the nature of the process itself, and is often activation (kinetically) controlled; i.e., the reaction rate or current is dependent on the potential, or more specifically the overpotential, rather than the

sweep rate. Under these circumstances, the current can be described by the Butler-Volmer equation for electrochemical kinetics; i.e.,

$$i = i_o\left[\exp\left(\frac{\alpha_a \eta F}{RT}\right) - \exp\left(-\frac{\alpha_c \eta F}{RT}\right)\right] \quad [5]$$

where i_o is the exchange current density (A/g) that can be used as an indicator of reaction kinetics, α_a and α_c are the anodic and cathodic transfer coefficients, respectively, and η is the overpotential (V) defined as $\eta = V - E$, where V is the applied potential (V) and E is the reversible potential for the redox process (V). Note that the Butler-Volmer equation is independent of sweep rate. An example of this response is shown in Figure 1d, with the parameters used shown in the figure.

The suggestion of a charge transfer mechanism associated with electrode instabilities will very much depend on the material being studied. For instance, the study of activated carbon with grafted functional groups gives rise to a peak in voltametric data corresponding to a redox process in a localized domain. The charge passed for such a process can be then used to assess the redox mechanism and the availability of anthroquinone grafted on the electrode surface. Studying electrode instability processes using the Butler-Volmer equation can be used to suggest a mechanism provided the nature of the instability reactions have been identified using other techniques. Here the extraction of the transfer coefficient, either anodic or cathodic, can be used to suggest a possible mechanism. For example, the mechanism of the hydrogen evolution reaction can be differentiated using the cathodic transfer coefficient to identify whether the Tafel, Heyrovsky or Volmer step is rate determining. This example is particularly relevant for the use of carbon materials in aqueous electrolytes.

It is quite often encountered in the study of electrochemical capacitor materials that the electrodes are resistive, leading to the voltametric data appearing to have a general upward slope for an anodic potential sweep. A resistance was included in the prediction of the double layer capacitance, which when related to real systems, likely corresponds to the resistance associated with electrolyte ions being ionically attracted to the electrode substrate. The effects of this are apparent in Figure 1 and in Reference 45. Generally, though, the electrode materials and electrolytes have a finite conductivity and so an ohmic resistance must be associated with the electrode as a whole. This ohmic resistance has the form:

$$i_{ohm} = \frac{V}{R_\Omega} + K \quad [6]$$

where i_{ohm} is the current (A/g) resulting from the ohmic resistance of the electrode (R_{ohm}; Ω.g), V is the applied electrode potential (V), and K is a constant (A/g) taking into account the fact that the effects of the ohmic resistance are not on an absolute scale, such as we would encounter in an electronic circuit, but instead are relative to the potential scale used here with respect to a reference electrode. Note that Eq. 6 is also independent of sweep rate. An example of this behavior is also shown in Figure 1d.

Synthetic voltammetry data.—Combinations of these processes have been made for further analysis into charge separation. The most significant component is the nature of the associated redox process, in which case Figure 2a includes redox processes in a localized domain, while Figure 2b shows combined data with a reversible diffusion-limited redox process. Each of the specific parameters used is also shown in the figure.

Analysis of Cyclic Voltammetry Data – Individual Components

The relationship between current and sweep rate in a cyclic voltammetry (CV) or linear sweep voltammetry (LSV) experiment has been used extensively as a means of differentiating charge storage mechanisms.[55–59] The basis of this assessment method is that the current flowing for a capacitive process is proportional to v, while the current flowing for a diffusion limited process is proportional to $v^{1/2}$.[32,33] Therefore, for systems exhibiting both capacitive and diffusional processes, the current flowing at a specific potential (i(V)) is defined as:

$$\begin{aligned} &i(V) = k_1 v + k_2 v^{1/2} \\ &or \\ &\tfrac{i(V)}{v^{1/2}} = k_1 v^{1/2} + k_2 \end{aligned} \quad [7]$$

where k_1 and k_2 are fitting parameters. Therefore, a plot of $i(V)/v^{1/2}$ versus $v^{1/2}$ should produce a straight line from which k_1 and k_2 can be determined, and hence the contributions to capacitive and diffusive current can be deduced.

Electrical double layer capacitance.—Application of Eq. 7 to the data in Figure 1a results in the plot shown in Figure 3a. Selected potentials are shown, with more at lower potentials where the deviation from the expected linearity is more apparent. Given that the data being analyzed here is purely from a double layer capacitor, we should expect from Eq. 7 that $k_2 = 0$ since there is no diffusional contribution to the overall current. Furthermore, we should also expect that the slope of the plot of $i(V)/v^{1/2}$ versus $v^{1/2}$ should be:

$$k_1 = C\left(1 - \exp\left(-\frac{t}{RC}\right)\right) \quad [8]$$

From this expression if t is substantially larger than the time constant ($\tau = RC$), then the exponential term will approach zero, meaning that $k_1 = C$, the capacitance of the electrode. This is the origin of the dashed line in Figure 3a. Conversely, what it also means is that if the time constant is too large compared to the duration of the experiment, most problematically with a large resistance or a high sweep rate experiment, then deviations from the expected result will occur. For the data shown in Figure 1a, R = 0.005 Ω.g and C = 100 F/g, meaning the time constant is 0.5 s. At the lower potentials, such as 0.025 V, which are reached very quickly after starting the potential sweep (e.g., 0.05 s at 0.5 V/s), the time passed is still considerably less than the time constant, and so substantial deviations from linearity in Figure 3a are expected. The implication is that if the resistance is too high then this method of analysis will fail to produce the expected result.

Redox processes in a localized domain.—In a similar fashion, Eq. 7 was applied to the data in Figure 1b, with the results shown in Figure 3b for selected potentials close to the peak maximum. Based on Eq. 3 a linear response was expected, with the line passing through the origin; i.e., $k_2 = 0$ again. The expected slope of this plot is:

$$k_1 = \frac{\frac{n^2M F^2}{RT}\exp\left(\frac{nF}{RT}(E_i + vt - E)\right)}{\left[1 + \exp\left(\frac{nF}{RT}(E_i + vt - E)\right)\right]^2} = \frac{\frac{n^2M F^2}{RT}\exp\left(\frac{nF}{RT}(V - E)\right)}{\left[1 + \exp\left(\frac{nF}{RT}(V - E)\right)\right]^2} \quad [9]$$

where V is the applied potential (V) and is equal to $E_i + vt$. Effectively what Eq. 9 indicates is that k_1 is dependent on the applied potential (V), as well as the amount of redox active species available (M). From this the slope is expected to be a maximum when V = E (inset in Figure 3b), in which case:

$$k_{1(V=E)} = \frac{n^2 M F^2}{4RT} \quad [10]$$

Note that this type of redox process generates a result that is similar in behavior to the electrical double layer capacitance, providing an example of pseudo-capacitance.

Reversible diffusion limited redox processes.—Application of Eq. 7 to the data in Figure 1c leads to the response shown in Figure 3c. The response in this figure is as expected for a purely diffusion limited process; i.e., the slope $k_1 = 0$, and the Y-intercept

$$k_2 = nFAC^*\left(\frac{\pi nFD}{RT}\right)\chi(\sigma t) \quad [11]$$

is a constant for a given potential through $\chi(\sigma t)$.

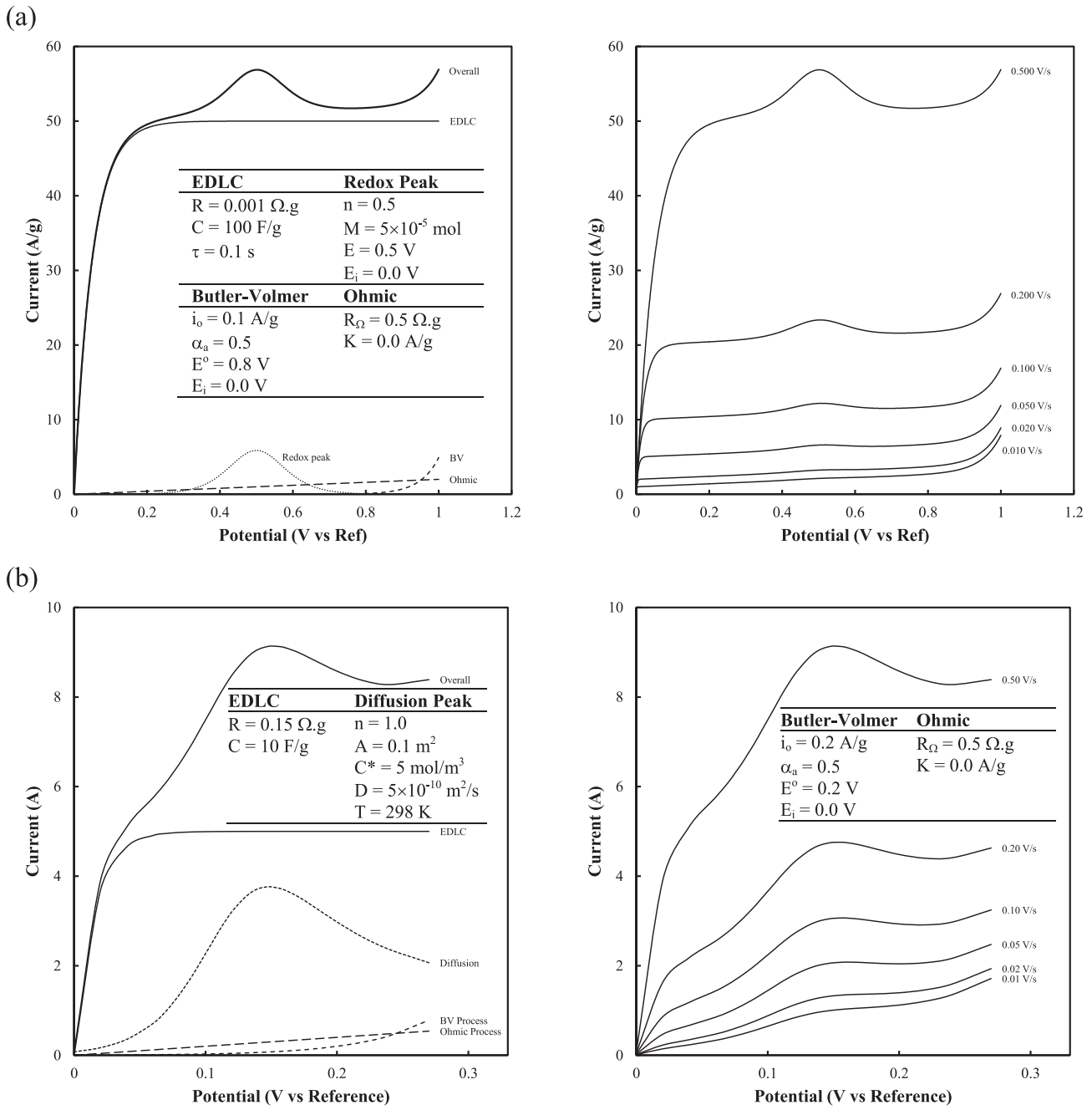

Figure 2. Synthetic voltametric data comprising an electrical double layer capacitor (series RC circuit (Eq. 2), a Butler-Volmer expression (Eq. 5) to describe electrode instabilities, and an ohmic contribution to describe electrode resistance (Eq. 6), together with (a) a redox process in a localized domain (Eq. 3) and (b) a diffusion limited redox process (Eq. 4). Also shown are the effects of sweep rate. Individual parameters are shown on the figures.

Electrode-Electrolyte instability – butler-volmer equation.— Given that the Butler-Volmer equation in Eq. 5 and in Figure 1d is independent of sweep rate, analysing it using Eq. 7 is expected to be problematic. Figure 3d shows a plot of $i/v^{1/2}$ versus $v^{1/2}$ for selected potentials based on data from the Butler-Volmer equation. Clearly this response is non-linear suggesting that kinetically controlled processes; i.e., those that are dependent on overpotential rather than sweep rate, are unable to be analyzed using this approach.

Electrode resistance – ohmic contributions.—In a similar fashion Eq. 7 has been applied to the linear ohmic data also shown in Figure 1d. As in the case of the Butler-Volmer processes, ohmic processes are also unable to be analyzed effectively using this approach (Figure 3e).

Analysis of Cyclic Voltammetry Data – Combined Data

The synthetic voltametric data shown in Figure 2a includes contributions from an EDLC, a redox process involving charge transfer in a localized domain, an anodic Butler-Volmer process and a linear ohmic contribution to the overall current. Based on the breakdown of contributions in this figure, we can identify the following potential ranges of importance:

(i) The potential range from 0.0−0.3 V is concerned mainly with the effects of the time constant of the double layer capacitance (Eq. 2);
(ii) From 0.3−0.7 V the presence of the localized redox process is apparent;

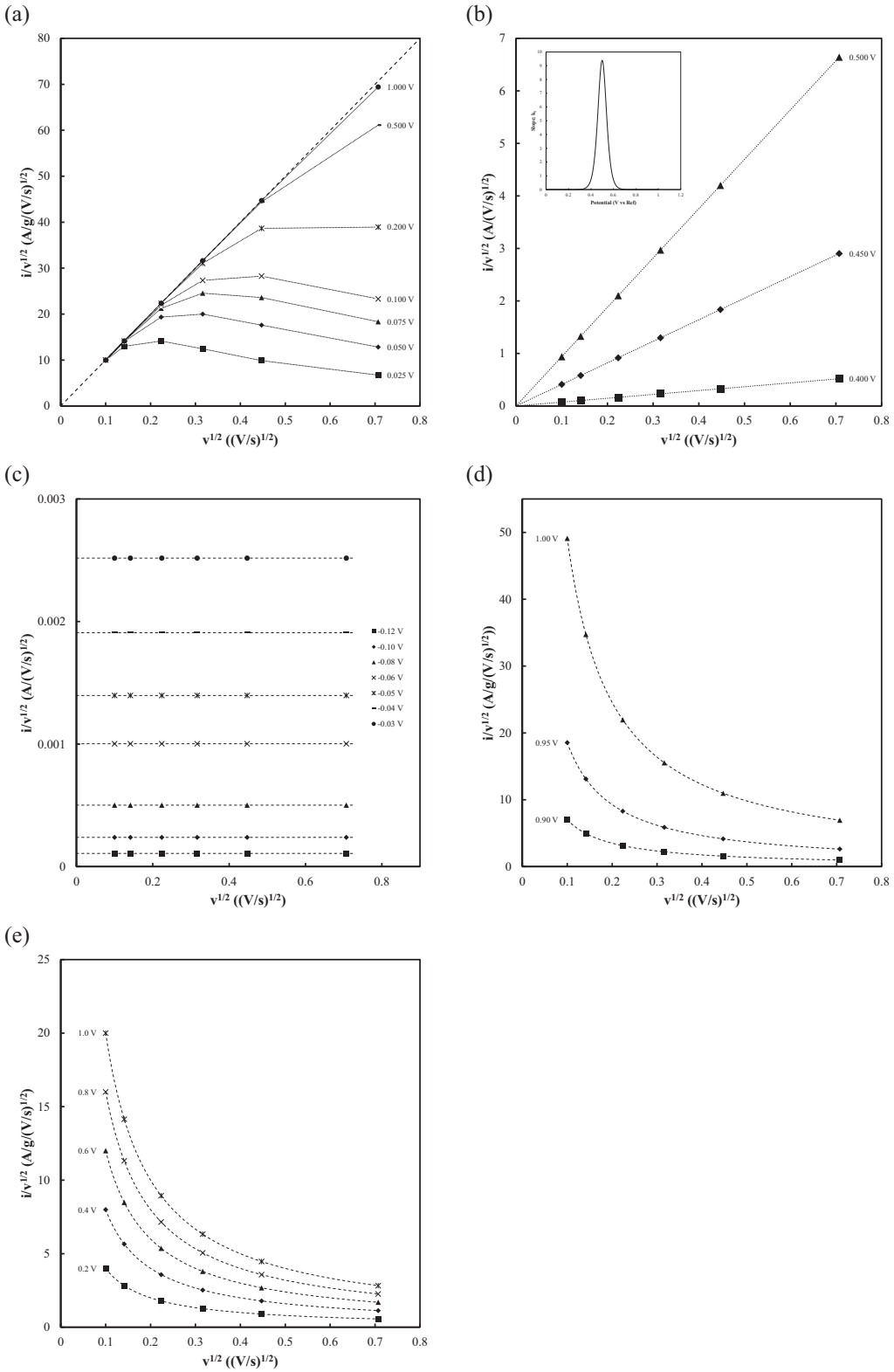

Figure 3. Outcomes from the application of Eq. 7 to the various individual data components. (a) electrical double layer capacitor; (b) redox process in a specific domain; (c) diffusion limited redox process; (d) Butler-Volmenr process; and (e) ohmic process.

(iii) At potentials higher than 0.8 V the Butler-Volmer process emerges; and,
(iv) The effects of ohmic contributions increase progressively across the potential window, becoming most significant at the highest potentials.

Analysis of the voltametric data in Figure 2a was carried out using Eq. 7 with a variety of different sweep rate ranges. In the first instance, data over all the sweep rates (0.01−0.50 V/s) was analyzed, followed by slow sweep rates (0.01−0.05 V/s) and fast sweep rates (0.10−0.50 V/s). The resultant values for k_1 (slope) and k_2 (Y-

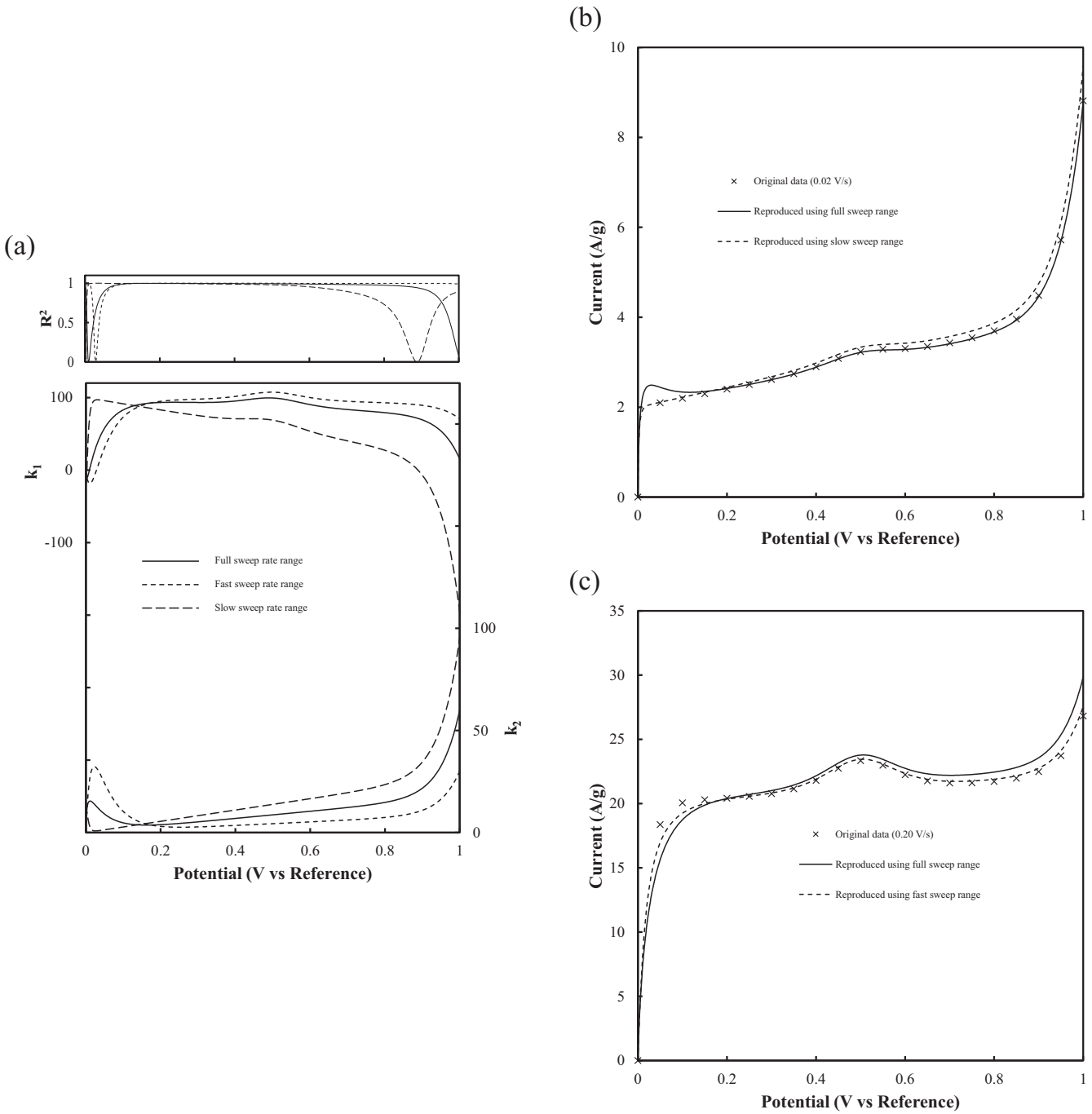

Figure 4. (a) Fitting parameters and goodness of fit as a result of the application of Eq. 7 to the synthetic voltametric data in Figure 2a comprised of and electrical double layer capacitor (series RC circuit), a redox process in a localized domain, a Butler-Volmer process, and an ohmic process. (b) and (c) show the ability of the method to reproduce the original data for slow and fast sweep rates, respectively.

intercept) are shown in Figure 4a, together with the correlation coefficient (R^2) for each analysis. When the full range of sweep rates was used the R^2 value indicating goodness of fit was close to one over the majority of the potential window, except at low potentials, where the time constant of the double layer capacitance is comparable to the duration of the experiment, and at high potentials above 0.9 V where the contributions from the anodic Butler-Volmer process and ohmic resistance processes are most significant. When the relatively fast sweep rates were used to analyse the data the R^2 value was essentially one across the entire potential range, except for potentials less than 0.1 V. Conversely, when slow sweep rates were used to analyse the data the greatest variation was noted at relatively high potentials above 0.6 V. It would seem that the use of fast sweep rates to analyse the voltametric data is preferred, likely because of the problematic (in terms of analysis) Butler-Volmer and ohmic processes contribute a greater proportion to the overall current at slower sweep rates.

The ability of the analysis technique to reproduce the original electrochemical data is demonstrated in this case in Figure 4b. Here the ability of the analysis conducted (Eq. 7) using the full range of potential sweep rates is compared with the use of both the fast and slow sweep rate ranges in their ability to reproduce appropriate original data. In Figure 4b we examine the ability of the approach to reproduce relatively slow sweep rate voltametric data (0.02 V/s). When using the full range of sweep rates for analysis the original data was readily able

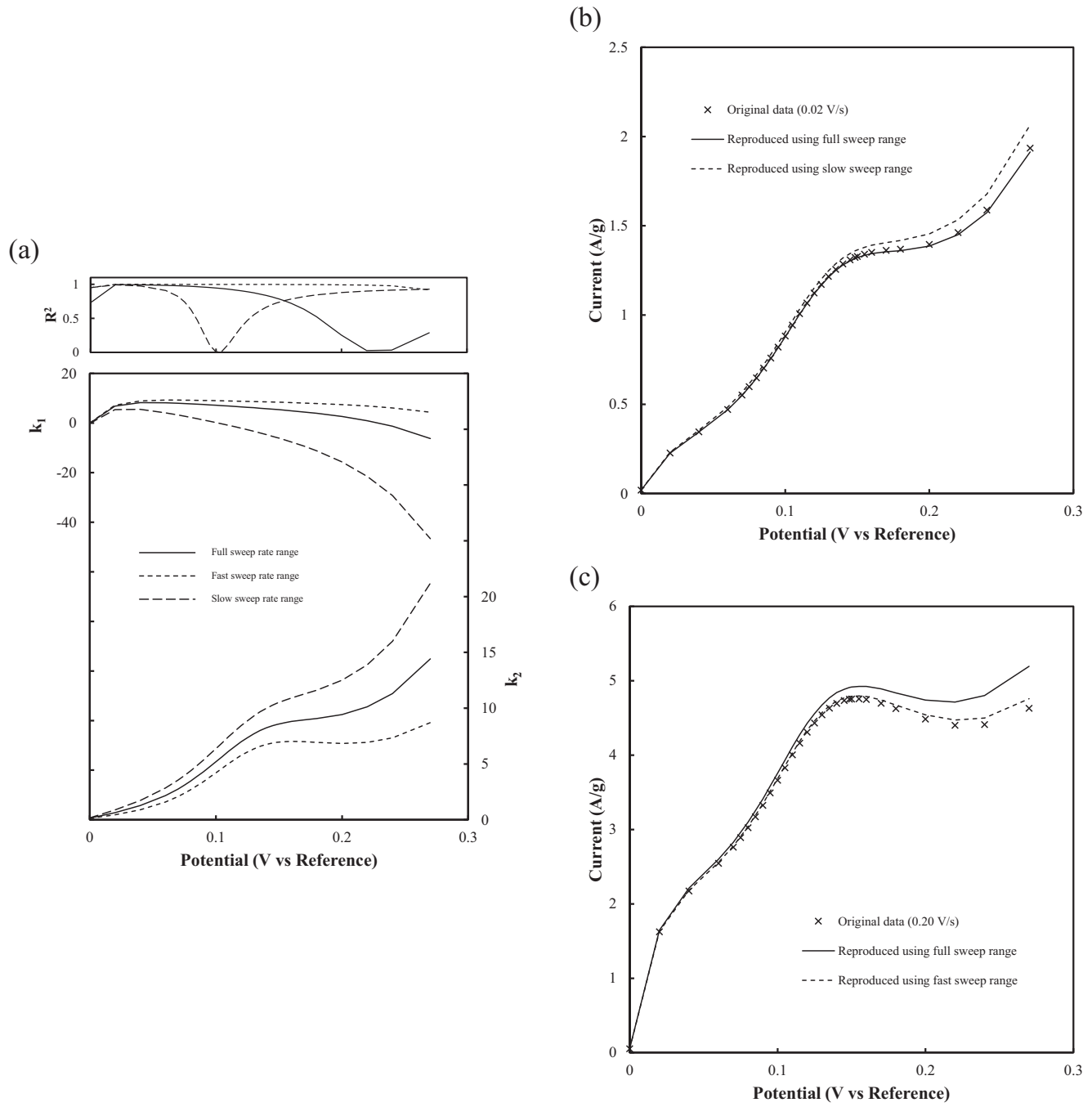

Figure 5. (a) Fitting parameters and goodness of fit as a result of the application of Eq. 7 to the synthetic voltametric data in Figure 2b, comprised of and electrical double layer capacitor (series RC circuit), a diffusion limited redox process, a Butler-Volmer process, and an ohmic process. (b) and (c) show the ability of the method to reproduce the original data for slow and fast sweep rates, respectively.

to be reproduced, except at low potentials. Overall, the variation between original and reproduced data in this case was on average ±2.1%. However, when the relatively slow voltametric sweep rates were used for the analysis (0.01−0.10 V/s), the reproduced data quite closely matched the original data at low potentials, but this got progressively worse as the potentials increased above ∼0.3 V. The variation here was on average ±3.2% over the full potential window. In Figure 4c a similar assessment has been done except now for fast sweep rate data (0.20 V/s). From this figure it would seem as though the analysis done with the fast sweep rates was able to best reproduce the original data, in this case with a variation of ±1.3% across the full potential window. When the full range of sweep rates was used a variation of ±3.8% was noted.

In a similar fashion, the voltametric data in Figure 2b was subjected to the same analysis. In this instance the voltametric data contained contributions from an EDLC, a diffusion limited redox process, as well as an anodic Butler-Volmer process and a linear ohmic contribution to the overall current. The main contributors to the overall current are as follows:

(i) From 0.00−0.07 V the current is dominated by the EDLC, more specifically the early curvature in the data indicating that the performance here is affected mostly by the EDLC resistance;
(ii) From 0.1−0.2 V the main characteristic is the diffusion limited redox process superimposed on the EDLC response;

(iii) In the potential range from 0.2 V and above contributions from the anodic Butler-Volmer process are apparent; and,
(iv) Across the full potential window the ohmic contributions to the current are progressively increasing.

Analysis of the voltametric data in Figure 2b was conducted using Eq. 7 giving rise to the outcomes in Figures 5a–5c. Figure 5a shows the fitting parameters as a function of potential using the full range of sweep rates, as well as slow and fast sweep rate ranges. Also shown in this figure is the good ness of fit data for each fitting (R^2). In this case the use of both the full sweep rate range and the slow sweep rate range had serious deficiencies in their ability to fit to the voltametric data, particularly at high potentials for the full sweep rate range, and at intermediate potentials (∼0.1 V) for the slow sweep rate data. Conversely, the fast sweep rate fitting was quite good over the complete potential range, exhibiting only slightly at both the high and low potential extremes. Under these circumstances it would appear as though the use of the full sweep rate range was affected primarily by the anodic Butler-Volmer and ohmic contributions, since these dominate at high potentials. However, when fitting using the slow sweep rate range it would seem as though this was most affected by the onset of the diffusion based redox process which corresponds to the same potential region. The reason why the fast sweep rate range best fit the data is perhaps because under these conditions the anodic Butler-Volmer and ohmic contributions are a much lower contribution to the overall current, meaning their negative impact on fitting (cf. Figures 3d and 3e) is minimized.

Conclusions

In this work we have explored some of the complications associated with using a common approach to deconvoluting double layer and diffusion limited contributions to the performance of an electrochemical capacitor electrode; i.e., the combined v (double layer) and $v^{1/2}$ (diffusion limited) contributions to the total current in a voltammetry experiment. This assessment was based upon synthetic (calculated) voltammetry data where each of the contributions to the total current were known. The total current in each case was comprised of contributions from an electrical double layer capacitance (modelled using the response of a series RC circuit), redox processes in a localized domain, diffusion limited redox processes, system instabilities modelled using the Butler-Volmer equation, and ohmic processes due to electrode resistance. Key findings from this analysis include:

(i) The response from an electrical double layer capacitor (RC series circuit) is best analyzed when the timeframe of the voltammetry experiment (i.e., sweep rate) is large compared to the time constant of the double layer capacitor. Under these circumstances the effects of electrode resistance on the rate of current increase are minimized.
(ii) For a redox process in a localized domain, such as a surface confined process or a distinct solid state domain, the current response is dependent on v, and as such the modelling approach functions as expected.
(iii) Similarly, for a diffusion controlled redox process, in which case the current is dependent on $v^{1/2}$, the modelling approach also functions as expected.
(iv) Significant complications to the modelling approach become apparent when the electrode exhibits instabilities at the extremes of potential, as described by the Butler-Volmer equation, as well as for a resistive electrode, as described by ohmic contributions. In both cases there is a distinct non-linear response to the modelling procedure which greatly affects the outcome.

Composite voltametric data consisting of contributions from each of these individual components was generated and modelled, with the outputs reinforcing the findings from studies on the individual components.

Acknowledgments

MF acknowledges the University of Newcastle for the provision of a PhD scholarship.

ORCID

Scott W. Donne https://orcid.org/0000-0001-9389-7870

References

1. I. Dincer, "Renewable energy and sustainable development: a crucial review." *Renewable and sustainable energy reviews*, **4**(2), 157 (2000).
2. M. Dresselhaus and I. Thomas, "Alternative energy technologies." *Nature*, **414**(6861), 332 (2001).
3. R. K. Singh, A. Sarkar, and J. P. Chakraborty, "Influence of Alternate Fuels on the Performance and Emission from Internal Combustion Engines and Soot Particle Collection Using Thermophoretic Sampler: A Comprehensive Review." *Waste and Biomass Valorization*, 1 (2018).
4. N. Armaroli and V. Balzani, "The future of energy supply: challenges and opportunities." *Angewandte Chemie International Edition*, **46**(1−2), 52 (2007).
5. S. Rahman, "Green power: What is it and where can we find it?" *IEEE Power and Energy Magazine*, **99**(1), 30 (2003).
6. A. M. Omer, "Energy, environment and sustainable development." *Renewable and sustainable energy reviews*, **12**(9), 2265 (2008).
7. P. J. Hall and E. J. Bain, "Energy-storage technologies and electricity generation." *Energy policy*, **36**(12), 4352 (2008).
8. H. D. Abruña, Y. Kiya, and J. C. Henderson, "Batteries and electrochemical capacitors." *Phys. Today*, **61**(12), 43 (2008).
9. B. Dunn, H. Kamath, and J.-M. Tarascon, "Electrical energy storage for the grid: a battery of choices." *Science*, **334**(6058), 928 (2011).
10. M. Beaudin et al., "Energy storage for mitigating the variability of renewable electricity sources: An updated review." *Energy for sustainable development*, **14**(4), 302 (2010).
11. Z. Yang et al., "Electrochemical energy storage for green grid." *Chemical reviews*, **111**(5), 3577 (2011).
12. P. Simon and Y. Gogotsi, "Materials for electrochemical capacitors." *Nature materials*, **7**(11), 845 (2008).
13. E. Frackowiak and F. Béguin, "Carbon materials for the electrochemical storage of energy in capacitors." *Carbon*, **39**(6), 937 (2001).
14. E. T. Mombeshora and V. O. Nyamori, "A review on the use of carbon nanostructured materials in electrochemical capacitors." *International Journal of Energy Research*, **39**(15), 1955 (2015).
15. V. Khomenko, E. Raymundo-Piñero, and F. Béguin, "High-energy density graphite/AC capacitor in organic electrolyte." *Journal of Power Sources*, **177**(2), 643 (2008).
16. P. J. Hall et al., "Energy storage in electrochemical capacitors: designing functional materials to improve performance." *Energy & Environmental Science*, **3**(9), 1238 (2010).
17. J. R. Miller, R. Outlaw, and B. Holloway, "Graphene double-layer capacitor with ac line-filtering performance." *Science*, **329**(5999), 1637 (2010).
18. K. Okajima et al., "High rate performance of highly dispersed C60 on activated carbon capacitor." *Electrochimica Acta*, **51**(5), 972 (2005).
19. A. Cross et al., "Enhanced manganese dioxide supercapacitor electrodes produced by electrodeposition." *Journal of Power Sources*, **196**(18), 7847 (2011).
20. H. Zhang, G. Cao, and Y. Yang, "Carbon nanotube arrays and their composites for electrochemical capacitors and lithium-ion batteries." *Energy & Environmental Science*, **2**(9), 932 (2009).
21. V. Barranco et al., "Amorphous carbon nanofibers and their activated carbon nanofibers as supercapacitor electrodes." *The Journal of Physical Chemistry C*, **114**(22), 10302 (2010).
22. X. Yang et al., "Functionalized porous carbon with appropriate pore size distribution and open hole texture prepared by H 2 O 2 and EDTA-2Na treatment of loofa sponge and its excellent performance for supercapacitors." *RSC Advances*, **6**(6), 4365 (2016).
23. M. Inagaki, H. Konno, and O. Tanaike, "Carbon materials for electrochemical capacitors." *Journal of power sources*, **195**(24), 7880 (2010).
24. C. Portet, G. Yushin, and Y. Gogotsi, "Electrochemical performance of carbon onions, nanodiamonds, carbon black and multiwalled nanotubes in electrical double layer capacitors." *Carbon*, **45**(13), 2511 (2007).
25. V. Augustyn, P. Simon, and B. Dunn, "Pseudocapacitive oxide materials for high-rate electrochemical energy storage." *Energy & Environmental Science*, **7**(5), 1597 (2014).
26. A. J. Downard, "Electrochemically assisted covalent modification of carbon electrodes." *Electroanalysis: An International Journal Devoted to Fundamental and Practical Aspects of Electroanalysis*, **12**(14), 1085 (2000).
27. B. Mendoza-Sánchez et al., "Scaleable ultra-thin and high power density graphene electrochemical capacitor electrodes manufactured by aqueous exfoliation and spray deposition." *Carbon*, **52**, 337 (2013).
28. K. G. Latham and S. W. Donne, "Nitrogen Doped Heat-Treated and Activated Hydrothermal Carbon: Examination of Electrochemical Performance Using Step Potential Electrochemical Spectroscopy." *Journal of The Electrochemical Society*, **165**(11), A2840 (2018).

29. K. C. Pillai, A. S. Kumar, and I.-S. Moon, "Combined effect of inherent residual chloride and bound water content and surface morphology on the intrinsic electron-transfer activity of ruthenium oxide." *Journal of Solid State Electrochemistry*, 1 (2018).
30. V. Augustyn et al., "High-rate electrochemical energy storage through Li+ intercalation pseudocapacitance." *Nature materials*, **12**(6), 518 (2013).
31. K. Naoi et al., "Ultrafast charge–discharge characteristics of a nanosized core–shell structured LiFePO 4 material for hybrid supercapacitor applications." *Energy & Environmental Science*, **9**(6), 2143 (2016).
32. M. Forghani and S. W. Donne, "Method comparison for deconvoluting capacitive and pseudo-capacitive contributions to electrochemical capacitor electrode behavior." *Journal of The Electrochemical Society*, **165**(3), A664 (2018).
33. T. C. Liu et al., "Behavior of molybdenum nitrides as materials for electrochemical capacitors comparison with ruthenium oxide." *Journal of the Electrochemical Society*, **145**(6), 1882 (1998).
34. S. Ardizzone, G. Fregonara, and S. Trasatti, ""Inner" and "outer" active surface of RuO2 electrodes." *Electrochimica Acta*, **35**(1), 263 (1990).
35. D. Baronetto, N. Krstajić, and S. Trasatti, "Reply to "note on a method to interrelate inner and outer electrode areas" by H. Vogt." *Electrochimica acta*, **39**(16), 2359 (1994).
36. L. M. Doubova, S. Daolio, and A. De Battisti, "Examination of RuO 2 single-crystal surfaces: charge storage mechanism in H 2 SO 4 aqueous solution." *Journal of Electroanalytical Chemistry*, **532**(1), 25 (2002).
37. M. F. DuPont et al., "Effect of electrolyte cation on the charge storage mechanism of manganese dioxide for electrochemical capacitors." *Electrochimica Acta*, **271**, 337 (2018).
38. M. Forghani and S. W. Donne, "Duty Cycle Effects on the Step Potential Electrochemical Spectroscopy (SPECS) Analysis of the Aqueous Manganese Dioxide Electrode." *Journal of The Electrochemical Society*, **165**(3), A593 (2018).
39. M. F. DuPont and S. W. Donne, "A Step Potential Electrochemical Spectroscopy Analysis of Electrochemical Capacitor Electrode Performance." *Electrochimica Acta*, **167**, 268 (2015).
40. M. F. DuPont and S. W. Donne, "Separating faradaic and Non-faradaic Charge Storage Contributions in Activated Carbon Electrochemical Capacitors Using Electrochemical Methods: I. Step Potential Electrochemical Spectroscopy." *Journal of the Electrochemical Society*, **162**(7), A1246 (2015).
41. M. F. DuPont and S. W. Donne, "Separating the faradaic and Non-faradaic Contributions to the Total Capacitance for Different Manganese Dioxide Phases." *Journal of The Electrochemical Society*, **162**(5), A5096 (2015).
42. M. F. DuPont and S. W. Donne, "Electrolytic Manganese Dioxide Structural and Morphological Effects on Capacitive Performance." *Electrochimica Acta*, **191**, 479 (2016).
43. M. F. DuPont and S. W. Donne, "faradaic and Non-faradaic Contributions to the Power and Energy Characteristics of Electrolytic Manganese Dioxide for Electrochemical Capacitors." *Journal of The Electrochemical Society*, **163**(6), A888 (2016).
44. M. F. DuPont and S. W. Donne, "Charge storage mechanisms in electrochemical capacitors: Effects of electrode properties on performance." *Journal of Power Sources*, **326**, 613 (2016).
45. H. M. Fellows et al., "Modelling voltametric data from electrochemical capacitors." *Journal of Power Sources*, **417**, 193 (2019).
46. Allen J. Bard and L. R. Faulkner, *Electrochemical Methodes: Fundamentals and Applications*, SECOND EDITION ed. 2001: John Wiley & Sons.
47. A. Bousquet, M. Ceccato, M. Hinge, SU Pedersen, and K. Daasbjerg, "Redox grafting of diazotated anthraquinone as a means of forming thick conducting organic films," *Langmuir*, **28**(2), 1267 (2012).
48. A. Le Comte, T. Brousse, and D. Belanger, "Simpler and Greener Method for Improving the Stability of Anthraquinone Modified Carbon Electrode in Alkaline Media," *Electrochim. Acta*, **137**, 447 (2014).
49. J. O'M. Bockris and A. K. N. Reddy, *Modern Electrochemistry*, Volume 2, Kluwer Academic / Plenum Publishers, New York (1970).
50. G. J. Browning and S. W. Donne, "Electrochemical kinetic behavior of the aqueous manganese dioxide electrode," *J. Appl. Electrochem.*, **35**(5), 437 (2005).
51. Z. Hong, C. Zhenhai, and X. Xi, "Diffusion Model and Filling Mechanim of Proton in Alkaline γ-MnO_2 Electrode," *J. Electrochem. Soc.*, **136**, 2771(1989).
52. J. R. Miller and P. Simon, "Fundamentals of electrochemical capacitor design and operation," *Electrochemical Society Interface*, **17**(1), 31 (2008).
53. C. Yu et al., "Composite Li [Li0. 11Mn0. 57Ni0. 32] O2: Two-step molten-salt synthesis, oxidation state stabilization, and uses as high-voltage cathode for lithium-ion batteries." *Journal of Alloys and Compounds*, **528**, 121 (2012).
54. J. Zheng et al., "Li-and Mn-Rich Cathode Materials: Challenges to Commercialization." *Advanced Energy Materials*, **7**(6), 1601284 (2017).
55. J. Haetge, C. Suchomski, and T. Brezesinski, "Ordered mesoporous MFe2O4 (M = Co, Cu, Mg, Ni, Zn) thin films with nanocrystalline walls, uniform 16 nm diameter pores and high thermal stability: template-directed synthesis and characterization of redox active trevorite." *Inorganic chemistry*, **49**(24), 11619 (2010).
56. Á. León-Reyes et al., "Analysis of the Different Mechanisms of Electrochemical Energy Storage in Magnetite Nanoparticles." *Int. J. Electrochem. Sci*, **9**, 3837 (2014).
57. M. C. Lopez et al., "Improved energy storage solution based on hybrid oxide materials." *ACS Sustainable Chemistry & Engineering*, **1**(1), 46 (2012).
58. J. Wang et al., "Pseudocapacitive contributions to electrochemical energy storage in TiO2 (anatase) nanoparticles." *The Journal of Physical Chemistry C*, **111**(40), 14925 (2007).
59. J. Shao et al., "Mechanism analysis of the capacitance contributions and ultralong cycling-stability of the isomorphous MnO 2@ MnO 2 core/shell nanostructures for supercapacitors." *Journal of Materials Chemistry A*, **3**(11), 6168 (2015).

Chapter 8: Modification of the Step Potential Electrochemical Spectroscopy Analysis Protocol to Improve Outcomes

Overview

In this chapter, the SPECS method has been further improved to generate a rigorous synthetic voltammogram which is comparable to the actual voltammetric data. The revised methodology for analysing SPECS data is based on this fact that the formation of a double layer on the electrode-electrolyte interface for each subsequent potential steps in a SPECS experiment are independent of each other. The comparison between the experimental CV data and synthetic voltammogram generated from the revised SPECS analysis has been presented here.

The following publication is reproduced from the Journal of the Electrochemical Society, Volume 166, Issue 13, p. A2727-A2735 (2019), with permission of the Electrochemical Society.

Journal of The Electrochemical Society, **166** (13) A2727-A2735 (2019)
0013-4651/2019/166(13)/A2727/9/$38.00 © The Electrochemical Society

Modification of the Step Potential Electrochemical Spectroscopy Analysis Protocol to Improve Outcomes

Marveh Forghani* **and Scott W. Donne** **,z

Discipline of Chemistry, University of Newcastle, Callaghan NSW 2308, Australia

Here we present an improved methodology for the analysis of i-t transients collected as part of step potential electrochemical spectroscopy (SPECS) experiments. This approach is improved over previous methodologies because it takes into consideration interactions between i-t transients resulting from subsequent potential steps in the SPECS experiment. The improved output of the new methodology is demonstrated with simulated and experimental data. The revised methodology also highlights the independence of non-faradaic charge storage processes, as compared to faradaic processes in which case i-t transients are demonstrated to have an inherent contribution from previous steps in the SPECS experiment.
 [DOI: 10.1149/2.0091913jes]

Manuscript received May 28, 2019. Published August 7, 2019.

Electrochemical capacitors are an emerging power source ideally suited at this time for use in high power pulse applications[1] because of their excellent specific power (W/kg) and cyclability ($>10^5$ cycles with minimal fading).[2–4] An obstacle to their ongoing commercial development is their specific energy density (Wh/kg) which is inferior to other electrochemical energy storage and conversion devices, such as batteries and fuel cells.[5,6] Consequently, the cost per unit energy for electrochemical capacitors is relatively high.[7,8] Nevertheless, this shortcoming is driving substantial global research into the development of higher energy materials for use in electrochemical capacitors.[9]

A wide range of materials have been examined in terms of their behavior in electrochemical capacitor systems.[10] Generally, these materials can be categorized individually into either (i) carbon-based materials,[11] (ii) metal oxides, nitrides, sulfides, etc.,[12,13] or (iii) conducting polymers.[9,14] Substantial effort is ongoing to develop these material categories individually, as well as in the form of composite materials,[15,16] where the goal is to improve overall electrode behavior through synergistic interaction between the electrode components.[17,18]

In parallel with material development are ongoing effort to understand the various charge storage mechanisms that these materials exhibit.[19] Electrodes made from all of these materials have a contribution from double layer formation; i.e., the physical separation of charge at the electrode-electrolyte interface.[20] Beyond this, select materials have the capacity to undergo redox processes that can also contribute to energy storage.[21] In the context of electrochemical capacitors this is often referred to a pseudo-capacitance,[22] and in some instances this has enabled materials that were previously considered battery materials to make the transition to capacitor systems;[23,24] e.g., manganese dioxide.[25,26] An important criteria here is that the electrochemical response of the redox process is indistinguishable from that expected from electrical double layer formation, hence the name 'pseudo'-capacitance.[27] Typically this is associated with charge delocalization over the electrochemically active material.[28] Conversely, charge localization leads to the observation of distinct voltametric processes within a relatively narrow potential window; e.g., functionalized carbons,[29] and the $NiOOH/Ni(OH)_2$ redox couple.[30] In any case, whatever the approach to improving energy density, the important output is that the electrode materials retain the expected high specific power density and cyclability of an electrochemical capacitor system.[31]

A number of experimental methods have been reported in the literature focused on deconvoluting the contributions made by each type of charge storage mechanisms.[32] Methods based on the analysis of voltametric data at different sweep rates have been used, in which case the current at a specified potential (i(V); $A.g^{-1}$) as a function of sweep rate (v; $V.s^{-1}$) can be used;[33] i.e.,

$$i(V) = a_1 v + a_2 v^{1/2} \quad [1]$$

where a_1 and a_2 are fitting parameters. Capacitive processes are expected to be proportional to v ($a_1 v$) while diffusion limited (redox) processes are proportional to $v^{1/2}$ ($a_2 v^{1/2}$). An alternate approach is to link the charge passed in a voltametric experiment (q(v); C/g) to the sweep rate;[34] i.e.,

$$q_T = q_i + q_o \quad [2]$$

$$q(v) = q_o + \frac{b_1}{v^{1/2}} \quad \text{when} \quad v \to \infty \quad [3]$$

$$\frac{1}{q(v)} = \frac{1}{q_T} + b_2 v^{1/2} \quad \text{when} \quad v \to 0 \quad [4]$$

where q_i and q_o are the inner (redox) and outer (capacitive) surfaces of the electrode material (C/g), q_T is the total voltametric charge (C/g), and b_1 and b_2 are again fitting parameters. The validity of both of these methodologies has been discussed in detail elsewhere.[32]

An alternate approach to charge storage differentiation uses step potential electrochemical spectroscopy (SPECS),[35,36] in which case the various electrochemical processes are differentiated based on their current response after the imposition of a small potential step. The resultant i-t transient can then be modelled according to the expected response from various processes. Capacitive processes (i_C; $A.g^{-1}$) can be represented by the series arrangement of a resistor (R; Ω.g) and capacitor (C; $F.g^{-1}$), in which case the response to a potential step (ΔE; V) is given by:[37]

$$i_C = \frac{\Delta E}{R} \exp\left(-\frac{t}{RC}\right) \quad [5]$$

The subtlety of the model is such that double layer formation can be differentiated on different surfaces within the electrode (e.g., geometric or porous surfaces) due to the different time constants ($\tau = RC$; s) for the individual processes.[38] Diffusion limited processes (i_D; $A.g^{-1}$) can be modelled using the Cottrell equation,[37] in which case:

$$i_D = \frac{B}{t^{1/2}} \quad [6]$$

where B is a fitting constant taking into consideration the electrochemically active area, the diffusion coefficient of species, as well as the concentration of electroactive species.[39] The overall response (i_T; $A.g^{-1}$) is therefore given by:

$$i_T = i_C + i_D + i_R \quad [7]$$

where the last parameter (i_R; $A.g^{-1}$) represents a constant residual current underpinning the capacitive and diffusive contributions.[40] The application of a series of small potential steps across the full potential window, in both the anodic and cathodic half-cycles, allows for the examination of how these processes change with applied potential.[41]

In addition to the extraction of fitting parameters a protocol has been developed whereby the SPECS data can be converted into voltametric data, enabling the determination of performance data for the electrode under study; i.e., capacitance as a function of sweep rate,

*Electrochemical Society Student Member.
**Electrochemical Society Member.
zE-mail: scott.donne@newcastle.edu.au

as well as power and energy (Ragone) data.[38] The protocol for converting the i-t transient from the SPECS analysis into voltametric data is based on determining the average current out to a specific time after the imposition of the potential step. Plotting this average current, determined in the same way for all potential steps, gives rise to a voltammogram for subsequent analysis. The assumption made during this approach is that the i-t response during each step is independent of all other steps.[42] While this approach has been shown to provide a good relative comparison between different processes and different materials,[32,43–45] the absolute performance is different when compared to actual cyclic voltammetry data, except at very slow sweep rates.[35] As such, what we report here is an improved approach to the analysis of SPECS data, one that allows not only for the relative comparison of results but also the absolute comparison with voltametric data. This will be demonstrated using both artificial and experimental means.

Methodology

Material synthesis.—To demonstrate the improved methodology for analyzing SPECS data we have made use of electrodeposited manganese dioxide (EMD) as the electroactive material. EMD was prepared via the electrolysis (anodic current density of 65 $A.m^{-2}$) of a hot (98°C), acidic (0.3 M H_2SO_4; prepared from concentrated (98%) H_2SO_4 supplied by Sigma-Aldrich) solution of 0.5 M $MnSO_4$ (prepared by dissolution of solid $MnSO_4.H_2O$ supplied by Sigma-Aldrich). The electrochemical reactions carried out were:

$$\text{Anode (Ti)}: \quad Mn^{2+} + 2H_2O \rightarrow MnO_2 + 4H^+ + 2e^- \qquad [8]$$

$$\text{Cathode (Cu)}: \quad 2H^+ + 2e^- \rightarrow H_2 \qquad [9]$$

$$\text{Overall}: \quad Mn^{2+} + 2H_2O \rightarrow MnO_2 + H_2 + 2H^+ \qquad [10]$$

After sufficient electrodeposition had occurred the current was turned off and the EMD coated anode was removed from the cell. The EMD was then mechanically removed from the titanium substrate and then milled to a mean particle size of ~45 μm before being suspended in Milli-Q ultrapure water (>18.2 MΩ.cm resistivity) which was neutralized with the addition of 0.1 M NaOH. After neutralization the suspension was filtered and washed thoroughly with more Milli-Q water before being dried at 100°C in air.

Electrode preparation and electrochemical protocol.—Electrodes were prepared by casting of an ink. The working electrode ink was made from EMD, carbon black as a conductive agent (Cabot Vulcan XC72R), and poly(vinylidene difluoride) (PVdF; Fluka) as a binder with a ratio of 15:80:5. The high proportion of conductive additive was to ensure that electrode behavior was not limited by electrode design. The dry ingredients were ground lightly using a ceramic mortar and pestle for ~5 minutes, after which they were suspended in 1-methyl-2-pyrrolidinone (NMP; 99+%; Sigma-Aldrich) with a weight ratio of 20:1 NMP to EMD. Stirring of the suspension was continued for 30 min using a magnetic stirrer to obtain a homogenized ink. The counter electrode ink was produced in a similar manner using homemade activated carbon as the active material. Each electrode substrate was a 13 mm stainless steel rod, the end of which had been polished with 1200 grit emery paper and subsequently washed with Milli-Q water. 50 μL of the working electrode ink and 100 μL of the counter electrode ink were drop cast onto separate stainless steel substrates before being dried at 60°C in air. Electrode loadings were ~0.3 $mg.cm^{-2}$ of manganese dioxide on the working electrode and ~0.6 $mg.cm^{-2}$ of activated carbon on the counter electrode.

The electrochemical cell was a 13 mm diameter perfluoroalkoxyalkane (PFA) T-junction Swagelok cell. Firstly, the dried counter electrode was inserted into the Swagelok cell. Two layers of porous paper, which were to be used as a separator, were wetted with electrolyte solution to ensure a fast equilibration before they were placed over the counter electrode. Then the working electrode was inserted into the opposite ends of the electrochemical cell. The electrodes were pressed at 1.7 MPa using a hydraulic press to increase the conductivity and secured in place while under load. After that the electrochemical cell was filled with 0.5 M K_2SO_4 electrolyte solution. The reference electrode (saturated calomel electrode; SCE; Radiometer Analytical) was then inserted into the perpendicular port of the Swagelok cell and sealed using Parafilm. Finally, the electrochemical cell was left to equilibrate for 1 hour before use. Unless otherwise stated, all potentials are with respect to the SCE.

In this study, an Iviumstat Multichannel Potentiostat controlled by Iviumstat software, was used to run the electrochemical experiments. The electrochemical cell was cycled in the range 0.0−0.8 V for 5 cycles at sweep rates ranging from 0.1 to 100 mV/s. This was followed by the SPECS experiment with a 0.025 V potential step and 300 s equilibration time. In the SPECS experiment from the initial minimum potential (0.0 V), a series of equally sized ±0.025 V potential steps were applied to the working electrode. After each potential step, the working electrode was allowed to equilibrate for 300 s before applying the next potential step, until the full potential window (0.0−0.8 V) was covered. This process was then reversed from the maximum potential of 0.8 V to the minimum potential of 0.0 V. The current response from each potential step was recorded as a function of time until one entire charge/discharge cycle was completed. The time base for data collection was 0.02 s.

Simulation of voltametric data.—To demonstrate the revised approach to analysing SPECS data the response of a series arrangement of a resistor (R; Ω.g) and capacitor (C; $F.g^{-1}$) was employed. The response of this electrical circuit (i; $A.g^{-1}$) to the imposition of a linear potential ramp is given by:[37]

$$i = vC\left\{1 - \exp\left(-\frac{t}{RC}\right)\right\} \qquad [11]$$

where v is the potential sweep rate ($V.s^{-1}$), and t is the corresponding time (s). Since this is defined for an electrical circuit rather than a real electrochemical capacitor system, the choice of potential window is arbitrary. Therefore, we have chosen a 0–1 V potential window for demonstration purposes. What is advantageous with this approach is that the resistance and capacitance are known beforehand, thus providing a reference point for comparison with outcomes from the SPECS analysis. Examples of the voltametric data resulting from Eq. 11 is shown in Figure 1.

Results and Discussion

Previous SPECS methodology.—The original methodology for analysing SPECS data enabled the conversion of the series of i-t transients for each potential step into voltametric data.[35] Of course when the voltametric data has been generated it can be converted subsequently into specific capacitance, power and energy data. This approach was based on the way in which a modern digital potentiostat applies a linear potential scan to an electrode. In this case, the potential scan is broken down into a series of small potential steps with a rest period after each step corresponding to the desired linear potential sweep rate; e.g., a 0.1 mV step with a 0.1 s rest period corresponds to a sweep rate of 1 $mV.s^{-1}$. The current flow after each potential step is recorded and the average presented as being indicative of the voltametric behavior. In the context of a SPECS experiment the average current was determined out to a specified time after each potential step, thus allowing for voltametric data to be generated. Figure 2a demonstrates this approach to converting SPECS i-t transient data into voltametric data. In this case the i-t transient was purely capacitive in nature, generated using Eq. 5, with $\Delta E = 0.01$ V, $R = 0.01$ Ω.g and $C = 100$ $F.g^{-1}$. The average current (i_{ave}; $A.g^{-1}$) after a specified time

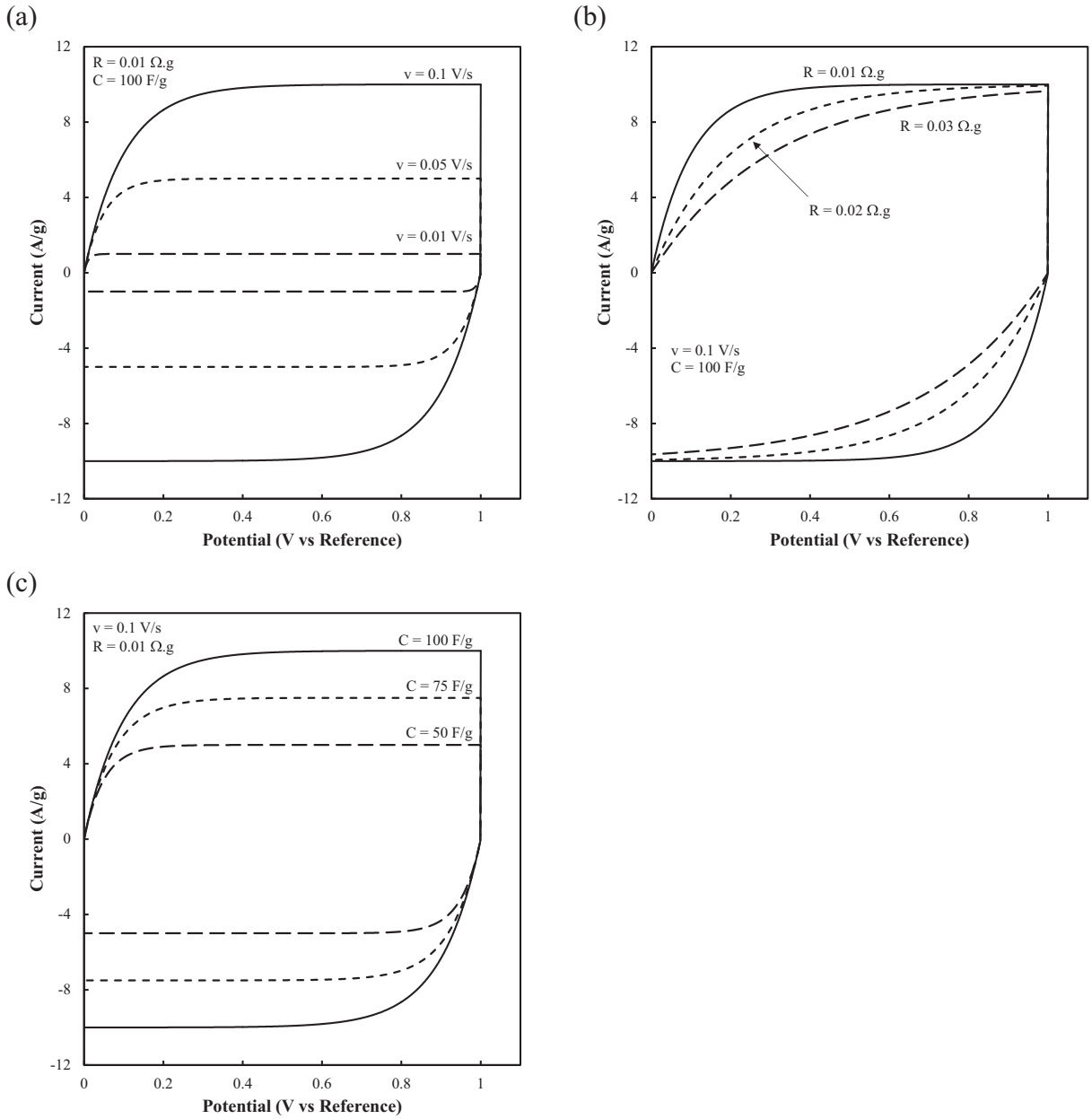

Figure 1. Examples of the voltametric response arising from the application of a linear potential ramp (v; $V.s^{-1}$) from 0 V to 1 V and then back to 0 V to a series combination of a resistor (R; Ω.g) and capacitor (C; $F.g^{-1}$). Figures show the effect of (a) sweep rate, (b) resistance and (c) capacitance.

(t; s) after the potential step in this case can be determined using:

$$i_{ave} = \frac{q}{t} = \frac{\Delta E}{Rt}\int_0^t \exp\left(-\frac{t}{RC}\right)dt = \frac{\Delta EC}{t}\left\{1 - \exp\left(-\frac{t}{RC}\right)\right\} \quad [12]$$

where q is the charge passed after each potential step ($C.g^{-1}$) determined as the integral of current (Eq. 5) with respect to time. Figures 2b and 2c provide an example of the comparison between the expected voltametric behavior based on Eq. 5 with the synthetic voltametric behavior resulting from the SPECS analysis using sweep rates of 0.1 and 0.01 $V.s^{-1}$. From these figures it is clear that there is a substantial divergence between the behavior predicted from the current SPECS analysis methodology and that predicted from a purely voltametric approach, with the voltametric data exceeding that of the SPECS data at all times. It is also apparent that the divergence decreases as the sweep rate decreases. This is also apparent in Figure 2d which is a direct comparison between the electrode performance predicted from both analysis methods. Ultimately the electrode capacitance determined from both methods approaches the expected value (100 $F.g^{-1}$); however, as before, that predicted from the voltametric approach is always greater than that predicted from the SPECS methodology.

Despite this divergence the present SPECS analysis method still provides an excellent means by which to compare the relative performance of various electrodes.[32] However, on an absolute scale, the divergence between actual voltametric data and that predicted from SPECS has been demonstrated here to be substantial, particularly at fast sweep rates. One of the underlying assumptions with the SPECS analysis method described above is that the current flowing after the cutoff time can be ignored and that it does not influence subsequent voltametric behavior. The comparisons shown in Figure 2 would suggest otherwise, and so an appropriate revised SPECS analysis method is required to compensate for this apparent interaction between subsequent i-t transients.

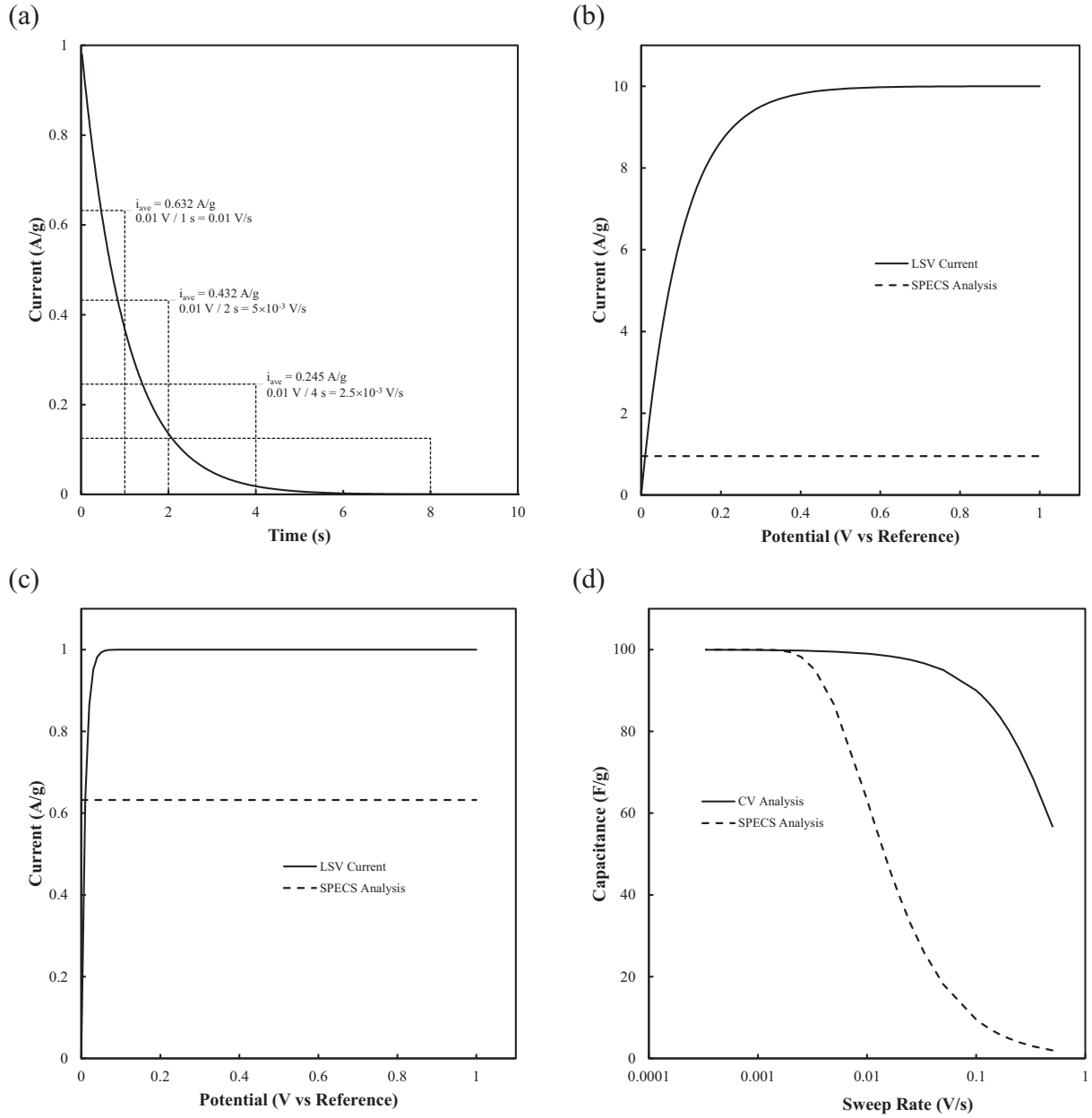

Figure 2. (a) Demonstration of the previous methodology for analysing SPECS data; (b) and (c) compare the predicted voltametric current from a series resistor and capacitor circuit (Eq. 11) and the previous SPECS analysis method at sweep rates of 0.1 and 0.01 $V.s^{-1}$, respectively; and (d) a specific capacitance comparison for both methodologies.

Revised methodology.—To enable the interaction between subsequent i-t transients in a SPECS experiment a methodology has been developed whereby the timing of the individual responses can be shifted according to the required rate. Figure 3a shows the response from a simulated SPECS experiment on a series RC circuit (R = 0.01 Ω.g, C = 100 $F.g^{-1}$, ΔE = 0.01 V, and the rest time is 30 s). As an example to demonstrate the new methodology Figure 3b shows each i-t transient resulting from a potential step has been shifted forward to represent a step every 2 s. It is important to note here that the i-t transient is the same as in Figure 3a, although here the time axis has been compressed, in this case so that the step timing is 2 s. What this leads to is an apparent current flowing from multiple steps at the same time. To account for this in the conversion of SPECS data to voltametric data the sum of the average current (i_{TOT}) flowing from each of the overlapping i-t transients within the step timeframe is determined; i.e.,

$$i_{TOT} = \sum_{n=1}^{n} i_{ave,n} = \sum_{n=1}^{n} \frac{\Delta E C_n}{\Delta t} \left\{ \exp\left(-\frac{t_n}{R_n C_n}\right) - \exp\left(-\frac{t_{n+1}}{R_n C_n}\right) \right\} \quad [13]$$

where $i_{ave,n}$ is the average current flowing from the nth overlapping i-t transient, R_n and C_n are the resistance and capacitance of the nth step, and $\Delta t = t_{n+1} - t_n$ which is the shifted time base on the SPECS analysis. Figure 3c provides a graphical depiction of this analysis example. Repeating this process of summing the average current for each potential step across the full potential window, both anodic and cathodic, leads to a voltammogram as shown in Figure 3d, in this case for v = 0.1 $V.s^{-1}$, R = 0.01 Ω.g, C = 100 $F.g^{-1}$ and ΔE = 0.01 V. Also shown

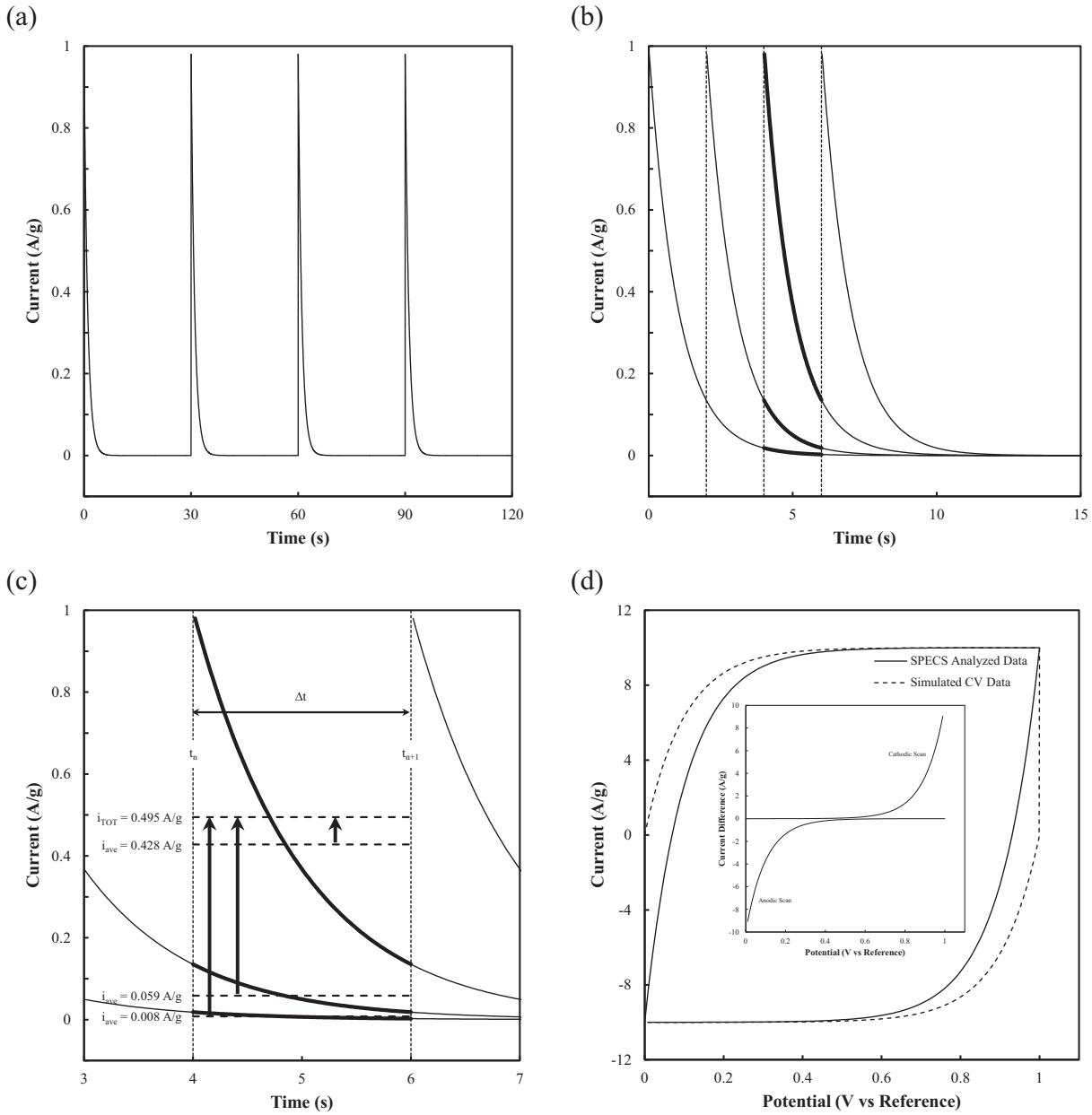

Figure 3. (a) A series of i-t transients resulting from a simulated SPECS experiment on a series RC circuit (R = 0.01 Ω.g, C = 100 $F.g^{-1}$, ΔE = 0.01 V, and the rest time is 30 s); (b) an example demonstrating the revised methodology in which the sequence of i-t transients have been compressed to simulate a potential step every 2 s; (c) graphical depiction of the revised methodology used to calculate the voltametric current; and (d) the resultant voltametric data from the revised methodology compared to the expected response from Eq. 11. Inset: Deviation between the different methodologies.

here is the corresponding voltammogram based on Eq. 11 using the same v, R and C values.

The comparison in Figure 3d shows that SPECS analyzed data provides a better indication of actual voltametric data than that predicted from Eq. 11 because of the ability of the SPECS approach to factor in current contributions from nearby potential steps. This is particularly apparent at the extremes of potential where the opposite polarity scan or steps contribute to the overall current. This phenomena is not built into the predicted voltametric data based on Eq. 11. Inset in Figure 3d is the difference in current between the SPECS derived voltametric data and that determined from Eq. 11. It shows an exponentially increasing current as the potential limits are approached. This observation provides further evidence to support the inclusion of such an exponential expression in the modelling of voltametric data, as we have done previously.[21]

Faradaic versus non-faradaic processes.—This approach has demonstrated nicely how the revised methodology can accurately predict synthetic cyclic voltammetry data from non-faradaic processes In all instances where we have used the SPECS technique to understand electrode behavior, each i-t transient has been modelling with a combination of capacitive (geometric and porous), diffusive and residual contributions. Two capacitive processes are typically included to differentiate the responsiveness (time constant) of the geometric (external interface) and porous processes. Here the differences arise as a result of the freedom of movement of electrolyte ions in the bulk electrolyte compared to the constrained electrolyte within pores, as well as the relative surface area differences.[38] A diffusive contribution has been included to represent the intercalation of species into the host structure and their subsequent diffusion away from the electrode-electrolyte interface, as well as the mass transport of electrolyte into

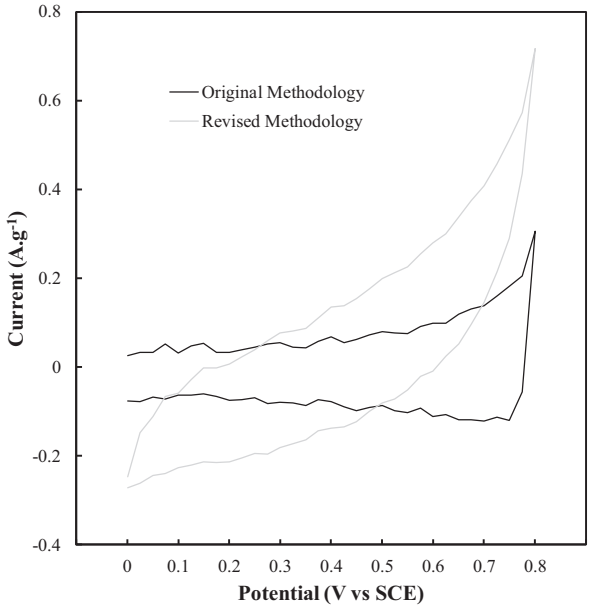

Figure 4. Comparison between the original and revised SPECS methodologies applied to diffusional processes with the electrode.

pores. Diffusion here has been represented by the Cottrell equation for semi-infinite planar diffusion;[37] i.e.,

$$i_D = nFA\Delta C\left(\frac{D}{\pi t}\right)^{1/2} = \frac{B}{t^{1/2}} \quad [14]$$

where i_D is the diffusion limited current ($A.g^{-1}$), A the electrochemically active surface area ($m^2.g^{-1}$), and all other terms have their usual electrochemical significance. B is a parameter combining all these terms together. An analysis similar to that described above for capacitive charge storage can be applied; i.e.,

$$i_{TOT} = \sum_{n=1}^{n} i_{ave,n} = \sum_{n=1}^{n} \frac{2B}{\Delta t}\left(t_{n+1}^{1/2} - t_n^{1/2}\right) \quad [15]$$

A comparison of the original and revised SPECS analysis methodologies is shown in Figure 4 and it would seem as though the original methodology provides a better estimate of diffusion-based voltammetry than the revise methodology.

The reason for this difference originates from the various charge storage mechanisms and the independence of the charge carriers for double layer versus faradaic charge storage processes. For double layer formation charge carriers moving toward or away from the electrode-electrolyte interface are independent of each other. That is, the charge carriers added or removed from the interface in one potential step are independent, or not influenced, in any way by those added or removed in a subsequent potential step. Another way to express this is to consider that the electrode surface has a finite (although large) number of charge storage sites available with which ions from the electrolyte can associate. Addition of charge to this interface as a result of a potential step leads to the fractional occupancy of these sites whereby the formation of a uniform distribution of charge carriers occurs on the surface, such that the level of interaction between the charge carriers is minimal. Hence the independent nature of the charge carriers.

In the example used here, faradaic charge and discharge of manganese dioxide involves electron and cation (M^+) intercalation into the host structure; i.e.,

$$MnO_2 + xM^+ + xe^- \leftrightarrow M_xMnO_2 \quad [16]$$

where x is the fraction of charge available used in the discharge process. This is followed by diffusion of these species away from the interface into the material bulk in response to a concentration gradient. The level of material utilization in this case is dependent primarily on the rate of diffusion of charge carriers into the bulk material compared to the rate of intercalation. If diffusion is too slow or the rate of discharge too fast, then the electrode-electrolyte interface will become saturated with charge carriers and excessive electrode polarization will result. Under these circumstance we can surmise that the intercalation of charge into the manganese dioxide structure is very much dependent on charge that has already been intercalated into the structure in the sense that it limits its ability to diffuse away from the surface. The net result therefore is that the current flow due to diffusion in response to a potential step already contains contributions from previous steps and so to add them together such as proposed in the revised analysis

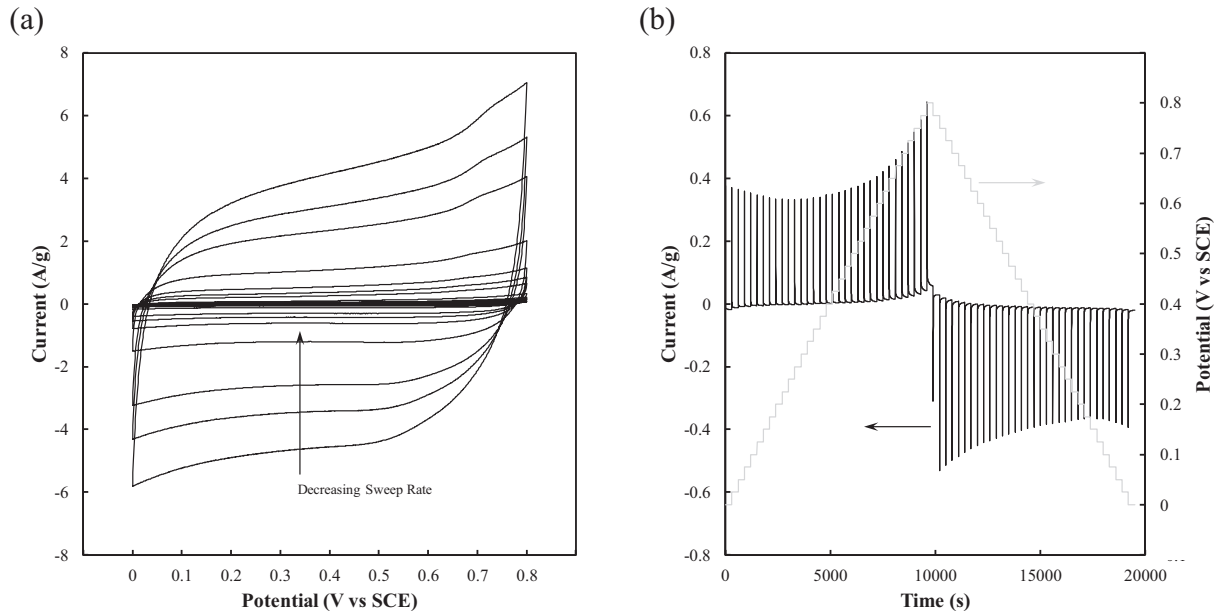

Figure 5. (a) Voltametric data on the EMD electrode in 0.5 M K_2SO_4 corresponding to different sweep rates ranging from 0.0001 to 0.1 $V.s^{-1}$; and (b) SPECS data resulting from a ±0.025 V steps with a 300 s rest period.

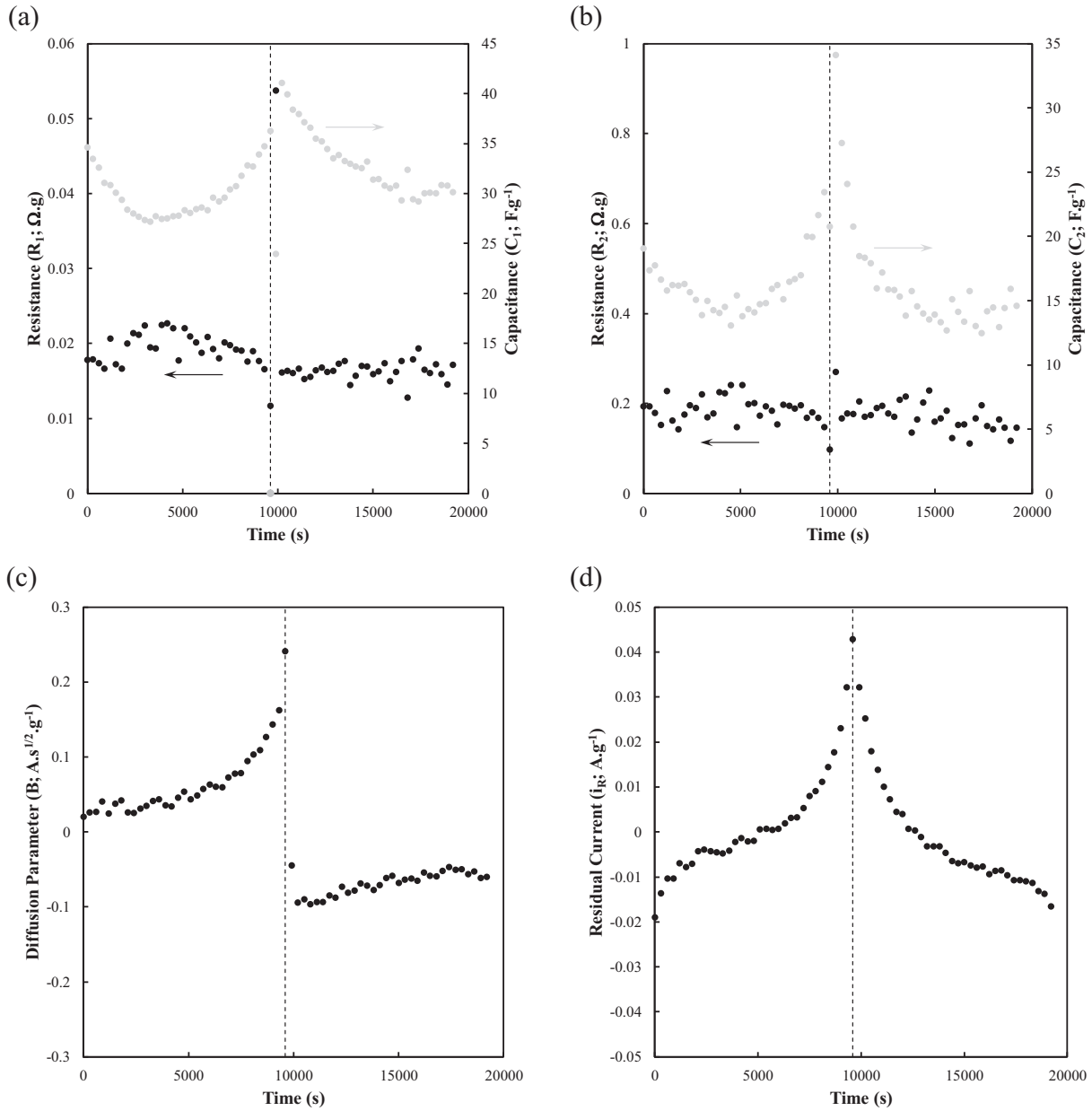

Figure 6. Fitting parameters resulting from the linear least squares analysis of the SPECS data. (a) R_1 and C_1 corresponding to the geometric capacitance; (b) R_2 and C_2 corresponding to the porous capacitance; (c) diffusional parameter (B); and (d) the residual current (i_R).

methodology is inappropriate and would be an overestimate of the true current flowing.

The application of this revised methodology to the residual current is also inappropriate because the link between residual current and the applied potential is a voltammogram in itself. As such, the cumulative nature of the revised methodology would again overestimate the expected current.

Experimental CV and SPECS data.—The CV response of the EMD electrode to different cycling rates is shown in Figure 5a, while Figure 5b shows the raw SPECS data. The analysis of each i-t transient within the SPECS experiment was carried out using linear least squares regression analysis to fit the following expression:

$$i_T = i_{DL1} + i_{DL2} + i_D + i_R = \frac{\Delta E}{R_1}\exp\left(-\frac{t}{R_1C_1}\right) + \frac{\Delta E}{R_2}\exp\left(-\frac{t}{R_2C_2}\right) + \frac{B}{t^{1/2}} + i_R \quad [17]$$

Here i_{DL1} and i_{DL2} are the currents flowing due to double layer formation on the geometric and porous surfaces within the active material, respectively, i_D is the diffusion limited current, and i_R is the residual current, all with units of A.g^{-1}. All other terms have been described previously. Lastly, i_R is the residual current used to account for the non-zero current at the end of the equilibration period (cf. Figure 5b). The fitting parameters arising from the linear least squares regression analysis are shown in Figures 6a–6d.

Demonstration with experimental data.—The overall protocol proposed for analysing SPECS data has been applied to the parameters shown in Figure 6. That is, the revised protocol proposed here for analysing non-faradaic capacitive processes, as well as the existing protocol for diffusive and residual currents. Figures 7a–7c show examples of the ability of the proposed methodology to match to the corresponding experimental CV data. Here three different sweep rates were examined; namely 0.1, 0.01 and 0.001 V.s^{-1}. As can be seen in these figures, at the faster sweep rates the capacitive processes

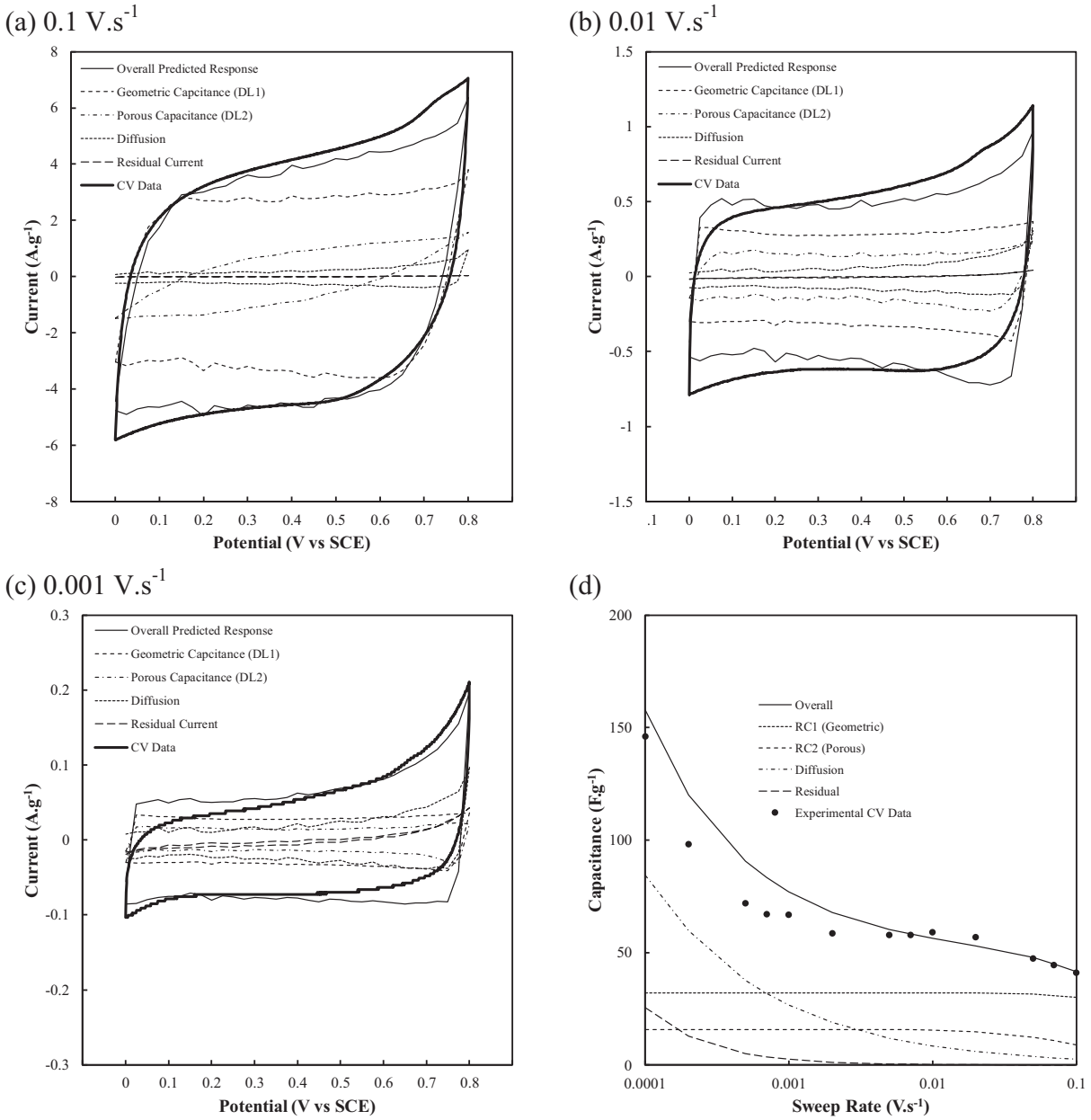

Figure 7. Comparison between experimental voltametric data and that extracted from the revised SPECS analysis methodology for sweep rates of (a) 0.1, (b) 0.01 and (c) 0.001 V.s^{-1}, as well as (d) the specific capacitance versus sweep rate comparison.

dominate the voltametric data, while at slower sweep rates it is the diffusive and residual contributions that contribute the most to the overall capacitance.

The comparison between the experimental CV data and that generated from the SPECS analysis is also very good, indicating that the revised protocol devised here is appropriate. If there was to be a criticism of the comparison it would be that the as the sweep rate decreased, the revised SPECS analysis method slightly overestimated the specific capacitance, particularly just after the reversal of the potential sweep direction. This is emphasized in Figure 7d which compares the specific capacitance of the CV data compared to that predicted from the revised SPECS analysis method. At high sweep rates the comparison is excellent; however, as the diffusional can residual contributions increase the SPECS method overestimates the specific capacitance. This is likely the result of the differences in the independence of the charge storage mechanisms discussed above.

Conclusions

Herewith we describe an improved methodology for the interpretation of step potential electrochemical spectroscopy (SPECS) data. Previous analysis protocols assumed that each i-t transient resulting from a potential step was independent of subsequent transients. While this protocol provided excellent relative information it was unable to reproduce the performance of actual cyclic voltammetry (CV) data on similar electrodes. The revised methodology presented here provides an analysis method that produces performance data much closer to CV data, thus enabling both relative and absolute characterization of electrochemical capacitor electrodes, as well as increasing the versatility of the SPECS analysis method. As a consequence of the development of this methodology the independence of non-faradaic charge storage processes was identified, arising as a result of charge delocalization at the electrode-electrolyte interface. This is in contrast to faradaic

charge storage processes in which each i-t transient contains an in-built dependence on previous transients.

Acknowledgments

The authors acknowledge the University of Newcastle for the provision of a PhD scholarship (MF).

ORCID

Scott W. Donne https://orcid.org/0000-0001-9389-7870

References

1. A. Shukla et al., Electrochemical capacitors: Technical challenges and prognosis for future markets. *Electrochimica Acta*, **84**, 165 (2012).
2. E. Frackowiak and F. Béguin, Carbon materials for the electrochemical storage of energy in capacitors. *Carbon*, **39**(6), 937 (2001).
3. E. T. Mombeshora and V. O. Nyamori, A review on the use of carbon nanostructured materials in electrochemical capacitors. *International Journal of Energy Research*, **39**(15), 1955 (2015).
4. P. Simon and Y. Gogotsi, Materials for electrochemical capacitors. *Nature Materials*, **7**(11), 845 (2008).
5. M. Winter and R. J. Brodd, What are batteries, fuel cells, and supercapacitors? ACS Publications, 2004.
6. B. D. McCloskey, Expanding the Ragone plot: Pushing the limits of energy storage. *ACS Publications*, 2015.
7. G. Lota, et al., Improvement of the structural and chemical properties of a commercial activated carbon for its application in electrochemical capacitors. *Electrochimica Acta*, **53**(5), 2210 (2008).
8. J. R. Miller and A. F. Burke, Electrochemical capacitors: challenges and opportunities for real-world applications. *The Electrochemical Society Interface*, **17**(1), 53 (2008).
9. M. Vangari, T. Pryor, and L. Jiang, Supercapacitors: review of materials and fabrication methods. *Journal of Energy Engineering*, **139**(2), 72 (2012).
10. G. Wang, L. Zhang, and J. Zhang, A review of electrode materials for electrochemical supercapacitors. *Chemical Society Reviews*, **41**(2), 797 (2012).
11. V. V. Obreja, On the performance of supercapacitors with electrodes based on carbon nanotubes and carbon activated material—a review. *Physica E: Low-dimensional Systems and Nanostructures*, **40**(7), 2596 (2008).
12. P. Yang and W. Mai, Flexible solid-state electrochemical supercapacitors. *Nano Energy*, **8**, 274 (2014).
13. X. Lu, G. Li, and Y. Tong, A review of negative electrode materials for electrochemical supercapacitors. *Science China Technological Sciences*, **58**(11), 1799 (2015).
14. Y. Han and L. Dai, Conducting Polymers for Flexible Supercapacitors. *Macromolecular Chemistry and Physics*, **220**(3), 1800355 (2019).
15. M. Zhi, et al., Nanostructured carbon–metal oxide composite electrodes for supercapacitors: a review. *Nanoscale*, **5**(1), 72 (2013).
16. A. Borenstein, et al., Carbon-based composite materials for supercapacitor electrodes: a review. *Journal of Materials Chemistry A*, **5**(25), 12653 (2017).
17. S. Wu, et al., A review of performance optimization of MOF-derived metal oxide as electrode materials for supercapacitors. *International Journal of Energy Research*, **43**(2), 697 (2019).
18. Q. Li, et al., A Review of Supercapacitors Based on Graphene and Redox-Active Organic Materials. *Materials*, **12**(5), 703 (2019).
19. M. Forghani and S. W. Donne, Complications When Differentiating Charge Transfer Processes in Electrochemical Capacitor Materials: Assessment of Cyclic Voltammetry Data. *Journal of The Electrochemical Society*, **166**(8), A1370 (2019).
20. B. E. Conway and Electrochemical Supercapacitors, Scientific Fundamentals and Technological Applications. New York: Kluwer Academic/Plenum Publishers 1999.
21. H. M. Fellows, et al., Modelling voltametric data from electrochemical capacitors. *Journal of Power Sources*, **417**, 193 (2019).
22. Y. Jiang and J. Liu, Definitions of pseudocapacitive materials: a brief review. *Energy & Environmental Materials*, **2**(1), 30 (2019).
23. V. Augustyn, P. Simon, and B. Dunn, Pseudocapacitive oxide materials for high-rate electrochemical energy storage. *Energy & Environmental Science*, **7**(5), 1597 (2014).
24. P. Simon, Y. Gogotsi, and B. Dunn, Where do batteries end and supercapacitors begin? *Science*, **343**(6176), 1210 (2014).
25. A. D. Cross, et al., Active mass analysis on thin films of electrodeposited manganese dioxide for electrochemical capacitors. *Electrochimica Acta*, **87**, 133 (2013).
26. A. Cross, et al., Enhanced manganese dioxide supercapacitor electrodes produced by electrodeposition. *Journal of Power Sources*, **196**(18), 7847 (2011).
27. T. Brousse, D. Bélanger, and J. W. Long, To be or not to be pseudocapacitive? *Journal of The Electrochemical Society*, **162**(5), A5185 (2015).
28. T. Brousse, et al., Crystalline MnO2 as possible alternatives to amorphous compounds in electrochemical supercapacitors. *Journal of The Electrochemical Society*, **153**(12), A2171 (2006).
29. T. Cordero-Lanzac, et al., Role of different nitrogen functionalities on the electrochemical performance of activated carbons. *Carbon*, **126**, 65 (2018).
30. G. Hu, et al., The sol-gel-derived nickel-cobalt oxides with high supercapacitor performances. *Journal of The Electrochemical Society*, **158**(6), A695 (2011).
31. J. Cherusseri, et al., Novel mesoporous electrode materials for symmetric, asymmetric and hybrid supercapacitors. *Nanotechnology*, **30**(20), 202001 (2019).
32. M. Forghani and S. W. Donne, Method comparison for deconvoluting capacitive and pseudo-capacitive contributions to electrochemical capacitor electrode behavior. *Journal of The Electrochemical Society*, **165**(3), A664 (2018).
33. T. C. Liu, et al., Behavior of molybdenum nitrides as materials for electrochemical capacitors comparison with ruthenium oxide. *Journal of the Electrochemical Society*, **145**(6), 1882 (1998).
34. S. Ardizzone, G. Fregonara, and S. Trasatti, "Inner" and "outer" active surface of RuO2 electrodes. *Electrochimica Acta*, **35**(1), 263 (1990).
35. M. F. DuPont and S. W. Donne, A Step Potential Electrochemical Spectroscopy Analysis of Electrochemical Capacitor Electrode Performance. *Electrochimica Acta*, **167**, 268 (2015).
36. M. F. DuPont, et al., Effect of electrolyte cation on the charge storage mechanism of manganese dioxide for electrochemical capacitors. *Electrochimica Acta*, **271**, 337 (2018).
37. Allen J. Bard and L. R. Faulkner, Electrochemical Methodes Fundamentals and Applications SECOND EDITION ed. John Wiley & Sons, 2001.
38. M. F. DuPont and S. W. Donne, faradaic and Non-faradaic Contributions to the Power and Energy Characteristics of Electrolytic Manganese Dioxide for Electrochemical Capacitors. *Journal of The Electrochemical Society*, **163**(6), A888 (2016).
39. M. F. DuPont and S. W. Donne, Separating faradaic and Non-faradaic Charge Storage Contributions in Activated Carbon Electrochemical Capacitors Using Electrochemical Methods: I. Step Potential Electrochemical Spectroscopy. *Journal of the Electrochemical Society*, **162**(7), A1246 (2015).
40. M. F. DuPont and S. W. Donne, Charge storage mechanisms in electrochemical capacitors: Effects of electrode properties on performance. *Journal of Power Sources*, **326**, 613 (2016).
41. M. Forghani and S. W. Donne, Duty Cycle Effects on the Step Potential Electrochemical Spectroscopy (SPECS) Analysis of the Aqueous Manganese Dioxide Electrode. *Journal of The Electrochemical Society*, **165**(3), A593 (2018).
42. M. F. DuPont and S. W. Donne, Separating the faradaic and Non-faradaic Contributions to the Total Capacitance for Different Manganese Dioxide Phases. *Journal of The Electrochemical Society*, **162**(5), A5096 (2015).
43. A. J. Gibson, et al., A synchrotron X-ray powder diffraction and step potential electrochemical spectroscopy study on the change in manganese dioxide capacitive behavior during cycling. *Electrochimica Acta*, **260**, 630 (2018).
44. M. A. Hughes, J. A. Allen, and S. W. Donne, The properties and performance of carbon produced through the electrochemical reduction of molten carbonate: A study based on step potential electrochemical spectroscopy. *Electrochimica Acta*, **278**, 340 (2018).
45. M. F. DuPont and S. W. Donne, Electrolytic Manganese Dioxide Structural and Morphological Effects on Capacitive Performance. *Electrochimica Acta*, **191**, 479 (2016).

Chapter 9: Summary & Conclusions

9.1. Thesis Overview and Key Findings

This thesis has focused on improving and developing the two main electrochemical methods; step potential electrochemical spectroscopy (SPECS) and cyclic voltammetry (CV).

This thesis has presented the development of SPECS method, which has been applied for deconvoluting double layer and diffusion-limited contributions to the performance of an electrochemical capacitor electrode materials such as carbon-based material and metal oxides. The SPECS method is based on applying a series of equal magnitude potential steps on a working electrode, with sufficient rest time to allow for equilibrium to be established for each step throughout an applied potential window. This slow scan rate enables an electrode to approach its maximum charge storage capabilities. More importantly, it allows separation of the charge storage mechanisms, such as electrical double layer charge storage and diffusional processes.

The effect of the two main experimental variables in SPECS; namely, the potential step size and the electrode rest time, on the behaviour of the aqueous manganese dioxide electrode has been described in chapter 5. Generally, the potential step size dictates polarisation at the electrode-electrolyte interface, and hence the driving force for charge storage, while the electrode rest time effects the extent to which the electrode has equilibrated before the subsequent potential step. These experimental variables influence geometric and porous double layer formation, as well as diffusion-limited and residual electrode processes. In this study, a duty cycle of experimental parameters was examined on the EMD electrode, including the potential steps of 10, 25 and 50 mV and equilibration times of 120, 300 and 600 s. The effect of potential step size on the resultant SPECS data arises because of its ability to influence

electrode polarization, and hence the driving force for charge storage in the electrode. Conversely, the rest time between potential steps influences the extent to which the electrode equilibrates before the next step is taken. When combined, these variables essentially influence the rate of electrode cycling, with its corresponding effects on performance.

A comparison between the CV and SPECS methods that can be applied to characterise the different charge storage mechanisms of materials used in electrochemical capacitors was given in Chapter 6. These methods were compared experimentally and also their limitations, and their advantages for interpreting the current data and their abilities to distinguish between the different charge storage mechanisms were discussed. Overall, there was a good agreement between the SPECS and voltammetric current-sweep rate dependence models over the full range of sweep rates. Comparison of the specific capacitances indicates that both models behave similarly, especially at lower sweep rates. However, at higher sweep rates, the SPECS method was better able to characterise the behaviour of the electrical double layer processes at the surface of the electrode. Moreover, the SPECS method could differentiate between different charge storage mechanisms such as via electrical double layer processes at the geometric and porous surface areas, diffusional process and residual process.

Cyclic voltammetry is one of the most common methods for characterising the behaviour of electrochemical devices such as batteries and capacitors. Moreover, The relationship between a voltammetric current and scan rate has been widely used to determine the contribution of different charge storage mechanisms such as via the electrical double layer and diffusion-limited processes. Some of the complications associated with this method such as an electrical double layer capacitance, redox processes in a localized domain, diffusion-limited redox processes, system instabilities modelled using the Butler-Volmer equation, and ohmic processes due to electrode resistance have been explored in chapter 7. It was shown that the electrical double layer is distanced from its optimum capacitance when the time constant is too

large compared to the duration of the experiment, probably due to a large resistance or a high sweep rate. Also, it was indicated that the current response for a redox process in a localised domain and a diffusion controlled redox process, is dependent on sweep rate and the square root of sweep rate, respectively. Finally, significant complications to the modelling which appear due to the electrode instabilities at the extremes of potential and a resistive electrode were described by the Bulter-Volmer equation and ohmic contributions respectively.

Finally, the SPECS method has been revised in chapter 8. In both of the conventional and revised methods, individual i-t transients within the overall SPECS experiment were modelled using a combination of capacitive, diffusion-limited and residual processes. The capacitive processes were further differentiated in terms of geometric and porous processes. This deconvoluted data was then converted into synthetic voltammetric data, from which the specific capacitance for each process was determined as the function of an effective scan rate. However, the revised model is based on this fact that the formation of a double layer on the electrode-electrolyte interface for each subsequent i-t transients in a SPECS experiment are independent of each other. It was presented in this thesis that the revised SPECS methodology can accurately predict synthetic voltammetry data from non-faradaic processes.

9.2. Directions for Further Research

This thesis has developed the most common electrochemical techniques; cyclic voltammetry (CV) and step potential electrochemical spectroscopy (SPECS). These methods have been widely used for deconvoluting different charge storage mechanisms such as electrical double layer processes and diffusion-limited processes in electrochemical energy storage technologies. In this thesis, we have applied CV and SPECS methods to investigate the electrochemical behaviour of some electrode materials in electrochemical capacitors, such as activated carbon and manganese dioxide.

It has already been proven that the SPECS method is a highly effective technique to characterise the electrochemical behaviour of different electrode materials. In this method, the rest time between potential steps allows an electrode to be fully equilibrated and reach its maximum capacity. More importantly, the contribution of the electrical double layer and diffusion-limited processes can be calculated. The SPECS method also provides the contribution of the electrical double layer processes at the geometric as well as porous surface areas based on their time constants.

Thus, one potential research project that could be conducted is utilising the SPECS method to determine the contribution of porous surface areas on overall capacitance and also to obtain relative porosity of electrode materials. Currently, the most common method to find the porosity of electrode materials is obtaining the BET surface area of materials, which is an expensive method, and it is not accurate for all type of materials. Furthermore, the nature of pores might be change during the charging/discharging processes so the same material can have different relative porosity due to different scan rates or various ion sizes. Hence the SPECS method is a strong tool that can be applied in many research areas which aim to characterise the porosity of electrode materials.

The second potential research area that could be investigated is using the developed SPECS and CV methods presented in this thesis to characterise the performance of different electrode materials and different electrolytes.

Developing the engineering design of electrochemical cells is also can be an important research area that needs to be investigated to optimise the performance of electrochemical capacitors. Hence, the modified electrochemical methods presented in this research can be applied to examine the engineering design of electrochemical cells.

APPENDIXES

A. Electroanalytical Characterization of Electrochemical Capacitor Systems

Electroanalytical Characterization of Electrochemical Capacitor Systems

by
Marveh Forghani, Julien McCarthy, Helena Mavroudis and Scott W. Donne*
Discipline of Chemistry, University of Newcastle, Callaghan NSW 2308, Australia

Abstract
Herein we report on an in-situ electroanalytical technique to investigate electrode-electrolyte behaviour during cycling in a conventional symmetrical electrochemical capacitor system based on an activated carbon (AC) electrodes with 1 M tetraethylammonium tetrafluoroborate ($TEABF_4$) in acetonitrile (ACN) as the electrolyte. The electrochemical cell is based on a Swagelok T-junction, with the perpendicular port being used for a Ag/Ag^+ (0.01 M $AgNO_3$ in ACN) reference electrode. Situated between the opposing AC electrodes, between two separators, is a Pt sensing electrode, the potential of which is either monitored or controlled to explore either electrolyte fluxes during cycling, or the formation of soluble species in the electrolyte, respectively. It was deduced that electrolyte ions are strongly associated with the AC electrodes rather than between the electrodes even without an applied potential. Furthermore, aging of the electrochemical system with cycling (cyclic voltammetry) is also explored. Even with identical electrodes it is noted that the individual electrodes behaved differently as a result of anion versus cation association. Finally, at cell voltages approaching 2 V, oxidation of the positive electrode is observed, liberating species into the electrolyte. The implications of these observations have been discussed.

* Communicating author (Scott W. Donne)
P: +61 2 4921 5477; F: +61 2 4921 5472; E: scott.donne@newcastle.edu.au

Keywords: electrochemical capacitors; electroanalytical characterization; activated carbon

1. INTRODUCTION

Electrochemical capacitors are an electrochemical energy storage and conversion technology providing high power density (W/kg) but low energy density (Wh/kg) compared with various battery and fuel cell technologies [1, 2]. Much research has been focused on increasing the energy density of electrochemical capacitors through the development of advanced electrode materials or composites [3-5]. In parallel, several studies have been undertaken to improve electrolyte properties (both organic and aqueous), as well as to introduce potentially next generation solvent-free systems, such as ionic liquids [6, 7].

Of course, a key element of research and development associated with electrochemical capacitors, and indeed any other type of electrochemical energy storage and conversion device, is electrochemical characterization [8]. Most often the reason for electrochemical characterization is to achieve some measure of performance, which is the motivation for a large proportion of studies in this area. The application of these electrochemical methodologies can be used to examine individual material performance, such as in a three-electrode cell, or device performance, such as in a two-electrode cell [9, 10]. Techniques such as cyclic voltammetry (CV) and galvanostatic charge-discharge (GCD) cycling, at a range of different rates, provide an excellent indication of material or device performance [11-15]. An added advantage of these methods is that they can be carried out over extended cycling periods to provide some indication of performance retention and thus stability. Data such as this is expected for publications in the electrochemical capacitor area because of the expectation that these devices provide high power outputs, as indicated by cycling at increasingly faster rates, as well as exhibit excellent cyclability and stability [16-18].

Going beyond a strictly performance measure, electrochemical impedance spectroscopy (EIS) has found widespread application, although the interpretation of results in many cases can be quite limited [19]. EIS is a steady state technique dependent on the reversibility of the electrochemical processes in the small amplitude sinusoidal potential window being considered, typically <0.01 V, providing a snapshot of the electrical response of the electrode or system over a broad range of frequencies [20, 21]. Quite often EIS results are presented for only a limited number of electrode conditions (e.g., states of charge, cycling, etc.), with the results being extrapolated to represent overall electrode behaviour [22].

Floating measurements have been developed to explore the stability of electrodes and systems under extreme conditions. Here the potential of the electrode or system is clamped at an extreme value, typically the anodic potential limit but the cathodic limit can also be used, with the intent of accelerating any degradation reactions that might occur that otherwise would not be evident unless the electrode or system was cycled extensively. Periodically the electrode is cycled to determine the extent of degradation that has occurred [23-26].

For the techniques described thus far the electrochemical output provides little in the way of mechanistic understanding. To address this shortcoming several more sophisticated electrochemical methods have been developed to elucidate the charge storage mechanisms apparent in various electrochemical capacitor systems. Methods based on the analysis of CV data collected at various sweep rates have been used [8, 27-34], as well as the analysis of step potential electrochemical spectroscopy (SPECS) outcomes [35-44].

While these electrochemical methods provide some performance data and mechanistic insight, there is still considerable scope for boosting their intrinsic electroanalytical capabilities. As such, here we report on our efforts at inserting sensing electrodes within the electrochemical cell to produce an in-situ measurement of electrolyte fluxes within the cell, as well as stability measurements focused on the dissolution of electrode materials [45, 46], in particular during cyclic voltammetry experiments.

2. EXPERIMENTAL

2.1. Materials and Electrode Preparation

The electroactive material used here was a homemade activated carbon prepared via a two-

stage pyrolysis and activation process. The first stage involved the pyrolysis of coconut husks (biomass) at 500°C under a N_2 atmosphere for 3 hours. After cooling the resultant char was milled in a zirconia mill (Fritsch Pulverisette 6) to produce a free-flowing powder with a mean particle size of 5-10 μm (Malvern Laser Mastersizer). In the second stage, activation of the char was carried out with the addition of a small volume of concentrated H_3PO_4 (85% in water; Sigma-Aldrich; 1 mL to 20 g of char), with the resultant paste pyrolyzed at 700°C under a N_2 atmosphere for 1 hour. After cooling the activated carbon was washed thoroughly with Milli-Q ultra-pure water (resistivity >18.2 MΩ.cm) until the pH of the filtrate was the same as the wash water. The surface area of this material was determined by N_2 adsorption at 77 K using a Micromeritics ASAP2020 Surface Area and Porosity Analyzer and the linearized BET isotherm. This produced a highly microporous activated carbon with a BET surface area of 1800 $m^2.g^{-1}$.

Electrodes were prepared here from inks. The inks were made from a mixture of homemade activated carbon as the active material, carbon black as a conductive agent (Cabot Vulcan XC72R), and polyvinylidene difluoride (PVdF; Fluka) as a binder with a ratio of 80:15:5. Firstly, these dry ingredients were ground lightly using a ceramic mortar and pestle for ~5 minutes. Then N-methyl-2-pyrrolidinone (NMP; 99+%; Sigma-Aldrich) was added to the dry powdered mixture in a weight ratio of 20:1 (liquid:solid) after which the suspension was stirred magnetically for 30 min to obtain a homogenized ink. Substrates were 13 mm diameter stainless steel rods, for which the ends had been polished with 1200 grit emery paper and subsequently washed with Milli-Q water before use. 50 μL of the ink was drop cast onto the polished substrate end. The electrodes were then allowed to dry in air at 60°C. This led to an electrode loading of active material of 2.5 $mg.cm^{-2}$. The intent here was to produce a symmetrical electrochemical device so all efforts were made to ensure that electrodes were identical.

2.2. Electrochemical Cell

The electrochemical cell was based on a 13 mm diameter perfluoroalkoxyalkane (PFA) T-junction Swagelok cell. The Pt mesh which was used as the indicator or sensing electrode (GoodFellow; 99.9%; 0.12 mm nominal aperture and 0.04 mm wire diameter) was cut to make a rectangular electrode with dimensions of 5 mm × 50 mm. The aperture and wire dimensions where chosen to make the total area coverage by the sensing electrode as small as possible. The dried negative electrode made previously was inserted into the middle of the Swagelok cell and covered with one layer of porous separator (Celgard 2400). The Pt sensing electrode was inserted into the perpendicular port of the Swagelok cell and placed over the separator which was then covered with another layer of separator. This was followed by inserting the positive electrode into the opposite end of the Swagelok cell. Under these conditions the Pt sensing electrode was sandwiched between two layers of separator and positive and negative electrodes. The area of the sensing electrode between the positive and negative electrodes was 5 mm × 10 mm. Given the Pt wire dimensions and the aperture size of the mesh, the presence of the mesh represents an ~21% coverage. The electrodes were pressed at 1.7 MPa using a hydraulic press and secured in place while under load. The cell then was transferred to an Ar-filled glove box after which it was filled with a 1 M tetraethylammonium tetrafluoroborate ($TEABF_4$; >99%; Sigma-Aldrich) in acetonitrile (ACN; 99.8%; Sigma-Aldrich) electrolyte solution. A Ag/Ag^+ reference electrode (0.01 M $AgNO_3$ in ACN) was then inserted into the perpendicular port of the Swagelok cell, together with another Pt mesh (5 mm × 40 mm in the electrolyte). This design enabled a much larger counter electrode area compared to the sensing electrode. Schematics of the electrochemical cell are shown in Figures 1(a) and (b). All joints were sealed in the glovebox using Parafilm. The electrochemical cell was then left in the glovebox to equilibrate overnight (18 hours). After this it was removing it from the glove box and placed in a test container under a flowing (200 $mL.min^{-1}$) dry N_2 atmosphere.

2.3. Electrochemical Protocol

A multichannel VMP Potentiostat/Galvanostat supplied by Perkin Elmer Instruments, and controlled by EC-Lab v6.80 software, was used to run the experiments. This system was used because

of its ability to synchronize channels. It is important to note here that the electrochemical cell was controlled primarily as a symmetrical two-electrode cell.

For the purposes of this report characterization of the device was by cyclic voltammetry (CV) between 0.0-2.0 V for 300 cycles at a scan rate of 0.025 $V.s^{-1}$. At the same time as the CV experiment was being carried out, using separate channels on the potentiostat, the potential of both the positive and negative electrodes were measured with respect to the Ag/Ag^{+} reference electrode, as shown schematically in Figures 1(c) and (d). This allowed for measurement of individual electrode potentials to determine their extent of polarization while the full cell was under load. Additionally, in one type of experiment the potential of the Pt sensing electrode sandwiched between the positive and negative electrodes was measured with respect to the reference electrode (Figure 1(c)), while in another type of experiment the potential of the Pt sensing electrode was fixed at specific values relative to the reference electrode and the current flow recorded during the CV experiment (Figure 1(d)). These in-situ techniques enable observation of electrolyte fluxes through the electrochemical cell during charging and discharging processes, as well as any dissolution occurring from the electrodes.

3. RESULTS AND DISCUSSION

3.1. Performance

A typical cyclic voltammogram of this electrode system is shown in Figure 2. It has the box-like appearance expected of an activated carbon-based electrode system in the electrolyte used here. Charge storage in this case is via the formation of an electrical double layer at the electrode-electrolyte interface on both the geometric (or external) surface of the activated carbon particles, as well as on the porous surfaces that electrolyte can access in the interior of the particles. For reasons that will become apparent in the next section, the current has not been normalized to consider the mass of electroactive material. The charge passed during each half cycle (Q; C) was determined using:

$$Q = \frac{1}{v}\int_{E_i}^{E_f} IdE \qquad \ldots(1)$$

where v is the sweep rate ($V.s^{-1}$), E_i and E_f are the initial and final voltages (V), respectively, and I is the absolute current (A). The capacitance (C; F) was then determined using:

$$C = \frac{Q}{\Delta V} \qquad \ldots(2)$$

where ΔV ($= E_f - E_i$) is the voltage window used (V). In this case the plateau cathodic capacitance decreased quite quickly initially but by 300 cycles had stabilized at ~0.095 F, with a coulombic efficiency (A:C) of 100.3%, as shown inset in Figure 2.

3.2. Individual Electrode Behaviour

With the cell controlled as a two-electrode device by one channel on the potentiostat, other synchronized channels were used to measure the potential of the individual electrodes relative to the reference electrode according to the configurations shown in Figures 1(c) and (d). Figure 3(a) shows the change in individual electrode potential with time during a full cycle, together with the overall cell voltage. The example here is for cycle 300, the last cycle in the series. Also shown as dashed lines in Figure 3(a) are the expected changes in potential if the overall cell voltage was split evenly between both electrodes; i.e., 1.000 V each. Clearly this is not the case, with the positive electrode having a larger potential window (1.079 V) compared to the negative electrode (0.921 V). The implication here is that anion (BF_4^{-}) adsorption and/or cation (TEA^{+}) desorption from the positive electrode requires greater polarization to carry the same charge as the opposite processes on the negative electrode.

What is also apparent from Figure 3(a) is that while the change in voltage on the overall cell is linear, the change in potential of the individual electrodes is not linear. To demonstrate this, Figure 3(b) shows the instantaneous change in potential (sweep rate) for both the positive and negative electrodes. Also shown in this figure as dashed lines are the expected sweep rates for the individual

electrodes (±0.0125 $V.s^{-1}$), which when combined match the voltage sweep rate applied to the overall device (0.025 $V.s^{-1}$). Consistent with Figure 3(a) is the fact that the sweep rate is incrementally larger on the positive electrode. Upon sweep reversal the same phenomena limit charge storage, although in this case on the opposite electrode.

Combining the individual electrode potentials with the overall current flowing through the cell allows us to generate individual electrode voltammograms, as shown in Figure 3(c). Note there that with a focus on individual electrode behaviour the current has been normalized with respect to the amount of electroactive material on each electrode. In this figure it is again clear that the potential window of the positive electrode is larger than the negative electrode. Of course, since the same current is flowing through both electrodes it must mean that the charge passed through both electrodes is also the same. Figure 3(d) shows the charge passed through each electrode, calculated using Eqn (9), as a function of overall cell voltage. The hysteresis between the positive and negative voltage half cycles for both electrodes arises as a result of electrode resistance. The capacitance of each electrode can then be determined using Eqn (10), except with specific current, giving rise to positive and negative electrode capacitances (C_+ and C_-, respectively) of 69.6 $F.g^{-1}$ and 81.7 $F.g^{-1}$, with the differences arising as a result of the different potential windows. Overall device capacitance (C_T) can be determined using:

$$\frac{1}{C_T} = \frac{1}{C_+} + \frac{1}{C_-} \qquad \ldots(3)$$

which in this case was 37.6 $F.g^{-1}$. The capacitance here is of course dominated by the electrode with the smaller capacitance. If the capacitance of the full cell was calculated using the total electroactive mass then the capacitance would be 18.7 $F.g^{-1}$. The reason for this difference is that in the calculation of device capacitance leading up to the use of Eqn (3), the total current flow through the device has been used twice; i.e., once each for the determination of the positive and negative electrode capacitances. Nonetheless, the approach used here quite clearly indicates individual electrode behaviour, rather than just device behaviour.

Changes in positive and negative electrode potential windows, together with the individual cathodic and anodic limits for each electrode, are shown in Figures 4(a) and (b), respectively. This is perhaps a measure of the stability of the electrode because changes in these potentials indicate changes in the composition of the electrode-electrolyte interface. The potential window for the positive electrode was shown to be increasing with cycling, indicating that the adsorption of anions and/or the desorption of cations is getting progressively worse with cycling. While the anodic and cathodic limits of this process show essentially the same behaviour; i.e., a slight drop after the first few cycles, followed by a gradual increase, it is the anodic limit that is increasing faster causing the larger positive electrode potential window. Conversely, the potential window of the negative electrode is decreasing with cycle number, due primarily to the cathodic limit changing the most. These observations are not surprising since the anodic limit on the positive electrode and the cathodic limit on the negative electrode are the potentials where the overall cell is at its maximum polarization.

The effects of cycling on individual electrode performance are shown in Figure 5. Figure 5(a) shows selected cycles for both the positive and negative electrodes, with the arrows indicating a decreasing current with increasing cycle number. This is consistent with the decreasing specific capacitance for each electrode shown in Figure 5(b). This figure again emphasizes the effect that voltage window has on individual electrode capacitance.

3.3. Electrolyte Fluxes

With the placement of a Pt mesh sensing electrode between the separator papers in the electrochemical cell we have enabled what is effectively and in-situ measurement of electrolyte flux between the electrodes. Based on the configuration shown schematically in Figure 1(c), we can measure independently the open circuit potential of the Pt mesh as a function of the overall cell voltage. The first point to be addressed relates to what is being assessed by the open circuit potential measurement.

Logically the first thing considered is the concentration of the electrolyte. As shown in Figure 6(a), changing the concentration of the $TEABF_4$ electrolyte in ACN changes the potential. In the confines of an Ar-filled glove box the Pt mesh was immersed in the electrolyte under study and the open circuit potential with respect to the Ag/Ag^+ reference electrode was measured over the course of 1 hour. The average potential was determined and then plotted versus $TEABF_4$ concentration. These measurements were conducted in triplicate giving rise to the vertical error bars shown in Figure 6(a). The slope of this plot is negative, at -0.038 $V.decade^{-1}$, indicating that the BF_4^- anion is potential determining. In general, cation ion selective electrodes have a positive slope in a potential versus log(concentration) plot, whereas anionic ion selective electrodes have a negative slope. As some examples, consider the responses shown in a Pourbaix diagram (E_h vs pH ($-\log([H^+])$) where the H^+ is potential determining, and a Ca^{2+} ion selective electrode, both of which have positive slopes, compared to a F^- ion selective electrode, which has a negative slope [47]. For a monovalent potential determining anion the slope is expected to be Nernstian; i.e., -0.059 $V.decade^{-1}$ [48]; however the deviation here may be the result of cation influence. Certainly, another contributor to this deviation from expected behaviour is the junction potential difference between the reference electrode and the electrolyte in the cell [9]. Since experiments were conducted under isothermal conditions this junction potential difference cannot be determined. Nevertheless, it is a good indicator of electrolyte concentration changes, even though it contains contributions from both electrolyte concentration changes and the junction potential difference.

Another possible contributor to the measured potential is the difference in mobility of the TEA^+ and BF_4^- ions leading to an imbalance in the number of cationic versus anionic charge carriers in the vicinity of the Pt mesh. Tyunina et al. have reported the limiting ionic conductivity (λ; $S.m^2.mol^{-1}$) of TEA^+ and BF_4^- in propylene carbonate to be 13.2×10^{-4} $S.m^2.mol^{-1}$ and 20.2×10^{-4} $S.m^2.mol^{-1}$, respectively. Thus the ionic mobility of TEA^+ is 1.37×10^{-8} $m^2.s^{-1}.V^{-1}$ and BF_4^- is 2.09×10^{-8} $m^2.s^{-1}.V^{-1}$ in this solvent [49]. While we have used ACN here, similar trends in mobility are expected. The potential difference arising from this mismatch is also Nernstian in behaviour, with an order of magnitude difference in charge carriers leading to a 0.059 V change in potential. This phenomenon can arise as a result of the electric field established between the opposing electrodes causing migration of ions to the oppositely charged electrode.

The final possible contributor to the potential of the Pt mesh sensing electrode are oxidized or reduced species formed as a result of redox reactions on the activated carbon surface at the extremes of cell voltage, although likely at high cell voltage [37]. Under these latter circumstances oxidized species could be evolved on the positive electrode, or reduced species could be evolved on the negative electrode that will change the potential of the electrolyte. Of course, oxidized species would increase the Pt electrode potential, while reduced species would lower the potential. The formation of these species is an indication of electrode-electrolyte instability under the applied conditions, reflecting the occurrence of a redox process that may or may not be reversible. Electrical double layer formation on activated carbon in a non-aqueous electrolyte involves physical charge separation, which is a highly reversible process. Redox processes are less reversible and as such their occurrence can give rise to poor coulombic efficiencies. Even a slight deviation in coulombic efficiency in one cycle is magnified over the course of extended cycling, which is expected for electrochemical capacitor systems. In addition, any level of irreversibility associated with such processes causes the consumption of material, which again after extended cycling, can lead to cell failure. While this characteristic of cell behaviour is important, it is likely best examined using a fixed potential sensing electrode, as will be discussed in the next section.

Over the course of the CV experiments the potential of the Pt mesh was monitored continuously, as shown in Figure 6(b). The first thing to note here is that the potential of the Pt mesh during cycling is much greater than the measurements made during calibration. The implication here is that the bulk of the electrolyte is depleted of electrolyte ions, in preference for them being associated with the highly porous activated carbon electrodes. This has implications on device conductivity because with a depleted electrolyte its resistance is much higher, which would in turn affect overall device performance.

While the data over the duration of the cyclic voltammetry experiments is not that informative, the zoomed in example inset in Figure 6(b) shows clearly that there are systematic changes in the Pt mesh potential with cycling. Figure 6(c) shows an example (cycle 300, the last cycle) of how the Pt mesh sensing electrode potential changes with overall cell voltage, together with the corresponding cell current. Starting at 0 V and applying an anodic voltage sweep to the cell, the potential of the Pt sensing electrode decreases initially suggesting that the electrolyte concentration is increasing. This is inconsistent with the charging process in that ions from the electrolyte are expected to be adsorbing onto their respective electrodes. At ~1.0 V the sensing electrode potential goes through a minimum, after which it increases linearly up to the anodic vertex potential, and beyond, reaching a maximum at ~1.75 V during the cathodic sweep. This increase in sensing electrode potential is consistent with the charging process because ions are migrating towards and adsorbing onto their respective electrodes. At lower cell voltages the Pt sensing electrode continues to decrease, which is again consistent with expected behaviour; i.e., ion desorption and migration into the bulk electrolyte.

A general characteristic of the example in Figure 6(c) is the apparent hysteresis loop between the anodic and cathodic voltage sweeps, demonstrating a mismatch between the electrochemical response of the cell and the sensing of electrolyte species. This was surprising given the proximity of the sensing electrode with the electrodes themselves. The separator paper used here is ~20 μm thick and porous, and together with the fact that the electrodes are pressed together means that the Pt mesh should provide essentially an in-situ measure of electrolyte speciation, particularly under the electric field between the electrodes. Ideally, with no interaction between the electrolyte ions and the activated carbon, and infinitely fast ion mobility in the electrolyte, the potential of the sensing electrode should be linear for an electrochemical capacitor, matching the charge added or removed from the electrodes, as shown in Figure 3(d). In fact, the hysteresis observed in Figure 3(d) was ascribed to resistance within the cell, so indeed the hysteresis within the electrolyte would suggest that ionic mobility contributes substantially to the resistance. The hysteresis in sensing electrode potential is also asymmetric, particularly at low potentials, unlike the electrode charging profile in Figure 3(d), suggesting that there is considerable electrolyte association with the activated carbon even in the absence of the electric field during cell cycling. This is well supported by the fact that activated carbon is already used extensively as a medium for ion adsorption, as well as the observed increase in sensing electrode potential from the calibration solutions to the in-situ sensing potentials mentioned above.

This technique of measuring the potential of an in-situ sensing electrode can also be used to examine the aging of an electrode or device. Figure 6(d) shows the potential of the Pt sensing electrode as a function of cell voltage for selected cycles. Here the overall potential tends to increase with cycling, suggesting that the electrolyte concentration is decreasing, perhaps as a result of electrolyte ions being progressively scavenged by the activated carbon electrodes. In general, the appearance of the data for each cycle is similar, although the hysteresis between the anodic and cathodic sweeps tends to grow as cycling proceeds. This is clarified in Figure 6(e) in which the sensing electrode potential is adjusted to the same starting point and plotted as a change in potential. Figure 6(f) provides another view of the sensing electrode potential, this time at selected potentials in both the anodic and cathodic sweep, as well as at the anodic vertex potential. Overall, the suggestion from this data is that the activated carbon electrodes adsorb a considerable amount of electrolyte, leaving behind an electrolyte void that can have an impact on device performance via a decrease in conductivity.

3.4. Potentiostatic Sensing Electrode Control

While monitoring the open circuit potential of the Pt sensing electrode can be informative regarding electrolyte fluxes, it is complicated by the origin of the potential fluctuations. As discussed previously, these changes in potential can be due to electrolyte concentration changes, junction potential differences, different mobilities of the cations versus anions, as well as the presence of redox active species evolved from the electrode, the latter of which is of particular interest regarding the stability of the electrode system. Experiments have also been conducted whereby the potential of the Pt mesh sensing electrode was fixed relative to the Ag/Ag^+ reference electrode using the configuration

shown in Figure 1(d). Note that for these experiments an additional Pt wire counter electrode was also included in the cell to act as the source or sink of charge for the sensing electrode.

A significant variable regarding this type of experiment is the potential to apply to the Pt sensing electrode. The intent with this type of experiment is to sense the formation of species generated from either of the electrodes during electrochemical cycling, the point being that anything that was electrochemically generated in the cell could be reversibly detected on the sensing electrode. For instance, choosing a relatively anodic potential for the sensing electrode would allow for a focus on the negative electrode since any cathodic processes occurring here that evolved soluble species could be detected as a result of their re-oxidation on the sensing electrode. Conversely, selecting a relatively cathodic potential would allow for characterization of species evolved on the positive electrode. In this series of experiments potentials of +0.5 V and -0.5 V versus the Ag/Ag^+ reference electrode were selected because they lie within the potential window of the positive or negative electrode, respectively, as seen in Figure 3(c).

Figure 7(a) shows some selected outcomes from the sensing electrode with the application of +0.5 V versus the Ag/Ag^+ reference electrode. Presented here is the voltametric data from cycles 25 and 300, together with the corresponding sensing electrode current. The first point to note about the sensing electrode data shown in this figure is that the current is always anodic, suggesting an underlying oxidation occurring at the sensing electrode. The origin of this anodic current may arise from an impurity in the electrolyte, the most logical choice of which is water. However, given the potential of the Ag/Ag^+ (0.01 M) reference electrode (0.682 V vs SHE), coupled with the potential applied to the sensing electrode (+0.5 V), the resultant sensing electrode potential (1.182 V vs SHE) is not high enough to oxidize water, thus ruling it out as an option. Other possible impurities may enter the cell via the ACN solvent. It has been reported [50] that impurities present in the ACN can include acrylonitrile, α(β)-methacrylonitrile, cis/trans butenenitrile, acetaldehyde, acetone, methanol, ethylcyanide, acrolein, allylalcohol, propenoic acid, oxazol and acetic acid, at least some of which are expected to be redox active at the potential of the sensing electrode. In a similar way, impurities in the $TEABF_4$ could also contribute to the sensing electrode current. For both the electrolyte and solvent, though, the purity of species being used would suggest that this was a low possibility, particularly so since no specific redox processes associated with these potential impurities were observed in the overall voltametric response of the device. Gas impurities can also be ruled out because of cell construction in the Ar-filled glove box. Anyway, the only redox active gas possibly in contact with the cell is oxygen, which would be redox active, although as a reduction to give a cathodic current, which was not observed. In the absence of contributions from impurities, the anodic background current must be arising from the activated carbon electrodes.

During early cycling, as represented by cycle 25 in Figure 7(a), there is very little change in the sensing electrode current over the course of a full cycle. There is a slight dip in anodic current at the upper vertex potential (2.0 V) due to some species in the cell being reduced on the sensing electrode. In the voltametric data there is a slight increase in anodic current at 2.0 V suggesting that this process causes the formation of a species in the electrolyte that is correspondingly reduced on the sensing electrode. This process is exacerbated after 300 cycles, which shows a considerable decrease in the current due to a reduction process occurring on the sensing electrode. Changes in the sensing electrode current are shown for selected cell voltages during the anodic half cycle in Figure 7(b). The corresponding data for the cathodic sweep is not shown because of the symmetrical response of the sensing electrode (Figure 7(a)). Up to cycle 150 the response of the sensing electrode was quite similar irrespective of the cell voltage. However, beyond this cycle considerable divergence was observed, becoming much more reducing on the sensing electrode when high cell voltages were used.

A similar experiment was carried out with the sensing electrode potential set at -0.5 V versus the Ag/Ag^+ reference electrode, the response for which is shown in Figure 7(c). Here the sensing electrode current is overall much closer to zero suggesting that there are no background redox processes occurring. In cycle 25 there appears a cathodic spike in the current when the cell voltage approaches the upper limit (2.0 V). Just like in the previous case with a sensing electrode potential of +0.5 V, the positive electrode is apparently evolving an oxidized species that is subsequently reduced

on the sensing electrode. As cycling continues this sensing electrode current is dissipated to the point that by cycle 300 there is very little change in the sensing electrode current across the full cell voltage window. This suggests that the species causing the cathodic spike in current were irreversibly removed from the electrodes during the initial cycles. This is demonstrated further in Figure 7(d) which shows the sensing electrode current at selected cell voltages during the anodic half cycle as a function of cycle number. Here the sensing electrode current tends towards zero as cycling continues.

As a final discussion point it must be mentioned that while these experiments have shown the formation of soluble intermediates from the activated carbon electrodes used here, particularly at high cell voltages, they in no way identify what these species are. That type of experiment would require the use of more analytical tools to identify the nature of these species, which is beyond the scope of the present work. There is literature to suggest that these species could be gaseous in nature [51], or perhaps fragments of the activated carbon electrode surface oxidized into solution [37, 41]. Nevertheless, what has been demonstrated here is the impact that these processes have on overall cell efficiency. With species being evolved from the electrodes at high cell voltages there is an increased likelihood that they can be lost to the electrolyte leading to a decrease in overall coulombic efficiency. It is likely that this behaviour will change with the use of different electrode materials, making this electroanalytical method very relevant for both electrode and device characterization.

4. SUMMARY AND CONCLUSIONS

Here we report on an advanced electroanalytical technique to boost the information that can be extracted from a CV experiment. With the inclusion of a Ag/Ag^+ reference electrode and a Pt sensing electrode located intimately between the positive and negative electrodes of an electrochemical capacitor device, together with a number of synchronized channels from a multichannel potentiostat, we have developed an innovative approach to the in-situ electrochemical characterization of the activated carbon and electrolyte within such a device. Specific outcomes from the study include:

(i) While controlling the system as a two-electrode device, the potential of the individual electrodes has been measured versus the reference electrode. This has demonstrated that anion and cation association with the activated carbon electrodes is not identical, with greater electrode polarization required on the positive electrode to accommodate device charge. The conclusion deduced from this is that a symmetrical device, with similar mass loadings, does not lead to optimal performance. This approach was also utilized to explore electrode aging with cycling, possibly hinting at failure mechanisms within the device.

(ii) With the inclusion of a Pt sensing electrode positioned intimately between the positive and negative electrodes in the device, electrolyte fluxes have been measured as a function of cell voltage and cycle number. Here the open circuit potential of the Pt sensing electrode was monitored, showing systematic changes within an individual cycle. Factors contributing to these changes in potential were discussed, primarily in terms of changes in electrolyte concentration and the formation of soluble species from the electrodes, as well as in terms of junction potential differences and the differences in mobility between the cations and anions in the electrolyte. The main conclusions reached here were that electrolyte ions associate strongly with the activated carbon electrodes, decreasing the electrolyte concentration between electrodes considerably. This has the potential to affect cell resistance, particularly in an electrolyte starved cell.

(iii) In a separate where the potential of the Pt sensing electrode was fixed, it was demonstrated that there is considerable dissolution from the activated carbon electrodes at high potentials. This has considerable implications on the efficiency of these devices because with electrode dissolution there is a higher probability of losing charge to the electrolyte, thus decreasing coulombic efficiency.

5. ACKNOWLEDGEMENTS

MF acknowledges the University of Newcastle for the provision of a PhD scholarship to undertake this research project.

6. REFERENCES

[1] Simon, P., Y. Gogotsi, and B. Dunn, *Where do batteries end and supercapacitors begin?* Science, 2014. **343**(6176): p. 1210-1211.

[2] Dunn, B., H. Kamath, and J.-M. Tarascon, *Electrical energy storage for the grid: a battery of choices.* Science, 2011. **334**(6058): p. 928-935.

[3] Simon, P. and Y. Gogotsi, *Materials for electrochemical capacitors.* Nature materials, 2008. **7**(11): p. 845-854.

[4] Zhi, M., et al., *Nanostructured carbon–metal oxide composite electrodes for supercapacitors: a review.* Nanoscale, 2013. **5**(1): p. 72-88.

[5] Borenstein, A., et al., *Carbon-based composite materials for supercapacitor electrodes: a review.* Journal of Materials Chemistry A, 2017. **5**(25): p. 12653-12672.

[6] Fic, K., et al., *Novel insight into neutral medium as electrolyte for high-voltage supercapacitors.* Energy & Environmental Science, 2012. **5**(2): p. 5842-5850.

[7] Lewandowski, A., et al., *Performance of carbon–carbon supercapacitors based on organic, aqueous and ionic liquid electrolytes.* Journal of Power Sources, 2010. **195**(17): p. 5814-5819.

[8] Forghani, M. and S.W. Donne, *Method comparison for deconvoluting capacitive and pseudo-capacitive contributions to electrochemical capacitor electrode behavior.* Journal of The Electrochemical Society, 2018. **165**(3): p. A664-A673.

[9] Allen J. Bard and L.R. Faulkner, *Electrochemical Methodes : Fundamentals and Applications* SECOND EDITION ed. 2001: John Wiley & Sons.

[10] B.E. Conway, *Electrochemical Supercapacitors. Scientific Fundamentals and Technological Applications*. 1999, New York: Kluwer Academic/Plenum Publishers.

[11] Fellows, H.M., et al., *Modelling voltametric data from electrochemical capacitors.* Journal of Power Sources, 2019. **417**: p. 193-206.

[12] Forghani, M. and S.W. Donne, *Complications When Differentiating Charge Transfer Processes in Electrochemical Capacitor Materials: Assessment of Cyclic Voltammetry Data.* Journal of The Electrochemical Society, 2019. **166**(8): p. A1370-A1379.

[13] Kulkarni, S.B., et al., *High-performance supercapacitor electrode based on a polyaniline nanofibers/3D graphene framework as an efficient charge transporter.* Journal of Materials Chemistry A, 2014. **2**(14): p. 4989-4998.

[14] Wee, G., et al., *Printable photo-supercapacitor using single-walled carbon nanotubes.* Energy & Environmental Science, 2011. **4**(2): p. 413-416.

[15] Mai, L.-Q., et al., *Synergistic interaction between redox-active electrolyte and binder-free functionalized carbon for ultrahigh supercapacitor performance.* Nature communications, 2013. **4**: p. 2923.

[16] González, A., et al., *Review on supercapacitors: technologies and materials.* Renewable and Sustainable Energy Reviews, 2016. **58**: p. 1189-1206.

[17] Rahman, M.A.A. and M.K. Rahmat. *Performance Review on Small-Medium Scales Energy Storage System in term of Investment Aspect*. in *2018 IEEE 7th International Conference on Power and Energy (PECon)*. 2018. IEEE.

[18] Faraji, S. and F.N. Ani, *The development supercapacitor from activated carbon by electroless plating—A review.* Renewable and Sustainable Energy Reviews, 2015. **42**: p. 823-834.

[19] Ragoisha, G. and Y. Aniskevich, *False capacitance of supercapacitors.* arXiv preprint arXiv:1604.08154, 2016.

[20] Zou, C., et al., *A review of fractional-order techniques applied to lithium-ion batteries, lead-acid batteries, and supercapacitors.* Journal of Power Sources, 2018. **390**: p. 286-296.

[21] Dupont, M.F., A.F. Hollenkamp, and S.W. Donne, *Large Amplitude Electrochemical Impedance Spectroscopy for Characterizing the Performance of Electrochemical Capacitors.* Journal of The Electrochemical Society, 2014. **161**(4): p. A648-A656.

[22] Tesfaye, A.T., et al., *The electrochemical behavior of SnSb as an anode for Li-ion batteries studied by electrochemical impedance spectroscopy and electron microscopy.* Electrochimica Acta, 2017. **256**: p. 155-161.
[23] Piwek, J., et al., *Carbon-based electrochemical capacitors with acetate aqueous electrolytes.* Electrochimica Acta, 2016. **215**: p. 179-186.
[24] Weingarth, D., A. Foelske-Schmitz, and R. Kötz, *Cycle versus voltage hold–Which is the better stability test for electrochemical double layer capacitors?* Journal of Power Sources, 2013. **225**: p. 84-88.
[25] Ratajczak, P., et al., *Effect of accelerated ageing on the performance of high voltage carbon/carbon electrochemical capacitors in salt aqueous electrolyte.* Electrochimica Acta, 2014. **130**: p. 344-350.
[26] Yang, T., et al., *Lithium bisoxalatodifluorophosphate (LiBODFP) as a multifunctional electrolyte additive for 5 V LiNi 0.5 Mn 1.5 O 4-based lithium-ion batteries with enhanced electrochemical performance.* Journal of Materials Chemistry A, 2019. **7**(14): p. 8292-8301.
[27] Ardizzone, S., G. Fregonara, and S. Trasatti, *"Inner" and "outer" active surface of RuO2 electrodes.* Electrochimica Acta, 1990. **35**(1): p. 263-267.
[28] Baronetto, D., N. Krstajić, and S. Trasatti, *Reply to "note on a method to interrelate inner and outer electrode areas" by H. Vogt.* Electrochimica acta, 1994. **39**(16): p. 2359-2362.
[29] Augustyn, V., P. Simon, and B. Dunn, *Pseudocapacitive oxide materials for high-rate electrochemical energy storage.* Energy & Environmental Science, 2014. **7**(5): p. 1597-1614.
[30] Vogt, H., *Note on a method to interrelate inner and outer electrode areas.* Electrochimica acta, 1994. **39**(13): p. 1981-1983.
[31] Bandaru, P., et al., *Charge transfer and storage in nanostructures.* Materials Science and Engineering: R: Reports, 2015. **96**: p. 1-69.
[32] Liu, T.C., et al., *Behavior of molybdenum nitrides as materials for electrochemical capacitors comparison with ruthenium oxide.* Journal of the Electrochemical Society, 1998. **145**(6): p. 1882-1888.
[33] Ranjusha, R., et al., *Fabrication and performance evaluation of button cell supercapacitors based on MnO 2 nanowire/carbon nanobead electrodes.* RSC Advances, 2013. **3**(38): p. 17492-17499.
[34] Augustyn, V., et al., *Lithium-ion storage properties of titanium oxide nanosheets.* Materials Horizons, 2014. **1**(2): p. 219-223.
[35] Dupont, M.F., et al., *Effect of electrolyte cation on the charge storage mechanism of manganese dioxide for electrochemical capacitors.* Electrochimica Acta, 2018. **271**: p. 337-350.
[36] Dupont, M.F. and S.W. Donne, *A Step Potential Electrochemical Spectroscopy Analysis of Electrochemical Capacitor Electrode Performance.* Electrochimica Acta, 2015. **167**: p. 268-277.
[37] Dupont, M.F. and S.W. Donne, *Separating Faradaic and Non-Faradaic Charge Storage Contributions in Activated Carbon Electrochemical Capacitors Using Electrochemical Methods: I. Step Potential Electrochemical Spectroscopy.* Journal of the Electrochemical Society, 2015. **162**(7): p. A1246-A1254.
[38] Dupont, M.F. and S.W. Donne, *Separating the Faradaic and Non-Faradaic Contributions to the Total Capacitance for Different Manganese Dioxide Phases.* Journal of The Electrochemical Society, 2015. **162**(5): p. A5096-A5105.
[39] Dupont, M.F. and S.W. Donne, *Faradaic and Non-Faradaic Contributions to the Power and Energy Characteristics of Electrolytic Manganese Dioxide for Electrochemical Capacitors.* Journal of The Electrochemical Society, 2016. **163**(6): p. A888-A897.
[40] Dupont, M.F. and S.W. Donne, *Electrolytic Manganese Dioxide Structural and Morphological Effects on Capacitive Performance.* Electrochimica Acta, 2016. **191**: p. 479-490.

[41] Dupont, M.F. and S.W. Donne, *Charge storage mechanisms in electrochemical capacitors: Effects of electrode properties on performance.* Journal of Power Sources, 2016. **326**: p. 613-623.
[42] Forghani, M. and S.W. Donne, *Duty Cycle Effects on the Step Potential Electrochemical Spectroscopy (SPECS) Analysis of the Aqueous Manganese Dioxide Electrode.* Journal of The Electrochemical Society, 2018. **165**(3): p. A593-A602.
[43] Abbas, S.A., et al., *Carbon Hollow Spheres as Electrochemical Capacitors: Mechanistic Insights.* Energy Storage Materials, 2019.
[44] Malifarge, S., B. Delobel, and C. Delacourt, *Guidelines for the Analysis of Data from the Potentiostatic Intermittent Titration Technique on Battery Electrodes.* Journal of The Electrochemical Society, 2017. **164**(14): p. A3925-A3932.
[45] Donne, S.W., G.A. Lawrance, and D.A. Swinkels, *Redox processes at the manganese dioxide electrode III. Detection of soluble and solid intermediates during reduction.* Journal of The Electrochemical Society, 1997. **144**(9): p. 2961-2967.
[46] Bailey, M.R. and S.W. Donne, *Detection of Soluble Mn (III) Species during Cycling of Alkaline γ-MnO2 and the Influence of Barium Hydroxide Inclusion.* Journal of The Electrochemical Society, 2012. **159**(12): p. A2010-A2015.
[47] M. Pourbaix and J. A. Franklin. (Translated from the French, e.S.I., III5 and III6, which were original written in English). “Atlas of Electrochemical Equilibria in Aqueous Solutions”. NACE/Cebelcor. Houston, 1966.
[48] Ibanez, J.G., et al., *Chemistry Fundamentals, Part A.* Environmental Chemistry: Fundamentals, 2007: p. 11-42.
[49] Tyunina, E.Y., V.N. Afanasiev, and M.D. Chekunova, *Electroconductivity of tetraethylammonium tetrafluoroborate in propylene carbonate at various temperatures.* Journal of Chemical & Engineering Data, 2011. **56**(7): p. 3222-3226.
[50] Williams, S., *Ghost peaks in reversed-phase gradient HPLC: a review and update.* Journal of Chromatography A, 2004. **1052**(1-2): p. 1-11.
[51] Naoi, K., et al., *Second generation ‘nanohybrid supercapacitor’: evolution of capacitive energy storage devices.* Energy & Environmental Science, 2012. **5**(11): p. 9363-9373.

List of Figures

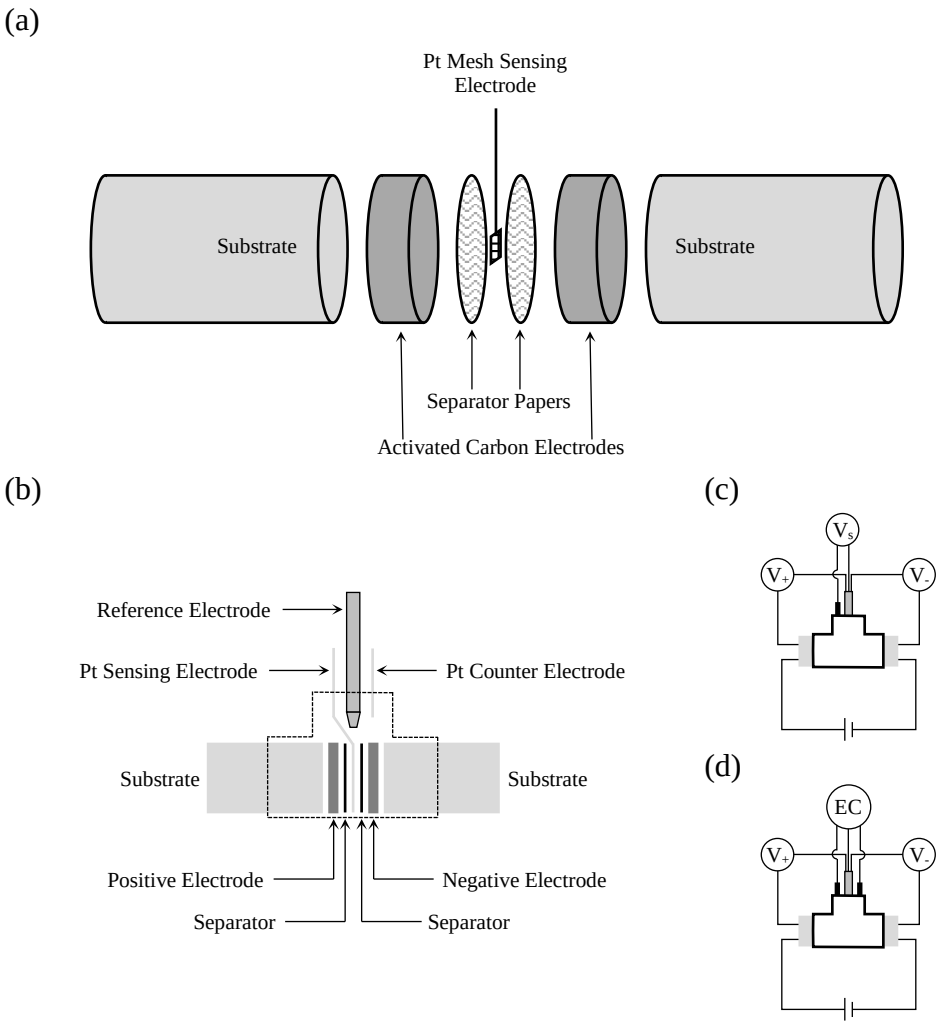

Figure 1. Schematic diagrams of the electrochemical cell used in this study. (a) Positive and negative electrode arrangement with the Pt sensing electrode sandwiched between separator papers; (b) full cell schematic showing the added reference, sensing and counter electrodes; and electrochemical control for experiments to measure (c) electrolyte fluxes (open circuit potential measurement of the Pt sensing electrode; V_s) and (d) electrode stability (fixed Pt sensing electrode potential with current flow measured; EC).

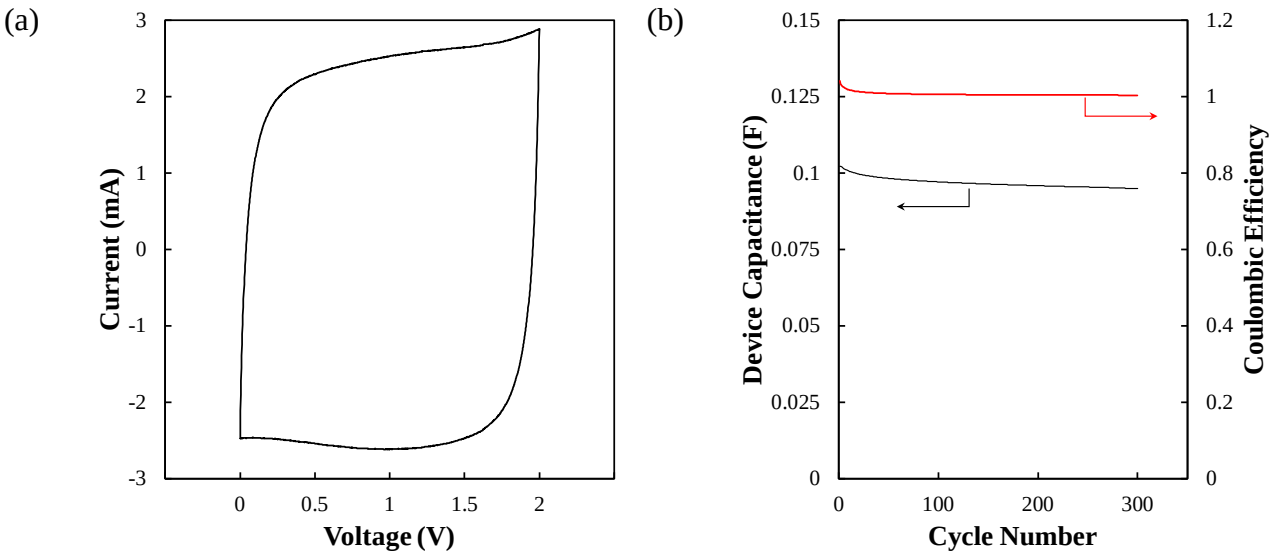

Figure 2. (a) Example of a typical cyclic voltammogram measured on a symmetrical (material and mass) activated carbon electrodes with 1 M $TEABF_4$ in ACN as the electrolyte using a sweep rate of 0.025 $V.s^{-1}$, while in (b) is shown the cell capacitance and coulombic efficiency.

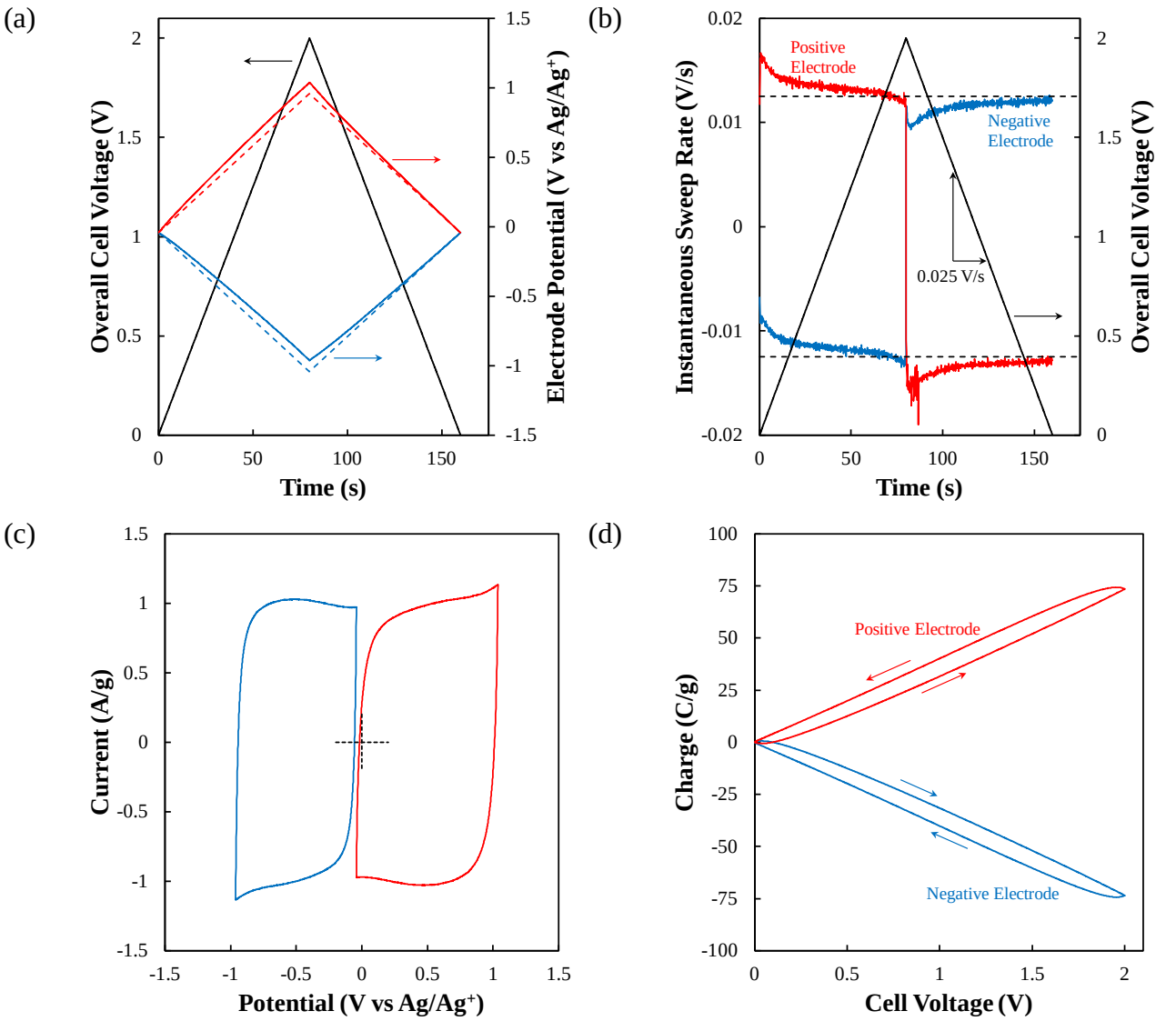

Figure 3. Individual electrode behaviour extracted from full cell two-electrode cycling. (a) Individual electrode potentials during cycling of the full two-electrode cell; (b) instantaneous individual electrode sweep rate during cycling; (c) individual electrode voltammograms with specific current; and (d) charge passed from each electrode. Note that solid lines represent measured cell voltage and individual electrode potentials, while the dashed lines represent the expected electrode potentials.

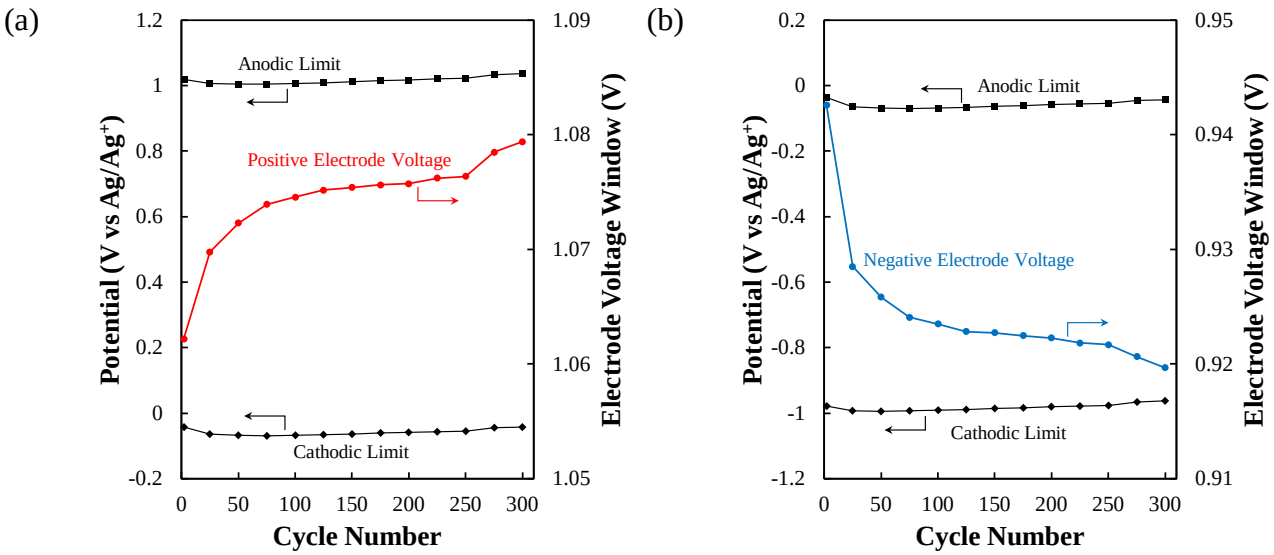

Figure 4. Assessment of (a) positive and (b) negative electrode stability with cycling. Shown are the anodic and cathodic potential limits for both electrodes, as well as the individual electrode potential window.

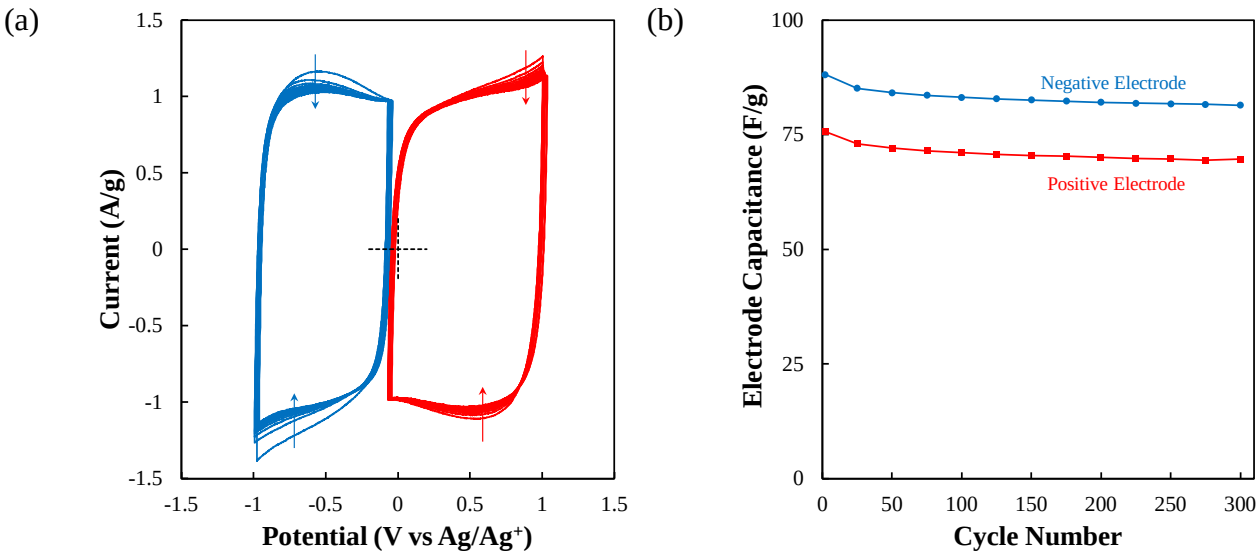

Figure 5. (a) Cycling of individual electrodes with arrows indicating ongoing cycling; and (b) individual electrode specific capacitance with cycling.

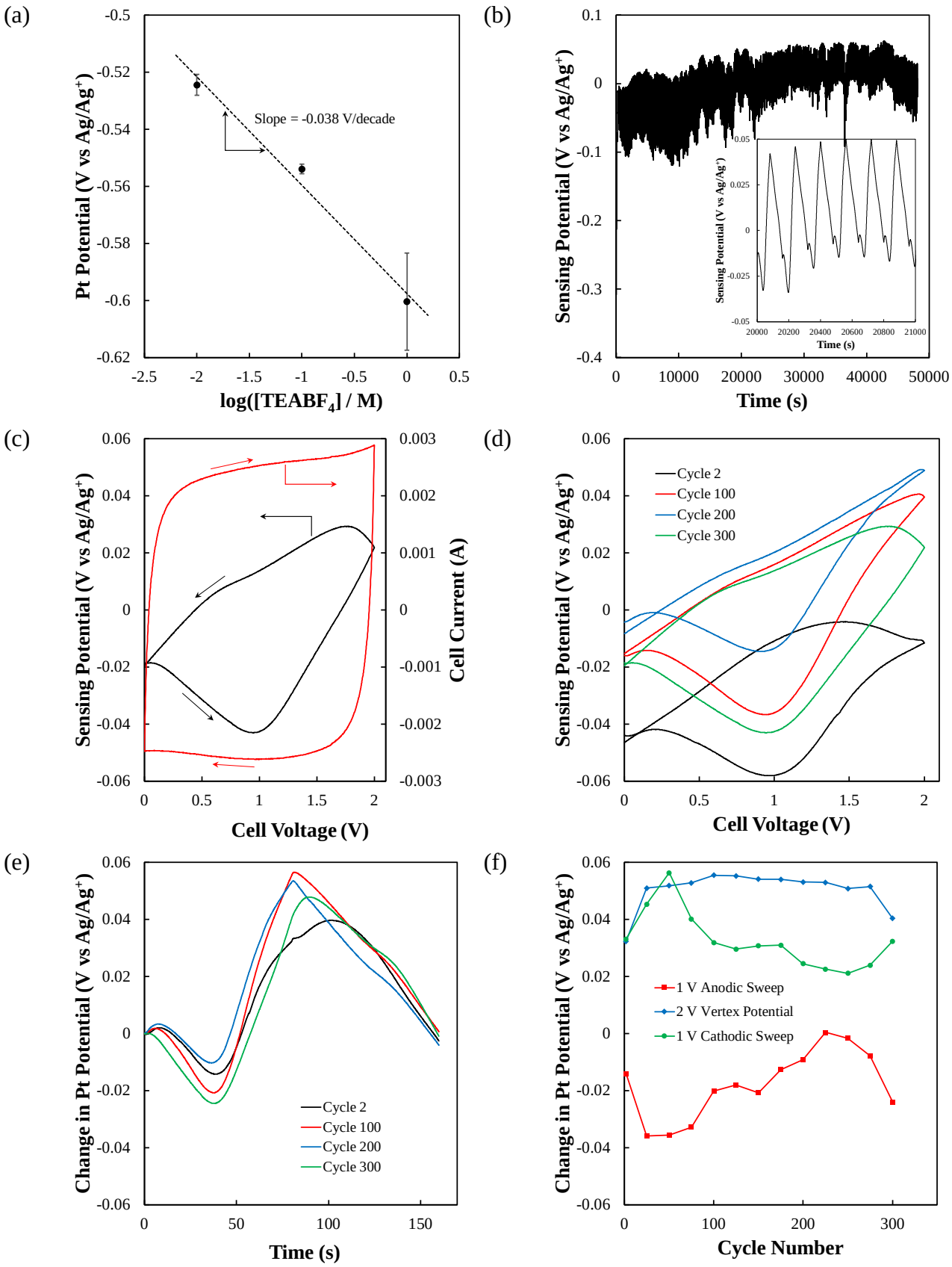

Figure 6. Pt sensing electrode potential (a) as a function of electrolyte concentration; (b) measured over the course of the cyclic voltammetry experiments (inset shows systematic changes with individual cycles); (c) as a function of cell voltage during cycling (cycle 300); (d) and (e) changes with cycle number indicating system aging; and (f) with cycling at specific potentials. Sweep rate is 0.025 $V.s^{-1}$.

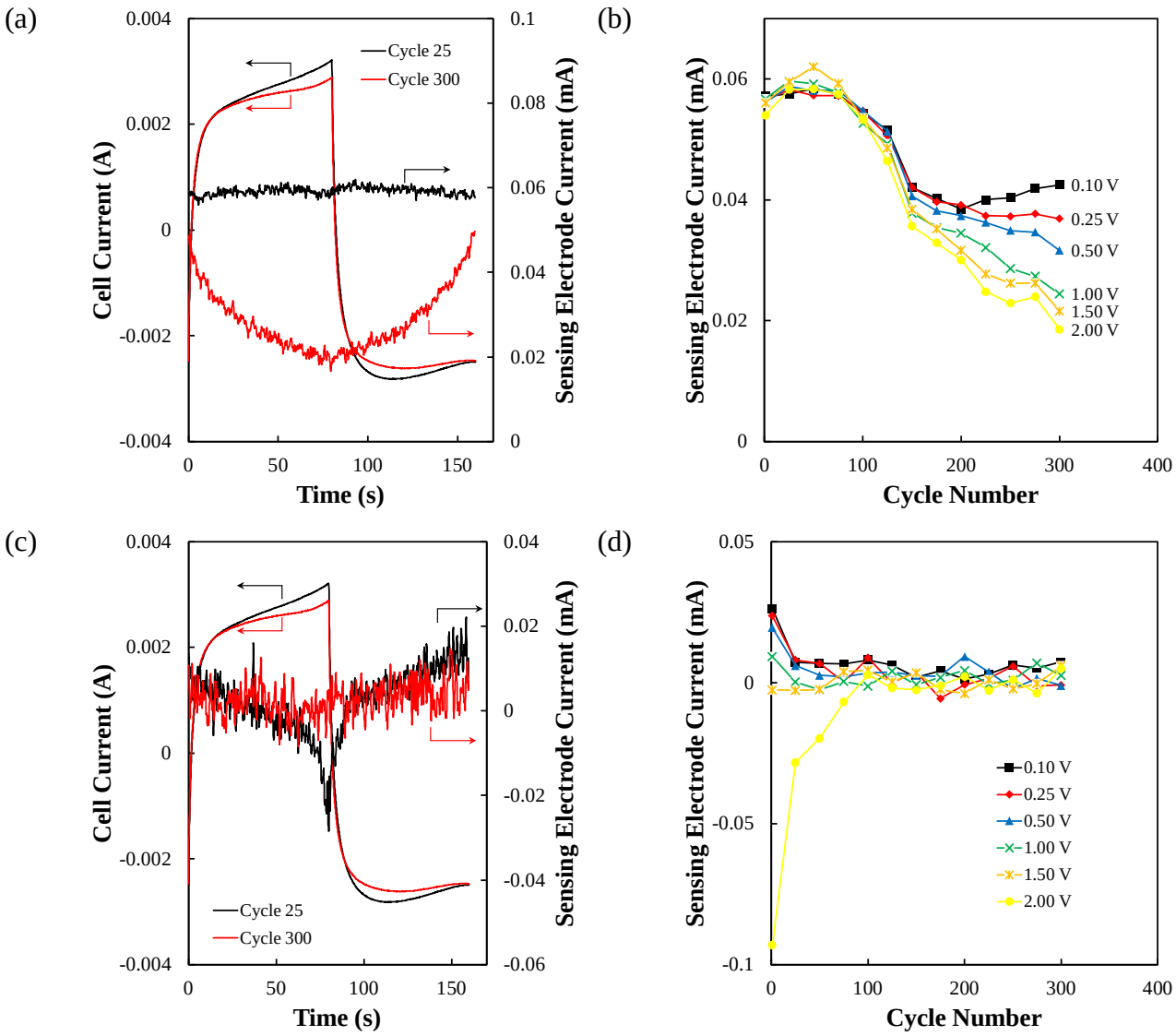

Figure 7. Outcomes from the potentiostatic control of the Pt sensing electrode set at (a) and (b) +0.5 V, and (c) and (d) -0.5 V versus the Ag/Ag^{+} reference electrode.

APPENDIXES

B. Oscillatory Current Behaviour in Energy Storage Electrode Materials

Oscillatory Current Behaviour in Energy Storage Electrode Materials

by

Marveh Forghani, Julien McCarthy and Scott W. Donne*

Discipline of Chemistry, University of Newcastle, Callaghan NSW 2308, Australia

Abstract

Here we report on unexpected oscillations in current observed during a step potential electrochemical spectroscopy (SPECS) study of manganese dioxide and nickel hydroxide electrodes in an alkaline electrolyte, conditions traditionally considered as a battery system, although more often now associated with electrochemical capacitors. These oscillations in current were observed at short times (<0.5 s) after each potential step in the SPECS experiment and were modelled in a similar fashion to a damped harmonic oscillator. They were associated with capacitive processes in the electrode because of their response time and were interpreted in terms of the competition between the rates of charge transfer and surface charge dissipation from the three-phase boundary between the electroactive material, the conductive additive and the electrolyte in the electrode. The presence of current oscillations in fundamentally insightful but detracts from the overall performance of these electrodes.

*Communicating author (Scott W. Donne)

P: +61 2 4921 5477; F: +61 2 4921 5472; E: scott.donne@newcastle.edu.au

Keywords: alkaline manganese dioxide and nickel hydroxide electrodes; electrochemical capacitors; current oscillations; three-phase boundary

1. INTRODUCTION

The sustainable supply of energy is a massive issue faced by society. The current global energy breakdown still shows considerable dependence on fossil fuels, which is neither sustainable nor environmentally friendly [1, 2]. Many renewable energy technologies exist and are being developed for commercial use [3]. What is of importance with the introduction of renewable technologies is to ensure a stable and reliable base load of energy supply [4]. Given the output variability associated with many renewable energy technologies, some form of energy storage will be required [5-7].

Energy can be stored in many ways, but electrochemical energy storage and conversion devices are an excellent option, providing efficient and cost-effective energy storage and delivery [8]. This category includes systems such as batteries, capacitors and fuel cells [9]. In contemporary society the importance and impact of these technologies continues to grow, mostly providing portable power for all scales of electronic device. Moreover, their use is also growing in larger scale stationary applications, such as in grid energy storage to complement renewable energy technologies [10].

Electrochemical capacitors are rapidly gaining popularity as a power supply because of their high specific power ($>10^3$ $W.kg^{-1}$) and excellent cyclability ($>10^5$ cycles with minimal fade) [9, 11, 12]. Their main limitation is their relatively low specific energy (<10 $Wh.kg^{-1}$) [13, 14], meaning that the cost per unit energy from electrochemical capacitors is relatively high [15, 16], and that devices based on this technology are somewhat limited to pulse applications [17]. Nevertheless, this shortcoming has stimulated considerable global efforts to overcome this issue [18]. Typically, the focus of these activities is on the development of advanced materials and electrolytes, as well as on device engineering [19, 20].

Commercially available electrochemical capacitors are based typically on carbon electrodes in a non-aqueous electrolyte [21]. The most common material is activated carbon, although many other polymorphs of carbon have been examined, including carbon nanotubes (CNTs), either single

or multi-walled, graphene, fullerenes and carbide derived carbons [22-29]. These materials store energy via charge separation at the electrode-electrolyte interface, otherwise known as the electrical double layer (EDL). In this case the amount of charge stored is dependent on the combination of the electrolyte ions (size, charge density, mobility and solvation) and the carbon electrode (conductivity, particle size, surface area and porosity), with the optimal combination providing the highest capacitance. This type of charge storage is quasi-2D in nature, being confined to the accessible electrode-electrolyte interface [30]. Generally, the specific capacitance of these materials is relatively low (~120 $F.g^{-1}$), which has a direct impact on their energy output [21].

An approach used widely in the literature to increase energy output is the use of materials exhibiting pseudo-capacitance [25, 31]. In this case the electrode material stores charge by a combination of electrical double layer formation coupled with facile redox reactions at or near the electrode-electrolyte interface [30]. The notion of pseudo-capacitance arises from the electrochemical behaviour of these redox active species being indistinguishable from those that exhibit electrical double layer formation [32]. The nature of the redox processes depends on the specific material being used, as well as the electrolyte [33]. Materials exhibiting pseudo-capacitive behaviour include metal oxides, nitrides, and sulfides, as well as conducting polymers [18, 34-37]. These types of materials can increase the specific capacitance by providing a higher density of charge storage sites at the electrode-electrolyte interface, as well as enabling 3D charge storage in the bulk of the electrode material [38]. This phenomenon has opened the door for materials conventionally considered as battery materials to make in-roads into the capacitor domain [39]. However, the importance of differentiating battery-like and capacitive behaviour is a current topic of serious debate [40, 41].

Here we report on a surprising outcome arising from work on a mechanistic comparison between battery and capacitive materials, in particular manganese dioxide and nickel hydroxide. With a focus on the intermittent cycling of these materials using step potential electrochemical spectroscopy (SPECS) [42-48], an oscillatory current response to a potential step at short times

(<0.5 s) has been noted for these materials under traditional battery conditions. These observations have been interpreted in terms of the apparent charge storage mechanisms occurring in these systems, in particular, the changing rate determining step at the electrode-electrolyte interface. The consequences of this behaviour on material performance have also been addressed [49-56].

2. EXPERIMENTAL

2.1. Electroactive Materials

2.1.1. Manganese(IV) Dioxide (MnO_2)

Manganese dioxide was prepared here via electrodeposition (electrolytic manganese dioxide, or EMD) in a similar approach to that used commercially. Essentially, the EMD is prepared via anodic electrolysis of a hot (~98°C), acidic (0.3 M H_2SO_4) solution of $MnSO_4$ (1 M) onto a titanium substrate. Hydrogen evolution is the cathodic process on a copper substrate; i.e.,

Anode (Ti): $Mn^{2+} + 2H_2O \rightarrow MnO_2 + 4H^+ + 2e^-$ …(1)

Cathode (Cu): $2H^+ + 2e^- \rightarrow H_2$ …(2)

Overall: $Mn^{2+} + 2H_2O \rightarrow MnO_2 + H_2 + 2H^+$ …(3)

After sufficient EMD had been deposited the coated anode was removed from the plating bath and physically stripped of its EMD, which was subsequently milled (Frtisch Pulverisette 6 zirconia mill) to a -107 μm particle size (mean of 45 μm), neutralized and washed to remove plating electrolyte, and then dried at 110°C before use.

2.1.2. Nickel(II) Hydroxide ($Ni(OH)_2$)

$NiSO_4.6H_2O$ (Sigma-Aldrich; >99%) was dissolved into Milli-Q water after which the pH was increased gradually (to a pH of 9) with the addition of 0.1 M NH_4OH to precipitate $Ni(OH)_2$. This suspension was then filtered and washed thoroughly with Milli-Q water before being dried at 200°C in air.

2.2. Material Characterization

Structural characterization of all materials was carried out using X-ray diffraction (Phillips XPert diffractometer) with Cu Kα radiation (λ = 1.5418 Å). Scans were recorded in the 2θ range from 10-90° using a step rate of 0.005°2θ.min^{-1}.

Morphology was assessed using a Ziess Sigma VP field emission scanning electron microscopy (FESEM) on samples that had been carbon coated to prevent charging.

Gas adsorption experiments were carried out using a Micromeritics ASAP2020 Surface Area and Porosity Analyzer. Samples were degassed under vacuum for 24 hours at 120°C. Adsorption measurements were conducted using N_2 as the adsorbate at 77 K over the partial pressure (P/P_o) range of 0.05-0.30. Material surface area was determined using the linearized BET isotherm.

The electronic conductivity was measured on a pellet of the material compressed to different pressures. The relationship between pellet resistance (R; Ω) and applied pressure (P; MPa) is asymptotic in nature with the asymptote (R_i; Ω) being the intrinsic resistance in the absence of grain boundary effects; i.e.,

$$R = a_1 \exp(-a_2 P) + R_i \quad \ldots(4)$$

where a_1 and a_2 are fitting parameters. The intrinsic resistance was then converted to conductivity (σ; S.cm^{-1}) using [44]:

$$\sigma = \frac{1}{\rho} = \frac{L}{R_i A} \quad \ldots(5)$$

where ρ is the material resistivity (Ω.cm), L and A are the pellet thickness (cm) and area (cm^2), respectively.

2.3. Electrochemical Cell Assembly

Electrode inks were prepared by mixing the solid components (active material (80%), conductive carbon black (Vulcan XC72R; Cabot; 15%) and binder (polyvinylidene difluoride;

PVdF; Fluka; 5%) with a mortar and pestle. This mixture was then dispersed in N-methylpyrrolidinone (NMP; Sigma-Aldrich) using a 20:1 solvent:solids mass ratio.

Electrode substrates were 10 mm diameter (50 mm long) 316 stainless steel rods, the end of which had been polished with 1200 grit emery paper. 50 μL of the previously prepared ink was drop-cast onto the polished end of the stainless steel substrate before being allowed to dry at ambient temperature to form the working electrode. The counter electrode was prepared similarly except with 100 μL of the activated carbon ink.

The electrochemical cell was a 10 mm Swagelok perfluoroalkane (PFA) T-junction. The coated working and counter electrodes were inserted from opposing ends of the T-junction separated by two layers of Celgard separator paper. These were pressed together at 170 MPa using a hydraulic ram and secured in place while under pressure. The cell was then filled with electrolyte and an appropriate reference electrode secured in place in the perpendicular port.

2.4. Electrochemical Protocol

All electrochemical experiments were conducted using an Iviumstat multichannel potentiostat. Before experimentation, the electrochemical cell was allowed to equilibrate for 24 h at open circuit potential, after which it was subjected to 250 cycles of cyclic voltammetry (CV) at 0.025 $V.s^{-1}$ between the anodic and cathodic potential limits to establish steady state cycling. CV cycling was finished at the cathodic potential limit, after which a step potential electrochemical spectroscopy (SPECS) experiment was carried out. Here the electrode was subjected to a series of anodic and then cathodic potential steps (0.010 or 0.025 V) with a rest time of 30-300 s between each step. Exact conditions depend on the electro-active material under study. During the rest time the current flow was measured as a function of time (i-t transient). This was carried out for one full cycle across the potential window.

3. RESULTS AND DISCUSSION

3.1. Physical Characterization

X-ray diffraction patterns of the electro-active materials are shown in Figure 1. The patterns are all consistent with the expected material phases. The EMD prepared is relatively crystalline and has the γ-MnO_2 structure consistent with alkaline grade manganese dioxide [57]. Likewise, the $Ni(OH)_2$ is also relatively crystalline with the expected structure (hexagonal brucite β-$Ni(OH)_2$ with space group $P\bar{3}m1$) [58]. Crystallite sizes estimated from the diffraction patterns and the Scherrer equation are shown in Table 1. Both materials are nano-structured, with the $Ni(OH)_2$ material being the most crystalline.

SEM images of the electroactive materials are shown in Figure 2. Here the γ-MnO_2 (EMD) and $Ni(OH)_2$ appear as agglomerates of much smaller particles.

BET specific surface area data is also shown in Table 1. The electroactive materials have modest surface areas compared to typical activated carbons used in electrochemical capacitors [44, 59, 60], although with varying degrees of micro-porosity. The chemical precipitation process carried out for $Ni(OH)_2$ has led to a reasonably high surface area. The electrodeposition process at relatively low current densities used to make γ-MnO_2 has led to the lowest surface area material.

Electronic conductivity data for the electroactive materials is also shown in Table 1. The technique used here to measure conductivity at increasing compaction pressures enables an assessment of the intrinsic material conductivity in the absence of grain boundary effects. EMD (γ-MnO_2) is also known to be a semiconductor, with the conductivity measured here consistent with the literature [61]. Conversely, $Ni(OH)_2$ is a very poor electronic conductor, with a conductivity several orders of magnitude lower [62, 63].

3.2. Cyclic Voltammetry

Each of the electroactive materials were cycled at 0.025 $V.s^{-1}$ in common electrolytes, as shown in Figure 3. This was done to establish steady state cycling, with the data shown in Figure 3

being cycle 250. Each of these experiments were conducted using a three-electrode cell in which the material of interest was the working electrode. Experimental conditions and output capacitance values are listed in Table 2.

Ruthenium dioxide is the prototypical pseudo-capacitive material [30], whereupon cycling in acidic electrolytes it undergoes a reversible redox reaction between Ru^{4+} and Ru^{3+}; i.e.,

$$RuO(OH)_x + \delta H^+ + \delta e^- \leftrightarrow RuO(OH)_{x+\delta} \quad \ldots(6)$$

where x is the extent of hydration of the starting material, and δ the extent of redox cycling. However, as a result of the cost of ruthenium (US$8134 per kg, [64]), electrochemical capacitors based on ruthenium dioxide have found use only in specialty applications. Lower cost alternatives with the same behaviour have been sought. In this regard, manganese dioxide has attracted considerable attention in the literature, where it has had a long history as a battery material [65-67], and in more recent times in electrochemical capacitors. Manganese dioxide can undergo redox cycling between Mn^{4+} and Mn^{3+}; i.e.,

$$MnO_2 + \delta M^+ + \delta e^- \leftrightarrow M_\delta MnO_2 \quad \ldots(7)$$

where δ is again the extent of ionic association with the manganese dioxide. In a neutral aqueous medium like 0.5 M K_2SO_4 the manganese dioxide behaves as expected for a pseudo-capacitive material; i.e., a box-like voltammogram, as in Figure 3. As indicated in Table 2, the γ-MnO_2 phase used here is a semiconductor and so can sustain potential differences in the bulk structure. As such, when redox processes such as Eqn (7) take place, the associated charge (M^+/e^-) can diffuse into the bulk of the material to more fully utilize the structure. γ-MnO_2 is known to form a solid solution of intercalated species within its structure, hence the non-stoichiometric redox reaction in Eqn (7). Ideally this is advantageous; however, relatively slow redox kinetics and mass transfer limit full material utilization [46, 68]. In 0.5 M K_2SO_4 the associated ionic species is K^+, which remains essentially on the surface of the manganese dioxide because of slow mass transfer. However, in 1 M KOH, where the γ-MnO_2 can function as a battery electrode [69], protons (H^+) are intercalated into the structure [70], and these are much more mobile [71]. This is very evident in Figure 3, where a

much larger current response is observed, together with a more substantial capacitance, indicating better material utilization. Also apparent in Figure 3 are processes associated with localized redox active sites, which is likely to do with the structure of the manganese dioxide [71]. In 0.5 M K_2SO_4 where only the surface is being utilized the coulombic efficiency is as expected (A:C ratio = 1.01) for a pseudo-capacitive material. However, in an alkaline medium where a much more substantial proportion of the structure is being utilized, reversible behaviour is not observed, with a significantly lower coulombic efficiency (A:C ratio = 0.95). The increasing current at the cathodic limit also likely contributed to this poor coulombic efficiency.

Another system used commonly in the battery industry is the alkaline nickel hydroxide electrode, in which case redox cycling occurs between Ni^{2+} and Ni^{3+}; i.e.,

$$Ni(OH)_2 \leftrightarrow NiOOH + H^+ + e^- \quad \ldots(8)$$

Note that the $Ni(OH)_2$ electrode is only used in strong alkaline electrolytes due to solubility in neutral and acidic electrolytes [72, 73]. Furthermore, Eqn (8) is written in a way to suggest that there is no fractional discharge. This is indeed the case because the alkaline $Ni(OH)_2$/NiOOH electrode is a two-phase system, with a moving boundary between the $Ni(OH)_2$ and NiOOH phases, as compared to single-phase solid solution behaviour for γ-MnO_2. This is likely the result of the very poor conductivity of the nickel hydroxide (Table 1). The voltametric behaviour of nickel hydroxide in Figure 3 shows a large current response, and thus a high capacitance, indicating that it is indeed a facile redox process. Anodic and cathodic peaks corresponding to redox processes in distinct localized sites are also apparent. As was the case with manganese dioxide, the coulombic efficiency is relatively low (A:C ratio = 0.86) suggesting a substantial difference in kinetic or mass transfer in the anodic versus cathodic sweep directions.

3.3. Step Potential Electrochemical Spectroscopy (SPECS)

3.3.1. Charge Storage Processes

To characterize these electrode systems further, SPECS has been applied. In this technique a

sequence of small potential steps is applied to the electrode under study to cover one full cycle. After each potential step (ΔE) the resultant current (i; $A.g^{-1}$) is measured as a function of time (t; s) to generate a series of i-t transients. As has been reported previously [43], the total current (i_T) can be broken down into contributions from capacitive (i_C), diffusive (i_D), and residual (i_R) processes, each of which are differentiable in terms of their response time; i.e.,

$$i_T = i_C + i_D + i_R \quad \ldots(9)$$

Capacitive processes are typically very facile, and are able to be modelled by the response to a potential step (ΔE; V) of an equivalent circuit consisting of the series arrangement of a resistor (R; $\Omega.g$) and capacitor (C; $F.g^{-1}$) [74]; i.e.,

$$i_C = \frac{\Delta E}{R}\exp\left(-\frac{t}{RC}\right) \quad \ldots(10)$$

The response of this type of process can be summarized via the time constant (τ; s), which is given by:

$$\tau = RC \quad \ldots(11)$$

Literature reports [46] have also shown that it is possible to differentiate capacitive processes within the electrode, in particular those associated with the geometric or porous surfaces, given the expectation that ionic movement in the electrolyte is inhibited in pores compared to the bulk electrolyte.

Diffusional processes within these electrodes can take on many different forms. Conventionally for intercalation electrodes like manganese dioxide, the expectation is that diffusion corresponds to the mass transport of intercalated ions into the bulk structure. Similar processes occur for the nickel hydroxide electrode, although in this case diffusion is associated with the movement of the boundary between the $Ni(OH)_2$ and NiOOH phases. Whatever guise diffusion takes, it is present in all electrochemical capacitor electrodes. The most straightforward representation of diffusion is based on the Cottrell equation for semi-infinite planar diffusion [74]; i.e.,

$$i_D = nFAC\left(\frac{D}{\pi t}\right)^{1/2} = \frac{a_0}{t^{1/2}} \quad \ldots(12)$$

where n, F, A, C and D have their usual electrochemical significance, and a_0 is a fitting constant compiling all constants in the expression. Alternative diffusion models can be used depending on the system at hand, such as finite length (rather than semi-infinite) planar, spherical and double plane models [75]. Whatever model is chosen, diffusional processes are invariably slower than capacitive processes.

Residual processes are the kinetically slow, background processes occurring in electrodes, that can be indicative of poor electrode stability. They become apparent as a non-zero current towards the end of the rest period after a potential step and can be modelled through the use of a constant current; i.e., i_R.

3.3.2. Pseudo-Capacitive System

Here the performance of manganese dioxide in 0.5 M K_2SO_4 has been used as an example of a pseudo-capacitive system. Figures 4(a) shows an example of an i-t transients for manganese dioxide in 0.5 M K_2SO_4 (+0.025 V anodic step to 0.40 V vs SCE). Here the current response to a 0.025 V potential step is quite large as a result of moderate kinetics associated with the redox process in Eqn (7).

The SPECS data for these pseudo-capacitive materials, including its breakdown into capacitive, diffusive and residual contributions, has also been converted into voltametric data, an example of which is shown in Figure 4(b) at 0.025 $V.s^{-1}$ [32, 38, 42-48]. For manganese dioxide the distribution of current at this sweep rate is equitable between the geometric and porous capacitances, and the diffusive processes. This is likely due to moderate charge transfer kinetics, as well as the semiconducting nature of the electro-active material limiting the distribution of charge throughout the electrode. Further information on the breakdown of charge storage for this electrode is shown in Figure 4(c).

3.3.3. Battery Electrode Systems

The manganese dioxide examined previously is a known pseudo-capacitive system, in which its response is similar in nature to the electrical double layer electrodes, hence the term pseudo-capacitance. Many articles have been published in recent times where the materials being examined for pseudo-capacitive behaviour originated in the battery literature [9]. Certainly, manganese dioxide is an example of this, although its use in a neutral 0.5 M K_2SO_4 electrolyte is apparently what makes it pseudo-capacitive, since in an alkaline electrolyte it exhibits battery-like behaviour [76]. Similarly, nickel hydroxide in an alkaline electrolyte is a battery electrode, as used extensively in Ni-Cd and Ni-MH rechargeable batteries [77]. Here we have explored these systems to compare and contrast their behaviour to pseudo-capacitive electrodes.

Figure 5 shows a typical i-t transient resulting from a potential step applied to (a) manganese dioxide and (b) nickel hydroxide electrodes in 1 M KOH. Clearly the response is different to the pseudo-capacitive system examined previously (Figure 4), exhibiting current oscillations at short times after the potential step. To confirm this behaviour we examined the relevant performance characteristics of the potentiostat being used to ensure it was not an electrical artefact. The Ivium Technologies potentiostat used here has a bandwidth of 800 kHz and a slew rate of 0.7×10^6 $V.s^{-1}$ [78], both of which are more than sufficient to cope with either a 0.01 or 0.025 V potential step with data sampling every 0.001 s; i.e., an expected ramp rate of 10 or 25 $V.s^{-1}$, respectively. This was also confirmed with an oscilloscope connected to the cell electrodes, showing essentially a square wave potential applied to the cell. Other circumstantial evidence to suggest that this was a real response is the fact that other electrode-electrolyte systems have been examined with this potentiostat [44, 47], using the same potential step conditions and sampling rate, without observing the phenomena here. The conclusion is that the response is representative of the electrode under study.

As mentioned previously, the response of these battery electrodes is very different compared to the pseudo-capacitive system shown previously, and as such the analysis tools and procedures we

have developed to examine SPECS data need to be modified to account for this oscillatory behaviour. Both the manganese dioxide and nickel hydroxide electrodes still have contributions from diffusive and residual processes at longer times and so this is the starting point for the analysis. It is evident from Figure 5 that the oscillatory behaviour is dissipated quite quickly, typically <0.5 s, after which only diffusive and residual processes are occurring. Therefore, diffusive (Eqn (12)) and residual currents were fitting to the i-t transient for times longer than 1 s to be certain that the oscillations had dissipated, as shown in Figures 5(a) and (b). The difference therefore between the fitted diffusional and residual processes and the experimental data was just due to the oscillations, as is shown inset in both these figures.

The starting point for modelling the oscillations is the expected current response to a potential step applied to the series combination of a resistor and capacitor, i.e., Eqn (10). This expression was chosen as the basis of the analysis because the current oscillations occur over a short timeframe, in which case the response is expected to be capacitive in nature. The appearance of the current oscillations with time is very similar in appearance to the displacement versus time response for a damped harmonic oscillator [79]. In this case an ideal harmonic oscillator is subjected to a damping force that opposes the oscillations, ultimately bringing motion to a standstill. The mathematical interpretation of the damped oscillator is given by [80]:

$$y(t) = A \cdot \exp(-\lambda t) \cdot \sin(\omega t + \phi) \qquad \ldots(13)$$

where y(t) is the instantaneous displacement of the oscillator at time t, A is the maximum amplitude of the oscillator, λ is the decay constant, ω is the angular frequency, and ϕ is the phase shift. If the decay constant is relatively large then the oscillator will essentially undergo exponential decay. Conversely, if λ is small, oscillations will continue for much longer.

In the present situation we have therefore coupled the exponential current decay for our series RC circuit with a sinusoidal oscillation; i.e.,

$$i_{C,O} = \frac{\Delta E}{R} \cdot \exp\left(-\frac{t}{RC}\right) \cdot \sin(\omega t + \phi) \qquad \ldots(14)$$

where $i_{C,O}$ is the oscillating capacitive current ($A.g^{-1}$), and ω and ϕ are the angular frequency ($rad.s^{-1}$) and phase shift (rad) of the oscillations, respectively, as described for Eqn (13). The physical origins of the sinusoidal component in the model will be addressed later. As with conventional analysis of capacitive data, where both the geometric and porous surfaces contribute to the overall response, two expressions have been used here to model the i-t transient. Figure 6 shows each of the components and their contribution to the current response of both the manganese dioxide and nickel hydroxide electrodes, respectively. From the modelling done here it is apparent that one of the fitted curves relates primarily to the current oscillations, while the other is a mostly capacitive process; i.e., little contributions from the sinusoidal component, with an opposing polarity to that which is expected. For the manganese dioxide electrode the oscillating component has a faster response compared to the opposing process, while for nickel hydroxide this arrangement is reversed; i.e., the oscillating process is slower than the opposing process. Given this differentiation the suggestion is that geometric processes are oscillating for the manganese dioxide electrode, while the porous capacitance processes are oscillating for the nickel hydroxide electrode.

With the development of this model, we have applied Eqn (14) to all i-t transients across the potential window of the electrode, in both the anodic and cathodic directions. The parameters have been analyzed using established methodologies for converting SPECS data into voltametric data [43], and hence into electrode performance data [43]. Figure 7 shows an example of the breakdown of the voltametric data predicted by analysis of SPECS data, in this case for 0.025 $V.s^{-1}$. In this data we have combined the capacitive processes together to demonstrate their effect, together with diffusive and residual processes. Figure 7(a) shows voltametric data for manganese dioxide in 1 M KOH, while Figure 7(b) contains corresponding data for the nickel hydroxide electrode in the same electrolyte. Both show evidence of the peaks observed previously in the CV data. They also show that at this sweep rate it is the capacitive processes that contribute the most to the measured current. Diffusion is more apparent in the case of the manganese dioxide electrode, likely because of its lower surface area. The background current is also similar in both cases, with apparently

irreversible electrolyte degradation (hydrogen evolution) occurring at low potentials. Electrode performance data has also been calculated from the voltametric data determined from SPECS. This is shown in Figures 7(c) and (d), corresponding to the manganese dioxide and nickel hydroxide electrodes, respectively. What is apparent initially is the substantial capacitive contributions at sweep rates higher than 0.1 $V.s^{-1}$. The effect of the current oscillations is also apparent in this sweep rate range, with a peak in capacitance at a sweep rate of ~10 $V.s^{-1}$. At higher rates the increasing capacitance is due to the high peak current in the individual potential steps, while the decrease in capacitance is due to the changing polarity of the current. Below 0.1 $V.s^{-1}$ the diffusive and residual processes begin to contribute to the capacitance, and at sweep rates slower than 0.01 $V.s^{-1}$, they are the dominant contributor.

3.4. Origin of Oscillatory Behaviour

Oscillations in electrochemical systems are not common; however, there are examples that have been reported in the literature [52]. The literature indicates that electrochemical oscillators are dependent on (i) a rate process that has a negative charge transfer resistance, and (ii) a resistive component that decreases the experimental control of the interfacial potential [56]. A negative charge transfer resistance occurs when, for example, the rate of oxidation in an electrochemical system becomes slower despite sweeping to more anodic potentials. The resistive component in the system can be associated with processes such as electrode film formation.

An oscillating system that has been reported and studied quite extensively is the electrochemical oxidation of formic acid to carbon dioxide on a platinum electrode [81, 82]. Here a dual pathway mechanism has been proposed; i.e., either direct formic acid oxidation to CO_2, or via a CO intermediate, that is dependent on oxide formation on the platinum surface. On a clean platinum electrode, direct oxidation of formic acid leads to a high current, with little contribution from the CO intermediate pathway. CO removal is related directly to the potential dependent formation of oxide on the platinum electrode. Interfacial resistance changes alter the true electrode

potential, which in turn affects oxide formation, and thus the activity of the electrode, through the dual mechanism. Another example that has been reported is the electrochemical oxidation of sulfur dioxide to sulfuric acid on a sulfur-activated platinum electrode [83, 84]. Here it was shown that this electrochemical oxidation is dependent on the applied potential, and the electrolyte sulfur dioxide and sulfuric acid concentrations. In this case the oscillations were deduced to be due to a changing rate determining step within the oxidation mechanism; i.e., switching between intermediate dithionate formation and dissociation kinetics [85]. In both of these examples of electrochemical oscillator systems it is apparent that the oscillations are due to changing interfacial or reaction rate behaviour. In this regard, and given the very short time frame of the processes observed here, we propose that the oscillations observed are due to the changing state of the active material surface as a result of the competition between the kinetics of charge transfer and the surface distribution of charge.

To attempt to explain this behaviour we will break the various processes occurring down into components dominated, or limited by, the kinetics of a particular process. It has been established previously that the electronic conductivity of manganese dioxide and nickel hydroxide materials is quite poor (Table 1), meaning that they cannot sustain significant currents individually within an electrode. As such, as is done almost invariably in the assembly of a cathode-active electrode, a conductive additive like graphite is used to ensure a good current distribution throughout the electrode. This then leads to the formation of a three-phase boundary between the electronic conductor (graphite), the ionic conductor (electrolyte), and the electroactive material, either manganese dioxide or nickel hydroxide in this case. The imposition of an applied potential different to the rest potential; e.g., a potential step in a SPECS experiment, causes redox reactions to occur in the electro-active material (Eqns (7) or (8)) at the three-phase boundary, leading to a change in composition characteristic of the new potential. This gives rise to the expected spike in current, with its magnitude dictated by the kinetics of the charge transfer process, and the electrode area associated with the three-phase boundary. With a poorly conducting electro-active material this

compositional change only occurs in the vicinity of the three-phase boundary, quickly saturating or passivating this region, even though there are unreacted sites remaining on the electro-active material surface. At this stage, mass transport across the surface of the active material begins in response to surface concentration differences. Note again that these are short time frame capacitive processes related to the surface of the electroactive material, rather than slower bulk diffusional processes. This dissipation of charge across the electro-active material surface then depletes the charge transfer sites near the three-phase boundary, causing the electro-active material composition in these regions to drop below that expected for the imposed potential. This is effectively a reverse in the redox reaction at the three-phase boundary, leading to a current of opposite polarity. In response, charge transfer at the three-phase boundary is accelerated in the forward direction, to be again followed by charge dissipation. This process continues until the entire surface has a uniform composition. A schematic of this process is shown in Figure 8 for the nickel hydroxide electrode.

What is important here are the relative rates of charge transfer and dissipation of surface charge. In systems where there are fast charge transfer processes (such as in a battery material or pseudo-capacitive material) or charge storage processes (such as in electrical double layer formation) there is expected to be a flood of charge added to the electrode under study in response to an instantaneous change in electrode potential. If the electro-active material is highly conductive, both electronically and/or ionically, then it is less dependent on the three-phase boundary and so these charge storage processes are distributed relatively uniformly across surfaces within the electrode. Under these circumstances the i-t transient is expected to have a high peak current followed by an exponential decay in current that represents full utilization of the active material surface. However, for poorly conducting electro-active materials the dissipation of charge across the electrode surface is kinetically less facile. If charge dissipation is considerably slower than the introduction of charge to the electrode, then the i-t transient is expected to be a slow exponential decay to a residual current representing the ongoing slow dissipation, such as the case with manganese dioxide in 0.5 M K_2SO_4. However, if the processes of charge transfer and/or charge

storage, and charge dissipation are limited and comparable, then there is the potential for alternating rate limiting processes, thus giving rise to oscillations. For the manganese dioxide electrode in 1 M KOH, where limited oscillations were observed, the charge was apparently dissipated relatively quickly through the electrode. This was certainly much faster than the dissipation of charge in the nickel hydroxide electrode, in which oscillations continued for a number of cycles before equilibrium was achieved.

4. SUMMARY AND CONCLUSIONS

Herein we report on unexpected results observed for two battery electrodes consisting of manganese dioxide and nickel hydroxide in 1 M KOH after being subjected to a step potential electrochemical spectroscopy (SPECS) experiment. The observed i-t transients for both electrodes exhibit oscillations at short times after each potential step that are dissipated quite quickly (<0.5 s). The behaviour of the alkaline manganese dioxide electrode is quite different to that observed for the same material examined in 0.5 M K_2SO_4. This oscillatory behaviour was interpreted in terms of the poor conductivity of both manganese dioxide and nickel hydroxide, and the competition between the kinetics of charge transfer at the three-phase boundary between the electro-active material, the electronic conductor (graphite) and the ionic conductor, compared to the dissipation of charge across the remainder of the electro-active material surface. The observation of this phenomena emphasizes the importance of the three-phase boundary in semi-conducting electrodes.

5. ACKNOWLEDGEMENTS

MF acknowledges the University of Newcastle for the provision of a PhD scholarship.

6. REFERENCES

1. Lin, B. and B. Xu, *How to promote the growth of new energy industry at different stages?* Energy Policy, 2018. **118**: p. 390-403.
2. Singh, R.K., A. Sarkar, and J.P. Chakraborty, *Influence of Alternate Fuels on the Performance and Emission from Internal Combustion Engines and Soot Particle Collection Using Thermophoretic Sampler: A Comprehensive Review.* Waste and Biomass Valorization, 2018: p. 1-23.
3. Bull, S.R., *Renewable energy today and tomorrow.* Proceedings of the IEEE, 2001. **89**(8): p. 1216-1226.
4. Balachandra, P., H.S.K. Nathan, and B.S. Reddy, *Commercialization of sustainable energy technologies.* Renewable Energy, 2010. **35**(8): p. 1842-1851.
5. Østergaard, P.A., *Transmission-grid requirements with scattered and fluctuating renewable electricity-sources.* Applied Energy, 2003. **76**(1): p. 247-255.
6. Andersen, A.N. and H. Lund, *New CHP partnerships offering balancing of fluctuating renewable electricity productions.* Journal of Cleaner Production, 2007. **15**(3): p. 288-293.
7. Soloveichik, G.L., *Battery technologies for large-scale stationary energy storage.* Annual review of chemical and biomolecular engineering, 2011. **2**: p. 503-527.
8. Hall, P.J. and E.J. Bain, *Energy-storage technologies and electricity generation.* Energy policy, 2008. **36**(12): p. 4352-4355.
9. Simon, P. and Y. Gogotsi, *Materials for electrochemical capacitors.* Nature materials, 2008. **7**(11): p. 845-854.
10. Dunn, B., H. Kamath, and J.-M. Tarascon, *Electrical energy storage for the grid: a battery of choices.* Science, 2011. **334**(6058): p. 928-935.
11. Frackowiak, E. and F. Beguin, *Carbon materials for the electrochemical storage of energy in capacitors.* Carbon, 2001. **39**(6): p. 937-950.
12. Mombeshora, E.T. and V.O. Nyamori, *A review on the use of carbon nanostructured*

materials in electrochemical capacitors. International Journal of Energy Research, 2015. **39**(15): p. 1955-1980.

13. McCloskey, B.D., *Expanding the Ragone plot: Pushing the limits of energy storage*. 2015, ACS Publications.
14. Winter, M. and R.J. Brodd, *What are batteries, fuel cells, and supercapacitors?* 2004, ACS Publications.
15. Lota, G., et al., *Improvement of the structural and chemical properties of a commercial activated carbon for its application in electrochemical capacitors.* Electrochimica Acta, 2008. **53**(5): p. 2210-2216.
16. Miller, J.R. and A.F. Burke, *Electrochemical capacitors: challenges and opportunities for real-world applications.* The Electrochemical Society Interface, 2008. **17**(1): p. 53.
17. Shukla, A., et al., *Electrochemical capacitors: Technical challenges and prognosis for future markets.* Electrochimica Acta, 2012. **84**: p. 165-173.
18. Vangari, M., T. Pryor, and L. Jiang, *Supercapacitors: review of materials and fabrication methods.* Journal of Energy Engineering, 2012. **139**(2): p. 72-79.
19. Zhi, M., et al., *Nanostructured carbon–metal oxide composite electrodes for supercapacitors: a review.* Nanoscale, 2013. **5**(1): p. 72-88.
20. Borenstein, A., et al., *Carbon-based composite materials for supercapacitor electrodes: a review.* Journal of Materials Chemistry A, 2017. **5**(25): p. 12653-12672.
21. Inagaki, M., H. Konno, and O. Tanaike, *Carbon materials for electrochemical capacitors.* Journal of power sources, 2010. **195**(24): p. 7880-7903.
22. Hall, P.J., et al., *Energy storage in electrochemical capacitors: designing functional materials to improve performance.* Energy & Environmental Science, 2010. **3**(9): p. 1238-1251.
23. Miller, J.R., R. Outlaw, and B. Holloway, *Graphene double-layer capacitor with ac line-filtering performance.* Science, 2010. **329**(5999): p. 1637-1639.
24. Okajima, K., et al., *High rate performance of highly dispersed C60 on activated carbon*

capacitor. Electrochimica Acta, 2005. **51**(5): p. 972-977.

25. Zhang, Y., et al., *Progress of electrochemical capacitor electrode materials: A review.* International journal of hydrogen energy, 2009. **34**(11): p. 4889-4899.
26. Yang, X., et al., *Functionalized porous carbon with appropriate pore size distribution and open hole texture prepared by H 2 O 2 and EDTA-2Na treatment of loofa sponge and its excellent performance for supercapacitors.* RSC Advances, 2016. **6**(6): p. 4365-4376.
27. Portet, C., G. Yushin, and Y. Gogotsi, *Electrochemical performance of carbon onions, nanodiamonds, carbon black and multiwalled nanotubes in electrical double layer capacitors.* Carbon, 2007. **45**(13): p. 2511-2518.
28. Barranco, V., et al., *Amorphous carbon nanofibers and their activated carbon nanofibers as supercapacitor electrodes.* The Journal of Physical Chemistry C, 2010. **114**(22): p. 10302-10307.
29. Arulepp, M., et al., *The advanced carbide-derived carbon based supercapacitor.* Journal of power sources, 2006. **162**(2): p. 1460-1466.
30. B.E. Conway, *Electrochemical Supercapacitors. Scientific Fundamentals and Technological Applications*. 1999, New York: Kluwer Academic/Plenum Publishers.
31. Chen, S.-M., et al., *Recent advancements in electrode materials for the high-performance electrochemical supercapacitors: a review.* Int. J. Electrochem. Sci, 2014. **9**(8): p. 4072-4085.
32. Forghani, M. and S.W. Donne, *Method comparison for deconvoluting capacitive and pseudo-capacitive contributions to electrochemical capacitor electrode behavior.* Journal of The Electrochemical Society, 2018. **165**(3): p. A664-A673.
33. Wang, G., L. Zhang, and J. Zhang, *A review of electrode materials for electrochemical supercapacitors.* Chemical Society Reviews, 2012. **41**(2): p. 797-828.
34. Yang, P. and W. Mai, *Flexible solid-state electrochemical supercapacitors.* Nano Energy, 2014. **8**: p. 274-290.
35. Lu, X., G. Li, and Y. Tong, *A review of negative electrode materials for electrochemical*

supercapacitors. Science China Technological Sciences, 2015. **58**(11): p. 1799-1808.

36. Han, Y. and L. Dai, *Conducting Polymers for Flexible Supercapacitors.* Macromolecular Chemistry and Physics, 2019. **220**(3): p. 1800355.
37. Cross, A., et al., *Enhanced manganese dioxide supercapacitor electrodes produced by electrodeposition.* Journal of Power Sources, 2011. **196**(18): p. 7847-7853.
38. Forghani, M. and S.W. Donne, *Duty Cycle Effects on the Step Potential Electrochemical Spectroscopy (SPECS) Analysis of the Aqueous Manganese Dioxide Electrode.* Journal of The Electrochemical Society, 2018. **165**(3): p. A593-A602.
39. Augustyn, V., P. Simon, and B. Dunn, *Pseudocapacitive oxide materials for high-rate electrochemical energy storage.* Energy & Environmental Science, 2014. **7**(5): p. 1597-1614.
40. Simon, P., Y. Gogotsi, and B. Dunn, *Where do batteries end and supercapacitors begin?* Science, 2014. **343**(6176): p. 1210-1211.
41. Brousse, T., D. Bélanger, and J.W. Long, *To be or not to be pseudocapacitive?* Journal of The Electrochemical Society, 2015. **162**(5): p. A5185-A5189.
42. Dupont, M.F. and S.W. Donne, *A Step Potential Electrochemical Spectroscopy Analysis of Electrochemical Capacitor Electrode Performance.* Electrochimica Acta, 2015. **167**: p. 268-277.
43. Forghani, M. and S.W. Donne, *Modification of the Step Potential Electrochemical Spectroscopy Analysis Protocol to Improve Outcomes.* Journal of The Electrochemical Society, 2019. **166**(13): p. A2727-A2735.
44. Dupont, M.F. and S.W. Donne, *Separating Faradaic and Non-Faradaic Charge Storage Contributions in Activated Carbon Electrochemical Capacitors Using Electrochemical Methods: I. Step Potential Electrochemical Spectroscopy.* Journal of the Electrochemical Society, 2015. **162**(7): p. A1246-A1254.
45. Dupont, M.F. and S.W. Donne, *Separating the Faradaic and Non-Faradaic Contributions to the Total Capacitance for Different Manganese Dioxide Phases.* Journal of The

Electrochemical Society, 2015. **162**(5): p. A5096-A5105.

46. Dupont, M.F. and S.W. Donne, *Faradaic and Non-Faradaic Contributions to the Power and Energy Characteristics of Electrolytic Manganese Dioxide for Electrochemical Capacitors.* Journal of The Electrochemical Society, 2016. **163**(6): p. A888-A897.
47. Abbas, S.A., et al., *Carbon hollow spheres as electrochemical capacitors: Mechanistic insights.* Energy Storage Materials, 2019.
48. Dupont, M.F., et al., *Effect of electrolyte cation on the charge storage mechanism of manganese dioxide for electrochemical capacitors.* Electrochimica Acta, 2018. **271**: p. 337-350.
49. Zhang, G., et al., *A One-Step and Binder-Free Method to Fabricate Hierarchical Nickel-Based Supercapacitor Electrodes with Excellent Performance.* Advanced Functional Materials, 2013. **23**(29): p. 3675-3681.
50. Laguna-Bercero, M., et al., *Improved stability of reversible solid oxide cells with a nickelate-based oxygen electrode.* Journal of Materials Chemistry A, 2016. **4**(4): p. 1446-1453.
51. Osterwald, J. and H.G. Feller, *Periodic phenomena at a nickel electrode in sulfuric acid.* Journal of The Electrochemical Society, 1960. **107**(5): p. 473-474.
52. Hudson, J.L. and T. Tsotsis, *Electrochemical reaction dynamics: a review.* Chemical Engineering Science, 1994. **49**(10): p. 1493-1572.
53. Fan, X., et al., *Periodic Current Oscillation Catalyzed by δ-MnO2 Nanosheets.* ChemPhysChem, 2015. **16**(1): p. 176-180.
54. Wojtowicz, J., *Modern aspects of electrochemistry.* J. O'M. Bockris and BE Conway, Eds, 1972. **8**: p. 47.
55. Poncet, P., et al., *Electrochemical oscillatory processes.* JOURNAL DE CHIMIE PHYSIQUE ET DE PHYSICO-CHIMIE BIOLOGIQUE, 1977. **74**(4): p. 452-458.
56. Koper, M.T., *Oscillations and complex dynamical bifurcations in electrochemical systems.* Advances in chemical physics, 1996. **92**: p. 161-298.

57. Cheng, F., et al., *High-Power Alkaline Zn–MnO2 Batteries Using γ-MnO2 Nanowires/Nanotubes and Electrolytic Zinc Powder.* Advanced Materials, 2005. **17**(22): p. 2753-2756.

58. Kazimirov, V.Y., et al., *Atomic structure and lattice dynamics of Ni and Mg hydroxides.* Solid State Ionics, 2010. **181**(39-40): p. 1764-1770.

59. Browning, G.J. and S.W. Donne, *Proton diffusion in γ-manganese dioxide.* Journal of applied electrochemistry, 2005. **35**(9): p. 871-878.

60. Luo, Z., et al., *One-dimensional β-Ni (OH) 2 nanostructures: ionic liquid etching synthesis, formation mechanism, and application for electrochemical capacitors.* CrystEngComm, 2011. **13**(23): p. 7108-7113.

61. Xia, X., H. Li, and Z.H. Chen, *The Study of Semiconduction Properties of γ-MnO2 with Different Degrees of Reduction.* Journal of The Electrochemical Society, 1989. **136**(1): p. 266-271.

62. Li, H., et al., *Amorphous nickel hydroxide nanospheres with ultrahigh capacitance and energy density as electrochemical pseudocapacitor materials.* Nature communications, 2013. **4**: p. 1894.

63. Motori, A., F. Sandrolini, and G. Davolio, *Electrical properties of nickel hydroxide for alkaline cell systems.* Journal of power sources, 1994. **48**(3): p. 361-370.

64. https://www.dailymetalprice.com/metalprices.php?c=ru&u=kg&d=1%20 Retrieved 20 July, 2019.

65. Dose, W.M. and S.W. Donne, *Monitoring the Effects of Thermal Treatment on Properties and Performance During Battery Material Synthesis.* Heat Treatment-Conventional and Novel Applications, 2012: p. 269-296.

66. Donne, S.W., G.A. Lawrance, and D.A. Swinkels, *The chemostat: A novel approach to the synthesis of manganese dioxide.* Materials research bulletin, 1995. **30**(7): p. 859-869.

67. Dose, W.M. and S.W. Donne, *Optimising heat treatment environment and atmosphere of*

electrolytic manganese dioxide for primary Li/MnO2 batteries. Journal of Power Sources, 2014. **247**: p. 852-857.

68. Fellows, H.M., et al., *Modelling voltametric data from electrochemical capacitors.* Journal of Power Sources, 2019. **417**: p. 193-206.
69. Kozawa, A. and J. Yeager, *The cathodic reduction mechanism of electrolytic manganese dioxide in alkaline electrolyte.* Journal of the Electrochemical society, 1965. **112**(10): p. 959-963.
70. Walanda, D.K., G.A. Lawrance, and S.W. Donne, *Hydrothermal MnO2: synthesis, structure, morphology and discharge performance.* Journal of power sources, 2005. **139**(1-2): p. 325-341.
71. Chabre, Y. and J. Pannetier, *Structural and electrochemical properties of the proton/γ-MnO2 system.* Progress in Solid State Chemistry, 1995. **23**(1): p. 1-130.
72. Liu, H., L. Xiang, and Y. Jin, *Hydrothermal modification and characterization of Ni (OH) 2 with high discharge capability.* Crystal growth & design, 2006. **6**(1): p. 283-286.
73. Hoppe, H.W. and H.H. Strehblow, *XPS and UPS examinations of the formation of passive layers on Ni in 1 M sodium hydroxide and 0.5 M sulphuric acid.* Surface and interface analysis, 1989. **14**(3): p. 121-131.
74. Allen J. Bard and L.R. Faulkner, *Electrochemical Methodes : Fundamentals and Applications* SECOND EDITION ed. 2001: John Wiley & Sons.
75. Dupont, M.F. and S.W. Donne, *Electrolytic Manganese Dioxide Structural and Morphological Effects on Capacitive Performance.* Electrochimica Acta, 2016. **191**: p. 479-490.
76. Long, J.W., et al., *Multifunctional MnO2− carbon nanoarchitectures exhibit battery and capacitor characteristics in alkaline electrolytes.* The Journal of Physical Chemistry C, 2009. **113**(41): p. 17595-17598.
77. Liu, Y., et al., *Advanced hydrogen storage alloys for Ni/MH rechargeable batteries.* Journal

of Materials Chemistry, 2011. **21**(13): p. 4743-4755.

78. *https://www.ivium.com/wp-content/uploads/2018/03/Ivium-Manual.pdf.*
79. Reed, R., *Analysis of structural response with different forms of damping.* 1967.
80. Joo, J.M., *Use of the Logarithmic decrement to assess the damping in oscillations.* Revista de Investigacion de Fisica, 2016. **19**: p. 161901551.
81. Seland, F., R. Tunold, and D.A. Harrington, *Impedance study of formic acid oxidation on platinum electrodes.* Electrochimica Acta, 2008. **53**(23): p. 6851-6864.
82. Schmidt, T., et al., *Oscillatory behavior in the electrochemical oxidation of formic acid on Pt (100): rotation and temperature effects.* Journal of Electroanalytical Chemistry, 2001. **500**(1-2): p. 36-43.
83. O'Brien, J., J. Hinkley, and S. Donne, *The electrochemical oxidation of aqueous sulfur dioxide I. Experimental parameter influences on electrode behavior.* Journal of the electrochemical society, 2010. **157**(9): p. F111-F115.
84. O'Brien, J., et al., *The electrochemical oxidation of aqueous sulfur dioxide: A critical review of work with respect to the hybrid sulfur cycle.* Electrochimica Acta, 2010. **55**(3): p. 573-591.
85. O'Brien, J.A., J.T. Hinkley, and S.W. Donne, *Observed electrochemical oscillations during the oxidation of aqueous sulfur dioxide on a sulfur modified platinum electrode.* Electrochimica Acta, 2011. **56**(11): p. 4224-4230.

List of Tables and Figures

Table 1. Physical characterization data of the electroactive materials.

Material	**Crystal Size [nm (Miller index)]**	**BET SA ($m^2.g^{-1}$)**	**Conductivity ($S.cm^{-1}$)**
γ-MnO_2	3.4 (110) 3.1 (130) 10.2 (021) 11.9 (121) 7.8 (221), (240)	30	6×10^{-4}
β-$Ni(OH)_2$	4.3 (001) 21.3 (100) 7.2 (101) 4.9 (102) 17.2 (110) 11.2 (111)	127	4×10^{-11}

Table 2. Electrochemical performance metrics arising the cyclic voltametric characterization of materials. Sweep rate = 0.025 $V.s^{-1}$.

Material	**Electrolyte**	**Window (V)**	**Capacitance ($F.g^{-1}$)**	**A:C Ratio**
EMD (γ-MnO_2)	0.5 M K_2SO_4	0.8	64.1	1.01
	1 M KOH	1.6	315.6	0.95
$Ni(OH)_2$	1 M KOH	1.6	286.4	0.86

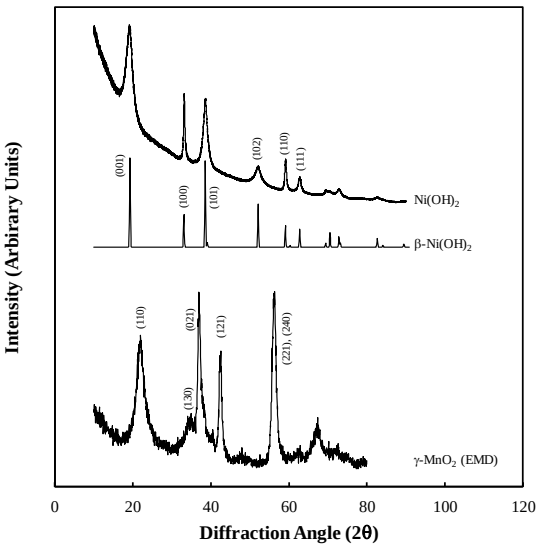

Figure 1. XRD patterns of the materials used in this study.

(a) (b)

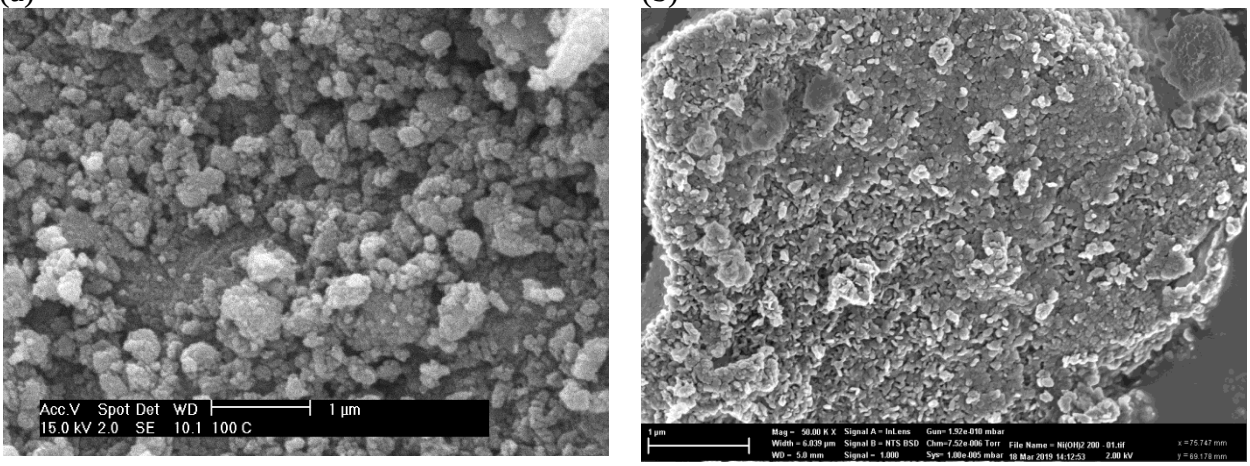

Figure 2. SEM images showing the morphology of the (a) EMD, and (b) $Ni(OH)_2$. used in this study.

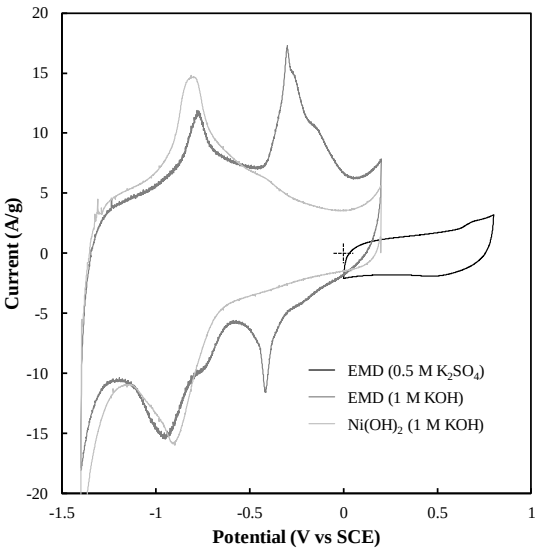

Figure 3. Cyclic voltammograms (0.025 $V.s^{-1}$) of EMD cycled in 0.5 M K_2SO_4, giving a pseudo-capacitive response, and 1 M KOH, to give a battery response, as well as $Ni(OH)_2$ in 1 M KOH, to again give a battery response.

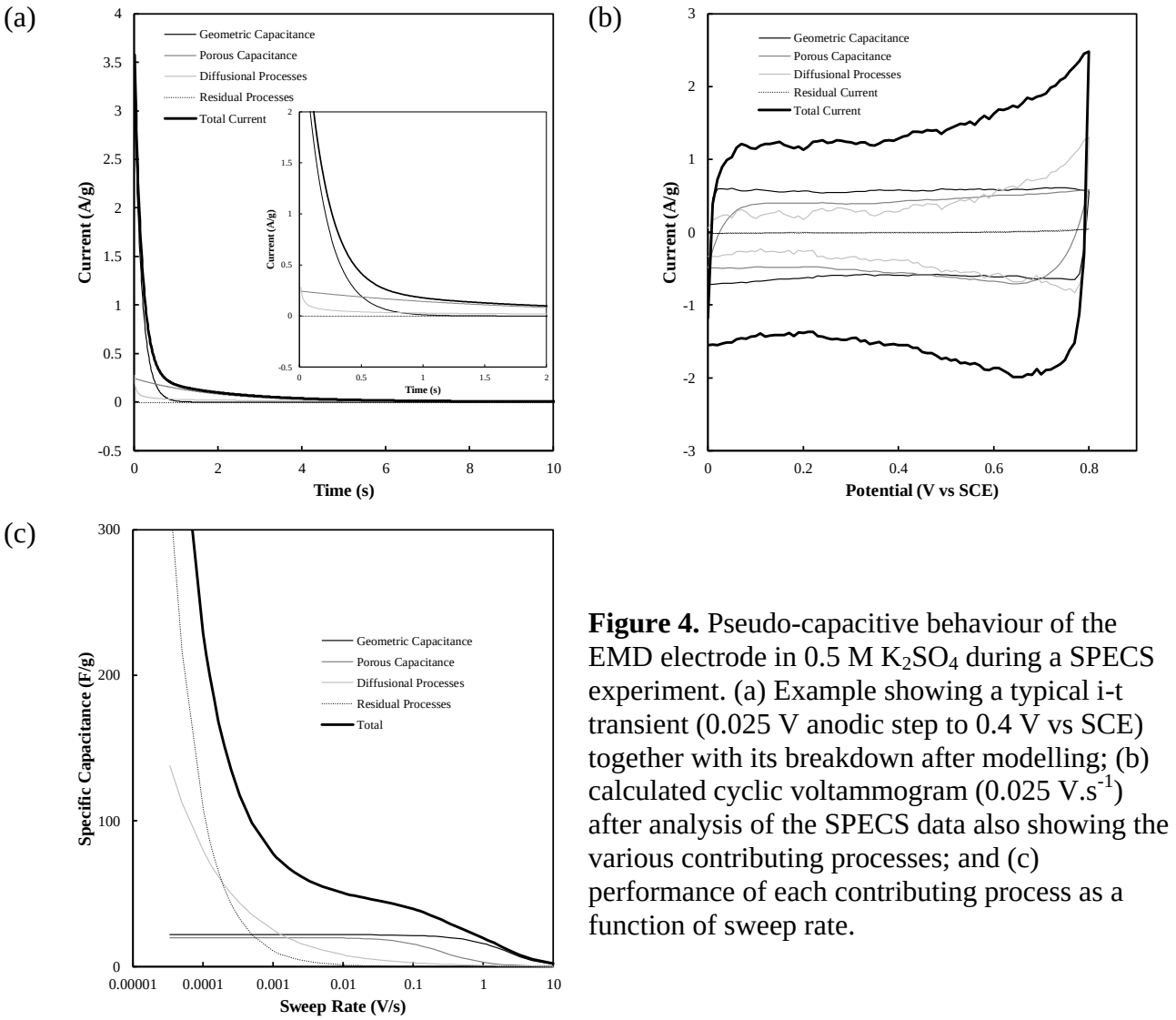

Figure 4. Pseudo-capacitive behaviour of the EMD electrode in 0.5 M K_2SO_4 during a SPECS experiment. (a) Example showing a typical i-t transient (0.025 V anodic step to 0.4 V vs SCE) together with its breakdown after modelling; (b) calculated cyclic voltammogram (0.025 $V.s^{-1}$) after analysis of the SPECS data also showing the various contributing processes; and (c) performance of each contributing process as a function of sweep rate.

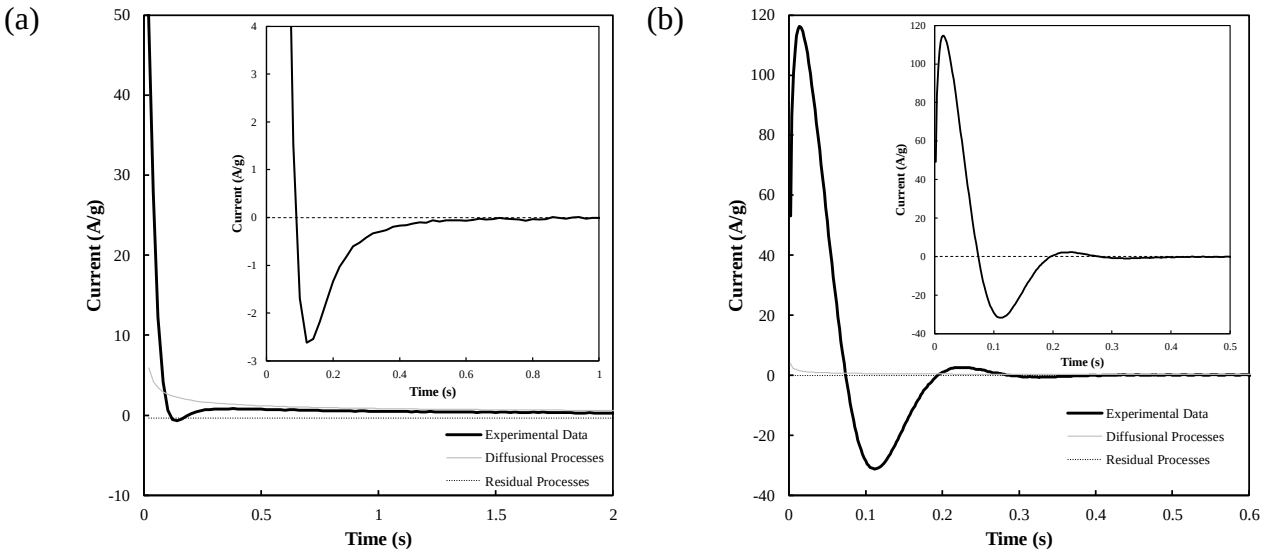

Figure 5. Typical examples of i-t transients for the (a) manganese dioxide and (b) nickel hydroxide electrodes in 1 M KOH, in this case for an anodic 0.025 V step to 0.6 V vs SCE, together with the diffusional and residual processes modelled based on i-t data for t>0.5 s. Inset in both (a) and (b) is the resultant capacitive data after the diffusive and residual processes have been subtracted.

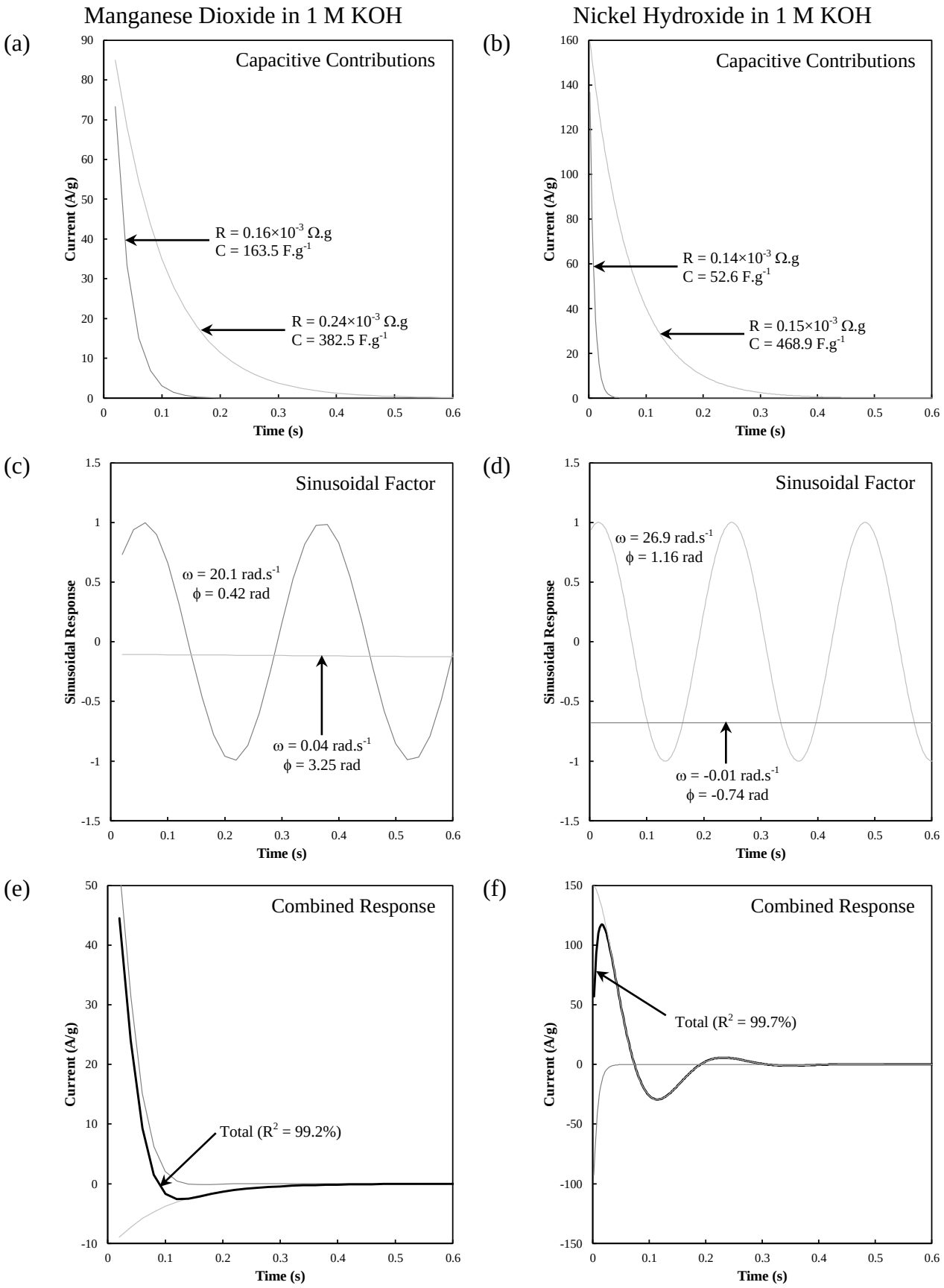

Figure 6. Analysis of the sinusoidal capacitive response for the manganese dioxide and nickel hydroxide electrodes in 1 M KOH. (a) and (b) show the capacitive contributions, (c) and (d) show the sinusoidal factors, and (e) and (f) show the combined responses for the manganese dioxide and nickel hydroxide electrodes, respectively.

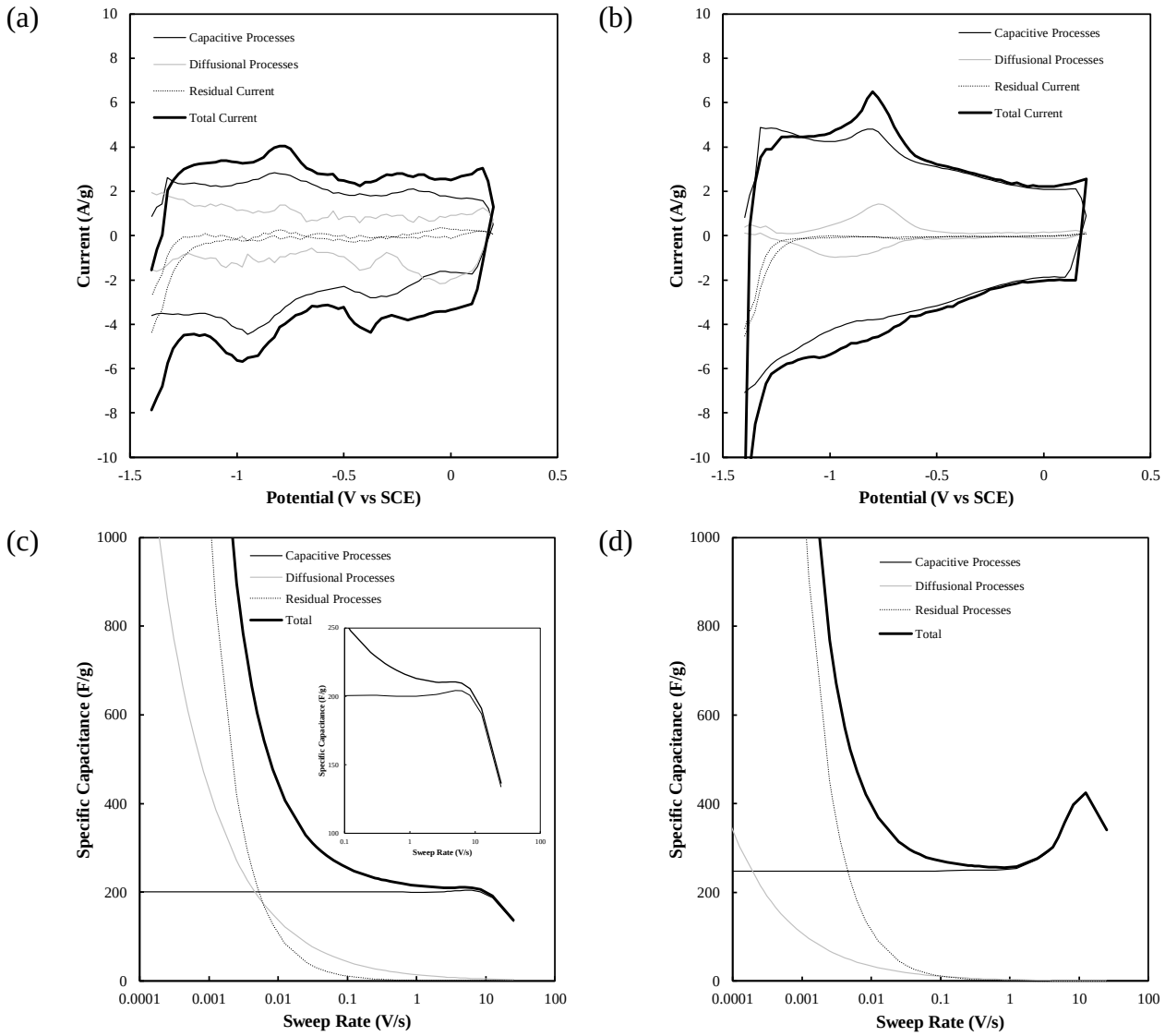

Figure 7. Example of voltametric data (a) and (b) predicted from SPECS (0.025 $V.s^{-1}$), as well as overall performance (c) and (d), including component breakdown, for the manganese dioxide and nickel hydroxide electrodes in 1 M KOH, respectively.

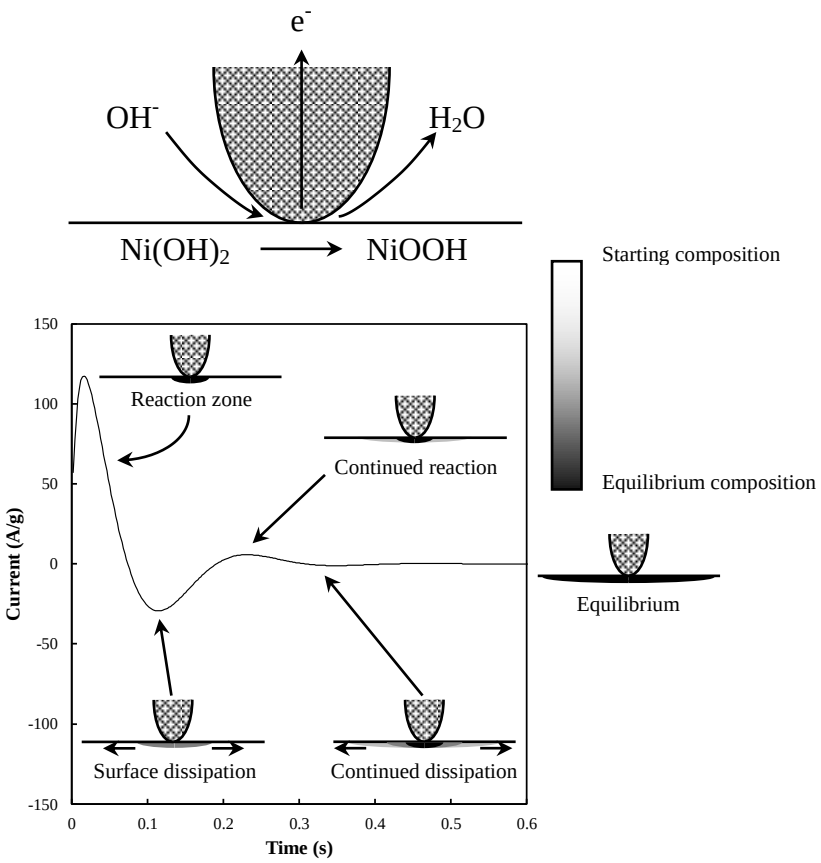

Figure 8. Schematic showing the origin of the oscillations within the i-t transient, in this case for a nickel hydroxide electrode in 1 M KOH. The model emphasizes the competition between charge transfer processes and surface dissipation of charge particularly for a poorly conducting electro-active material.